Die approbierte gedruckte Originalversion dieser Dissertation ist an der TU Wien Bibliothek verfügbar.
The approved original version of this doctoral thesis is available in print at TU Wien Bibliothek.

TECHNISCHE UNIVERSITÄT WIEN

CDL SE

DISSERTATION

Insights on the fracture and fatigue resistance of physical vapor deposited thin films

carried out for the purpose of obtaining the degree of Doctor technicae (Dr. techn.), submitted at TU Wien, Faculty of Mechanical and Industrial Engineering,

by

Lukas ZAUNER

[redacted]

under the supervision of

Ass. Prof. Dipl.-Ing. Dr.techn. Helmut Riedl-Tragenreif

Institute of Materials Science and Technology - E308-01-2
Applied Surface and Coating Technology

Wien, December 2022

reviewed by

Prof. Dr. Jochen Schneider
Department of Materials Chemistry
RWTH Aachen
52074 Aachen, Germany

Prof. Dr. Daniel Kiener
Department of Materials Science
Montanuniversität Leoben
8700 Leoben, Austria

TU Bibliothek Your knowledge hub WIEN

Die approbierte gedruckte Originalversion dieser Dissertation ist an der TU Wien Bibliothek verfügbar.
The approved original version of this doctoral thesis is available in print at TU Wien Bibliothek.

"*Das Volumen des Festkörpers wurde von Gott geschaffen, seine Oberfläche aber wurde vom Teufel gemacht.*"

– Wolfgang Pauli (1900-1958)

The financial support by the Austrian Federal Ministry for Digital and Economic Affairs, the National Foundation for Research, Technology and Development and the Christian Doppler Research Association is gratefully acknowledged (Christian Doppler Laboratory “Surface Engineering of high-performance Components”). We also thank for the financial support of Plansee SE, Plansee Composite Materials GmbH, and Oerlikon Balzers, Oerlikon Surface Solutions AG.

Die approbierte gedruckte Originalversion dieser Dissertation ist an der TU Wien Bibliothek verfügbar.
The approved original version of this doctoral thesis is available in print at TU Wien Bibliothek.

Affidavit:

I declare in lieu of oath, that I wrote this thesis and performed the associated research myself, using only literature cited in this volume. If text passages from sources are used literally, they are marked as such. I confirm that this work is original and has not been submitted elsewhere for any examination, nor is it currently under consideration for a thesis elsewhere. I acknowledge that the submitted work will be checked electronically-technically using suitable and state-of-the-art means (plagiarism detection software). On the one hand, this ensures that the submitted work was prepared according to the high-quality standards within the applicable rules to ensure good scientific practice ”Code of Conduct” at the TU Wien. On the other hand, a comparison with other student theses avoids violations of my personal copyright.

02.12.2022

Date

Signature

Acknowledgements

Here I would like to express my sincere gratitude to those who accompanied me during the past years, both on and off my academic path, who endured all the extra time I had to invest in research projects and helped me overcome the many hurdles in developing this thesis.

First of all, I owe special gratitude to my supervisor **Ass. Prof. Dr. techn. Helmut Riedl-Tragenreif** for providing me with the opportunity to join his research group and also take a share in his scientific career. Helmut, thank you for your everlasting commitment and support in the best way possible – whether on our shared journey through the world of fatigue, but also on topics beyond work life. Your trust in my work and the liberty you granted me for own ideas throughout this project will certainly leave a lasting impression on my future career. Thank you very much Helmut!

In line, I want to express my gratitude to the very special **CDL-SEC team – Körnsi, Ahmed, Thomas, Elias, Sophie, Anna, Tomasz, Philipp, Riße, Stefan, Arno, Alex, Philip** – with whom I had the pleasure to share a wonderful time in my life; together fighting against deadlines, broken deposition systems and last-minute presentation slides. Thank you for your sincere friendship, with you guys there was never a dull day at university. A special thank you goes to my office buddies **Rainer** and **Oliver**, I could not have asked for better everyday colleagues! Rainer you were a huge guidance during this thesis and you always helped me where I did not see the next steps. Oliver, I think it is hard for others to comprehend what we shared on our PhD journey, especially the bonding during "power hours" late at night. Thank you for always having my back (except on Mondays), and our very special "who is right"-fights.

I would also like to thank the entire **Thin Film Materials Science group** and in particular **Univ. Prof. Dr. mont. Paul Heinz Mayrhofer**, who welcomed me to this wonderful institute already many moons ago. Paul, thank you for all the fruitful discussions and your overwhelming enthusiasm for thin film science. I will particularly keep your joy for sweet coffee breaks in good memory.

A special thank you goes to **Dr. Peter Polcik, Dr. Szilárd Kolozsvári, Michael Sitter** and **Matthias Perl** from Plansee Composite Materials, without hesitating you always did

Die approbierte gedruckte Originalversion dieser Dissertation ist an der TU Wien Bibliothek verfügbar.
The approved original version of this doctoral thesis is available in print at TU Wien Bibliothek.
TU Bibliothek Your knowledge hub WIEN

your best to help me with special issues – be it sample preparation or last-minute target orders. Furthermore, I would like to thank **Dr. Oliver Hunold** and **Dr. Jürgen Ramm** from Oerlikon Balzers, for helping me keep our Innova in excellent shape and for sharing your expertise in thin film science with me. In general, thank you to our company partners for the great time we shared during meetings and conferences.

Finally, and most importantly, I would like to express my deepest gratitude to my family – **Marie-Theres, Mama, Papa, Elke, Oscar, Flo, Verena, and Frida** – for their unconditional support in every aspect of my life. It is to you **Marie-Theres**, who was the biggest force backing me up, keeping me motivated and taking huge loads off my shoulders so I could finish this thesis. My love, thank you for always being there for me, I enjoy every moment with you.

Die approbierte gedruckte Originalversion dieser Dissertation ist an der TU Wien Bibliothek verfügbar.
The approved original version of this doctoral thesis is available in print at TU Wien Bibliothek.

Contents

Die approbierte gedruckte Originalversion dieser Dissertation ist an der TU Wien Bibliothek verfügbar.
The approved original version of this doctoral thesis is available in print at TU Wien Bibliothek.

Die approbierte gedruckte Originalversion dieser Dissertation ist an der TU Wien Bibliothek verfügbar.
The approved original version of this doctoral thesis is available in print at TU Wien Bibliothek.
TU Bibliothek Your knowledge hub WIEN

List of Figures

Die approbierte gedruckte Originalversion dieser Dissertation ist an der TU Wien Bibliothek verfügbar.
The approved original version of this doctoral thesis is available in print at TU Wien Bibliothek.

Die approbierte gedruckte Originalversion dieser Dissertation ist an der TU Wien Bibliothek verfügbar.
The approved original version of this doctoral thesis is available in print at TU Wien Bibliothek.
TU Bibliothek Your knowledge hub WIEN

Die approbierte gedruckte Originalversion dieser Dissertation ist an der TU Wien Bibliothek verfügbar.
The approved original version of this doctoral thesis is available in print at TU Wien Bibliothek.

List of Symbols & Abbreviations

2θ	Diffraction angle
A_{pl}	Energy dissipated through plastic deformation
A_{tot}	Total area under load-displacement curve
B	Thickness
C, m	Paris-Erdogan fit parameters
D_{gen}	Generalized crack driving force
E	Young's modulus
E_i	Ion energy
E_{sep}	Energy of separation
F	Load
G	Energy release rate
H	Hardness
I	Intensity
I_n	Numerical constant
J	J-integral
K	Stress intensity factor
K_{Ic}	Critical stress intensity in mode I loading
L	Distance between indenter tip and cantilever pre-notch
L'	Distance between indenter tip and cantilever base
M_i	Mass of ions
M_t	Mass of target atoms
N	Number of load cycles
N_f	Load cycles to failure
P	Load
P	Potential energy
R	Micro-pillar radius
R_{gen}	Generalized crack growth resistance
S	Stress amplitude
T_i	Traction vector
U	Stored elastic energy

Die approbierte gedruckte Originalversion dieser Dissertation ist an der TU Wien Bibliothek verfügbar.
The approved original version of this doctoral thesis is available in print at TU Wien Bibliothek.
TU Wien Bibliothek Your knowledge hub

U_s ..... Binding energy of target atoms
W ..... Enegery for crack propagation
$Y(a/w)$ ..... Dimensionless geometry parameter
Z ..... Geometry factor
ΔG ..... Change in Gibb's free energy
ΔK ..... Stress intensity range
ΔK_{th} ..... Threshold stress intensity range
Γ ..... Arbitrary path around crack tip
α ..... Dimensionless factor
$\bar{\sigma}_{ij}(\theta,n)$ ..... Dimensionless function
δ ..... Crack tip opening displacement
ϵ ..... Elastic strain
η,γ ..... Constant
γ ..... Calibration parameter
γ_p ..... Plastic strain work
γ_s ..... Surface energy
λ ..... X-ray wavelength
$1/2s_2^{hkl}$, s_1^{hkl} ..... X-ray elastic constants of (hkl)-plane
ν ..... Poisson's ratio
ϕ ..... Strain energy density
ψ ..... Azimuthal tilt angle
ψ^*_{hkl} ..... Stress-free tilt angle of (hkl)-plane
σ ..... External stress
σ'_f ..... Fatigue strenght coefficient
σ_r ..... Residual stress
σ_{YS} ..... Yield strength
$\sigma_{||}$ ..... In-plane residual stress
θ ..... Angular coordinate
a ..... Half-diagonal of pyramidal indenter
a ..... Crack length
a_0 ..... Initial pre-notch depth
b ..... Cantilever width
b ..... Fatigue strenght exponent
bcc ..... Body-centered cubic
c ..... Radial crack length from indentation center
d ..... Crack depth
$d_{0,hkl}$ ..... Lattice spacing of (hkl)-plane in stress free direction
d_{hkl} ..... Lattice spacing of (hkl)-plane
f ..... Frequency

Die approbierte gedruckte Originalversion dieser Dissertation ist an der TU Wien Bibliothek verfügbar.
The approved original version of this doctoral thesis is available in print at TU Wien Bibliothek.
TU Bibliothek Your knowledge hub WIEN

$f(a/w)$	Dimensionless geometry parameter
fcc	Face-centered cubic
hcp	Hexagonal close packed
k	Stiffness
k_0	Stiffness of the unnotched cantilever
n	Diffraction order
n,α,σ_0	Ramberg-Osgood fit parameters
r	Nuclei radius
r	Radial coordinate
r^*	Critical nuclei radius
r_{pl}	Radius of the plastic zone around crack tip
rh	rhombohedral
t	Thickness
u_i	Displacement vector
v	Elongation
w	Cantilever height
x	Aluminium-Nitride mole fraction
CAE	Cathodic arc evaporation
CSM	Continuous stiffness measurement
CTOD	Crack tip opening displacement
DCMS	Direct current magnetron sputtering
DFT	Density functional theory
EPFM	Elastic-plastic fracture mechanics
FEM	Finite element method
FIB	Focussed ion beam milling
FWHM	Full width at half maximum
HCF	High-cycle fatigue
HiPIMS	High-power impulse magnetron sputtering
HRR	Hutchison, Rice, and Rosengren
LCF	Low-cycle fatigue
LEFM	Linear-elastic fracture mechanics
PSB	Persistent slip band
PVD	Physical vapor deposition
SL	Superlattice
TMB_2	Transition-metal diboride
TMN	Transition-metal nitride
VEC	Valence electron concentration
XEC	X-ray elastic constants
XRD	X-ray diffraction

Die approbierte gedruckte Originalversion dieser Dissertation ist an der TU Wien Bibliothek verfügbar.
The approved original version of this doctoral thesis is available in print at TU Wien Bibliothek.
TU Bibliothek Your knowledge hub WIEN

Die approbierte gedruckte Originalversion dieser Dissertation ist an der TU Wien Bibliothek verfügbar.
The approved original version of this doctoral thesis is available in print at TU Wien Bibliothek.

Abstract

Fatigue of structural components is classified among the most common forms of mechanical failure. For ductile materials, fatigue damage is correlated with the irreversible motion of dislocations, which manifests in surface stress concentrations followed by crack nucleation and growth. Surface engineering based on physical vapor deposited ceramic materials constitutes a promising solution to suppress this natural crack initiation and contributes to an increased fatigue life. While research has strived to unravel the mechanisms governing the coating to substrate behavior on a macro scale, limited information has been gathered on the independent response of nanostructured thin films under cyclic loads. Therefore, this thesis contributes to a fundamental understanding on the life cycle of PVD-deposited thin films targeted to improve the fatigue resistance in mechanically demanding environments. This framework ranges from the synthesis and detailed characterization of advanced thin film materials, to their micro-scale analysis under cyclic mechanical loads.

A novel methodology, connecting cyclic-bending of free-standing microcantilevers with *in-situ* synchrotron nanodiffraction, is used to investigate the intrinsic fracture and fatigue properties of thin film materials. This systematic analysis focusses on a model system of metallic *bcc*-Cr and Cr-based compounds (*fcc*-CrN, *hcp*-CrB_2, and *rh*-Cr_2O_3), to address the impact of altered bonding characters and crystal structures. Cyclic bending experiments performed up to the high cycle fatigue regime ($N = 10^7$) demonstrate that the fatigue strength of nanostructured thin films is governed by their inherent fracture resistance. In particular, cantilever cycling close to the critical stress intensity threshold is sustained without noticeable material damage, structural or stress-state changes. Within this journey, $Cr_{1.03}B_2$ was found with exceptional fracture and fatigue resistance, revealing a particular ductile character and a toughness value of $K_{Ic} = 4.3 \pm 0.3$ MPa$\sqrt{m}$.

Finding the impetus in these results, a Si alloying route is followed to evolve CrB_2 as a future protective coating material. Density functional theory calculations combined with atom probe tomography reveal a synthesis-independent Si solubility limit of ∼3-4 at.% in AlB_2-structured solid solutions. The addition of up to 17 at.% Si entails refinement of the columnar morphology, accompanied by the growth of mechanically weak Si grain boundary segregates. This microstructural separation is reflected in degraded mechanical properties,

with the film hardness and fracture resistance decreasing from $H \sim 30$ to 17 GPa and $K_{Ic} = 2.9$ to 1.7 MPa$\sqrt{m}$ with increasing Si-content, respectively. In contrast, outstanding oxidation resistance up to 1400 °C is revealed when alloying 8 at.% Si, owing to the thermally activated precipitation of Si and the B/Cr-ratio-independent growth of a stable SiO_2-based scale. Additional *in-situ* fracture toughness measurements up to 800 °C expose a brittle-to-ductile-like transition for CrB_2, increasing the fracture toughness to $K_{Ic} = 3.3$ MPa$\sqrt{m}$. Similarly, Si-precipitates in higher alloyed compositions enable extensive high-temperature plastic deformation combined with enhanced crack growth resistance.

The final part of this thesis is devoted to investigations on the synthesis of metastable Ti-Al-N thin films using high-power impulse magnetron sputtering and the particular role of increased ion-bombardment during film growth. A systematic variation of the synthesis and discharge parameters performed on $Ti_{1-x}Al_x$ composite targets cumulates in optimized deposition conditions for the low-temperature growth of cubic structured $Ti_{0.37}Al_{0.63}N$. The thin films obtain exceptional hardness of $H \sim 36$ GPa and simultaneously a low compressive stress state, with age-hardening capacity up to $H \sim 40$ GPa after annealing for 1h at 700 °C. Achieving this high Al solubility – being close to the theoretical limit of ∼67% – is seen in the preferred bombardment with process gas- and Al^+-ions, while the contribution of detrimental Ti^{n+} ($n = 1, 2$) ions is inherently low. In addition, particular sensitivity of the wurtzite phase formation for the nitrogen-to-argon flow ratio and substrate bias potential is revealed, both significantly influencing the arriving ion flux and adatom mobility on the substrate surface.

Die approbierte gedruckte Originalversion dieser Dissertation ist an der TU Wien Bibliothek verfügbar.
The approved original version of this doctoral thesis is available in print at TU Wien Bibliothek.

Chapter 1

Introduction

Today's society is inherently linked to the advances achieved in the field of materials science. The growing awareness for economic and environmental sustainability in many aspects of modern life is placing ever-increasing demands on the development of novel and superior materials. Particularly the progress of high-performance components used in aviation or internal combustion engines relies on the exploration of material systems with exceptional thermal and mechanical stability, over continuously longer service-lives [1–3]. While both technologies are certainly mature within their respective fields of application, increasing design efficiency and stringent emission standards require the current generation of material concepts to be pushed closer to their intrinsic limits [4, 5]. As a consequence, the sole optimization of bulk material properties to withstand increasing operating temperatures, oxidative and corrosive attack, while maintaining excellent mechanical properties for thousands of operating hours, is impracticable and an antiquated approach. Instead, complementary surface engineering based on the physical vapor deposition (PVD) of thin, protective coating materials takes a key-role in achieving further milestones for these technologies [6, 7].

In particular, the effect of metal fatigue – the cyclic weakening and cracking of the material from cyclic loads – receives increasing attention on this endeavor [1]. Fatigue in metals manifests in the irreversible motion of dislocation, with localized slip bands emerging on the material surface. These local stress concentrations serve to nucleate cracks, that eventually grow and extend to failure [1, 8–10]. It is the surface nature of the cracking mechanism that provides the incentive for a treatment of fatigue within surface engineering – following the intention to restrict plastic deformation in the substrate through the presence of a mechanically strong surface layer. As such, the effect of hard, ceramic coatings on the fatigue resistance of various alloys has been explored for cyclic loading conditions [11–17]. While general agreement is found within the failure pathways – originating from immediate coating fracture or interface failure [18–22] – a fundamental understanding of the mechanisms leading to the improved/degraded fatigue strengths for coated materials is still missing. Moreover,

Die approbierte gedruckte Originalversion dieser Dissertation ist an der TU Wien Bibliothek verfügbar.
The approved original version of this doctoral thesis is available in print at TU Wien Bibliothek.
TU Bibliothek Your knowledge hub WIEN

considering the fatigue failure of coated components from this macroscopic perspective, prevents an in-depth view on the actual response of the thin film material to cyclic loading.

In recent years, the increasing availability of precision micromechanical systems, along with sophisticated ion-based fabrication has opened new possibilities for small-scale fatigue testing [23]. Particular progress has been made in understanding the microscale fatigue mechanisms that govern the bulk material behavior of various metals, both from a methodical and a phenomenological point of view [24–28]. The application of micro-sized cantilever and pillar geometries further paved the way to fundamentally characterize the intrinsic fracture properties of thin films on their native length-scale [29–31]. Especially the fracture toughness of ceramic based coatings such as transition metal nitrides was extensively studied, leading to significant improvements in their fracture resistance through architectural and atomistic toughening designs [32–37]. Adopting similar micro-sized specimen, also the cyclic response of thin film materials was characterized. With the focus primarily on metallic materials (*e.g.*, Cu [38, 39], Ag [40]), interesting microstructural size-effects and dimensional constraints on crack formation have been revealed. However, despite these efforts and the available methodology, research on the microscale fatigue behavior of ceramic coatings remains a rather uncharted territory in comparison. Therefore, this field of research may serve many more exciting revelations, with great potential to guide the design of future coatings used in mechanically demanding environments.

The use of ceramic-based thin films in applications requiring increased fatigue resistance will be tied to the development of new material concepts and advances in synthesis technology. Where mechanical loads and environmental conditions exceed the property spectrum of current generation materials – focused on nitrides, carbides, and oxides – alternative classes such as transition metal diborides are highly desired [41]. These materials offer exceptional thermophysical properties, reflected in high hardness [42–44], outstanding thermal stability [45], chemical inertness, paired with unique functional behavior [46, 47]. While all ceramic coatings are considered brittle in nature, investigations have predicted [48] and verified excellent fracture tolerance of *e.g.*, W-Ta-B_2 thin films [49, 50]. Moreover, the potential of a Si-alloying route to almost universally achieve outstanding oxidation resistance within these materials, makes TMB_2s excellent candidates for future use [51, 52].

The same importance that is given to the material system will be required for the deposition technology. Although cathodic arc evaporation and magnetron sputtering have been the work horses of plasma-based deposition for decades, both technologies exhibit particular shortfalls. While the lack of ion-bombardment in sputtering is reflected in columnar and underdense film structures [53], coatings deposited through arc evaporation suffer from metallic macro-particle incorporation [54]. Both of these aspects are detrimental for the fracture resistance, generating preferred crack pathways as schematically visualized in Figure 1.1. Especially high-power

Die approbierte gedruckte Originalversion dieser Dissertation ist an der TU Wien Bibliothek verfügbar.
The approved original version of this doctoral thesis is available in print at TU Wien Bibliothek.
TU Bibliothek Your knowledge hub WIEN

impulse magnetron sputtering (HiPIMS) is seen as a promising solution, combining the benefits of the former technologies, while increasing the flexibility in the overall thin film design [55–57]. Contrary to conventional sputtering, a pulsed power-application allows to increase the contribution of ionized target species in the film forming flux, which enables denser thin film structures, enhanced mechanical properties [58], and new possibilities to access metastable thin film materials [59].

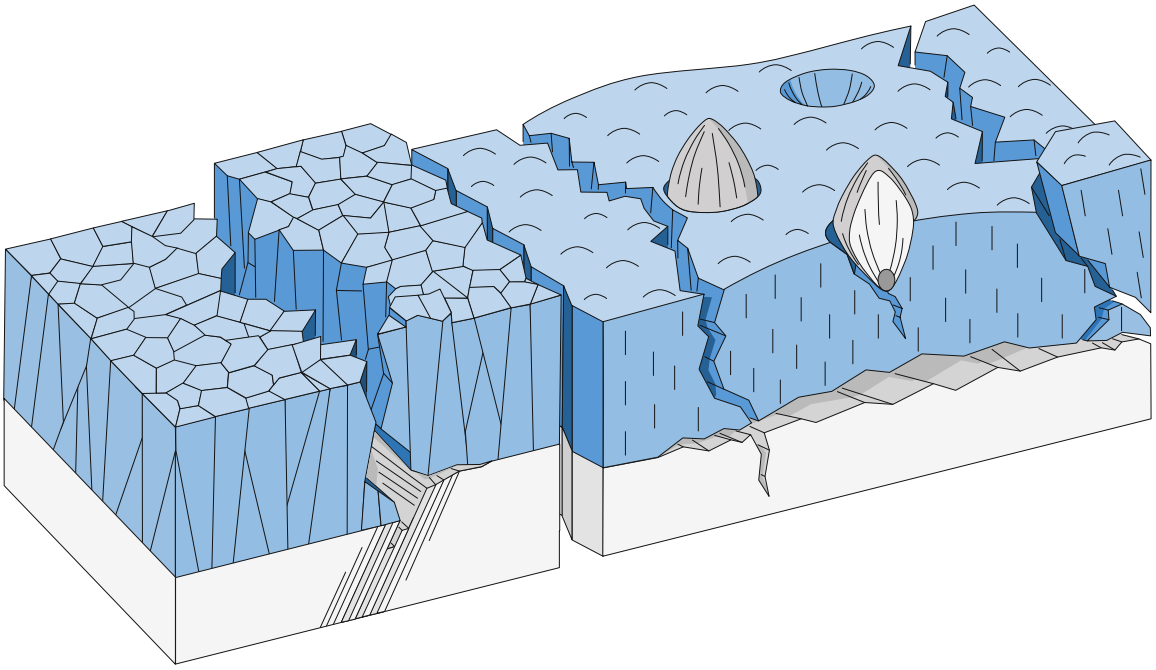

Fig. 1.1: Illustration of possible fracture pathways in PVD deposited thin films induced by static or cyclic loads. (Own unpublished work.)

In summary, this thesis aims for an increased understanding on the micro-scale behavior of nanostructure thin films under cyclic loads, to improve the mechanical durability of future thin film designs. The fracture and fatigue properties of metallic and ceramic coatings are investigated using cantilever-based micromechanics coupled with *in-situ* synchrotron analysis. The development of a Si-alloyed transition-metal diboride follows the established guidelines, with special emphasis placed on the structural, mechanical and high-temperature properties of the material. Furthermore, the complexity and challenges faced during the ion-assisted film growth of metastable nitride thin films are elucidated in the context of the HiPIMS deposition technology.

Die approbierte gedruckte Originalversion dieser Dissertation ist an der TU Wien Bibliothek verfügbar.
The approved original version of this doctoral thesis is available in print at TU Wien Bibliothek.
TU Bibliothek Your knowledge hub WIEN

Chapter 2

Physical Vapor Deposition

Today's society is to a large extent driven by technological advances, which requires engineering materials to perform more-and-more at the boundary of their intrinsic property spectrum. In this context, surface engineering based on physical vapor deposition adopts an increasingly important role, by extending the operating range and functionality of current generation materials. This is reflected in a wide range of applications that fundamentally rely on the enhanced properties provided by thin film materials, such as hard coatings for machining tools, erosion-resistant coatings for gas and aviation turbine blades, functional coatings for microelectronics, or optical coatings for laser technologies [6, 60, 61].

Physical vapor deposition is considered an atomistic process in which a thin surface layer composed of a single/several foreign/similar material(s) is deposited on a substrate material through condensation of a vapor phase in an atom-by-atom manner. The technique includes several variants, with the general differentiation according to the principles of source material evaporating. PVD processes are characterized by three common stages in the deposition sequence: (*i*) evaporation of a solid or liquid source material – typically referred to as "target" material – through physical processes such as thermal vaporization or ion bombardment, (*ii*) transport of the vaporized species (*i.e.*, atoms, molecules, or clusters) towards the substrate surface in a vacuum or low-pressure environment, (*iii*) condensation of the vapor phase and subsequent film growth on the substrate surface [62–64]. These principles enable an extremely versatile process with limited restrictions in terms of the material selection and substrate geometry, while providing a vast spectrum of possible thin film properties. In addition, the feasible thickness of the synthesized coatings ranges from a few atomic layers, up to several tens of micrometers [62]. The most commonly used PVD techniques include cathodic arc evaporation (CAE) and direct current magnetron sputtering (DCMS), both having individual advantages and shortcomings with respect to each other [63, 65]. Due to the importance for this thesis, the focus of the following sections will be placed on the magnetron sputtering technique and corresponding variations thereof.

Die approbierte gedruckte Originalversion dieser Dissertation ist an der TU Wien Bibliothek verfügbar.
The approved original version of this doctoral thesis is available in print at TU Wien Bibliothek.
TU Bibliothek Your knowledge hub WIEN

2.1 Sputtering

Sputtering is a plasma-based deposition technique that relies on the physical ejection of surface near target atoms through the bombardment with ionized particles and the resulting transfer of kinetic energy. The charged species – in particular noble gas ions – are attracted from a glow discharge created near the target surface due to the application of an electric field [62]. The simplest configuration for sputtering consists of two facing electrodes with the target material placed on the cathode, whereas the surrounding vacuum system is placed on the anode, generally maintained at ground potential [62, 64]. In the presence of a low-pressure process gas (*e.g.*, Ar, Kr, Xe), the application of a high voltage difference between the electrodes leads to the ignition of a glow discharge through continuous inelastic collisions between free electrons and neutral gas species [62, 63]:

$$e^- + Ar \rightarrow 2e^- + Ar^+ \tag{2.1}$$

Overall, the glow discharge simultaneously holds ionized process gas, free electrons and remaining gas neutrals, with the number of positive and negative charge carriers approximately balanced ("quasi-neutral" state) [63]. The available gas ions are subsequently extracted and accelerated onto the target surface at energies close to the potential difference of the electrodes. The bombarding species penetrates the target surface and causes a cascade of atomic displacements along the trajectory. The displaced atoms themselves create additional collision cascades that eventually lead to the ejection of surface near atoms (see Figure 2.1) to form a thin film on the substrate surface [63]. While a fraction of the incident ions is reflected as neutrals or implanted in the target material, the majority of the transferred

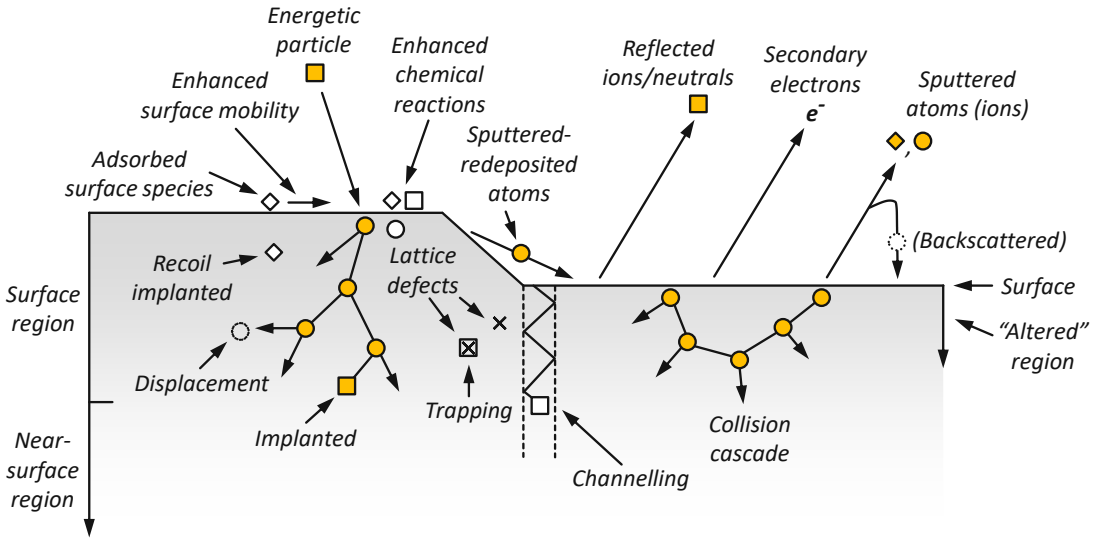

Fig. 2.1: Schematic of atomistic events on the target surface und subsurface during ion bombardment. The illustration is adapted from [63].

Die approbierte gedruckte Originalversion dieser Dissertation ist an der TU Wien Bibliothek verfügbar.
The approved original version of this doctoral thesis is available in print at TU Wien Bibliothek.
TU Bibliothek Your knowledge hub WIEN

kinetic energy dissipates in the form of heat (∼95%, [63]), and thus requires active cooling for the target material. In addition, inelastic collisions between the impinging species and electrons of target atoms result in the ejection of secondary electrons, which are essential to maintain the process gas ionization according to Equation 2.1 [62, 63].

Due to the relatively high deposition pressure required to ignite the discharge, both the process gas ions and the sputtered target atoms suffer from a high probability of mutual collisions on their trajectories. Moreover, the emission of secondary electrons is insufficiently utilized to sustain the glow discharge, instead, the majority is ejected from the cathode sheath at high kinetic energies and lost to the anode surface, resulting in undesired heating. As a result, the sputter and depositions rates of this simple configuration remain poor [62].

The sputtering technology is capable of operating with a wide spectrum of target materials for thin film synthesis, including pure elements, alloys, and compounds. Given that the latter material family often exhibits enhanced mechanical or functional properties over alloys, their deposition remains a core competence of the sputtering technique. A well-established approach to deposit compound materials from elemental targets is the so-called "reactive" deposition, which uses a mixture of process and reactive gases (*e.g.*, C_2H_2, N_2, O_2, Si_nH_{2n}, etc.) for the synthesis process [63]. While the noble gas ions remain responsible for the evaporation of the target material – the reactive species is typically too light to effectuate sputtering – the reactive gas component chemically bonds to the evaporated target material and forms a compound film on the substrate surface. The approach is not only economical for the target manufacturing route, production of standard elemental targets is always less demanding in terms of cost and labor than the compound version, but also allows for the important deposition of electrically insulating materials (*e.g.*, AlN, Al_2O_3, etc.). Nevertheless, while this deposition route may appear seemingly simple at first glance, the contribution of a reactive gas to the process adds significant complexity to the discharge and film growth conditions [62, 64].

In general, the sputtering process requires a minimum of electrical conductivity from the target material to maintain the glow discharge and prevent the build-up of a positive surface charge from ion bombardment [63]. While this circumstance prevents the actual sputtering of poorly conducting materials, similar effects can occur during reactive deposition processes. In particular the so-called "poisoning" effect, which involves the undesired formation of an electrically less conductive compound layer on the target surface, poses a significant problem to the process stability [63]. The effect essentially depends on the reactive-to-process gas ratio admitted to the deposition system, so that commonly three different target and thin film conditions are observed. (*i*) Too little reactive gas results in the deposition of elemental or understoichiometric compound thin films, while limited effect is recorded for the target surface chemistry. (*ii*) Increasing the reactive-to-process gas mixture permits the deposition

Die approbierte gedruckte Originalversion dieser Dissertation ist an der TU Wien Bibliothek verfügbar.
The approved original version of this doctoral thesis is available in print at TU Wien Bibliothek.
TU Bibliothek Your knowledge hub WIEN

of stoichiometric thin films, while the sputter rate of the target remains sufficiently high to avoid extensive coverage with the compound layer. (*iii*) Upon surpassing a threshold ratio, the gettering effect of the sputtered target atoms is too low to consume most of the reactive gas in the deposition system, at which point the excess reactive gas reduces the sputtering efficiency and the target gets fully covered by a compound layer. This reactive-gas-dependent target condition can be monitored in terms of the current-voltage curve or reactive gas partial pressure, which reveals a typical hysteresis-like characteristic at the transition from a metallic to a fully poisoned target surface (see Figure 2.2) [62–64].

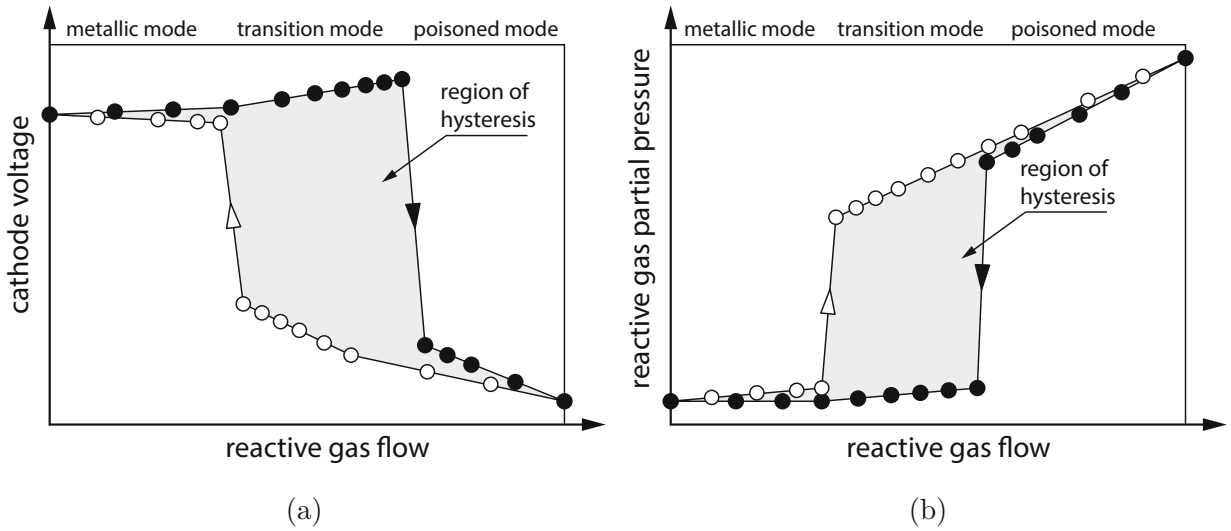

Fig. 2.2: Illustration of the (a) cathode voltage and (b) reactive gas partial pressure behavior during reactive magnetron sputtering. Both figures are adapted from [66].

Drastic improvements in the efficiency of the sputtering process were achieved by placing a circular magnetic system – the magnetron – on the reverse side of the target (see Figure 2.3) [62]. The combination of an electric and magnetic field forces electrons in the target vicinity on a confined, circular trajectory close to the surface, which increases the probability for electron - gas atom collisions, and thus an overall increase in plasma density. The enhanced number of process gas ions leads to an increased sputtering efficiency and permits a reduction of the required deposition pressure and discharge voltage. Simultaneously, reducing the overall deposition pressure translates into a lower number of collisions for the sputtered target species while traveling to the substrate surface, thus allows for enhanced deposition rates [62, 63]. A distinction in the magnetic configuration is made between balanced and unbalanced magnetrons. While a balanced configuration consists of fully closed magnetic field lines, the unbalanced magnetron obtains different magnetic strengths between the inner and outer segments in the magnetic assembly. Consequently, unbalanced magnetron sputtering

Die approbierte gedruckte Originalversion dieser Dissertation ist an der TU Wien Bibliothek verfügbar.
The approved original version of this doctoral thesis is available in print at TU Wien Bibliothek.
TU Bibliothek Your knowledge hub WIEN

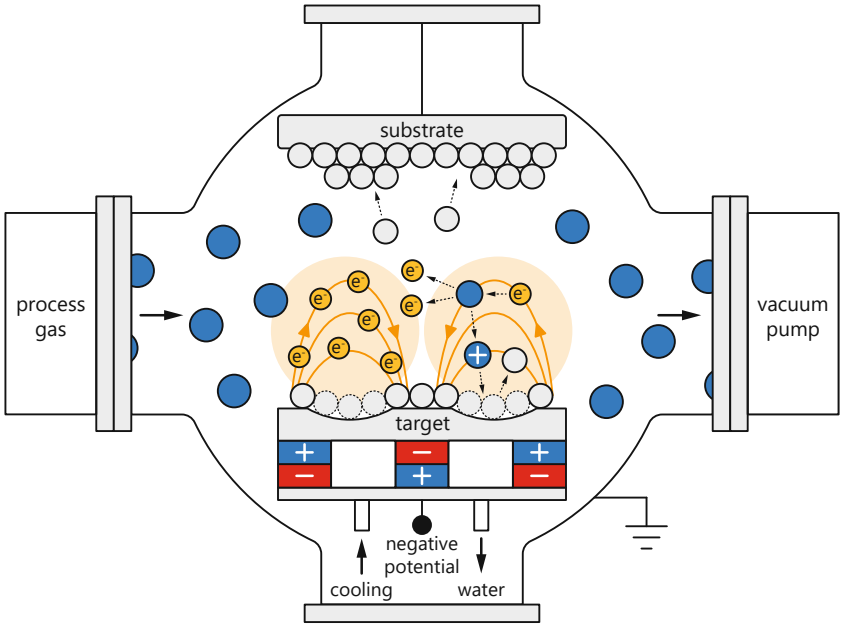

Fig. 2.3: Schematic of a simple DC magnetron sputtering system. Adapted from [64].

allows the glow discharge to extend further towards the substrate surface, resulting in an increased contribution of the charged species to the film growth process [62, 63].

An essential parameter to characterize the efficiency of the sputtering process is the so-called sputter yield, which is described by the ratio of successfully sputtered atoms to the number of ions bombarding the target surface. Essentially, the sputter yield depends on the chemical bond strength of the target atoms and the energy transfer from the incident ions [63]. An estimation for the sputter yield is given by [62]:

$$Y = \frac{3}{4\pi^2}\alpha\frac{4M_tM_i}{(M_t+M_i)^2}\frac{E_i}{U_s} \tag{2.2}$$

where α is a dimensionless factor depending on the mass-ratio of the target atoms (M_t) and incident ions (M_i) as well as the angle of incidence and energy E_i of the bombarding ions, and U_s is the binding energy of the target atoms. The sputter yield typically adopts a near parabolic behavior in terms of E_i, where increasing the ion energy results in enhanced values of Y, until a peak value is attained. Further increasing E_i results in the promoted implantation of process gas ions without effectively sputtering surface atoms. Moreover, the sputter yield increases to a maximum value for incident angles of $\sim$70° from the target normal [63] and M_i/M_t-ratios approaching 1 [62]. While the sputter yield is less decisive for single element targets, considerable difficulties may occur for multi-element or compound targets obtaining a pronounced difference in atomic mass between the constituents to maintain a comparable composition between the target and synthesized thin film [62–64, 67].

Die approbierte gedruckte Originalversion dieser Dissertation ist an der TU Wien Bibliothek verfügbar.
The approved original version of this doctoral thesis is available in print at TU Wien Bibliothek.

Several versions of pulsed magnetron sputtering were further introduced over the past decades, originally with the intention to improve the process stability when sputtering poorly conducting materials. These techniques circumvent the positive charge accumulation on the target surface by continuously alternating the target polarity. This allows for conventional sputtering due to bombardment with positively charged ions in the first half of the cycle (*i.e.*, the target is at a negative potential), whereas the subsequent half is utilized to attract free electrons from the glow discharge and reduce any charge build-up (*i.e.*, the target is at a positive potential). However, depending on the pulsing function, this effectively shortens the actual time of sputtering, which is reflected in the inherently low deposition rates [62, 63].

A relatively young technique in this family is high-power impulse magnetron sputtering (HiPIMS). The technology is targeted to combine the advantages of a highly ionized flux of target species similar to cathodic arc evaporation, with the principles of macro-particle free sputtering. Increasing the fraction of film forming ions during the deposition process opens new pathways of controlling the structure - property relationship for thin film materials through tuning the distribution and energy of the incident ions [55, 57, 68–71]. HiPIMS operates under unipolar pulsed power application in the form of short, high-energy pulses at a relatively low repetition frequency. Characteristic operating conditions for a HiPIMS discharge involve peak power densities ranging from 0.5 to 10 kW/cm^2, peak current densities of up to 4 A/cm^2, pulse repetition frequencies between 30 and 5000 Hz, with an actual duty cycle of 0.5 to 5% of the entire pulse duration [55]. Still, the time-averaged power supply to the cathode remains comparable to the conventional DC magnetron sputtering process. These operating conditions generate a high-density plasma in front of the target wherein a large fraction of the sputtered species is ionized due to the significantly increased probability for electron-neutral collisions and enhanced electron temperature. Depending on the actual target material and sputtering conditions, HiPIMS was reported to achieve ionization rates in excess of 90% of the entire sputtered flux, which stands in marked contrast to the single digit values commonly referenced for the DC magnetron sputtering technique [55, 71].

The increased density of gas- and film-forming ions near the target surface significantly contributes to the high discharge current in a HiPIMS process. A certain fraction of the positively charged ions is actually back-attracted onto the negatively charged target surface and thus constantly re-participates in the sputtering process. Depending on the type of ion, this mechanism is referred to as “process/reactive-gas recycling” or “self-sputtering” [72]. Evidently, ions trapped in this cycle cannot contribute to thin film growth, so that the peak current density is a measure for the deposition rate loss in a HiPIMS process [73]. Moreover, effects such as gas rarefaction during the HiPIMS pulse – *i.e.*, the temporary physical displacement or heat induced density reduction of the process gas – add to the reduced sputtering rates [74, 75]. Similar to the conventional process, HiPIMS can be operated in a reactive gas environment. While the importance for optimizing the reactive-to-process gas

Die approbierte gedruckte Originalversion dieser Dissertation ist an der TU Wien Bibliothek verfügbar.
The approved original version of this doctoral thesis is available in print at TU Wien Bibliothek.
TU Bibliothek Your knowledge hub WIEN

ratio is certainly amplified for a HiPIMS discharge to maintaining stable process conditions, the generally increased activation of the reactive gas component is highly beneficial for the film growth process [56].

A primary application for the HiPIMS technology involves the synthesis of high-quality thin films at significantly reduced deposition temperatures. The ability to produce thin films of equal quality at lower temperatures is essential not only from an economical point of view, but also to expand the applicability towards temperature-sensitive materials such as plastics. The enhanced contribution of ionized target species in the film growth process reduces the formation of pronounced crystal columns and intercrystalline voids – characteristic for low temperature depositions using conventional sputtering – through increased surface diffusion. This results in densified coating morphologies with often enhanced mechanical properties in terms of hardness and residual stress state [76, 77]. In addition, the high influx of ionized species on the substrate surface enables the coverage of complex shaped geometries due to the possibility of guiding the charged particles in an electric field (*i.e.*, bias voltage) [78].

Several studies have further highlighted a distinct influence of the ionized target material on the phase formation of thin films, in particular for metastable structures such as cubic Ti-Al-N or V-Al-N [79, 80]. Bombardment of the growing film surface with low-energy/low-momentum ions was demonstrated to yield single-phased coatings with high hardness and low residual stress [58]. Contrary, the presence of high-energy/high-momentum ions introduces defect sites in the crystal structure, which lead to the premature precipitation of secondary phases (*i.e.*, the thermodynamically preferred wurtzite AlN in Ti-Al-N or V-Al-N) and excessive stress states. Depending on the deposition setup, the undesired ions can be excluded by operating the corresponding target in DC sputtering mode or by tuning of the discharge conditions [81]. On the other hand, so-called "subplantation" – the deliberate attraction of a specific film constituent at high energies – can be used to control solubility limits in metastable structures. The moderate implantation effect of high energy ions in a pre-existing template structure prevents their simultaneous precipitation due to the limited diffusion rates below the film surface [59].

Examples for the time-dependent current-voltage behavior of different HiPIMS discharges and the corresponding time-averaged ion energy distribution functions are given in Figure 2.4. The data was recorded from an intermetallic $Ti_{50}Al_{50}$ target (diameter of 100 mm) operated in a $N_2/(Ar+N_2)$ ratio of 0.3, with an average cathode power supply of 1 kW, pulse frequencies of $f = 500$ and 1000 Hz, as well as pulse on-times of $t_{on} = 35$ and 75 μs, respectively. Comparison of the current-voltage data highlights the significantly increased discharge current of ~160 A for the shorter pulse duration and reduced repetition frequency. Simultaneously, the higher cathode current leads to an increased ionization of the target and gaseous species, visible in the time-averaged ion energy distribution functions. The increased peak current density

Die approbierte gedruckte Originalversion dieser Dissertation ist an der TU Wien Bibliothek verfügbar.
The approved original version of this doctoral thesis is available in print at TU Wien Bibliothek.
TU Bibliothek Your knowledge hub WIEN

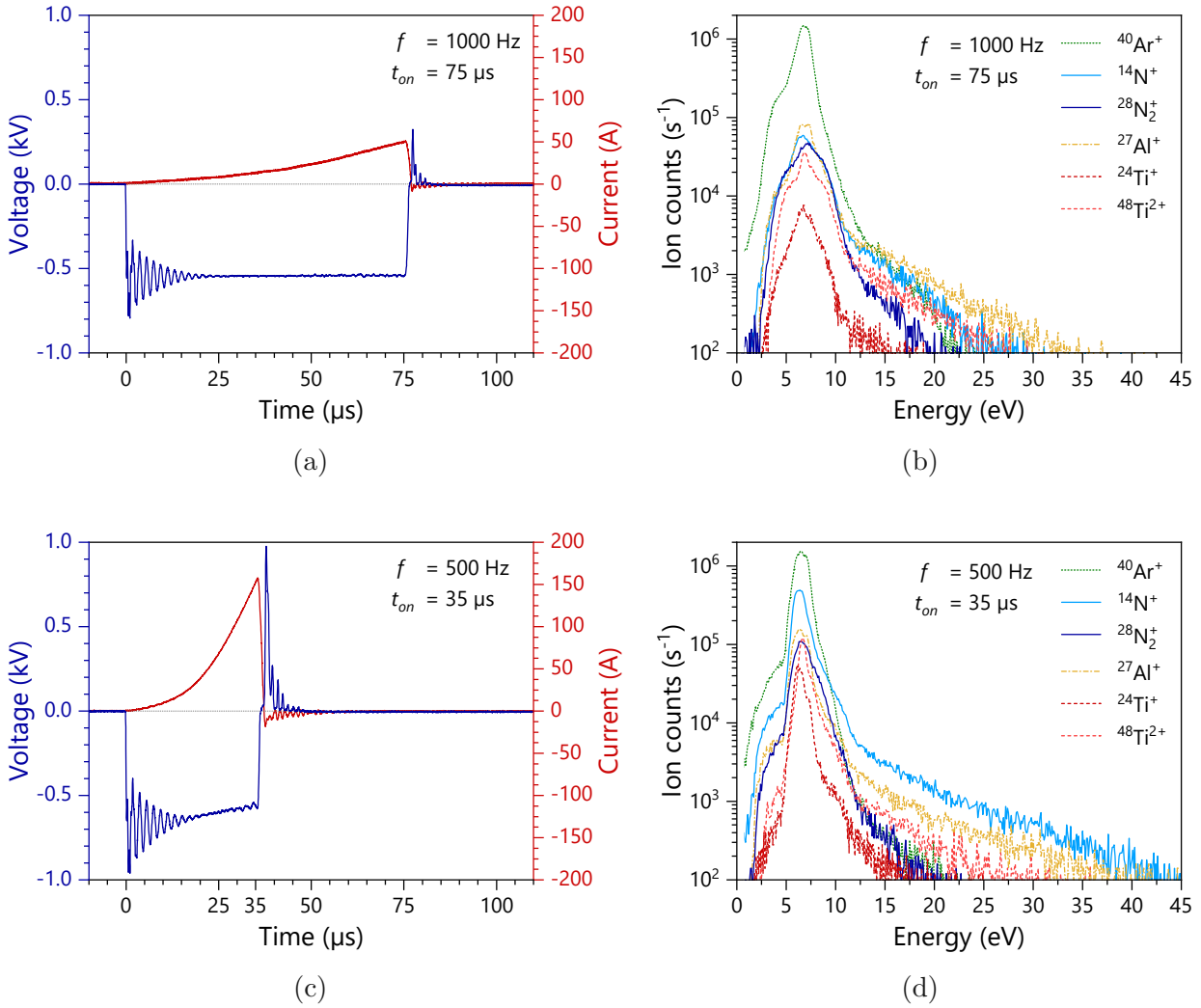

Fig. 2.4: (a) Current and voltage waveforms of a HiPIMS discharge ($f = 1000$ Hz, $t_{on} = 75$ µs) recorded during the reactive deposition of Ti-Al-N from a $Ti_{50}Al_{50}$ intermetallic target. (b) Time-averaged ion energy distribution at the substrate surface for the operating conditions in (a). (c) Current and voltage waveforms as well as the (d) time-averaged ion energy distribution for altered HiPIMS pulse parameters (other deposition parameters left unchanged). (Own, unpublished work)

especially amplifies the signals for both nitrogen – note the increasing contribution of atomic N – and titanium species. In addition, the shape of the distribution function suggests that the majority of all ions concentrates around a narrow energy band from 5 to 8 eV for the lower duty cycle conditions. Nevertheless, both distributions also feature the characteristic high energy tail with ion energies recorded up to ∼45 eV for the nitrogen and aluminium species.

Die approbierte gedruckte Originalversion dieser Dissertation ist an der TU Wien Bibliothek verfügbar.
The approved original version of this doctoral thesis is available in print at TU Wien Bibliothek.

2.2 Transport of vaporized species

Following the sputter evaporation of the target material, the species passes through the vacuum system on a line-of-sight trajectory and a spatial distribution that is typically element specific [64, 82]. At this stage, the vapor phase is particularly susceptible to scattering events through collisions with ambient process or reactive gas molecules, leading to a significant reduction of the initial kinetic energy, a loss of thin film material to the system walls, and thus reduced deposition rates. While the probability for atomic collisions is increased for larger/heavier target particles, the trajectory of smaller/lighter species is significantly more influenced by these events. Consequently, similar to the mass-dependence of the sputtering effect, vapor phase collisions can markedly alter the overall chemical composition of the sputtered flux. Nevertheless, it is also this step in the PVD synthesis process that allows access to extended solubility ranges and the deposition of metastable structures, as compositional limitations are removed in the vapor phase [62, 64].

2.3 Thin film growth

The deposition of PVD thin films is essentially dictated by thermodynamic and kinetic phenomena, that are strongly connected to the actual deposition conditions and the material system. The growth on substrate surfaces itself is the result of a complex sequence that initiates with the condensation of evaporated target material and the formation of a nucleus with critical dimensions [62]. The vapor phase species arrives at the substrate with an energy distribution that reflects the evaporation process, the amount of gas-phase collisions, and the energy gained through the use of a substrate bias potential. Depending on the particle energy, the arriving species undergoes: (*i*) immediate reflection from the substrate surface, (*ii*) desorption after limited time interval, or (*iii*) surface diffusion to a suitable nucleation site (*e.g.*, defects, impurities, etc.) [62, 63]. Consequently, to establish a permanent bond with the substrate surface or previously condensed atoms, the arriving particles are required to lose a specific amount of energy. Once a cluster with critical radius r^* is formed, the nucleus remains stable and continuous growth proceeds. Considering that the nucleus takes the shape of a sphere, the critical size can be expressed in terms of the Gibb's free energy change to the system [62]:

$$\Delta G = -\frac{4\pi r^3}{3} \cdot \Delta G_V + 4\pi r^2 \cdot \gamma \tag{2.3}$$

where ΔG_V is the volume specific decrease in free energy and γ is the area specific surface energy. Hence, stable nuclei are formed when the volumetric energy gain exceeds the energy consumed to introduce a new interface. These nucleation sites are uniformly distributed

Die approbierte gedruckte Originalversion dieser Dissertation ist an der TU Wien Bibliothek verfügbar.
The approved original version of this doctoral thesis is available in print at TU Wien Bibliothek.

over the substrate surface, so that the growing clusters form individual larger islands that eventually connect and form a continuous thin film.

The nucleation process and subsequent film growth is generally described according to three different mechanisms, which differ in the preferred binding partner for the arriving adatoms. Film growth in the *Frank - Van der Merwe* mode proceeds in a layer-by-layer type manner, where the arriving species repeatedly forms a continuous surface layer in order to grow in thickness (see Figure 2.5a). The arriving particles prefer the bond with the substrate surface or previously deposited layers, rather than the neighboring atoms. Contrary, the *Volmer - Weber* mode is characterized by a stronger connection between adjoined atoms, resulting in the preferred thickness growth of separate nuclei (see Figure 2.5b). Eventually, the gaps between these islands close, and a continuous but coarsely textured thin film is formed. The combination of both modes is referred to as *Stranski - Krastanov* film growth, which initiates by forming continuous layers and later shifts to distinct thickness growth of individual islands (see Figure 2.5c) [62, 64].

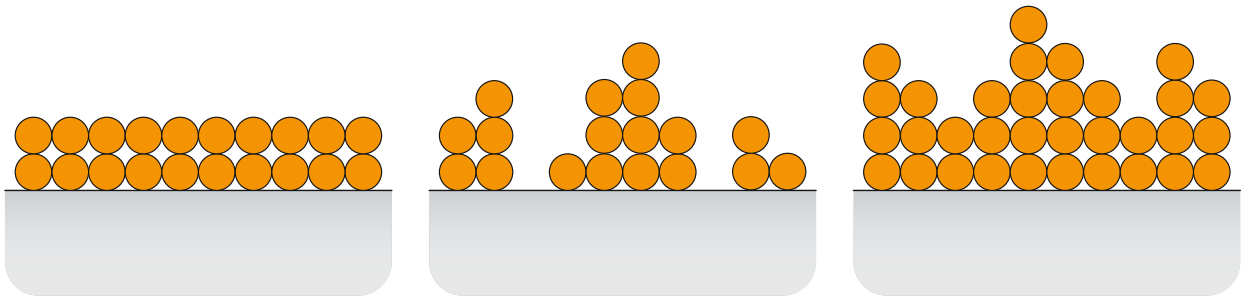

Fig. 2.5: Illustrations of thin film growth behavior after (a) *Frank – Van der Merwe*, (b) *Volmer – Weber*, and (c) *Stranski – Krastanov*. The illustrations are adapted from [64].

Of course, these mechanisms can only approximate the actual material behavior, which is essentially dependent on the prevalent deposition conditions. A schematic description of the resulting thin film morphology is presented by so-called "structure zone diagrams". These diagrams summarize the morphological features of thin films in dependence of a limited set of process parameters [62]. The concept originates in a work by Movchanm and Demchishin [83], who noticed that the morphology of various thin film materials could be categorized in three different zones (zone I, II, and III) according to the homologous growth temperature and film thickness. Their basic version of a structure zone diagram was subsequently improved and adapted over the following decades. Thornton [84] introduced a pressure dependence for the observed growth morphology and added an additional "transition" zone between zones I and II into his version of the diagram. While the deposition pressure can be used to describe the loss of kinetic energy for the arriving species through gas phase collisions, the parameter

Die approbierte gedruckte Originalversion dieser Dissertation ist an der TU Wien Bibliothek verfügbar.
The approved original version of this doctoral thesis is available in print at TU Wien Bibliothek.
TU Bibliothek Your knowledge hub WIEN

cannot capture the effect of increased surface mobility due to ion bombardment. This lead to the modifications of Messier *et al.* [85], who replaced the pressure dependence with an axis describing the average energy of the species arriving at the substrate surface. Especially in the past two decades, the importance of capturing the effect of ionized species on the film growth process considerably increased due to the growing application of ion-assisted film growth techniques (*e.g.*, the HiPIMS technology). To date, the most elaborate and complex version of a structure zone diagram was introduced by Anders (see Figure 2.6, [86]).

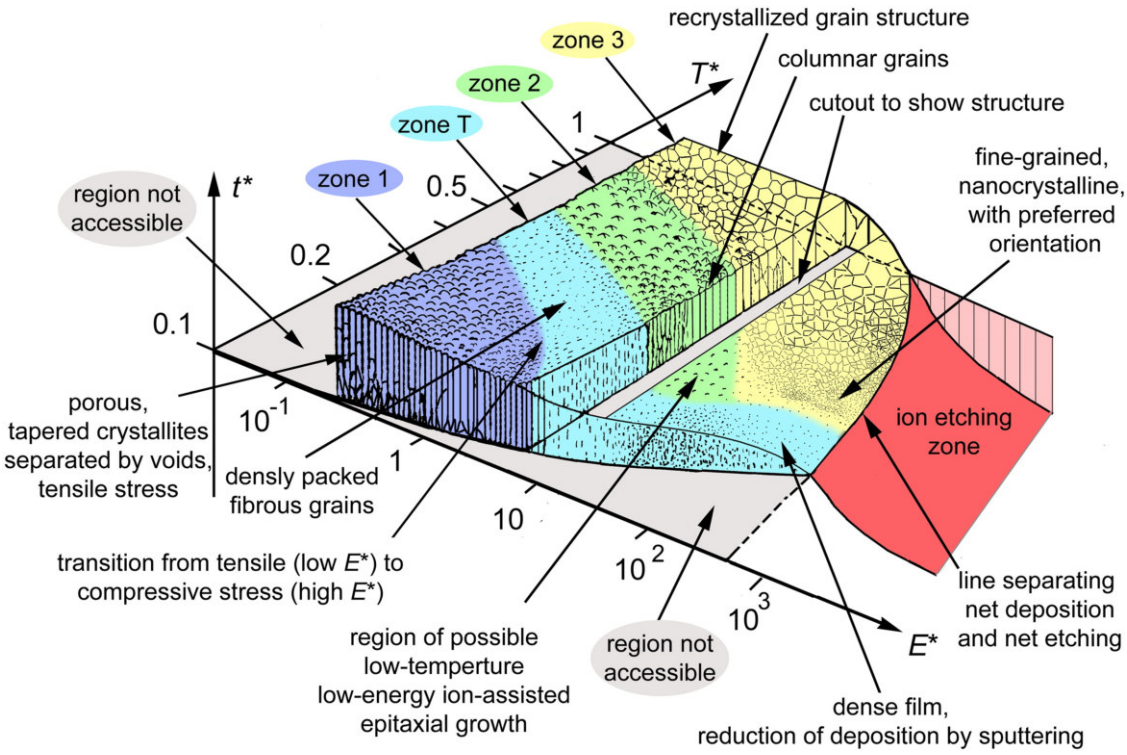

Fig. 2.6: Structure zone diagram for energetic thin film deposition processes [86].

Thin film growth in zone *I* is characterized by low surface mobility of the arriving film species, which prevents a proper re-distribution and causes atomic clustering. Eventually, the islands grow into amorphous or partly crystalline thin films with pronounced, fibrous columnar structure and extensive porosity. The following zone T features increased diffusion of adatoms within grain boundaries, which allows for the growth of crystalline thin films. The initial random orientation of the nuclei results in competitive growth, with faster growing crystal orientations overgrowing adjacent grains. This leads to the characteristic V-shaped columns in lower parts of the morphology [87]. Thin films deposited under zone *II* conditions exhibit a pronounced columnar, dense morphology enabled by grain boundary migration from enhanced surface and bulk diffusion. Finally, in zone *III*, thermal activation is high enough to enable recrystallisation and coarsening of the material. Crystal columns are replaced with globular shaped grains to minimize grain boundary volume [86].

Die approbierte gedruckte Originalversion dieser Dissertation ist an der TU Wien Bibliothek verfügbar.
The approved original version of this doctoral thesis is available in print at TU Wien Bibliothek.
TU Bibliothek Your knowledge hub WIEN

In general, the boundaries between the different zones vary in terms of the material system, the deposition temperature and the average energy available to each deposited particle. Especially the use of ion-assisted film growth significantly changes the resulting morphology through increased diffusivity, so that all zones are shifted to lower temperatures with increasing particle energy. A further extension of the structure zone diagram in Figure 2.6 involves the incorporation of surface etching effects and thus decreasing substrate thicknesses. Analogous to sputtering on the target surface, ionized process gas or target species can be utilized to evaporate substrate material. This technique is a vital step in the pretreatment of industrial deposition systems [86].

Die approbierte gedruckte Originalversion dieser Dissertation ist an der TU Wien Bibliothek verfügbar.
The approved original version of this doctoral thesis is available in print at TU Wien Bibliothek.

Chapter 3

Fracture Mechanics

The term "fracture" includes the complete or partial separation of what was originally treated as a whole. The description of the corresponding phenomena involved in the separation process are subject of the broad field designated as fracture mechanics. This theory treats the nucleation and propagation of cracks in a material, originating from pre-existing flaws or inhomogeneities located on the surface or within the structural volume [88]. Hence, fracture mechanics strives to find satisfactory solutions to basic engineering problematics, among which an essential question is: "Will a pre-existing crack in the material lead to failure at a given load"? Or in other words: "What is the residual strength of a material for a given crack length [88]"? Although finding an answer to these questions appears seemingly simple, no universal description has yet been established, providing a comprehensive treatment of the problem regardless of the material or the structural shape. In particular, the influence of non-linear material behavior, which manifests from *e.g.*, plasticity or viscoelasticity, necessitates a separate treatment for the crack tip description. This led to the general differentiation into the fields of linear-elastic fracture (LEFM) and elastic-plastic fracture mechanics (EPFM). Within these frameworks, several parameters have been conceptualized to describe the crack driving force as well as the crack growth resistance. The fundamental concepts of crack growth description in LEFM are based on either the balance of energy or the stress intensity [89–91]. Contrary, conditions of non-linear material response require a different approach, treated by EPFM and parameters such as the crack tip opening displacement (CTOD) or the J-integral [89–91]. Irrespective of the applied concept, the requirements for crack growth follow a similar relation in terms of a generalized crack driving force D_{gen} and a generalized crack growth resistance R_{gen} [92, 93]:

$D_{gen} > R_{gen}$	unstable crack growth
$D_{gen} = R_{gen}$	equilibrium crack growth
$D_{gen} < R_{gen}$	no crack growth

Die approbierte gedruckte Originalversion dieser Dissertation ist an der TU Wien Bibliothek verfügbar.
The approved original version of this doctoral thesis is available in print at TU Wien Bibliothek.

where D_{gen} (*i.e.*, energy release rate G, applied stress intensity K, applied J-integral J, or present crack tip opening displacement δ) is a parameter that describes the loading condition of the crack, given by the applied force and the strain energy stored in the material. R_{gen} (*i.e.*, critical energy release rate G_c, critical stress intensity K_c, critical J-integral J_c, or critical crack tip opening displacement δ_c) describes the resistance to crack growth, which is generally related to the material, the crack length, as well as the structural dimensions [92, 93]. Consequently, an existing crack will extend once D_{gen} equals or exceeds R_{gen}.

While the majority of fracture toughness and fatigue tests within this thesis were performed in the scope of LEFM, measurements on the interface toughness between a ceramic coating and two technical alloys required a treatment by EPFM, in particular the J-integral. Therefore, a brief overview of the main concepts will be given in the following.

3.1 Linear-elastic fracture mechanics

The theory of energy based LEFM is essentially founded in the considerations of Griffith in 1921 [94], who formulated a solution for the growth of a central crack in an infinite plate subject to a constant stress σ (see Figure 3.1a). Griffith stated that crack propagation can only occur if the change in stored strain energy is sufficient to overcome the energy required to create two free surfaces, *i.e.*, the new crack area [90]. The elastic strain energy stored in the plate is given in Figure 3.1b, represented by the area OAC. An incremental extension da of the crack reduces the internal stress state, so that the elastic energy will decrease in magnitude indicated by area OBC. Consequently, the energy required to extend the crack from a to $a + da$ is given by the area OAB [90]. This resulted in the following equilibrium condition for stable crack growth:

$$\frac{dU}{da} = \frac{dW}{da} \tag{3.1}$$

where U is the stored elastic energy and W the energy required for crack propagation [90]. In conjunction with stress-field calculations by Inglis [95], an expression for U was found per unit plate thickness:

$$U = -\frac{\pi\sigma^2 a^2}{E} \tag{3.2}$$

where E is the Young's modulus [89, 91]. In case of the energy required to introduce a newly formed crack surface area, Griffith suggested that in ideally brittle materials, this term would correspond to the surface energy. Thus, the creation of a crack with length $2a$ leads to:

$$W = 4a\gamma_s \tag{3.3}$$

Die approbierte gedruckte Originalversion dieser Dissertation ist an der TU Wien Bibliothek verfügbar.
The approved original version of this doctoral thesis is available in print at TU Wien Bibliothek.

where γ_s is the surface energy per unit plate thickness [89, 91]. Inserting equations 3.2 and 3.3 into 3.1 and rearranging yields the following equivalent expressions for crack growth:

$$\frac{\pi\sigma^2 a}{E} > 2\gamma_s = R \tag{3.4}$$

$$\sigma\sqrt{a} > \sqrt{\frac{2E\gamma_s}{\pi}} \tag{3.5}$$

Equation 3.5 shows that crack propagation in ideally brittle materials is governed by the product of the applied stress and the square root of the actual crack length, which is put into relation with a set of material properties. Since the right-hand side of the equation only consists of the constants E and γ_s, crack growth occurs when $\sigma\sqrt{a}$ exceeds a critical value [89].

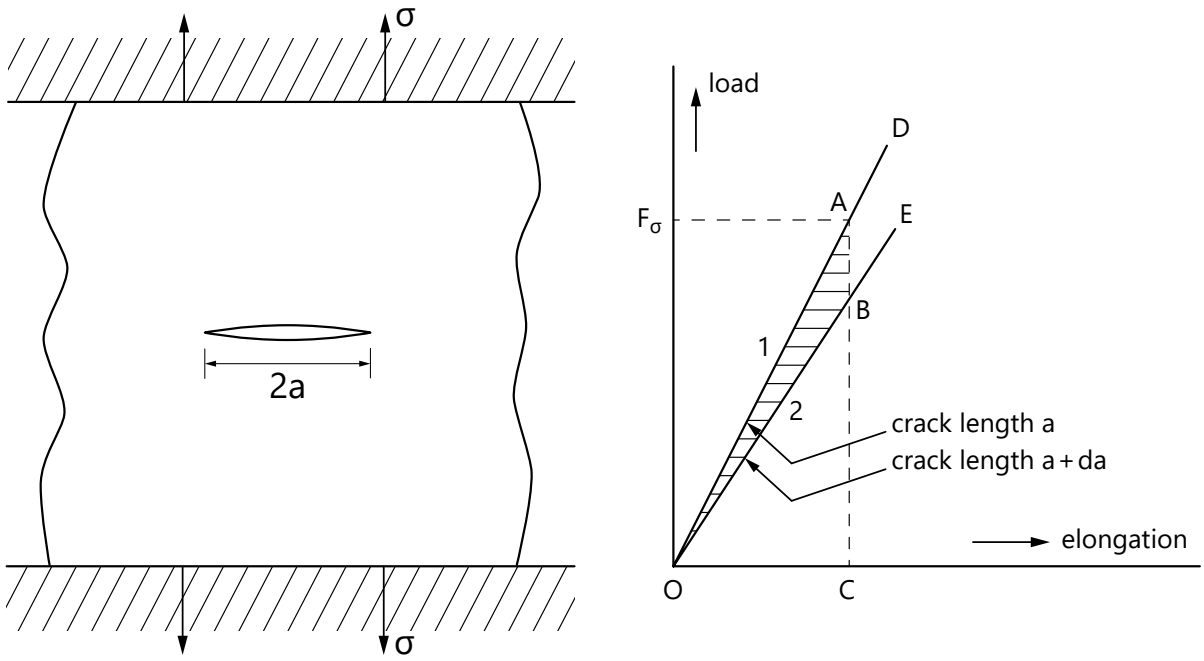

(a) (b)

Fig. 3.1: (a) Schematic of a plate with central crack and fixed ends. Corresponding load-displacement diagram for different crack lengths including the elastic energy release (hatched area). Both figures adapted from [90]

To extend the scope of Griffith's theory beyond the case of ideally brittle materials, *i.e.*, towards the applicability on materials capable of plastic flow, Irwin [96] and Orowan [97] independently proposed a modification to the current criteria in 1948. The extension

Die approbierte gedruckte Originalversion dieser Dissertation ist an der TU Wien Bibliothek verfügbar.
The approved original version of this doctoral thesis is available in print at TU Wien Bibliothek.

recognizes that crack growth is determined by the surface energy γ_s as well as an additional plastic strain work γ_p [89, 91], so that the resistance to crack growth takes the form:

$$R = 2(\gamma_s + \gamma_p) \tag{3.6}$$

In ideally brittle materials, crack growth is merely governed by the breaking of interatomic bonds, which is entirely reflected by γ_s. However, upon propagation through a ductile material, dislocation motion in the crack vicinity causes enhanced energy dissipation, so that $\gamma_p \gg \gamma_s$, and γ_s is rendered negligibly small. This initial concept sparked the development of EPFM.

Later in 1956, Irwin [98] summarized the term $\frac{\pi\sigma^2 a}{E}$ in equation 3.4 as the elastic energy release rate G (compare with Figure 3.1b), in order to improve the practicability of the energy based approach. G is essentially the available energy to incrementally extend a crack; thus crack extension occurs when a critical value G_c $(= R)$ is reached [91]. G_c can be directly determined by measuring the critical stress σ_c in a fracture experiment.

A critical step forward in the foundation of today's LEFM was achieved with the introduction of the so-called "stress intensity" approach, again proposed by Irwin in the 1950s. Based on considerations of the local stress fields in the crack vicinity, Irwin demonstrated that the stresses can be expressed as [89, 98, 99]:

$$\sigma_{ij} = \frac{K}{\sqrt{2\pi r}} f_{ij}(\theta) + ... \tag{3.7}$$

where r, θ are the coordinates of a point with respect to the crack tip; K represents the magnitude of the elastic stress field and is denoted the *stress intensity factor* [89]. The equation is inherently dependent on the load application, which can be expressed in terms of the three main crack opening directions, referred to as mode I through mode III (see Figure 3.2) [92].

Dimensional analysis of equation 3.7 indicated a link to equation 3.5, resulting in the general form of the stress intensity factor [89]:

$$K = \sigma\sqrt{\pi a} \cdot f\left(\frac{a}{W}\right) \tag{3.8}$$

where $f(\frac{a}{W})$ is a dimensionless parameter describing the specimen geometry, and σ resembles the applied load. Upon further comparison with equation 3.5, the following relation is established:

$$G = \frac{K^2}{E} \tag{3.9}$$

Die approbierte gedruckte Originalversion dieser Dissertation ist an der TU Wien Bibliothek verfügbar.
The approved original version of this doctoral thesis is available in print at TU Wien Bibliothek.
TU Bibliothek Your knowledge hub WIEN

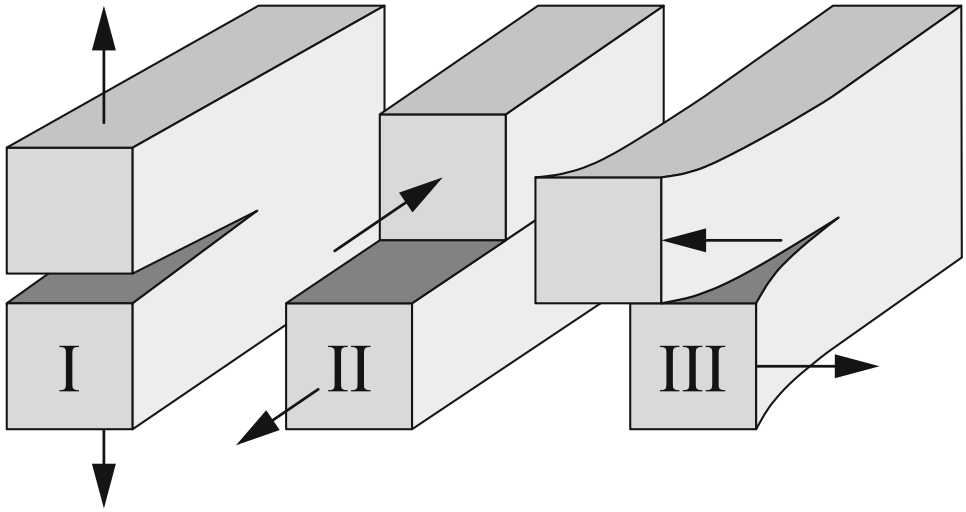

Fig. 3.2: Three modes of cracking. The opening mode I, the in-plane shear mode II, and the out-of-plane shear mode III. The figure is adapted from [91].

Consequently, the fracture dictating parameter can be expressed in the form of the *critical energy release rate* G_c or the *critical stress intensity* K_c.

The distribution of the elastic stress (see equation 3.7) shows that close to the crack tip, *i.e.*, for $r \to 0$, a singularity dominates the stress field. However, no structural material will be able to accommodate stresses above the yield point, therefore a plastic zone with radius r_{pl} will be established around the crack tip [92]:

$$r_{pl} = \beta_{pl} \frac{K^2}{\sigma_{YS}^2} \quad \text{with} \quad \beta_{pl} = \begin{cases} 1/6\pi & \text{for plane strain conditions} \\ 1/2\pi & \text{for plane stress conditions} \end{cases} \tag{3.10}$$

where σ_{YS} denotes the yield strength. Evidently, K also determines the proportionality at which the stresses increase close to the crack tip location [92]. Therefore, the stress intensity factor remains a meaningful parameter for the crack driving force as long as the plastic zone is small compared to the so-called "K-dominated" zone, which is given by the first term in equation 3.7 [91, 92]. It is then customary to reference the value of maximum constraint during loading, *i.e.*, in mode I direction, as K_{Ic}, which is then referred to as the fracture toughness [89].

Overall, it is the experimental accessibility of K_c through conventional stress analysis, combined with the single-parameter description of the crack tip conditions, which makes the stress intensity factor a fundamental descriptor of LEFM [91, 100].

Die approbierte gedruckte Originalversion dieser Dissertation ist an der TU Wien Bibliothek verfügbar.
The approved original version of this doctoral thesis is available in print at TU Wien Bibliothek.
TU Bibliothek Your knowledge hub WIEN

3.2 Elastic-plastic fracture mechanics

Linear-elastic fracture mechanics can only accept a limited contribution from non-linear material behavior at the crack tip, which implies that the extension of the plastic zone remains small compared to the crack size (compare with equation 3.10), and the specimen shows an overall linear response [89]. If these conditions are not met, an alternative framework of elastic-plastic fracture mechanics has to be considered. Within the field of EPFM, two main concepts evolved for the description of non-linear crack tip conditions and the formulation of fracture criteria: the crack tip opening displacement and the J-integral [91]. The latter parameter will be introduced in the following.

The J-integral is based on an energy-conservation concept for a non-linear elastic body that contains a crack. Introduced by Rice in 1968 [101], and founding on the works of Eshelby [102], an integral was introduced that could be evaluated along an arbitrary path enclosing the crack tip (see Figure 3.3a) [89]. In the two-dimensional case the integral takes the form:

$$J = \int_{\Gamma} \phi dy - T_i \frac{\partial u_i}{\partial x} ds \tag{3.11}$$

where Γ is the arbitrary integral path around the crack tip, $\phi = \int_0^{\epsilon_{ij}} \sigma_{ij} d\epsilon_{ij}$ resembles the strain energy density, $T_i = \sigma_{ij} n_j$ is the traction vector acting perpendicular on Γ, u_i being the displacement vector, and ds indicates an incremental step on Γ [92, 93]. Rice demonstrated,

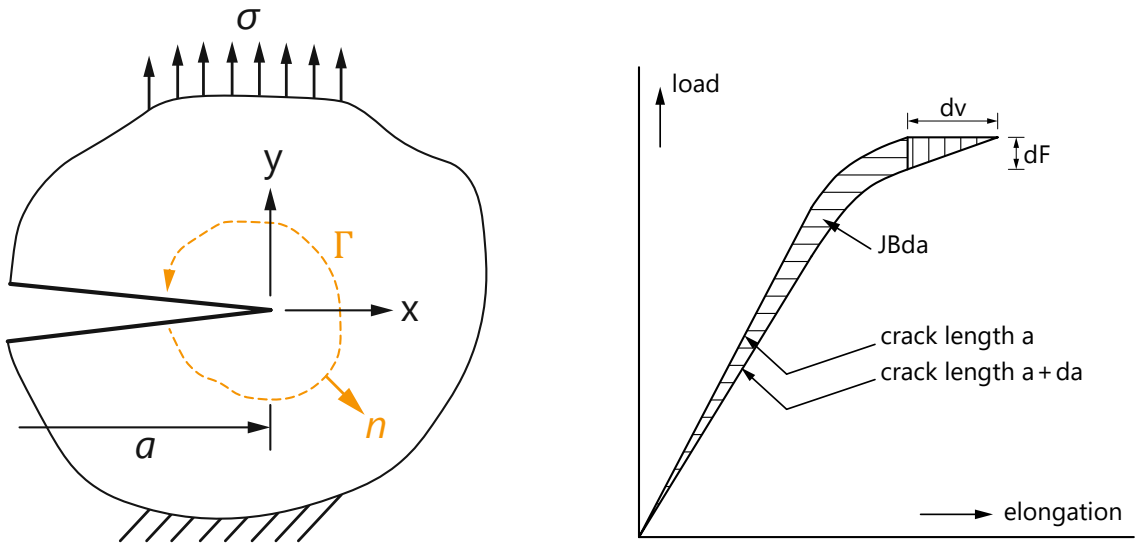

(a) (b)

Fig. 3.3: (a) J-contour integral along an arbitrary path Γ around the crack tip in a non-linear elastic material. Adapted from [103]. (b) Non-linear load-displacement diagram for different crack lengths including the non-linear elastic energy release rate (hatched area). Adapted from [91].

Die approbierte gedruckte Originalversion dieser Dissertation ist an der TU Wien Bibliothek verfügbar.
The approved original version of this doctoral thesis is available in print at TU Wien Bibliothek.

that J is equal to the energy release rate in the non-linear elastic material for a virtual crack extension da, taking the form:

$$J = -\frac{1}{B}\frac{dP}{da} \tag{3.12}$$

where P is the potential energy, and B is the thickness of the cracked specimen. As presented in Figure 3.3b, the change in potential energy $dP = -JBda$ can be extracted as the area between two load-displacement (F-v) curves for crack lengths a and $a + da$ [90, 92]. It is essential to note, that this approach implies an unloading of the material along which it was loaded (*i.e.*, no irreversible events occur), meaning that the material is non-linear but elastic. Consequently, the J-integral is a measure for the crack driving force for non-linear elastic materials. Naturally, in the case of a fully linear-elastic material, J equals G, and thus also $J = K^2/E$ [90, 92].

The experimental determination of the J-integral can be accomplished through measurements of several load-displacement curves on specimen with varying crack lengths, or on a single specimen with stepwise increasing crack length. The individual values of J determined in this manner are then extracted as function of the displacement v or crack length a, serving as reference curve to determine a critical value J_c [90, 91]. The procedures and guidelines for the experimental determination of the J-integral and other fracture toughness parameters are summarized in international standards including ASTM E1820 [104] or ISO 12135 [105].

Similar to the *stress intensity approach*, the J-integral can be utilised to describe the stress field around the crack tip. Based on the works of Hutchinson [106, 107], Rice and Rosengren [108], the stress distribution is expressed according to the so-called HRR-solution [89]:

$$\sigma_{ij} = \sigma_0 \left(\frac{E}{\alpha \sigma_0^2 I_n} \frac{J}{r} \right)^{\frac{1}{n+1}} \bar{\sigma}_{ij}(\theta, n) \tag{3.13}$$

To derive equation 3.13, a power-law hardening material was assumed, of which the stress-strain response can be expressed by the so-called Ramberg-Osgood equation [109]. Therein n, α, and σ_0 are fit parameters, I_n is a numerical constant depending on n and whether plane stress or plane stress conditions prevail, and $\bar{\sigma}_{ij}(\theta, n)$ is a dimensionless function. Consequently, analogous to equation 3.7, the J-integral characterizes the amplitude of the virtual stress singularity at the crack tip location [89, 91, 93, 110].

Die approbierte gedruckte Originalversion dieser Dissertation ist an der TU Wien Bibliothek verfügbar.
The approved original version of this doctoral thesis is available in print at TU Wien Bibliothek.

3.3 The fracture toughness of thin films

Qualitative and quantitative analysis of the fracture toughness for thin film materials has evolved to a central aspect in the ongoing development of both protective and functional coatings. Related to the application and structure of the thin film – metallic or ceramic, synthesized on technical or single-crystal substrate, monolithic or multilayered architecture, etc. – various methodologies have been specifically conceived or were adopted from other branches of materials sciences. Naturally, each technique places different emphasis on how the toughness measure is perceived, leading to inherent challenges and limitations in their applicability. However, the mere length-scale of thin films provides a common imperative for all techniques, in that they operate through high-resolution mechanical test devices and the results are validated with respect to designated models [111]. In the following, a short overview will be given on the most popular and well-established techniques designated towards fracture toughness testing of ceramic thin film materials. Moreover, a recently introduced approach targeting the characterization of plastically deformable materials and interfaces will be discussed.

3.3.1 Indentation based techniques

Indentation based models for fracture toughness evaluation of thin film materials are conceptualized around the direct measurement of radial cracks emanating from the corners of residual indentation marks produced by a sharp contact (see Figure 3.4a) [111]. The core ideas of this approach were first formulated in the works of Lawn, Evans, and Marshall [112–115], who quantified the fracture toughness by relating the crack length to the applied load and the mechanical material properties. Since the introduction, the application of this model has been restricted to brittle materials, where the length of the radial cracks significantly exceeds the dimensions of the remaining indentation mark, leading to the formation of so-called "hald-penny" cracks (see Figure 3.4b) [111, 116]. In the case of half-penny shaped crack geometries, the following formula is applicable to calculate the fracture toughness [116]:

$$K_{Ic} = \alpha \left(\frac{E}{H}\right)^{1/2} \left(\frac{F}{c^{3/2}}\right) + Z\sigma_r c^{1/2}, \quad \text{with} \quad Z = 1.12\sqrt{\pi}\frac{\frac{d}{c}}{\left(\frac{3\pi}{8}\right) + \left(\frac{\pi}{8}\right)\left(\frac{d}{c}\right)^2} \tag{3.14}$$

where E represents the elastic modulus, H the hardness, F the applied maximum load, c the total radial length of the crack measured from the indentation center, d the total crack depth measured from the original surface, σ_r the residual stress, and Z is a geometry factor based on the actual crack shape that scales the contribution of the residual stress. The formation of the half-penny shaped crack geometries is typically fulfilled upon $c \geq 2a$, which equally requires radial (so-called "Palmqvist") and median crack growth [116]. In the case were the crack geometry deviates significantly, various modifications of equation 3.14 have been

Die approbierte gedruckte Originalversion dieser Dissertation ist an der TU Wien Bibliothek verfügbar.
The approved original version of this doctoral thesis is available in print at TU Wien Bibliothek.
TU Bibliothek Your knowledge hub WIEN

introduced, which also account for different material property combinations [117, 118]. The necessity to accurately know the crack morphology prior to evaluation actually reveals one of the major shortcomings for this relatively simple technique. Given the small scale of the involved crack patterns, no simple approach is available for accurate in-volume measurements of the crack extension [117]. The use of sharp-angle indentation tips such as a cube-corner tip greatly enhance the formation of the crack pattern over conventional shapes applied for nanoindentation (*e.g.*, Berkovich or Vickers). The steep penetration angle of the cube-corner reduces the involved loads necessary for crack formation, whiles exerting significantly higher strain on the examined material [116].

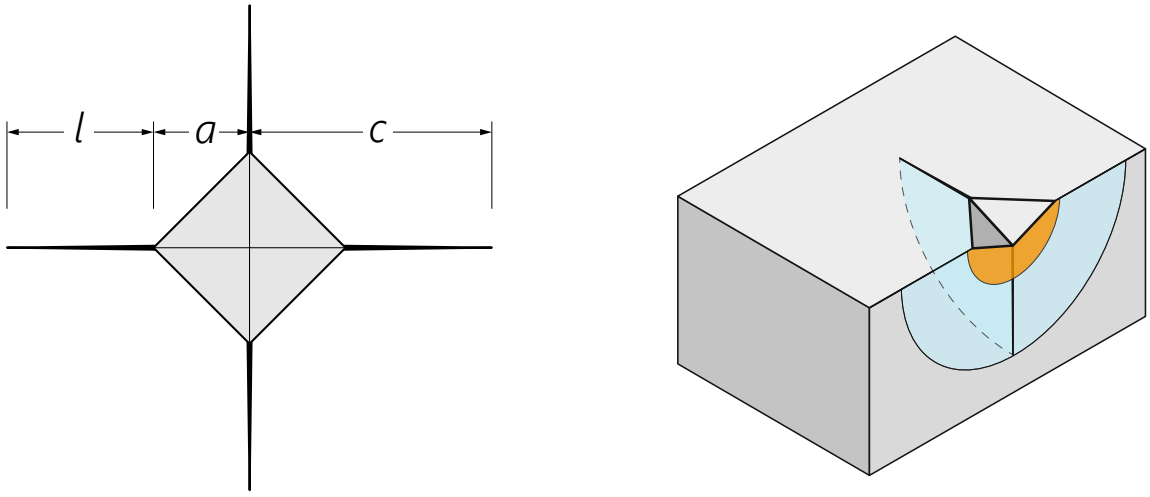

(a) (b)

Fig. 3.4: (a) Residual imprint of a cube corner test after indentation loading. (b) Representative half-penny shaped crack morphology. Both figures adapted from [119].

Although nanoindentation platforms in general provide a straightforward approach towards indentation-based fracture toughness measurements on thin film materials, certain limitations exist that restrict a widespread comparability of the data. As already mentioned, the actual size and shape of the produced crack morphology poses the initial hurdle in finding an accurate model. Moreover, the presence of residual stresses in thin films significantly influences the outcome. Although equation 3.14 and others try to take the impact of residual stresses into account, indentation-based fracture toughness testing generally fails to report comparable values for coating materials – in particular upon comparison to micromechanical testing procedures. In addition, the presence of high compressive stresses or an increased fracture toughness of the coating can make it impossible to initiate a crack pattern, given the systematic force threshold or geometrical restrictions from the coating thickness [111, 116].

Die approbierte gedruckte Originalversion dieser Dissertation ist an der TU Wien Bibliothek verfügbar.
The approved original version of this doctoral thesis is available in print at TU Wien Bibliothek.

3.3.2 Indentation based techniques – pillar splitting

With the aim to reduce the impact of residual stresses and geometrical constraints (*i.e.*, substrate influences) on the results of indentation-based fracture toughness measurements, Sebastiani *et al.* [30] introduced the micro-pillar splitting technique. Instead of indenting an arbitrary location on the thin film surface, the technique relies on the central indentation of a micro-pillar specimen, typically prepared by focused ion-beam (FIB) milling [111]. The sample geometry – with a height-to-diameter aspect ratio ≥ 1 – allows for a complete release of the tested volume from the surrounding thin film material, thus entirely eliminating the influence of residual stress [30]. Following an initial indentation of the pillar surface according to Kick's law, a median crack nucleates below the tip. Upon reaching a critical load value, the crack suddenly expands throughout the pillar and exits the surface, *i.e.*, splitting the pillar. Based on a sufficiently brittle material and knowledge on the pillar radius R, the critical splitting load P_c, and a calibration parameter γ, the fracture toughness can be calculated according to [30, 120]:

$$K_c = \gamma \frac{P_c}{R^{3/2}} \tag{3.15}$$

The novelty of this approach lies in the fact that no measurements of the crack length or geometry are necessary after the experiment, since these are predetermined by the pillar dimensions. However, although the technique appears relatively simple in terms of the experimental procedure and the sample preparation, the quantitative evaluation of K_c fully relies on complementary finite element analysis to extract γ [111]. This dimensionless coefficient in itself depends on several material and geometrical parameters, such as the elastic modulus, hardness, Poisson's ratio, and the utilized indenter geometry. Naturally, this poses a significant source of inaccuracy within the evaluation, although experience showed that accurate results are obtained when using sharp indenter tips and pillars with low taper angle [111]. Apart from the ease of manufacturing a large quantity of micro-pillar samples with today's capabilities of FIB microscopes, providing statistical validity to the data, the actual impact of the ion-based milling process is rather limited on the pillar geometry. Given the initial crack nucleation occurs in the unaffected volume of the pillar, Best *et al.* [121] demonstrated that limited influence from FIB damage on the critical load is to be expected [120]. An important aspect in achieving valid experiments is the placement of the tip, which has to be centered on the symmetric pillar, with the subsequent force application in line with the pillar axis. Despite the possibility to conduct *ex-situ* experiments, typically an approach using an *in-situ* nanoindentation system mounted in a scanning electron microscope (SEM) is chosen, to avoid positioning the tip off-center. In general, a rule-of-thumb guideline suggest a positioning accuracy of $\pm 10\%$ of the respective pillar diameter, to avoid any lowering influence on the critical load [122]. Finally, high temperature experiments highlighted an

Die approbierte gedruckte Originalversion dieser Dissertation ist an der TU Wien Bibliothek verfügbar.
The approved original version of this doctoral thesis is available in print at TU Wien Bibliothek.
TU Bibliothek Your knowledge hub WIEN

additional limitation for the technique. Temperature induced deformation/widening of the pillar circumference during testing of a nitride coating at 500 °C led to inconsistencies in the critical load, effectively lowering the accuracy of the calculated fracture toughness [123]. Consequently, similar to conventional indentation-based techniques, the use of low-angle indenter tips (*i.e.*, cube-corner tip) is advantageous due to the easier initiation of cracks, which additionally extends the applicability towards semi-brittle materials such as intermetallics or glasses [123–125].

3.3.3 Cantilever bending

A technique based on the bending and fracturing of pre-notched microcantilever geometries to obtain the fracture toughness of brittle thin film materials was first introduced by Di Maio and Roberts in 2005 [29]. Similar to the pillar splitting approach, the technique relies on the FIB preparation of the free-standing geometry, although other, significantly faster milling routes have recently also been reported [126]. Given the inertness of the thin film material, chemical etching of the substrate material is regularly employed to create a segment of free-standing thin film, which allows to avoid the cumbersome and error-prone removal of the base material through ion milling [31]. From the initial approach in [29], the technique was then extended to various other beam geometries including single and double cantilevers, clamped beams, as well as to different beam cross-sections of rectangular, pentagonal or triangular shape [121, 127, 128]. Although the rectangular, single-side supported cantilever remains the most widely used geometry, the shape restricts the preparation close to a free sample surface. Contrary, shapes with angled side walls have the advantage of an arbitrary placement on the sample surface, thus enabling experiments on various microstructural features [111]. Accurate fracture toughness evaluation additionally requires the introduction of a sharp pre-crack/notch close to the cantilever base, usually introduced by FIB milling, although electron-beam milling in a TEM has recently been reported [129]. Analogously, various shapes and forms were developed over the years, *e.g.*, the chevron-notch, triangular or straight notch [127, 130, 131], with the latter being the most popular due to the ease of manufacturing. The straight notch is typically prepared in such a way, that instead of extending over the entire cantilever width, small material ligaments ("bridges") remain on both ends, serving as nucleation sites for a sharp crack front during the bending experiment [131]. Similar to the pillar-splitting approach, *ex-situ* experiments are rather uncommon, given the complexity of nanoindenter tip positioning with respect to the cantilever free-end. Regarding the investigations within the framework of this thesis, an approach following the works of Matoy *et al.* [31] and Brinckmann *et al.* [131, 132] was chosen (see Figure 3.5).

During the actual fracture toughness measurement either a conical, spherical or wedge-shaped indenter tip is used to bend the cantilever until failure. Based on the recorded load-displacement curve and the geometrical dimensions of the fractured cantilever cross-

Die approbierte gedruckte Originalversion dieser Dissertation ist an der TU Wien Bibliothek verfügbar.
The approved original version of this doctoral thesis is available in print at TU Wien Bibliothek.
TU Bibliothek Your knowledge hub WIEN

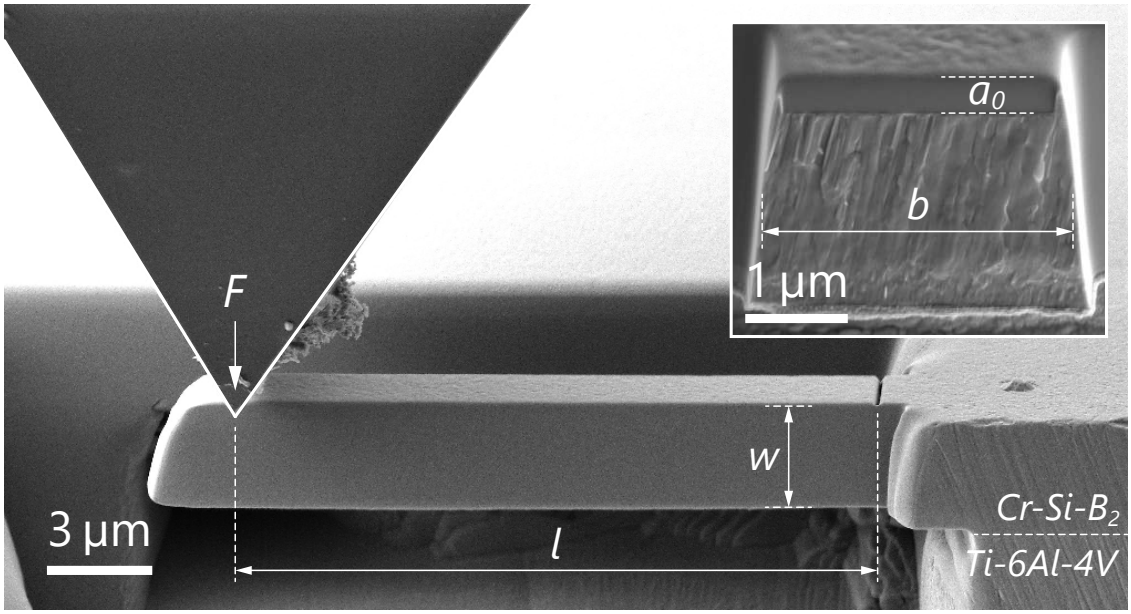

Fig. 3.5: SEM micrograph of a FIB prepared, pre-notched micro-cantilever of Cr-Si-B_2 as used for fracture toughness testing. The insert shows a post-mortem SEM micrograph of the fractured cantilever cross-section with the pre-notch depth a_0. (Own, unpublished work).

section, the critical stress intensity factor can be calculated from [31]:

$$K_{Ic} = \frac{F_{max} L}{b w^{3/2}} \cdot f\left(\frac{a_0}{w}\right) \tag{3.16}$$

where F_{max} denotes the bending force at failure, L the distance between the pre-notch and nanoindenter tip, b the cantilever width, w the cantilever thickness, and a_0 the initial notch depth. The dimensionless shape factor $f\left(\frac{a_0}{w}\right)$ is derived from finite element simulations and essentially depends on the beam geometry. A cubic polynomial valid for beam aspect ratios of H:L:w:B = 2:5:2.1:1.7 and a/w-ratios between 0.05 and 0.45 is given in Ref. [31, 133]:

$$f\left(\frac{a_0}{w}\right) = 1.46 + 24.36\left(\frac{a_0}{w}\right) - 47.21\left(\frac{a_0}{w}\right)^2 + 75.18\left(\frac{a_0}{w}\right)^3 \tag{3.17}$$

An alternative version can be found in Refs. [134, 135].

Despite the laborious sample preparation, the cantilever bending technique offers the advantage of being more error-resistant and insensitive in terms of sample-tip alignment and sample geometry deviations, when compared to the previously described methods [111]. In addition, comparable to the pillar splitting and unlike the cube-corner indentation approach, cantilever-based fracture toughness experiments permit testing of the intrinsic fracture toughness of the coating material. Due to the free-standing nature of the cantilever beam, an influence of residual stresses is excluded. Furthermore, the technique enables the analysis of

Die approbierte gedruckte Originalversion dieser Dissertation ist an der TU Wien Bibliothek verfügbar.
The approved original version of this doctoral thesis is available in print at TU Wien Bibliothek.
TU Bibliothek Your knowledge hub WIEN

specific microstructural interfaces, *e.g.*, a coating-substrate or coating-coating interface, by deliberately placing the location of interest at the pre-notch position [136, 137].

Although the technique is rather insensitive towards variations of the beam geometry within the abovementioned boundaries, it inherently depends on the fabrication of an as-sharp-as-possible pre-notch [133], which is determined by the FIB equipment and in particular the ion source used for the milling process [138]. Especially the use of Ga-ions was demonstrated to interact with the film microstructure at elevated temperatures, leading to embrittlement and thus lower fracture toughness values [121].

3.3.4 Cantilever bending – *J*-integral

Cantilever bending tests performed on brittle materials usually conclude in an instantaneous fracture of the beam, once the elastic loading regime is exceeded and cracks nucleate from the material bridges. The validity of equation 3.16 ends, however, if the material (pairing, *i.e.*, on interfaces) allows for non-negligible plastic deformation or energy dissipating mechanisms, typically resulting in stable crack growth during the bending experiment. This is due to an increased plastic zone around the crack tip, which prohibits a fracture toughness evaluation within LEFM. In this case, a stiffness-based analysis of the fracture process is required [111]. A corresponding methodology was first reported by Wurster *et al.* [139], who adapted the *J*-integral method for micro-scale applications.

Analogous to the macroscopic approach outlined in ASTM 1820 [104], multiple partial unloading segments are performed during the cantilever bending sequence, from which the cantilever-stiffness (more precisely the contact-stiffness) can be extracted in-between defined displacement intervals [111] (see Figure 3.6a). The decreasing stiffness correlates with a decreasing cantilever cross-section, thus an increasing crack length a_i. A rough correlation between the stiffness k_i of the i_{th} unloading segment and the current crack length is given by [139] (note, the relation is only accurate for unnotched cantilevers [111]):

$$w - a_i = \sqrt[3]{\frac{4k_i L^3}{bE}} \tag{3.18}$$

In addition, the quantity of energy dissipated by plastic deformation $A_{pl,i}$ can be extracted from the load-displacement curve as the area between two successive unloading segments (see Figure 3.6a) [111]. With the progress in nanoindentation equipment, the sequential unloading is typically replaced by so-called continuous-stiffness measurements (CSM). Instead of performing distinct unloading segments, a sinusoidal oscillation is superimposed on the nanoindenter motion (see Figure 3.6b), which allows for a continuous evaluation of the beam stiffness over the entire bending experiment [111, 140, 141]. The experimentally determined *J*-integral is then calculated from an elastic and plastic part, where the latter part is calculated

Die approbierte gedruckte Originalversion dieser Dissertation ist an der TU Wien Bibliothek verfügbar.
The approved original version of this doctoral thesis is available in print at TU Wien Bibliothek.
TU Bibliothek Your knowledge hub WIEN

in an iterative procedure, corresponding to every unloading segment i [104, 139]:

$$J_i = J_{el,i} + J_{pl,i} = \frac{K_{Iq,i}^2(1-\nu^2)}{E} + \left[J_{pl,i-1} + \frac{\eta(A_{pl,i} - A_{pl,i-1})}{b(w-a_{i-1})}\right] \times \left[1 - \gamma\frac{a_i - a_{i-1}}{w - a_{i-1}}\right] \quad (3.19)$$

where K_{Iq} represents the linear elastic stress intensity factor (see equation 3.16), ν the Poisson's ratio, E the Young's modulus, η and γ are constants, and A_{pl} the area under the load displacement curve excluding the elastic portion. The subscript "q" generally denotes the obtained values as "qualified", indicating that not all requirements for LEFM apply.

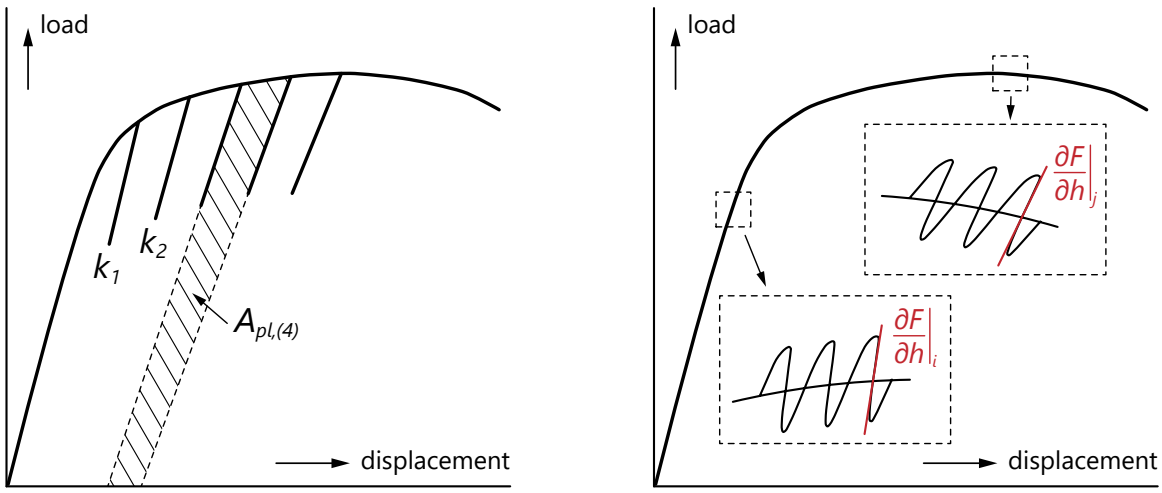

(a) (b)

Fig. 3.6: (a) Load-displacement curve with partial unloading segments for contact stiffness calculation. (b) Load-displacement curve with sinusoidal load oscillation for continuous stiffness measurements. Both figures adapted from [111].

Subsequently, a crack resistance curve J-Δa can be created, which allows to determine a critical value J_q for the onset of stable crack growth. In addition, for improved comparison to data and LEFM, the fracture toughness can be determined from [139]:

$$K_{Iq,J} = \sqrt{\frac{J_q E}{1-\nu^2}} \quad (3.20)$$

An intrinsic shortcoming of this approach was the actual stiffness-based calculation of the crack-length a_i, since a general relation for the notched cantilever geometry was missing until recently. Through a combination of FEM simulations and a series of stiffness measurements performed on cantilevers of varying materials and increasing notch depths, Alfreider *et al.* [142] generated a more universal formulation for the cantilever stiffness - notch-depth

Die approbierte gedruckte Originalversion dieser Dissertation ist an der TU Wien Bibliothek verfügbar.
The approved original version of this doctoral thesis is available in print at TU Wien Bibliothek.

behavior. Furthermore, the restriction towards single-material cantilevers was resolved by introducing an analytical, material-parameter-free (except for the Poisson's ratio) solution to the problem, thus extending the applicability towards heterogeneous materials [143–145]. Therein, the crack length a_n is calculated from the change in cantilever stiffness following:

$$\int_0^{a_n} \frac{a}{w} Y\left(\frac{a}{w}\right)^2 da = \frac{\left(\frac{k_0}{k_n} - 1\right) L^3}{18\pi(1-\nu^2)L'^2} \tag{3.21}$$

where w, L, and L' are factors corresponding to the cantilever dimensions, $Y\left(\frac{a}{w}\right)$ is a geometric factor taken from [135], ν is the Poisson's ratio, and k_n is the recorded cantilever stiffness at point n. Determining the stiffness k_0 of the unnotched cantilever can be challenging, however equation 3.21 can be rewritten to calculate this value from the initial stiffness of the notched cantilever $k_0(a_0)$ according to:

$$k_0 = k_0(a_0)\left(1 + \frac{18\pi(1-\nu^2)L'^2}{L^3}\int_0^{a_0} \frac{a}{w} Y\left(\frac{a}{w}\right)^2 da\right) \tag{3.22}$$

The integral on the left-hand side of equation 3.21 can be solved numerically for values of a_n covering a/w-ratios of *e.g.*, 0.1 to 0.9. When specifically applied to cantilevers fabricated from heterogenous materials, equation 3.19 additionally needs to be replaced by an older formalism to calculate the J-integral, given the lack of a general Young's modulus for the beam. The following version according to Rice *et al.* is applicable [146, 147]:

$$J_n = \frac{2A_{tot,n}}{b(w - a_n)} \tag{3.23}$$

where $A_{tot,n}$ is the total area under the load-displacement curve up to point n.

3.3.5 Cantilever bending – *J*-integral – interface toughness

A principal requirement in developing fatigue resistant thin films lies in the optimization of the interface adhesion between the coating and substrate material. While seemingly a simple premise, finding an optimum involves tuning of the entire coating-substrate system. In particular the interplay of the thermo-physical properties of both constituents, but also the synthesis parameters and coating architecture have to be considered. Qualitative assessment of the interface strength is typically realized using nanoindentation-based scratch tests [148, 149] or Rockwell indentation [150]. However, the techniques return limited information in terms of a quantitative comparison as well as the mode of failure. Here, microcantilever-based assessment of the coating-substrate interface is targeted towards bridging this gap by providing both visual and quantitative failure analysis based on fracture mechanics principles.

Die approbierte gedruckte Originalversion dieser Dissertation ist an der TU Wien Bibliothek verfügbar.
The approved original version of this doctoral thesis is available in print at TU Wien Bibliothek.
TU Bibliothek Your knowledge hub WIEN

Within this thesis, the formalism introduced by Alfreider *et al.* [144] to calculate the crack length a_n based on the stiffness evolution during elastic-plastic microcantilever bending experiments is applied to investigate the interface toughness between a Ti-Al-N coating and two different alloys within the continuous J-integral framework. Therefore, a $Ti_{0.50}Al_{0.50}N$ coating was synthesized by cathodic arc evaporation on both Ti-6Al-4V and IN718 substrates (mirror-polished, 1 μm grid) to a uniform thickness of $t = 12$ μm. The micro-cantilever fabrication was performed by FIB milling on mirror-polished cross-sections of the coated substrates, with at least 9 beams created at an aspect ratio of $W \times B \times L = 2 \times 2 \times 12$ μm^3 for every sample. The micro-cantilevers were oriented in growth direction of the $Ti_{0.50}Al_{0.50}N$ coating, thus positioning the coating-substrate interface at the pre-notch location. This crack nucleation site was introduced in the form of a straight notch at a depth of $a_0 \sim 500$ nm, with small material bridges remaining on both sides. Figure 3.7a presents an overview of the $Ti_{0.50}Al_{0.50}N$ cantilevers prepared on the Ti-6Al-4V alloy.

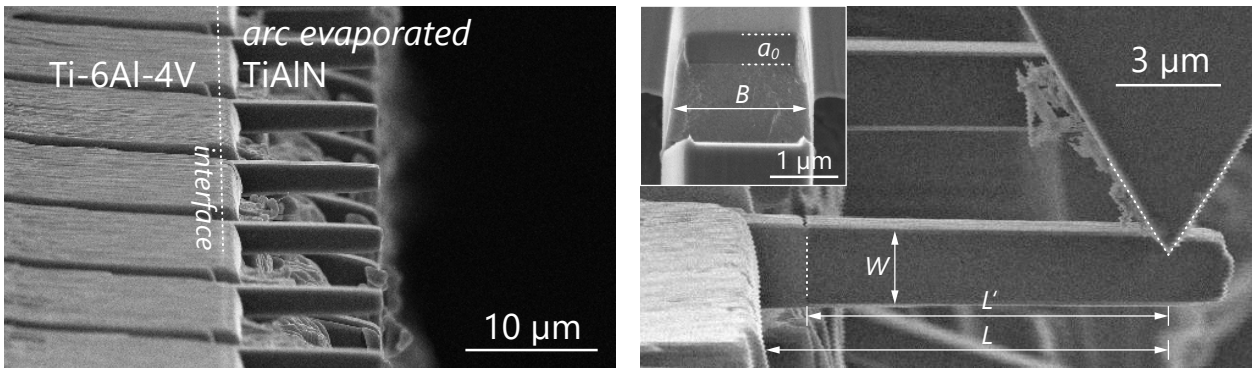

(a) (b)

Fig. 3.7: (a) Ensemble of cantilever specimens fabricated from arc evaporated $Ti_{0.50}Al_{0.50}N$ thin films on Ti-6Al-4V substrate. The cantilevers are produced in film growth direction with the coating-substrate interface placed at the pre-notch position. (b) Details on the geometry of a Ti-Al-N cantilever on IN718 substrate and the nanoindenter wedge-tip placement. The insert depicts the fractured cross-section along the interface as well as the pre-notch depth a_0. (Own, unpublished work)

The cantilevers were tested using an *in-situ* nanoindentation system equipped with a diamond wedge tip and operated in CSM mode. Thus, in addition to the load-displacement data, also the cantilever stiffness was continuously recorded. Cantilever loading was performed at 5 nm/s with a sinusoidal amplitude of 5 nm/s at a frequency of $f = 200$ Hz. Details on the nanoindenter tip placement with respect to a representative cantilever fabricated on the IN718 alloy in the as-prepared and post-fractured state are given in Figure 3.7b.

Figures 3.8a and b show the raw load- and continuous stiffness-displacement data for the cantilevers prepared on the IN718 and Ti-6Al-4V substrate, respectively. Since the deviations

Die approbierte gedruckte Originalversion dieser Dissertation ist an der TU Wien Bibliothek verfügbar.
The approved original version of this doctoral thesis is available in print at TU Wien Bibliothek.
TU Bibliothek Your knowledge hub WIEN

in the final cantilever geometries were insignificant, a comparability is given between the absolute values in both graphs. The data for the IN718-interface shows a load range of ∼350 μN when a noticeable deviation from the linear-elastic behavior occurs, while this is already noticeable at significantly lower values for the Ti-6Al-4V-interface, between 250 to 300 μN. Both sample types show a slight increase of the load data with progressing cantilever deflection, suggesting hardening of the substrate material. Moreover, small force drops without a concomitant stiffness loss are especially visible for the IN718-sample, which could be caused by the activation of glide planes. The corresponding stiffness data consistently shows a gradual increase within the initial 100 nm of beam deflection, until a rigid contact between the indenter tip and the cantilever is established. Afterwards, the data shows a very alike response for both interfaces with a slight decrease in stiffness up to a deflection of 1500 nm. In general, the results suggest a continuous plastic deformation occurring on both interfaces, without indications for distinct crack growth events (except for a single cantilever on both substrates at a similar deflection of ∼700 nm). Hence, the evaluation is conducted outside classical elastic-plastic fracture mechanics.

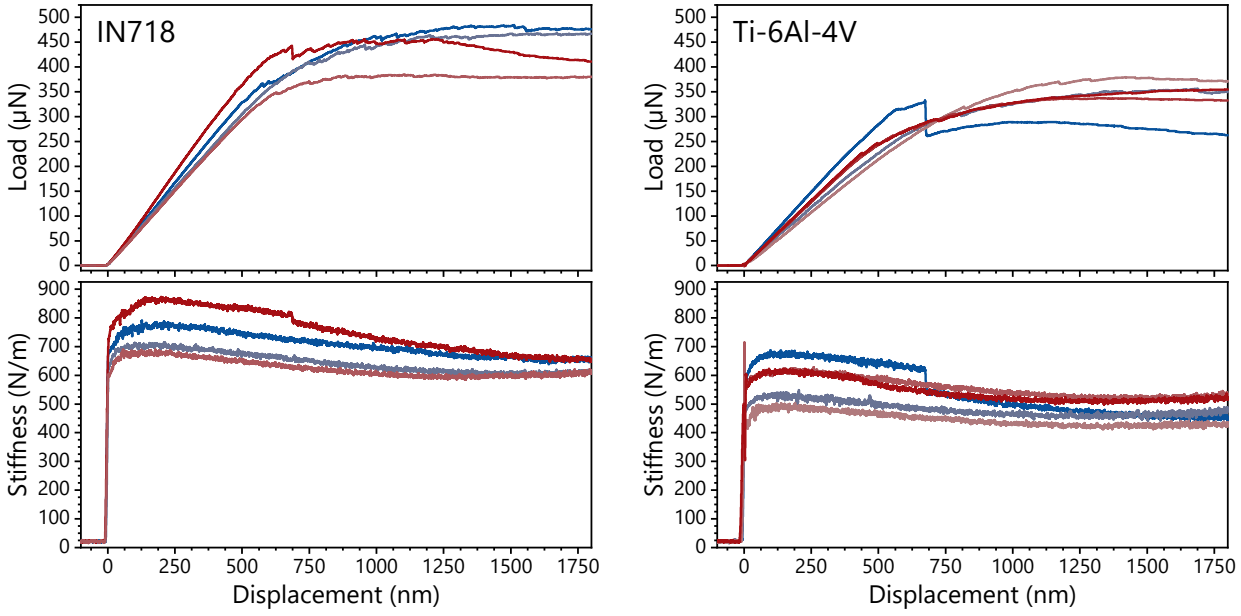

(a) (b)

Fig. 3.8: Raw load- and stiffness-displacement data for cantilevers prepared on (a) IN718 and (b) Ti-6Al-4V substrate. (Own, unpublished work)

Figures 3.9a and b show the corresponding crack resistance curves J - Δa determined using equations 3.21 to 3.23. Both material pairings show an immediate increase of the J-integral upon loading, corresponding to the plastic deformation of the substrate material and crack-tip blunting. Only a single cantilever within both sample types indicates a sudden crack extension at $J \sim 100$ J/m^2 for the Ti-6Al-4V-interface and at $J \sim 80$ J/m^2 for the IN718-interface.

Die approbierte gedruckte Originalversion dieser Dissertation ist an der TU Wien Bibliothek verfügbar.
The approved original version of this doctoral thesis is available in print at TU Wien Bibliothek.
TU Bibliothek Your knowledge hub WIEN

However, based on scanning electron microscopy investigations, these crack growth events could be linked to cleavage fracture within the substrate material, possibly occurring on grain-boundary sites located close to the pre-notch position. A general comparison of J-integral values up to a virtual crack extension of 150 nm reveals slightly higher values for the Ti-Al-N coating deposited on IN718, than on Ti-6Al-4V. Although this suggests an increased toughness for the IN718-interface, the statement has to be taken with care, especially since the absolute values between the samples are rather close. Nevertheless, the individual cantilevers for both samples reveal consistent results, which underlines the capabilities of this methodology.

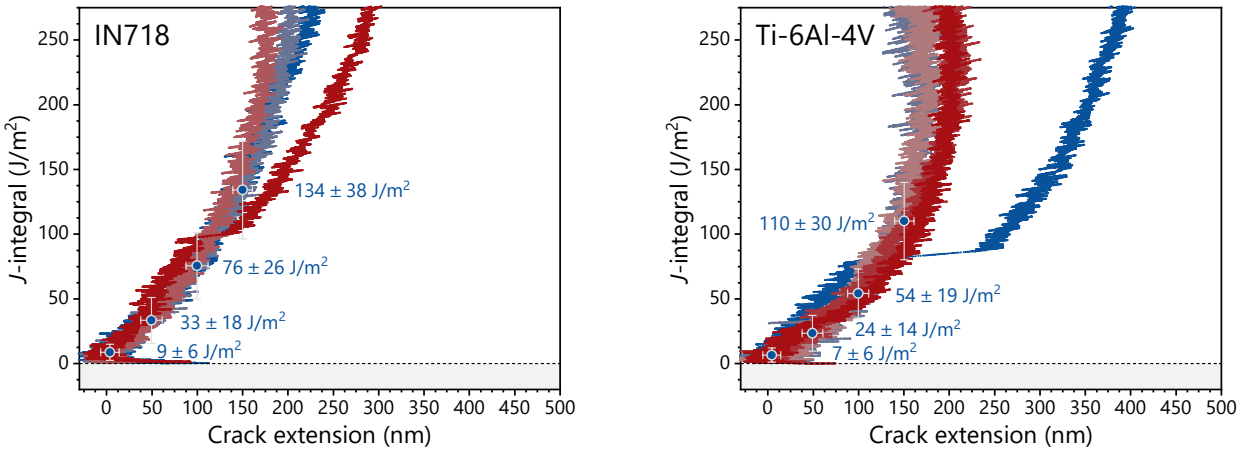

(a) (b)

Fig. 3.9: Crack resistance curves J - Δa for cantilevers prepared on (a) IN718 and (b) Ti-6Al-4V substrate. (Own, unpublished work)

In the following, distinct shortcomings of the applied testing strategy will be briefly addressed.

- The preparation of multiple micro-cantilevers on a single sample is advantageous in terms of high throughput during *in-situ* testing, and providing statistical validity to the results. However, the juxtaposition of several cantilevers as presented in Figure 3.7a prohibits a viewpoint parallel to the notch line, *i.e.*, obscuring the view of the fracture process and crack growth.
- Moreover, the cantilever orientation restricts the FIB milling of the rectangular shape – especially the bottom and top surface – so that the ion-beam has to be oriented parallel to the cantilever length. This results in a tapered geometry (see Figure 3.7b) and an undefined removal of the substrate base material on the cantilever bottom, which promotes extensive slip deformation of the substrate during the bending process.
- The type of pre-notch used in the experiments is designed for the fracture toughness evaluation of brittle materials, thus not in line with the derivation of the employed formalism. Instead, a straight-through notch should be used for the testing of elastic-plastic specimen.

Die approbierte gedruckte Originalversion dieser Dissertation ist an der TU Wien Bibliothek verfügbar.
The approved original version of this doctoral thesis is available in print at TU Wien Bibliothek.
TU Bibliothek Your knowledge hub WIEN

3.4 Influencing the fracture toughness of thin films

Several decades of thin film research were dedicated to increasing the hardness of ceramic coating materials [60]. Increasing the hardness is, however, typically accompanied by an increasing brittleness of the material [34]. Although this approach seemed to be sufficient for generic "hard coating" applications (*e.g.*, milling, drilling, etc.), modern thin film solutions increasingly demand hard-yet-tough materials [151, 152]. The search for the "right" materials or their combination gained increasing importance in recent years, with solutions found at various length scales of materials science. The following is a brief, but by no means complete, introduction to various approaches of increasing the toughness in thin film materials.

3.4.1 Electronic-structure design

Instead of attempting to increase the toughness from an extrinsic point-of-view, understanding the physical properties of thin films from an intrinsic perspective on the level of interatomic bonds reveals the origins of the ductility-brittleness relationship [34]. Therein, electronic-structure investigations based on first-principles calculations showed great potential in revealing descriptors that enable a targeted synthesis of toughened thin films. Especially the valence electron concentration (VEC) takes a key role in predicting the ductile character of cubic transition metal nitride (TMN) thin films. Increasing the VEC in these materials was shown to enhance the contribution of metallic bonds (*i.e.*, delocalized electrons), thus spanning a direct connection to the ability for plastic deformation during crack growth [34, 153]. This concept was experimentally underpinned by several studies, connecting the synthesis of ternary, high VEC, TMN coatings (VEC $>$ 8.5) with enhanced intrinsic toughness, while maintaining their hardness close to the binary constituents (*e.g.*, Ti-W-N [34, 154], V-Mo-N [155], Ti-Mo-N [156]). In addition, instead of tuning the VEC by TM alloying, the concept works in a similar manner for alloying on the non-metal sublattice, as demonstrated for the Ta-C-N system [36, 157]. Alternatively, in view of Griffith's theory of fracture (see equation 3.4), an increased toughness can also be expected for brittle materials through enhanced bond strengths between the atomic constituents – translating into an increased energy of separation E_{sep} along a crack plane. Experimentally, this idea is based on a trial & error approach, whereas density functional theory calculations enable high throughput research of vast material fields, with promising materials (and their combinations) found for TMN, TM-carbides and related carbo-nitrides [158]. Overall, tuning of the electronic structure and bonding character of potential thin film materials is reflected in altered elastic constants. Moreover, the increasing scientific efforts devoted to this branch of materials science indicate a clear trend towards designing future materials down to the atomic scale.

Die approbierte gedruckte Originalversion dieser Dissertation ist an der TU Wien Bibliothek verfügbar.
The approved original version of this doctoral thesis is available in print at TU Wien Bibliothek.
TU Bibliothek Your knowledge hub WIEN

3.4.2 Architectural & morphological design

General improvements in the fracture toughness of thin film materials are also realized by replacing monolithic-, with more complex hierarchical designs. Inspired by toughening effects observed in nature and likewise in metallic or ceramic bulk materials, spatial heterogeneity in terms of structure and/or composition allows a variation of the mechanical properties, that can lead to a significant increase in damage tolerance [110, 159–161]. In this context, a layered arrangement of alternating ductile (metal) and mechanically strong (ceramic) thin films proved successful in increasing the overall fracture toughness, while retaining the hardness of the stronger, ceramic material (*e.g.*, TiN/Ti [162], CrN/Cr [161]). The toughening mechanisms involved in such heterogenous multilayers include the reduction of the local crack tip stress intensity (for a given load and crack length), but also the energy dissipation through crack deflection on interfaces or plastic deformation within the ductile layer. In addition, architectural designs involving the coherent growth of nanometer scale multilayers (*i.e.*, "superlattice" (SL) films) can achieve a simultaneous increase in film hardness and fracture toughness [32, 163]. While the hardness increase in SL coatings is well described in terms of dislocation mobility [164], the origins of enhanced fracture toughness are still under debate. Recently, a correlation was found between the layer-period dependent fracture resistance and the coherency stresses originating from the lattice-mismatch between the layers [165]. SL thin films further permit the stabilization of metastable phases (*e.g.*, cubic AlN) within the nano-structured architecture by providing a template effect for the otherwise unstable configuration. Upon crack propagation and release of coherency stresses a transformation into the stable structure is enabled, effectively causing a transformation toughening effect. In the case of AlN, the transition towards the wurtzite structure entails a specific volume increase of ∼26%, reducing the crack driving force through compressive stresses or crack deflection. This concept proved especially effective in increasing the toughness of CrN/AlN superlattice structures, as revealed by DFT calculations and micromechanical experiments [166, 167]. Finally, also tuning of the weakest link within the thin film morphology – the grain boundaries – can be utilized to improve the fracture toughness, as demonstrated for a zig-zag patterned growth morphology (*i.e.*, crack deflection mechanisms) [168] or strengthening through population with a separate phase (*e.g.*, nanocomposite of TiN/SiN_x) [169].

3.4.3 Stress state design

Tuning the residual stress state of a thin film is probably the most obvious parameter in achieving fracture-resistant thin films, since it overlaps with all aspects mentioned above. Increasing the compressive stress enhances the load-range of a material before a crack nucleates, whereas tensile stresses proportionally lower the fracture tolerance and favor crack growth. Adjusting the thin film stress state relies on various aspects along the synthesis chain, with strong links to the substrate material and the deposition conditions.

Die approbierte gedruckte Originalversion dieser Dissertation ist an der TU Wien Bibliothek verfügbar.
The approved original version of this doctoral thesis is available in print at TU Wien Bibliothek.
TU Bibliothek Your knowledge hub WIEN

Chapter 4

Fatigue

The origins of fatigue research are largely based on historical disasters that resulted in spectacular material failure or even the loss of life, such as the railroad accident near Versailles in the year 1842 [170, 171]. With the increasing use of ferrous structures in buildings and the railway sector in the mid-19th century, an increasing number of similar accidents occurred, where the cause could be traced to fatigue failure [170]. Despite the extensive research conducted in the following 150 years, understanding fatigue failure remains a complex, multi-scale endeavor given its sensitivity towards a variety of factors such as the loading conditions, the material type and microstructure, as well as the environmental conditions [8, 23]. Therefore, establishing a fundamental understanding of the mechanisms involved in fatigue failure remains a core aspect of current materials science, with the objective to provide accurate predictions of the accessible fatigue life.

Given the fact that a majority of structural components relies on various types of metals, research focus was primarily placed on this material family. Their ability for plastic deformation and cyclic slip was long considered a principal requirement for fatigue failure to occur. Nowadays it is recognized that also kinematic irreversibilities within the microstructure of nonmetallic materials similarly entail mechanical fatigue under cyclic loads, despite the absence of distinct dislocation motion [170]. The following will present an overview of the principal mechanisms governing fatigue failure in metals, but also summarize the main aspects in the fatigue characterization of non-metals. Finally, an overview of the current research status in cyclic testing of ceramic thin film materials will be given.

Die approbierte gedruckte Originalversion dieser Dissertation ist an der TU Wien Bibliothek verfügbar.
The approved original version of this doctoral thesis is available in print at TU Wien Bibliothek.

4.1 Metals

A microscopically small crack can nucleate in a metallic component subject to cyclic loading, which subsequently grows to macroscopic size, until component failure occurs during the final load cycle of the fatigue life [10]. Hence, fatigue failure refers to the modification of material properties due to the application of cyclic stress, that eventually leads to failure. From a broader perspective, this avenue of material degradation can be split into several successive stages [170]:

- (Sub-)microstructural changes that lead to permanent damage within the material.
- Nucleation of microscopic cracks.
- Coalescence and growth of microscopic cracks to form a macroscopic crack.
- Stable crack propagation of the macroscopic crack.
- Unstable crack propagation and failure.

The initiation and growth of fatigue micro-cracks are a consequence of periodic slip, *i.e.*, cyclic dislocation motion [9, 10]. At an early stage, research notice that fatigue damage is strongly surface related. Considering that fatigue damage occurs at stress amplitudes well below the tensile strength of a material, coordinated material slip will be focused towards surface near grains given the lack of deformation restrictions from the environment (*e.g.*, ambient air). However, for cyclic slip to occur, a specific shear stress is required, which inherently depends on the size, shape and crystallographic orientation of grains. Consequently, certain grains will exhibit more favorable conditions for slip than others due to the inherent anisotropy of most materials [10, 171]. In the case of a slip event, so called "slip-steps" will be created on the grain surface (see Figure 4.1a and b). Naturally, this newly exposed material will immediately be covered by a native oxide layer. In addition, strain hardening may occur. Since both phenomena are far from reversible, subsequent slip events will take place on adjacent planes, forming a persistent slip band (PSB, see Figures 4.1b and c) [171]. As evidenced by Forsyth [172], this eventually cumulates in a distinct surface topography with stepped features, referred to as "intrusions" or "extrusions" (see Figure 4.1c and d). Related to Schmid's law [173] on shear stresses, these surface features tend to appear at a 45° angle to the external stress axis [171]. The PSB and related surface features lead to the formation of initial micro-cracks of the order of the grain size (see Figure 4.1d). Once the crack passes through grain boundaries into adjacent grains, increasing constraints are imposed on cyclic slip displacement, leading to the activation of additional slip systems and a tendency for crack growth perpendicular to the loading axis [10, 171] (see Figure 4.1e). Apart from this natural crack initiation, factors including notch effects of the geometry, surface roughness, environmental attack (*e.g.*, corrosion,

Die approbierte gedruckte Originalversion dieser Dissertation ist an der TU Wien Bibliothek verfügbar.
The approved original version of this doctoral thesis is available in print at TU Wien Bibliothek.
TU Bibliothek Your knowledge hub WIEN

fretting, etc.), but also internal defects, can be the source of cyclic crack growth. The following stage of crack extension is inherently dependent on the crack growth resistance of the material.

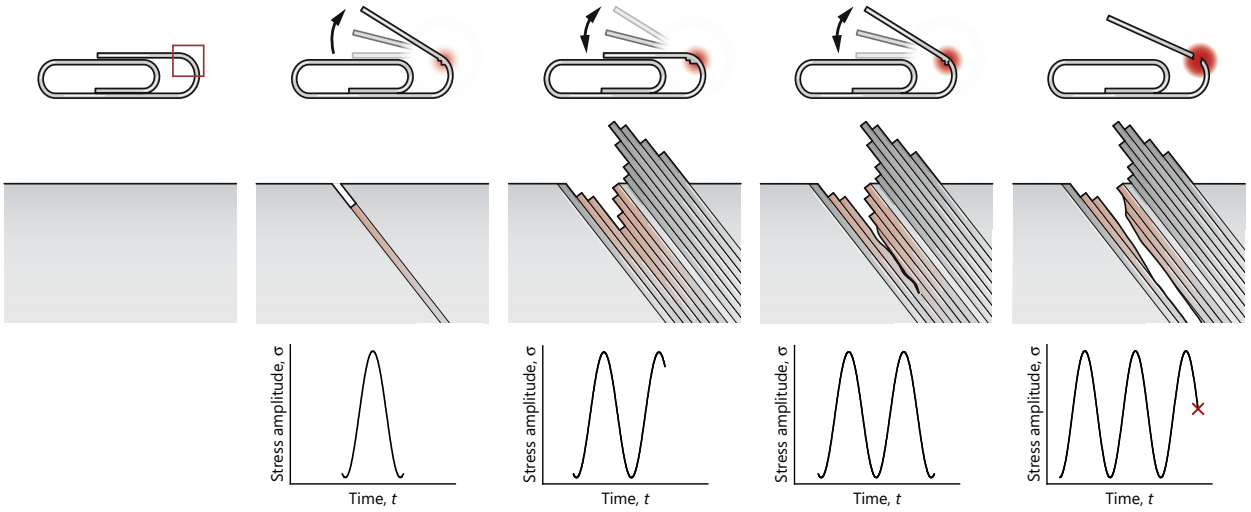

Fig. 4.1: Schematic evolution of the fatigue crack initiation mechanism in metals on the example of a cyclically bent paperclip. The schematic is adapted from [1].

Cracks originating from aforementioned material flaws or defect sites typically grow at stress intensities well below the actual fracture toughness, thus, the phenomenon is generally termed "subcritical crack growth" [170]. For conditions of small-scale yielding (small plastic zone at crack tip in otherwise elastic material), Paris, Gomez & Anderson [174] postulated that crack growth rates under cyclic loading are correlated with the stress intensity factor K. Indeed, a subsequent work by Paris & Erdogan [175] introduced the following empirical power-law relation [170]:

$$\frac{da}{dN} = C\Delta K^m \tag{4.1}$$

connecting the extension in crack length a per load cycle N, with the stress intensity range $\Delta K = K_{max} - K_{min}$, where K_{max} and K_{min} correspond to the maximum and minimum applied stress during a load cycle. The parameters C and m are functions of the material properties, the loading conditions, temperature, environmental influences, etc. [170]. The general nature of fatigue crack growth in metallic materials is schematically illustrated in Figure 4.2 [176], presenting the crack growth rate as function of the stress intensity range. For descriptive purposes, typically, a distinction between two regions of asymptotic crack growth (regimes A and C) and the so-called "Paris"-region is made.

Die approbierte gedruckte Originalversion dieser Dissertation ist an der TU Wien Bibliothek verfügbar.
The approved original version of this doctoral thesis is available in print at TU Wien Bibliothek.

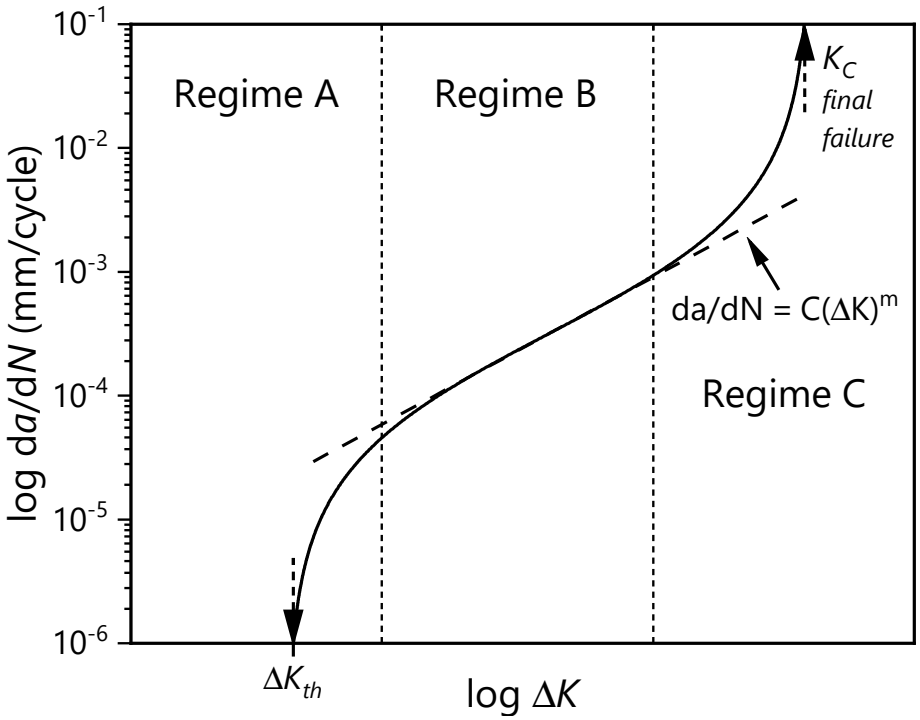

Fig. 4.2: Schematic evolution of the fatigue crack-growth rates as function of the applied stress intensity range for metallic materials. The illustration is adopted from [176].

Regime A At extremely low stress intensity ranges, where ΔK approaches a threshold value ΔK_{th}, crack growth is markedly sensitive to microstructures and environments [176]. Even if micro-cracks were nucleated on the surface, the applied loads may be too low to effectively advance a crack beyond microstructural barriers [10]. Thus, for $\Delta_K < \Delta K_{th}$, cracks are generally considered inactive.

Regime B: *Paris region* Increasing ΔK leads to stable crack extension with growth rates following Paris' law 4.1. In this regime, many metals and alloys are characterized by a general ductile striation mechanism. Such striations are visible in the crack wake and correspond to single crack-length increments per load cycle [176]. The actual crack advance follows a cyclic "blunting" and "resharpening" mechanisms of the crack tip. Under load, the crack opens and plastic deformation of the tip leads to an incremental extension. This is followed by closing and resharpening of the crack tip at the opposite end of the cycle [10]. Outside this regime, Paris' law fails to capture the asymptotic behavior crack growth rates.

Regime C: At very high stress intensity ranges, crack growth becomes unstable and crack growth rates increase asymptotically until final material failure occurs when K_{max} approaches K_c. However, K_c usually is not a constant material property, since the final rupture may involve large scale plastic deformation within the remaining ligament. The drastic increase in

Die approbierte gedruckte Originalversion dieser Dissertation ist an der TU Wien Bibliothek verfügbar.
The approved original version of this doctoral thesis is available in print at TU Wien Bibliothek.

growth rates is realized through the contribution of monotonic fracture mechanisms, such as cleavage, intergranular fracture and microvoid coalescence. Thus this regime is sensitive to microstructural features and K_{max} [10, 170, 176].

The first noteworthy, systematic research on cyclic fatigue of materials was conducted by August Wöhler circa 1860, who pioneered a characterization in terms of stress amplitude - cycles to failure (S-N_f) curves and the concept of a fatigue "endurance limit" [170]. S-N_f curves are the result of several fatigue tests conducted at different stress levels, yet on identical sample geometries and loading conditions. The stress amplitude is plotted as function of the number of load cycles to failure, with both parameters generally displayed on a logarithmic scale (see Figure 4.3). S-N_f curves show an initial plateau at low values of N_f, which corresponds to the tensile strength of the material (*i.e.*, the single cycle strength). Lowering the stress amplitude evidently increases the cycle life until a lower plateau is reached ($\sim 10^6$ load cycles). This corresponding stress amplitude is referred to as the fatigue limit, below which a defect-free sample may be cycled indefinitely without resulting in failure [10]. Technically, this is only valid for *bcc* structured metals (capable of dynamic strain aging), since *fcc* metals tend to show a continued decrease in the endurable stress amplitude (see dashed line in Figure 4.3). Thus, commonly the value at $N_f \sim 10^7$ is referenced as fatigue limit for these metals [170]. The data commonly presents a linear relationship on logarithmic scales, for which several mathematical descriptions were introduced to predict the material behavior. A commonly used expression is the Basquin relation [170]:

$$S = \sigma_f^{'}(2N_f)^b \tag{4.2}$$

where $\sigma_f^{'}$ corresponds to a fatigue strength coefficient and b denotes the fatigue strength exponent.

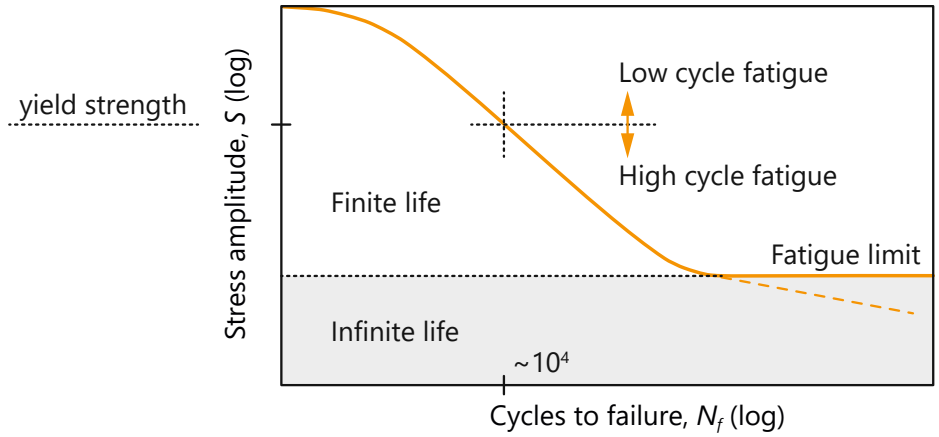

Fig. 4.3: Characteristic stress-amplitude vs. cycles to failure (S-N_f) curve for metallic materials. The illustration is adopted from [10].

Die approbierte gedruckte Originalversion dieser Dissertation ist an der TU Wien Bibliothek verfügbar.
The approved original version of this doctoral thesis is available in print at TU Wien Bibliothek.
TU Bibliothek Your knowledge hub WIEN

Fatigue failure in the regime of high stress amplitudes and cycles to failure in the order of $N_f < 10^4$ is referred to as *low-cycle fatigue* (LCF). Contrary, if fatigue occurs at a larger number of cycles $N_f > 10^5$ and lower stress amplitudes, the failure is denoted as *high-cycle fatigue* (HCF). The distinction between low- and high-cycle fatigue is not linked to a specific number of load cycles, but rather to the general loading conditions. Low-cycle fatigue involves considerable macroplastic deformation during cyclic loading, whereas high-cycle fatigue is associated with elastic loading of the material [10, 170]. Based on the independent works of Coffin and Manson, low-cycle fatigue is typically characterized in terms of the applied strain-, rather than the stress-amplitude [10, 177, 178].

4.2 Ceramics

Ceramic materials are characterized by a strong directionality of the atomic bonds, high Peierls-Nabarro barrier, and thus limited dislocation mobility. While these properties provide a recipe for high strength materials, ceramics inevitably suffer from pronounced brittleness and low fracture toughness [159]. In this sense, the synthesis of high strength - high fracture resistance materials requires mutually excluding properties, so that their design is invariably based on a compromise [159]. It is this trade-off that necessitates particular attention to the fracture properties of ceramic materials. Hence, prior to focusing on the principles of cyclic damage and fatigue failure, it is worthwhile to address their resistance to fracture under quasi-static loads and possible toughening mechanisms.

In the absence of toughening mechanisms, crack growth in ceramic materials is essentially determined by the rupture of atomic bonds at the crack tip, with unstable crack growth occurring simultaneously with crack nucleation [159]. This causes the materials to exhibit particularly low intrinsic fracture toughness values. The process of crack growth in brittle materials can be understood as a competing processes between intrinsic mechanisms promoting crack advance through microstructural damage ahead of the crack tip, whereas extrinsic shielding mechanisms act in the crack wake to reduce crack driving forces [176]. This notion can be similarly utilized to describe various toughening strategies in brittle materials. Intrinsic toughening relies entirely on the properties of the material, as such these mechanisms are active independently of the crack size and geometry [179]. The mechanisms act in front of the crack tip, aiming to increase the microstructural damage tolerance by essentially promoting plastic deformation. However, owing to the complete lack of dislocation mobility in most ceramics, intrinsic toughening was found to be virtually impossible [159, 180]. In contrast, extrinsic toughening relies on microstructural mechanisms behind the crack front, and thus depends on the actual crack size. This behavior manifests in a crack size-dependent fracture resistance (*i.e.*, resistance- or R-curve behavior), meaning that continuous crack growth requires increasing crack driving force. Due to the absence of an initial crack size, extrinsic

Die approbierte gedruckte Originalversion dieser Dissertation ist an der TU Wien Bibliothek verfügbar.
The approved original version of this doctoral thesis is available in print at TU Wien Bibliothek.
TU Bibliothek Your knowledge hub WIEN

toughening takes limited influence on the crack nucleation process [159, 176, 181].

An overview of the different toughening mechanisms is presented in Figure 4.4. Their effectiveness is particularly emphasized when considering that conventional ceramics exhibit a fracture toughness of $K_c \sim$ 1-3 MPa$\sqrt{m}$, whereas toughening mechanisms allow for values an order of magnitude higher (*e.g.*, $ZrO_2 \sim 20$ MPa$\sqrt{m}$, Al_2O_3/Al ~ 25 MPa$\sqrt{m}$, Al_2O_3/SiC > 30 MPa$\sqrt{m}$) [159, 180].

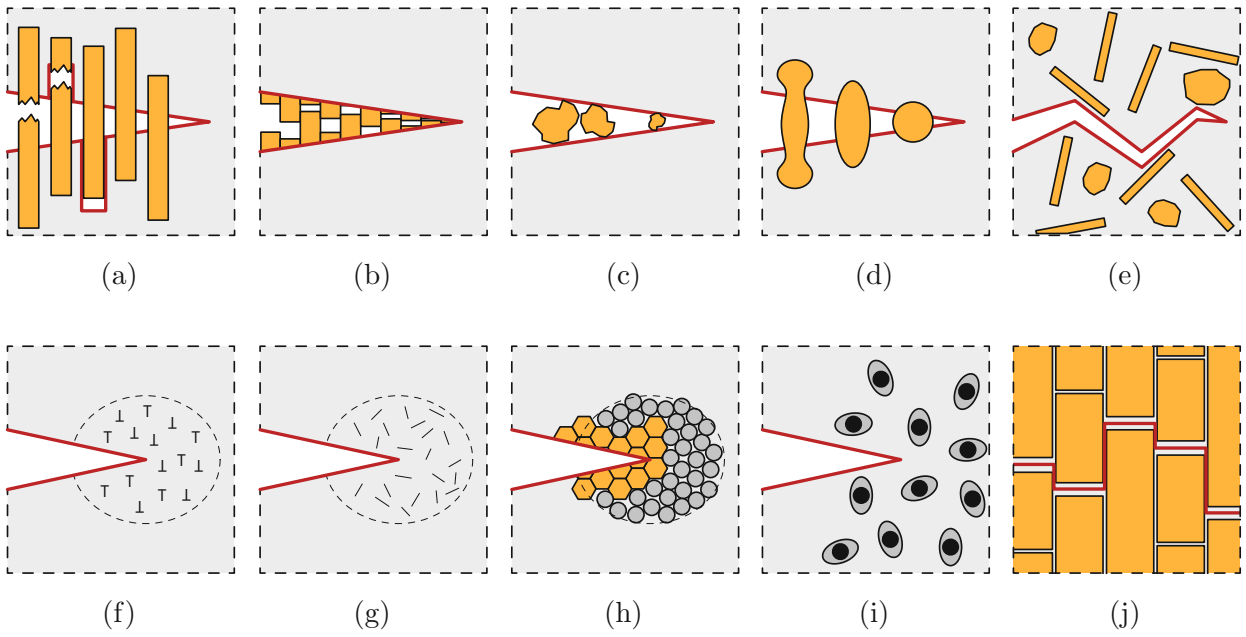

Fig. 4.4: Overview of possible crack tip shielding mechanisms in ceramic materials to increase the crack growth resistance. (a) fiber bridging, (b) grain bridging/interlocking, (c) oxide wedging, (d) ductile second phase bridging, (e) crack deflection trough fibers/whiskers or hard second phase, (f) dislocation cloud, (g) microcrack cloud, (h) phase transformation, (i) void formation, (j) crack deflection in nacre-like structure. The illustration is adapted from [182].

An ironic aspect of toughened ceramic materials is their increasing susceptibility to premature failure from cyclic fatigue damage. While untoughened ceramics are essentially unaffected by cyclic loads [183] – analogous to the static fracture limit, their fatigue strength is dictated by the inherent fracture toughness – the use of crack-size dependent toughening leaves the materials vulnerable for cyclic degradation of the shielding mechanisms, and thus structural failure at subcritical loads [181].

Historically, the presence of cyclic slip events has been considered a prerequisite for fatigue failure based on the observations in ductile materials. Given the very limited crack tip plasticity in ceramics, the notion of true cyclic material damage and crack growth has long been disregarded and reduced to external mechanisms such as stress corrosion cracking.

Die approbierte gedruckte Originalversion dieser Dissertation ist an der TU Wien Bibliothek verfügbar.
The approved original version of this doctoral thesis is available in print at TU Wien Bibliothek.
TU Bibliothek Your knowledge hub WIEN

However, it is now recognized that mechanical irreversibilities due to microscopic deformations under cyclic loads can lead to crack initiation and mechanical fatigue failure even in brittle materials [170, 184]. Still, the characteristics and macroscopic appearance of cyclic damage in ceramics is in clear contrast to fatigue failure in ductile metals [176]. Important aspects include:

- Crack nucleation in brittle solids is invariably connected to the presence of pre-existing flaws within the material, commonly referred to as "Griffith flaws". In contrast to metals, where crack initiation is often connected to cyclically emerging surface irregularities (*i.e.*, extrusions and intrusions), cracks are not considered to nucleate naturally in brittle solids [176]. A variety of internal and external flaws can be present in as-fabricated ceramics, including pores and inclusions, thermal contraction induced microcracking along grain boundaries/interfaces, or inconsistencies on the free surface [170].

- While cyclic crack extension in ductile materials is characterized by a distinct striation mechanism, as opposed to the crack advance under static loads, surface features of fractured ceramics are very similar for both static and cyclic loading conditions. Hence, in brittle materials the preferred pathway for crack advance along grain boundaries is independent of the loading condition [176].

- The average grain size within ceramics can have a significant effect on the fatigue crack growth rate, so that a smaller grain size often results in reduced fatigue strength (smaller crack sizes reduce the effectivity of extrinsic crack tip shielding). Moreover, when compared to the corresponding fracture toughness, the microstructural influence appears to have a similar effect on cyclic and overload fracture [176, 185].

- The sensitivity of the crack growth rates da/dN versus the stress intensity range ΔK, respectively the critical stress intensity K_c, is extremely high for brittle materials. While for metals the exponent in equation 4.2 takes values of $m \sim$ 2-4, ceramics can exhibit values above 50 [176, 186]. This behavior makes experimental testing difficult, since a minute increase in the applied load implies a significant change to the crack growth rates or even instantaneous fracture. A schematic comparison of crack growth rates between ductile and brittle materials under cyclic loads is given in Figure 4.5.

While the primary mechanism of crack growth in metals is associated with cyclic blunting and resharpening of the crack tip, crack advance in brittle materials is connected to kinematically irreversible deformations. (i) Intrinsic damage mechanisms encompass the cyclic degradation of the ceramic microstructures ahead of the crack tip. This includes phenomena such as localized microcracking, frictional sliding and/or contact of mating crack surfaces during unloading, local plasticity leading to blunting/resharpening effects, or crack formation due

Die approbierte gedruckte Originalversion dieser Dissertation ist an der TU Wien Bibliothek verfügbar.
The approved original version of this doctoral thesis is available in print at TU Wien Bibliothek.
TU Bibliothek Your knowledge hub WIEN

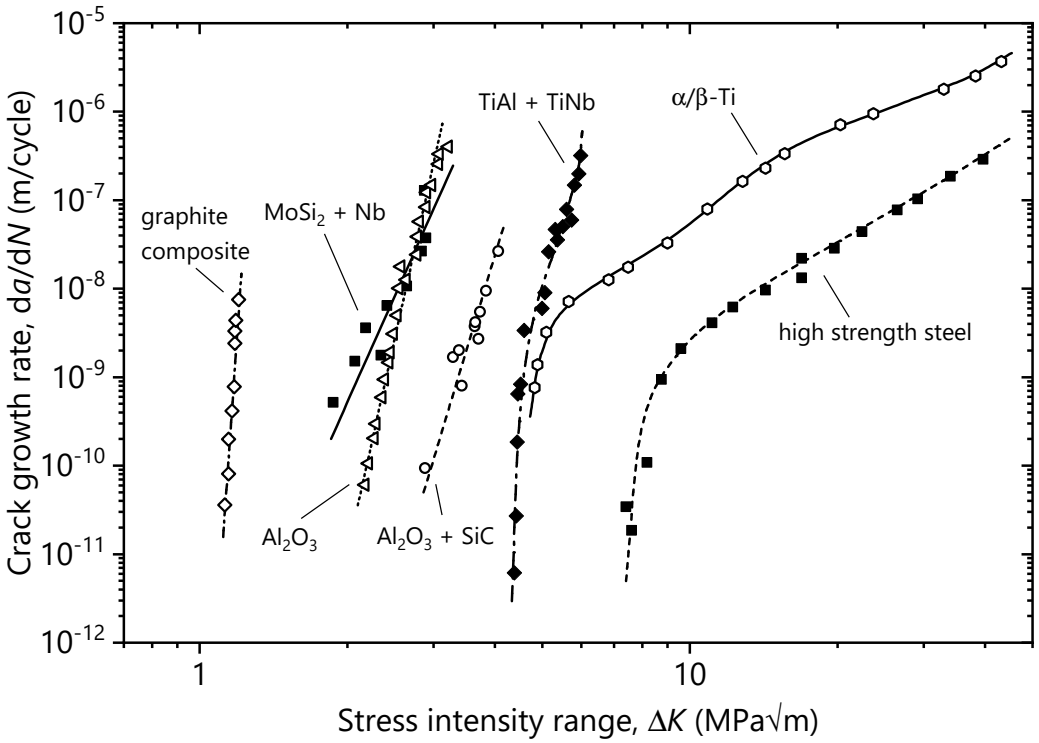

Fig. 4.5: Schematic comparison of the crack growth rate behavior for various brittle and ductile materials. The schematic is adopted from [176]

to residual stress relaxation [170, 184, 186]. (*ii*) Conversely, extrinsic damage mechanisms involve the cyclic reduction of toughening strategies acting in the crack wake to effectively increase the crack tip stress intensity in the loading phase. These mechanisms include the cyclic reduction and accommodation of transformation toughening stress fields, progressive breakdown of crack bridging ligaments or interlocking grains, as well as cyclic fatigue of ductile reinforcing phases [170, 186].

4.3 Thin films & coated components

Understanding the degradation mechanisms of thin film materials under cyclic loads is an important aspect to achieve enhanced reliability and increased service life of coated components. Related to their excellent thermo-mechanical properties, PVD synthesized coatings are regularly employed in harsh environments to serve as wear-, oxidation-, or corrosion-protection. However, the widespread application on cyclically loaded components designed for long-term usability is still faltering, since the impact of PVD coatings on the fatigue properties of metallic substrates remains unsatisfactory explored. Therefore, the purpose of this section is to briefly address the current status of fatigue related research on PVD coatings and summarize the challenges faced within the field.

Die approbierte gedruckte Originalversion dieser Dissertation ist an der TU Wien Bibliothek verfügbar.
The approved original version of this doctoral thesis is available in print at TU Wien Bibliothek.

Important considerations on the material response of PVD-coated metallic substrates during quasi-static loading were achieved in works by Guo *et al.* [22, 187]. Analysis of the deformation behavior of TiN coated brass substrates and WC-Co-Cr spray-coated AISI1020 steel substrates revealed a consistently negative impact of brittle coating materials on the tensile strength and plastic deformability of ductile substrates. For both material combinations, surface plasticity of the substrate was significantly inhibited due to the local constraints imposed by the stiffer coatings. These effectively suppress the activity of surface near dislocation sources and hinder pre-existing dislocations from escaping at the substrate surface. Moreover, brittle coating fracture is associated with accelerated cleavage cracking of the substrate materials due to introducing stress concentrations at the coating-substrate interface. The severity of this stress concentrations was further linked to the initial crack depth, which increases with coating thickness and thus increased crack velocity during brittle coating fracture (see Figure 4.6a).

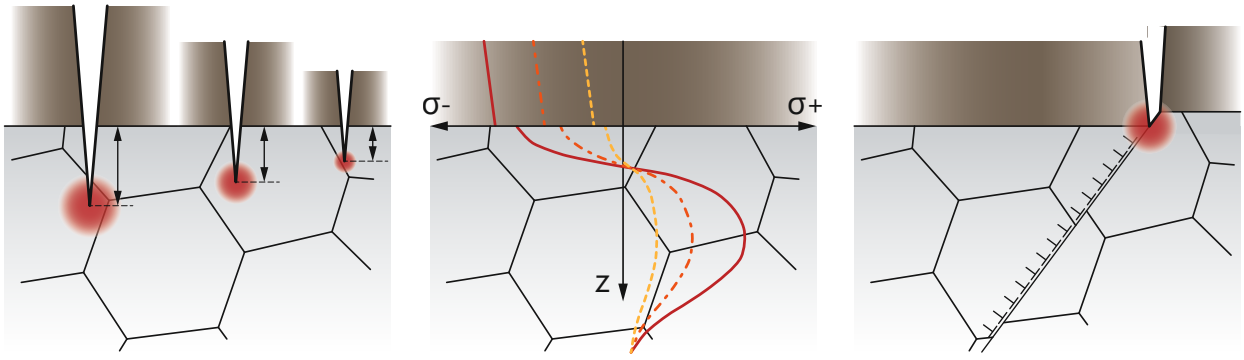

(a) (b) (c)

Fig. 4.6: (a) Initial crack depth in the substrate material after brittle coating fracture for varying coating thicknesses. (b) Schematic of the residual stress gradient in a PVD coated substrate for varying compressive stress levels in the coating. (c) Schematic of dislocation pile-up and subsurface coating fracture. The illustrations are adapted from [18, 188]

A comprehensive analysis of the fatigue strength in terms of the residual stress state for arc evaporated Ti-Al-N coatings on Ti-alloy substrates was conducted by Sivagnanam Chandra *et al.* [19] using tension-tension fatigue tests. The work demonstrated a stress-state dependent fatigue life for the coated specimen, where samples deposited at a bias voltage of at least -50 V – corresponds to a residual compressive stress above -4 GPa – achieved an increased number of cycles to failure compared to the uncoated reference. Depending on the applied tensile stress amplitude and the available "compressive stress reservoir" in the thin films, conclusions similar to Guo *et al.* [22, 187] were drawn (see Figure 4.6b). While lower compressive stresses were associated with brittle coating fracture and premature substrate failure, higher compressive stresses left coatings intact and shifted crack nucleation below the coating-substrate interface, where dislocation motion is impeded by the stiffer thin film material (see Figure 4.6c). However, significant shortcomings of the work can be found in

Die approbierte gedruckte Originalversion dieser Dissertation ist an der TU Wien Bibliothek verfügbar.
The approved original version of this doctoral thesis is available in print at TU Wien Bibliothek.
TU Bibliothek Your knowledge hub WIEN

an inconsistent film thickness (mind the difference in crack velocity upon fracture) and a significant decrease in the average macro-particle size with increasing substrate bias – hence, additional factors may cause the inferior performance of coatings deposited at lower bias voltage.

These issues were partially resolved in a follow-up work [20], which addressed the effect of coating thickness variations on the fatigue strength of the same coating-substrate combination. The results from cyclic tension-tension tests indicate a film thickness optimum at ∼5 μm, whereas coatings deposited at a thickness of 1 and 15 μm showed earlier fatigue failure. This was additionally verified for coatings deposited at higher bias voltage, revealing the same thickness dependence, yet with enhanced fatigue strength over uncoated specimen due to increased compressive residual stresses. The following origins are suggested for the thickness-dependent fatigue properties: (*i*) thin films with too low thickness are strongly affected by plastic deformation of the substrate material, leading to coating fracture from the subsurface and stress concentrations at the interface. (*ii*) thin films with increased thickness and compressive residual stress state induce higher tensile stress fields in the substrate material, thus promoting fatigue crack initiation in the subsurface. Considering this effect, it seems surprising that Lee *et al.* [14] were able to achieve similar increased fatigue lives irrespective of the stress amplitude during cyclic 4-point bending tests on TiN and metallic-glass coated Ti-6Al-4V substrates, at a bare film thickness of ∼200 nm. Analogously, the absence of brittle coating fracture and suppression of extrusion/intrusion formation are proposed to result in the prolonged sample lives.

Besides the research on Ti-based substrate materials [11], also various types of steel and aluminum alloys received great attention in terms of their fatigue properties when combined with ceramic PVD coatings such as TiN, TiCN, BCN, CrN, CrAlN, or TiAlN [12, 13, 188–191]. Depending on the substrate-coating combination, cyclic tests showed slightly to significantly improved fatigue performance, both in the low- and high-cycle fatigue regime. Consistent with previous works, authors concluded that the ceramic coatings protect the substrate surface from the intrinsic crack nucleation mechanism, whereas brittle coating fracture is avoided through sufficient residual compressive stress levels.

At this point, one may conclude that PVD coatings are indeed capable of extending the fatigue properties of metallic substrate materials, with the impact of residual stress states and thickness variations reasonably well understood. Unfortunately, the proposed improvements and fatigue behavior are hardly reproducible, even for similar coating-substrate combinations, so that an equal number of studies report on drastically reduced fatigue lives for coated substrate materials [15–18, 21, 188, 192].

A recent work by Bai *et al.* [18] addressed the worsening effect of TiN hard coatings on the fatigue life of Ti-6Al-4V alloys. While the crack initiation mechanisms observed by Sivagnanam

Die approbierte gedruckte Originalversion dieser Dissertation ist an der TU Wien Bibliothek verfügbar.
The approved original version of this doctoral thesis is available in print at TU Wien Bibliothek.
TU Bibliothek Your knowledge hub WIEN

Chandra *et al.* [19, 20] could be confirmed through fracture morphology investigations and FEM simulations – *i.e.*, brittle coating fracture vs. subsurface crack nucleation – a stress-dependent transition between the failure modes was revealed from a two-fold characteristic of the S-N_f curve. In fact, the transition was sharply defined by a distinct stress amplitude value. Moreover, the incorporation of a ductile Cr layer (although the ductility of Cr is rather questionable, see *Publication I*) between the brittle coating and substrate material was shown to result in slightly improved performance, reducing the loss in fatigue strength from ∼40 to 20%. The additional layer reduces the impact of both crack initiation mechanisms by absorbing brittle surface cracks and accommodating plastic deformation of the substrate material to a certain extent. Bai *et al.* [21] also demonstrated the negative impact of CrAlN coatings with varying thicknesses on the fatigue strength of Ti-6Al-4V. Although the fatigue live of the coated samples was consistently reduced throughout the S-N_f curve, CrAlN coated specimen showed slightly improved performance over the TiN coated reference. Considering the elastic modulus for the involved materials ($E_{Ti\text{-}6Al\text{-}4V} \sim 145$ GPa, $E_{CrAlN} \sim 340$ GPa, $E_{TiN} \sim 415$ GPa), it appears that minimizing their difference in the layered arrangement could contribute to reduced stress concentrations at the coating-substrate interfaces. This would further support the effectivity of a Cr interlayer with a typical elastic modulus of $E_{Cr} \sim 300$ GPa [193].

Apart from the physical properties of a coating, also the quality in terms of growth morphology and defect density can influence the performance under cyclic loads, as demonstrate by Costa *et al.* [16]. A comparison between samples coated by arc evaporation (CrN, TiN) and magnetron sputtering (DLC) highlighted the detrimental effect of macro-particles on the crack initiation process. Irrespective of the difference in mechanical properties between the thin films, both, the CrN and TiN coated samples showed markedly reduced fatigue lives in cyclic tension-tension experiments.

Moreover, Cassar *et al.* [15] pointed out that the overall comparability between studies is significantly hampered due to the lack of information on the substrate microstructure and mechanical properties in most works. The importance was highlighted through rotating-bending tests on uncoated Ti-6Al-4V samples in the as-received and annealed state. The latter samples showed a decrease of ∼20% in fatigue strength solely from recovery effects within the microstructure. Similar influences are to be expected from varying production routes of the same substrate material. Given that PVD depositions are conducted over a wide temperature range, such microstructural effects should always be considered in a quantitative comparison to uncoated, and thus unannealed samples.

In conclusion, the presented studies show an overall consistency in explaining crack nucleation and cyclic degradation mechanisms during fatigue testing of PVD coated metallic substrates. However, to the best of the authors knowledge, it seems that each work is a case study itself,

Die approbierte gedruckte Originalversion dieser Dissertation ist an der TU Wien Bibliothek verfügbar.
The approved original version of this doctoral thesis is available in print at TU Wien Bibliothek.
TU Bibliothek Your knowledge hub WIEN

which investigates a specific material-pairing and the related physical properties. Therefore, finding a general explanation why certain coating-substrate combinations show enhanced fatigue resistance over uncoated materials, while others perform significantly worse, remains a task for future research. Until then, every coating-substrate system will require individual treatment in order to understand, and possibly optimize the fatigue properties of the base material.

The above studies were all conducted at a length-scale of standardized fatigue tests, which were originally established for bulk material comparison. While this scenario permits a valid view on the impact of PVD coatings on the fatigue properties of a substrate material, only limited access is granted to study the cyclic behavior of the coating materials itself. In fact, mostly post-mortem analysis of the sample surface and fracture-cross-section is possible, however, the actual crack initiation process remains concealed. This presented a major driving force to conduct the research discussed in *Publication I*, and perform cyclic fatigue tests on the characteristic length-scale of PVD thin films.

Die approbierte gedruckte Originalversion dieser Dissertation ist an der TU Wien Bibliothek verfügbar.
The approved original version of this doctoral thesis is available in print at TU Wien Bibliothek.
TU Bibliothek Your knowledge hub WIEN

Chapter 5

Synchrotron X-ray Diffraction

Similar to the omnipresent use of conventional, lab-scaled X-ray diffraction (XRD), synchrotron radiation has evolved to an ubiquitous instrument in various scientific fields, from cell analysis to identifying chemical compositions, and from the examination of archaeological discoveries to thin film material science [194]. In fact, scientific demand for synchrotron radiation has already exceeded the capacity of current facilities, sparking the development of next generation synchrotron systems around globe. In the following, a brief introduction of synchrotron technology and the working principles of the primary components will be given. Subsequently, the use of a synchrotron light source to obtain nanofocused X-ray beams for detailed structural and residual stress analysis of thin film cross-sections will be discussed.

5.1 Synchrotron light source

A Synchrotron is a special type of particle accelerator, that is focused either on ions/protons or electrons. In this work, the configuration using electrons as a "light" source will be presented (see Figure 5.1). Within the system, electrons are accelerated and maintained on a closed-loop trajectory through the application of magnetic fields, which are synchronously increased in strength as electron velocity increases. Hence, the name "synchrotron". The high-energy electrons circulate in an evacuated "storage" ring at highly relativistic speeds and serve as photon light-source. To extract electromagnetic radiation, the electrons are diverted from their straight trajectory either by bending magnets at arc sections of the storage ring or on straight sections by insertions devices. Beamlines positioned tangentially to those locations utilize the generated radiation at various energy levels, from far infrared to the hard X-ray regime, and provide them for experimental purposes (*e.g.*, X-ray diffraction, X-ray microscopy, etc.) [194–196].

Die approbierte gedruckte Originalversion dieser Dissertation ist an der TU Wien Bibliothek verfügbar.
The approved original version of this doctoral thesis is available in print at TU Wien Bibliothek.

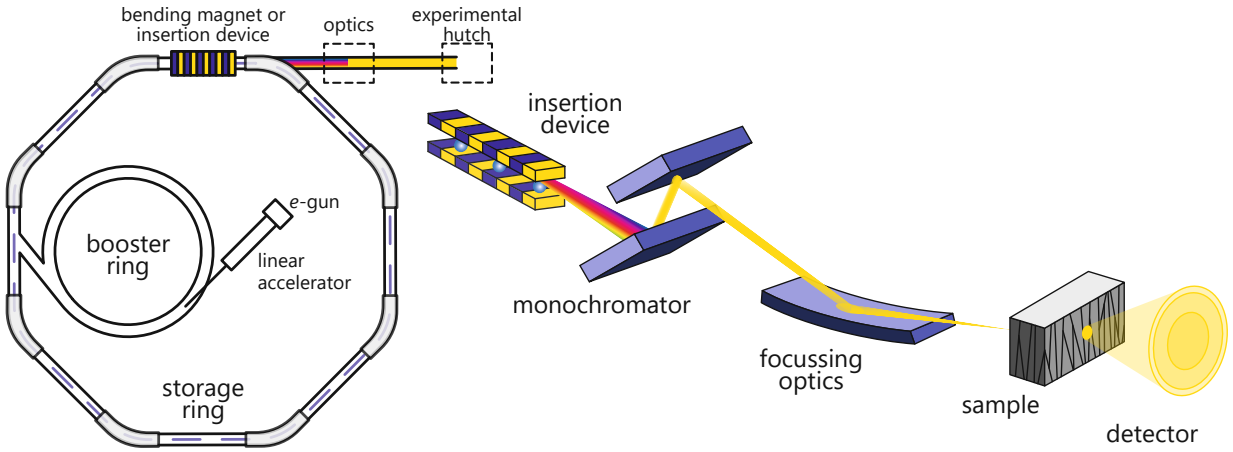

Fig. 5.1: Schematic of the most important components in a synchrotron facility including the principles of X-ray beam formation for transmission nanodiffraction experiments. The illustration is adapted from [194].

Modern synchrotron facilities are based on five main components:

- An electron gun that serves as the main source of electrons. These are typically generated through thermal emission from a glowing filament. The electrons are subsequently accelerated in a linear accelerator to an initial energy level of ∼100 MeV. The electron source operates continuously to compensate for the inevitable loss of electrons inside the entire synchrotron facility [194].

- The "medium" energy electrons are fed into a so-called "booster" ring, where they experience additional acceleration, either to the level of the main storage ring or slightly below. Subsequently, they are quasi-continuously injected into the storage ring to maintain an almost constant level of current. This provides enhanced operational stability and an uninterrupted, stable beam quality for the beamline user [194, 195].

- The storage ring houses the accelerated electrons and guides them on a circular trajectory through an array of magnets. The electron energy in the storage ring reaches values in the GeV range, with electron velocities just below the speed of light. The ring-shape is typically composed of straight and bent sections, wherein the straight sections are used to obtain highest-quality synchrotron ration [194].

- The electron energy emitted in the form of synchrotron radiation is then replenished by radio frequency cavities. These cavities provide an electromagnetic field through which the electrons travel, again increasing their energy to the nominal value inside the storage ring [194].

- The generated synchrotron radiation is extracted at beamlines, positioned tangentially to the storage ring. Depending on the source of the radiation – either from bending

Die approbierte gedruckte Originalversion dieser Dissertation ist an der TU Wien Bibliothek verfügbar.
The approved original version of this doctoral thesis is available in print at TU Wien Bibliothek.
TU Bibliothek Your knowledge hub WIEN

magnets or insertion devices – the beamlines are located at curved or straight sections of the main ring, respectively. The front section of the beamline performs several tasks: blanking of the X-ray beam to the following section if necessary, separation of storage ring and beamline vacuum, beam position monitoring, and filtering of the synchrotron radiation in terms of energy and acceptance angle. The following optics section focusses and monochromatizes the beam prior to entering the experimental hutch [194].

The quality of a synchrotron light source is typically benchmarked in terms of its flux and brilliance. The flux resembles the number of photons per second and per unit bandwidth in a defined area. Brilliance on the other hand is a measure for the beam intensity and its directionality, thus defines the theoretical limit in spot size to which the X-ray beam can be focused. Practically, the accuracy of beam focusing is additionally limited by the efficiency of the X-ray optics [194]. Nevertheless, synchrotron light sources exhibit both flux and brilliance several orders of magnitude higher than conventional laboratory X-ray systems. Moreover, compared to typical diffraction experiments restricted to reflection geometries, synchrotron radiation enables enhanced possibilities in terms of the sample position in relation to the incident X-ray beam, which laid the foundation for cross-sectional X-ray nanodiffraction on thin film materials [197].

An overview of current synchrotron facilities in order of the storage ring energy is given in table 5.1 [194, 196]. The primary facilities used for thin film research in central Europe are the Petra-III and ESRF synchrotron light sources, both offering X-ray focusing capabilities in the sub-micrometer range.

Table 5.1: Short overview of available synchrotron facilities [194, 196].

Facility, Country	Energy (GeV)	Current (mA)	Circumference (m)	Emittance (x,y) (nm·rad × pm·rad)	Brilliance (ph/s/mm^2/ mrad^2/0.1% BW)
SPring8, Japan	8	100	1436	2.8×6	2×10^{21}
APS, USA	7	100	1104	3.0×25	8×10^{19}
ESRF, France	6	300	846	3.8×10	8×10^{20}
Petra-III, Germany	6	100	2304	1.0×10	2×10^{21}
NSLS-II, USA	3	500	792	0.6×8	3×10^{21}
MAX IV, Sweden	3	500	528	0.25×6	-
Diamond, England	3	300	562	2.7×27	3×10^{20}

Die approbierte gedruckte Originalversion dieser Dissertation ist an der TU Wien Bibliothek verfügbar.
The approved original version of this doctoral thesis is available in print at TU Wien Bibliothek.

5.2 Transmission X-ray nanodiffraction

X-ray diffraction analysis is a versatile and well-established tool for the structural analysis of crystalline solids, which encompasses most metallic and ceramic thin film materials [198, 199]. The technique provides information on the phase composition within the sample volume, the phase-specific grain orientation distribution (*i.e.*, texture), the size of coherently diffracting domains (*i.e.*, average grain size), as well as the residual stress state. The principles of XRD are based on diffraction phenomena occurring from the interaction between coherent electromagnetic waves and periodic structures such as a crystal lattice [198–201]. This principle is formulated in Bragg's law, which follows [202]:

$$2d_{hkl}sin(\theta) = n\lambda \tag{5.1}$$

where d_{hkl} is the lattice spacing between (hkl)-planes, θ is the incident beam angle with respect to the (hkl)-lattice plane (*i.e.*, "Bragg" angle), n is an integer giving the order of the diffraction reflex, and λ is the X-ray wavelength. A geometrical description of equation 5.1 is presented in Figure 5.2, showing two initially coherent X-ray waves that are scattered on adjacent lattice planes of a crystal. The incident waves are elastically scattered on two parallel planes of the crystal lattice, resulting in constructive interference at an angle 2θ with respect to the primary beam direction. Following equation 5.1, constructive interference occurs for values of 2θ, where the phase shift after scattering equals a multiple of the X-ray wavelength (see Figure 5.2a), while for other conditions destructive interference occurs (see Figure 5.2b) [199]. Evaluation of the recorded diffraction pattern – a set of 2θ diffraction angles and corresponding lattice parameters – permits the unique assignment to a specific or a multitude of phases.

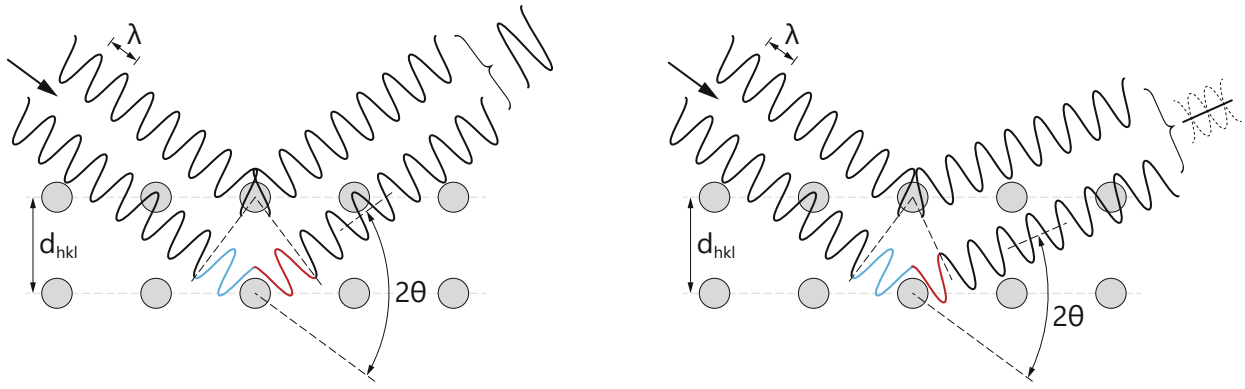

(a) (b)

Fig. 5.2: Schematic illustration of the X-ray diffraction process in a crystalline solid. (a) Constructive interference of scattered X-rays forms a "Bragg-reflection". (b) Destructive interference of scattered X-rays. The illustration is adapted from [199].

Die approbierte gedruckte Originalversion dieser Dissertation ist an der TU Wien Bibliothek verfügbar.
The approved original version of this doctoral thesis is available in print at TU Wien Bibliothek.

The diffraction spectra are commonly recorded in either Bragg-Brentano or Grazing-incidence reflection geometries, generating an intensity distribution as function of the diffraction angle. A primary shortcoming of the reflection geometries is, however, the inevitable averaging of the crystallographic information over the X-ray illuminated area and the penetration depth [198, 201].

Although thin films appear as seemingly uniform materials from a macroscopic perspective, the progress in cross-sectional analysis such as transmission X-ray nanodiffraction regularly reveals the opposite, unravelling significant structural changes and strain gradients in film growth direction. This type of localized transmission analysis was first applied onto thin films by Keckes *et al.* [197], and since then significantly advanced. Due to the distinct requirements for the X-ray beam quality, the technique inherently relies on the use of synchrotron radiation: (*i*) Given the limited thickness of thin films, height-dependent diffraction experiments of the cross-section require a high brilliance X-ray source to achieve sub-micrometer focusing of the incident beam. With recent advances in X-ray optics, spot sizes on the order of a few tens of nanometers are feasible, allowing for not only the detailed analysis of the film cross-section, but also individual sublayers in a multilayered architecture [203]. (*ii*) Since beam focusing and intensity are mutually excluding parameters, high X-ray flux of the incident beam is necessary to penetrate a minimum sample volume and maintain short exposure times during experiments. This becomes especially important during time-dependent studies (*i.e.*, *in-situ* oxidation) or experiments requiring several thousands of individual diffractograms. With respect to the available literature, a number of synchrotron facilities provide the capabilities to perform such high-quality transmission X-ray nanodiffraction experiments and reveal nanoscale gradients across the thin film cross-section.

5.2.1 Phase analysis

The interpretation of the structure-property relationship of thin film materials relies on the detailed knowledge of the individual phases present within the coating cross-section, which is among the primary tasks for transmission X-ray nanodiffraction. Therefore, polished slices of a coated substrate with a total width of up to 100 μm in beam direction are placed in transmission geometry. The focal point of the X-ray beam is located in the sample center, with the substrate-coating interface positioned parallel to the beam direction (see Figure 5.3). Depending on the smallest possible X-ray beam size, the sample height is repeatedly scanned either in vertical or additionally in lateral direction to obtain a linear or two-dimensional phase analysis, respectively. The incident beam is diffracted in all directions within the crystalline material following equation 5.1, creating phase specific diffraction cones which eventually intersect with a 2D detector to produce so-called “Debye-Scherrer” rings. These ring patterns are recorded for every measurement position and contain the total crystallographic information across the sample width in beam direction. To perform phase analysis

Die approbierte gedruckte Originalversion dieser Dissertation ist an der TU Wien Bibliothek verfügbar.
The approved original version of this doctoral thesis is available in print at TU Wien Bibliothek.
TU Bibliothek Your knowledge hub WIEN

analogous to conventional XRD – *i.e.*, compare a set of diffraction angles and lattice parameters with standardized reference data – the recorded ring patterns are integrated in azimuthal direction, creating an intensity distribution as function of the diffraction angle (I-2θ). Various open-source software solutions are available for synchrotron data manipulation, the most widely used variants include DPDAK [204], PyFAI [205] and Fit2D [206]. Correct azimuthal integration additionally requires precise knowledge of the detector alignment with respect to the incident beam and the sample position. These geometrical parameters include the beam center on the 2D detector, the rotational and tilt misalignment of the detector, and the detector distance from the sample position. These unknowns are usually determined from measurements on well-defined, powdered reference samples and accounted for during ring-pattern integration. The resulting I-2θ data is plotted for every point of the scan as function of the vertical or lateral coordinate in the form of an intensity plot, where the individual phases are identifiable through referencing with standardized powder diffraction data.

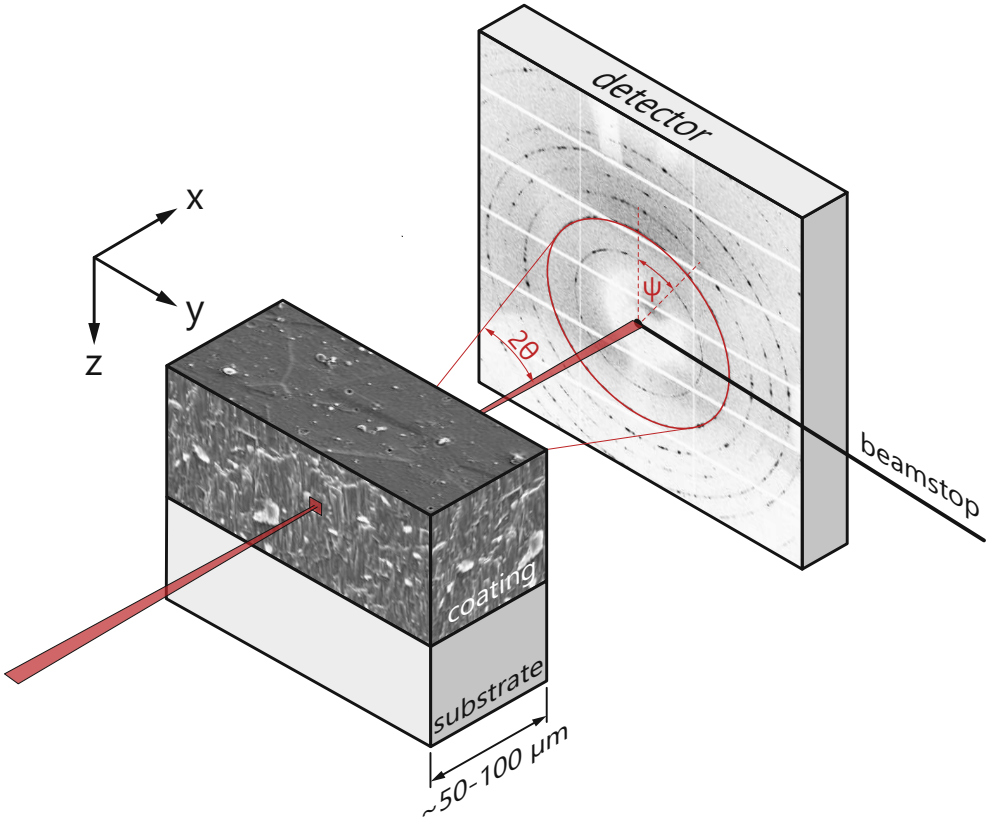

Fig. 5.3: Schematic of the sample-beam alignment in transmission X-ray nanodiffraction experiments. An incident X-ray beam is diffracted by the crystalline coating material, with the diffraction cones (Debye-Scherrer rings) recorded by a 2D detector. The illustration is adapted from [197].

An example of cross-sectional phase analysis is given in Figure 5.4, showing the height dependent crystal structure of a monolithic Cr_2O_3 cantilever at the pre-notch position. The

Die approbierte gedruckte Originalversion dieser Dissertation ist an der TU Wien Bibliothek verfügbar.
The approved original version of this doctoral thesis is available in print at TU Wien Bibliothek.
TU Bibliothek Your knowledge hub WIEN

data was acquired during coupled synchrotron X-ray nanodiffraction and cyclic micromechanical experiments performed at beamline P03 of the PETRA III synchrotron facility in Hamburg, Germany. Details on the employed transmission setup and cantilever geometry can be obtained from *Publication I*. According to the diffraction results, the cantilever is single-phased throughout the cross-section, revealing almost no change in the diffraction peak positions. Comparison to conventional XRD results recorded on the same sample in Bragg-Brentano reflection geometry highlights the vastly increased information content included in the synchrotron obtained data. The height-dependent structural analysis not only shows the clear contribution from additional lattice planes to the diffraction signal, but also indicates slight shifts of several peaks from their indexed position, indicating that the hexagonal Cr_2O_3 phase is not entirely stoichiometric. Moreover, exemplary evaluation of the full width at half maximum (FWHM) of the (110)-peak shows an increasing trend from the bottom to the top surface of the cantilever, which suggests a decreasing size of the coherently diffracting domains. In contrast, the diffracted intensity of the corresponding peak clearly increases in the same direction, thus indicating an opposite trend for the average grain size.

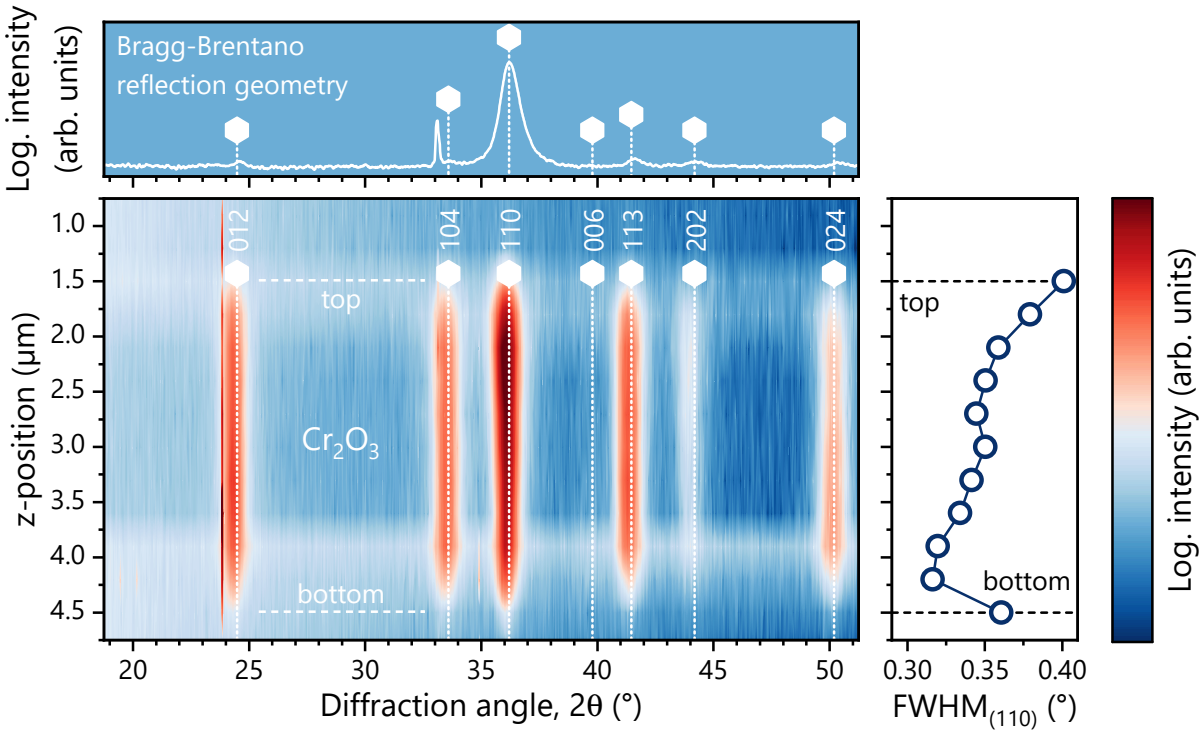

Fig. 5.4: Exemplary cross-sectional phase analysis of a Cr_2O_3 cantilever specimen recorded during transmission X-ray nanodiffraction experiments. The illustration contains a comparison to conventional top-view, Bragg-Brentano X-ray diffraction results and an analysis of the FWHM evolution as function of the cross-sectional position within the Cr_2O_3 coating. (Own, unpublished work)

Die approbierte gedruckte Originalversion dieser Dissertation ist an der TU Wien Bibliothek verfügbar.
The approved original version of this doctoral thesis is available in print at TU Wien Bibliothek.
TU Bibliothek Your knowledge hub WIEN

A possible explanation for this contradicting result may be found in a tilt misalignment of the coating surface with respect to the incident beam axis, resulting in the superposition of diffraction signal from various locations in the film cross-section.

In a similar manner, transmission X-ray nanodiffraction was used in previous works to reveal the cross-sectional phase composition and related crystallographic parameters. These include the (*i*) texture analysis of nanostructured ceramic coatings with alternating orientation of the crystal columns [168], (*ii*) phase analysis of spatially heterogenous metal-ceramic and ceramic-ceramic multilayers [161], (*iii*) estimation of coherently diffracting domains within bi-layer diamond-based thin films [207], (*iv*) phase distribution and stress field analysis of mechanically stressed multilayer thin films [208], (*v*) as well as the deconvolution of complex phase gradients of oxidized thin films [209–212], among others.

5.2.2 Stress analysis

Reliable measurements of the residual stress state within monolithic or multilayered thin films on a submicron scale are essential in many fields of application. Residual stresses in thin films originate from a complex interaction between the film growth conditions, morphology, microstructure, as well as the deposition temperature and substrate material. These competing stress sources are far from static during deposition, which converts into residual stresses that can significantly vary over the thin film cross-section. The actual stress state can become of major concern, since excessive levels may impair the performance and reliability of coated components [213]. Therefore, understanding the correlation of synthesis conditions and resulting stress fields provides a major driving force to improve the capabilities of spatially resolved stress analysis by transmission X-ray nanodiffraction. Methodically-similar to stress measurements by laboratory X-ray diffraction, synchrotron-based nanodiffraction is used to quantify macroscopic strain and stress gradients in crystalline thin films. Through the elastic properties of the material, mechanical residual stress is coupled to the elastic strain, such that the interatomic distances within the crystal lattice are changed upon force application. This elastic shrinkage or expansion in lattice spacing can be accurately determined through X-ray nanodiffraction in all directions of space, and subsequently converted into corresponding stress values provided the elastic material properties are known. Hence, X-ray stress analysis is fundamentally based on strain measurements [198, 199].

In most applications, the residual stress state of thin film materials is considered equi-biaxial due to the symmetry of the deposition processes and the structural properties, so that all entries in the stress tensor disappear except for the in-plane component $\sigma_{||}$ [198]. In this case, Hooke's law for an isotropic material takes the simplified notation:

$$\epsilon(\psi) = \frac{1+\nu}{E}\sigma_{||} \cdot sin^2\psi - \frac{2\nu}{E}\sigma_{||} \tag{5.2}$$

Die approbierte gedruckte Originalversion dieser Dissertation ist an der TU Wien Bibliothek verfügbar.
The approved original version of this doctoral thesis is available in print at TU Wien Bibliothek.
TU Bibliothek Your knowledge hub WIEN

where ϵ is the elastic strain which depends solely on the azimuthal tilt angle ψ (see Figure 5.3) and the elastic properties ν and E. However, due to the elastic anisotropy of most materials in relation to their crystal structure, strain values determined from X-ray diffraction measurements depend on the lattice plane from which they are calculated. This is accounted for by replacing the constants $\frac{1+\nu}{E}$ and $\frac{-\nu}{E}$ with the lattice plane dependent X-ray elastic constants (XEC) $\frac{1}{2}s_2^{hkl}$ and s_1^{hkl} [198, 199]. The XEC are commonly calculated following grain interaction models proposed by Voigt [214], Reuss [215], or Hill [216], wherein the latter is a linear combination of the prior concepts. These models require detailed knowledge of the single crystal properties, in particular the stiffness tensor [217]. The orientation dependent lattice strain is then calculated for a specific lattice plane from:

$$\epsilon_{hkl}(\psi) = \frac{d_{hkl}(\psi) - d_{0,hkl}(\psi)}{d_{0,hkl}(\psi)} \tag{5.3}$$

where $d_{0,hkl}(\psi)$ is the lattice spacing in the stress-free direction ψ^*_{hkl}, which itself is expressed in terms of the XEC following:

$$sin(\psi^*_{hkl}) = \sqrt{-\frac{2s_1^{hkl}}{\frac{1}{2}s_2^{hkl}}} \tag{5.4}$$

The stress-free direction corresponds to the azimuthal angle at which the measured interplanar spacing corresponds to a value obtained from an unstrained sample [198]. Eventually, this leads to the following form of equation 5.2, from which the in-plane stress component of a macroscopically isotropic material can be calculated at every position and for every phase present in the X-ray probed volume [198]:

$$\epsilon_{hkl}(\psi) = \frac{1}{2}s_2^{hkl}\sigma_{||} \cdot sin^2(\psi) + 2s_1^{hkl}\sigma_{||} \tag{5.5}$$

Equation 5.5 is a linear expression in $sin^2(\psi)$, so that the in-plane stress component can be determined from linear regression of the orientation dependent lattice-strain $\epsilon_{hkl}(\psi)$ data. In practice, $\epsilon_{hkl}(\psi)$ is determined from Debye-Scherrer ring patterns through segment-wise, azimuthal integration of the intensities (*e.g.*, 10° segments), from which the orientation-dependent lattice spacing $d_{hkl}(\psi)$ can be retrieved through peak fitting with a Pseudo-Voigt model. Moreover, $d_{0,hkl}(\psi)$ is obtained from the linear regression to the $\epsilon_{hkl}(\psi)$ - $sin^2\psi$ curve.

An example of cross-sectional stress analysis using synchrotron X-ray nanodiffraction is presented in Figure 5.5 for a monolithic Cr_2O_3 micro-cantilever in the unloaded (0% K^*_{Ic}) and in the loaded (50% K^*_{Ic}) state. Details on the employed transmission nanodiffraction setup are summarized in *Publication I*. The load range is referenced to the critical stress intensity determined during conventional cantilever bending experiments, however the cantilever

Die approbierte gedruckte Originalversion dieser Dissertation ist an der TU Wien Bibliothek verfügbar.
The approved original version of this doctoral thesis is available in print at TU Wien Bibliothek.
TU Bibliothek Your knowledge hub WIEN

geometry was outside the guidelines of Refs. [31, 131] (thus, the notation with an asterisk). An array of 20 × 20 diffraction scans was performed along the z- and y-axis (see Figure 5.3), with the center located at the cantilever notch position. The in-plane stress was evaluated from the (110)-diffraction ring of the Cr_2O_3 material using XEC of $\frac{1}{2}s_2^{110} = 4.664{\cdot}10^{-3}$ GPa^{-1} and $s_1^{110} = -1.032{\cdot}10^{-3}$ GPa^{-1}. The constants were determined using a Hill-type grain interaction model [218] and stiffness properties derived from density functional theory calculations [219].

The data shows a non-uniform, compressive stress state in the unloaded condition, with slightly increasing values from bottom to top (see Figure 5.5a). However, considering that the cantilever is free-standing, residual stresses should be fully relaxed, so that values close to $\sigma_{||}$(y,z) = 0 GPa were anticipated. The calculated offset is interpreted as a measurement artefact derived from the experimental setup, the prevalent beam quality and sample-beam interaction. Loading the cantilever to $K_I \sim 50\%$ of K_{Ic}^* results in a slight stress reduction in the upper section, whereas the lower section exhibits an increase in compressive stress (see Figure 5.5b). In order to extract the intrinsic offset from the results and solely highlight the change due to load application, both stress distributions were subtracted to obtain the relative change of the in-plane stress state (see Figure 5.5c). In addition, a row-average of the stress data corresponding to similar vertical positions on the cantilever cross-section is presented (see Figure 5.5d). The data shows a linear change of the in-plane stress state over the sample cross-section, with average values of $\Delta\bar{\sigma}_{||}$(y,4.25) ∼ -0.5 GPa and $\Delta\bar{\sigma}_{||}$(y,1.75) ∼ 0.25 GPa on the bottom and top surfaces, respectively. The unequal stress values could be related to the pre-notch on the cantilever top, causing a local reduction of the in-plane stress state. A similar stress analysis was performed on a CrN cantilever in *Publication I*, which includes additional information on the employed diffraction setup and the behavior of ceramic thin film materials under static and cycling loads.

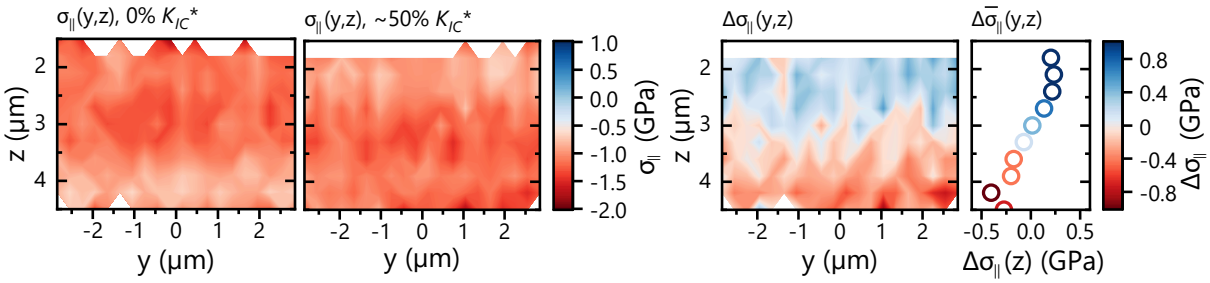

Fig. 5.5: Exemplary in-plane stress analysis of a Cr_2O_3 cantilever specimen recorded during transmission X-ray nanodiffraction experiments at the pre-notch location. Stress analysis was performed in the (a) unloaded and (b) loaded state ($K_I \sim 50\%$ K_{Ic}^*) of the cantilever. (c) Delta map showing the difference between the stress data in (a) and (b). (d) Corresponding cross-sectional row-average of the data in (c). (Own, unpublished work)

Die approbierte gedruckte Originalversion dieser Dissertation ist an der TU Wien Bibliothek verfügbar.
The approved original version of this doctoral thesis is available in print at TU Wien Bibliothek.
TU Bibliothek Your knowledge hub WIEN

Several studies have similarly employed synchrotron-based X-ray nanodiffraction to determine the residual stress distribution within complex thin film architectures, and coatings which were prior/simultaneously exposed to thermal, chemical, or mechanical impact. These works include: (*i*) phase-specific strain analysis of compositionally graded hard coatings [220], (*ii*) analysis of the residual stress gradient of oxidized thin films – from the unaffected coating material through various oxide layers [221], (*iii*) the in-plane, out-of-plane and shear stress calculation of mechanically loaded metal-ceramic and ceramic-ceramic multilayers [222–224], as well as (*iv*) the texture and stress evaluation of hard coatings deposited onto complex-shaped geometries [225].

Die approbierte gedruckte Originalversion dieser Dissertation ist an der TU Wien Bibliothek verfügbar.
The approved original version of this doctoral thesis is available in print at TU Wien Bibliothek.

Bibliography

[1] M. M. Omar and J. A. El-Awady, Science (80-.). **377**, 1047 (2022).

[2] J. H. Perepezko, Science (80-.). **326**, 1068 (2009).

[3] W. G. Fahrenholtz and G. E. Hilmas, Scr. Mater. **129**, 94 (2017).

[4] H. Clemens and W. Smarsly, Adv. Mater. Res. **278**, 551 (2011).

[5] F. Shuaeib, K. Benyounis, and M. Hashmi, in *Ref. Modul. Mater. Sci. Mater. Eng.* (Elsevier, 2017) pp. 1–30.

[6] P. H. Mayrhofer, R. Rachbauer, D. Holec, F. Rovere, and J. M. Schneider, in *Compr. Mater. Process.*, Vol. 4 (Elsevier, 2014) pp. 355–388.

[7] S. Vepřek, J. Vac. Sci. Technol. A Vacuum, Surfaces, Film. **17**, 2401 (1999).

[8] H. Mughrabi, Procedia Eng. **2**, 3 (2010).

[9] H. Mughrabi, Metall. Mater. Trans. B **40**, 431 (2009).

[10] J. Schijve, *Fatigue Struct. Mater.* (Springer Netherlands, Dordrecht, 2009).

[11] M. Hein, N. F. Lopes Dias, D. Kokalj, D. Stangier, K. P. Hoyer, W. Tillmann, and M. Schaper, Int. J. Fatigue **166**, 107235 (2023).

[12] J. F. Correa Jácome, J. C. Caicedo Angulo, and Y. A. Castro, Int. J. Adv. Manuf. Technol. **119**, 3995 (2022).

[13] M. J. Twu, C. C. Hu, D. W. Liu, C. Y. Hsu, and C. G. Kuo, J. Exp. Nanosci. **11**, 581 (2016).

[14] C. Lee, J. Chu, W. Chang, J. Lee, J. Jang, and P. Liaw, Thin Solid Films **561**, 33 (2014).

[15] G. Cassar, J. C. Avelar-Batista Wilson, S. Banfield, J. Housden, M. Fenech, A. Matthews, and A. Leyland, Int. J. Fatigue **33**, 1313 (2011).

Die approbierte gedruckte Originalversion dieser Dissertation ist an der TU Wien Bibliothek verfügbar.
The approved original version of this doctoral thesis is available in print at TU Wien Bibliothek.

[16] M. Y. Costa, M. L. Venditti, M. O. Cioffi, H. J. Voorwald, V. A. Guimarães, and R. Ruas, Int. J. Fatigue **33**, 759 (2011).

[17] E. S. Puchi-Cabrera, M. H. Staia, J. Lesage, L. Gil, C. Villalobos-Gutiérrez, J. La Barbera-Sosa, E. A. Ochoa-Pérez, and E. Le Bourhis, Int. J. Fatigue **30**, 1220 (2008).

[18] Y. Bai, T. Guo, J. Wang, J. Gao, K. Gao, and X. Pang, Acta Mater. **217**, 117179 (2021).

[19] N. G. P. Sivagnanam Chandra, Y. Otsuka, Y. Mutoh, and K. Yamamoto, Int. J. Fatigue **131**, 105338 (2020).

[20] N. P. Sivagnanam Chandra, Y. Otsuka, Y. Mutoh, and K. Yamamoto, Int. J. Fatigue **140**, 105767 (2020).

[21] Y. Bai, Y. Xi, K. Gao, H. Yang, X. Pang, X. Yang, and A. A. Volinsky, Int. J. Fatigue **125**, 432 (2019).

[22] T. Guo, Y. Chen, R. Cao, X. Pang, J. He, and L. Qiao, Acta Mater. **152**, 77 (2018).

[23] S. Lavenstein, *Micro-scale fatigue mechanisms in metals: An in situ high frequency experimental approach*, Doctoral thesis, The Johns Hopkins University (2019).

[24] S. Lavenstein, Y. Gu, D. Madisetti, and J. A. El-Awady, Science (80-.). **370** (2020).

[25] S. Lavenstein, B. Crawford, G.-D. Sim, P. A. Shade, C. Woodward, and J. A. El-Awady, Acta Mater. **144**, 154 (2018).

[26] A. Wimmer, W. Heinz, T. Detzel, W. Robl, M. Nellessen, C. Kirchlechner, and G. Dehm, Acta Mater. **83**, 460 (2015).

[27] D. Kiener, C. Motz, W. Grosinger, D. Weygand, and R. Pippan, Scr. Mater. **63**, 500 (2010).

[28] C. Szczepanski, S. Jha, P. Shade, R. Wheeler, and J. Larsen, Int. J. Fatigue **57**, 131 (2013).

[29] D. Di Maio and S. G. Roberts, J. Mater. Res. **20**, 299 (2005).

[30] M. Sebastiani, K. Johanns, E. Herbert, F. Carassiti, and G. Pharr, Philos. Mag. **95**, 1928 (2015).

[31] K. Matoy, H. Schönherr, T. Detzel, T. Schöberl, R. Pippan, C. Motz, and G. Dehm, Thin Solid Films **518**, 247 (2009).

Die approbierte gedruckte Originalversion dieser Dissertation ist an der TU Wien Bibliothek verfügbar.
The approved original version of this doctoral thesis is available in print at TU Wien Bibliothek.
TU Bibliothek Your knowledge hub WIEN

[32] R. Hahn, M. Bartosik, R. Soler, C. Kirchlechner, G. Dehm, and P. H. Mayrhofer, Scr. Mater. **124**, 67 (2016).

[33] M. Bartosik, R. Hahn, Z. L. Zhang, I. Ivanov, M. Arndt, P. Polcik, and P. H. Mayrhofer, Int. J. Refract. Met. Hard Mater. **72**, 78 (2018).

[34] H. Kindlund, D. Sangiovanni, I. Petrov, J. Greene, and L. Hultman, Thin Solid Films **688**, 137479 (2019).

[35] J. Buchinger, N. Koutná, A. Kirnbauer, D. Holec, and P. H. Mayrhofer, Acta Mater. **231**, 117897 (2022).

[36] T. Glechner, R. Hahn, T. Wojcik, D. Holec, S. Kolozsvári, H. Zaid, S. Kodambaka, P. H. Mayrhofer, and H. Riedl, Acta Mater. **179**, 17 (2019).

[37] R. Daniel, M. Meindlhumer, W. Baumegger, J. Zalesak, B. Sartory, M. Burghammer, C. Mitterer, and J. Keckes, Acta Mater. **122**, 130 (2017).

[38] G. Zhang, C. Volkert, R. Schwaiger, P. Wellner, E. Arzt, and O. Kraft, Acta Mater. **54**, 3127 (2006).

[39] J. Y. Zhang, X. Zhang, G. Liu, R. H. Wang, G. J. Zhang, and J. Sun, Mater. Sci. Eng. A **528**, 7774 (2011).

[40] R. Schwaiger and O. Kraft, Acta Mater. **51**, 195 (2003).

[41] M. Magnuson, L. Hultman, and H. Högberg, Vacuum **196**, 110567 (2022).

[42] P. H. Mayrhofer, C. Mitterer, J. G. Wen, J. E. Greene, and I. Petrov, Appl. Phys. Lett. **86**, 1 (2005).

[43] T. Fiantok, V. Šroba, N. Koutná, V. Izai, T. Roch, M. Truchlý, M. Vidiš, L. Satrapinskyy, Š. Nagy, B. Grančič, P. Kúš, and M. Mikula, J. Vac. Sci. Technol. A **40**, 033414 (2022).

[44] C. Fuger, R. Hahn, L. Zauner, T. Wojcik, M. Weiss, A. Limbeck, O. Hunold, P. Polcik, and H. Riedl, Mater. Res. Lett. **10**, 70 (2022).

[45] V. Moraes, L. Zauner, T. Wojcik, M. Arndt, P. Polcik, H. Riedl, and P. H. Mayrhofer, Acta Mater. **186**, 487 (2020).

[46] J. Nagamatsu, N. Nakagawa, T. Muranaka, Y. Zenitani, and J. Akimitsu, Nature **410**, 63 (2001).

[47] E. Sani, L. Mercatelli, M. Meucci, L. Zoli, and D. Sciti, Sci. Rep. **7**, 1 (2017).

Die approbierte gedruckte Originalversion dieser Dissertation ist an der TU Wien Bibliothek verfügbar.
The approved original version of this doctoral thesis is available in print at TU Wien Bibliothek.
TU Bibliothek Your knowledge hub WIEN

[48] V. Moraes, H. Riedl, C. Fuger, P. Polcik, H. Bolvardi, D. Holec, and P. H. Mayrhofer, Sci. Rep. **8**, 9288 (2018).

[49] C. Fuger, V. Moraes, R. Hahn, H. Bolvardi, P. Polcik, H. Riedl, and P. H. Mayrhofer, MRS Commun. **9**, 375 (2019).

[50] A. A. Tymoszuk, *Einfluss der Superlattice-Struktur auf die mechanischen Eigenschaften dünner Übergangsmetall-Diborid-Schichten*, Diploma thesis, TU Wien (2021).

[51] T. Glechner, A. Bahr, R. Hahn, T. Wojcik, M. Heller, A. Kirnbauer, J. Ramm, S. Kolozsvari, P. Felfer, and H. Riedl, Corros. Sci. **205**, 110413 (2022).

[52] T. Glechner, H. G. Oemer, T. Wojcik, M. Weiss, A. Limbeck, J. Ramm, P. Polcik, and H. Riedl, Surf. Coatings Technol. **434**, 128178 (2022).

[53] I. Petrov, P. B. Barna, L. Hultman, and J. E. Greene, J. Vac. Sci. Technol. A Vacuum, Surfaces, Film. **21**, S117 (2003).

[54] C. M. Koller, A. Kirnbauer, R. Hahn, B. Widrig, S. Kolozsvári, J. Ramm, and P. H. Mayrhofer, J. Vac. Sci. Technol. A Vacuum, Surfaces, Film. **35**, 061601 (2017).

[55] J. T. Gudmundsson, N. Brenning, D. Lundin, and U. Helmersson, J. Vac. Sci. Technol. A **30**, 030801 (2012).

[56] A. Anders, J. Appl. Phys. **121**, 171101 (2017).

[57] V. Kouznetsov, K. Macák, J. M. Schneider, U. Helmersson, and I. Petrov, Surf. Coatings Technol. **122**, 290 (1999).

[58] G. Greczynski, J. Lu, J. Jensen, I. Petrov, J. E. Greene, S. Bolz, W. Kölker, C. Schiffers, O. Lemmer, and L. Hultman, Thin Solid Films **556**, 87 (2014).

[59] G. Greczynski, S. Mráz, M. Hans, J. Lu, L. Hultman, and J. Schneider, Coatings **9**, 17 (2018).

[60] P. H. Mayrhofer, C. Mitterer, L. Hultman, and H. Clemens, Prog. Mater. Sci. **51**, 1032 (2006).

[61] K. Bobzin, CIRP J. Manuf. Sci. Technol. **18**, 1 (2017).

[62] P. M. Martin, *Handb. Depos. Technol. Film. Coatings Sci. Appl. Technol.*, 3rd ed. (Elsevier, 2010) pp. 1–912.

[63] D. M. Mattox, *Handbook of Physical Vapor Deposition (PVD) Processing*, 2nd ed. (Elsevier, 2010).

Die approbierte gedruckte Originalversion dieser Dissertation ist an der TU Wien Bibliothek verfügbar.
The approved original version of this doctoral thesis is available in print at TU Wien Bibliothek.
TU Bibliothek Your knowledge hub WIEN

[64] K. Wasa, I. Kanno, and H. Kotera, *Handbook of Sputtering Technology* (Elsevier, 2012) pp. 1–644.

[65] A. Anders, *Cathodic Arcs*, Springer Series on Atomic, Optical, and Plasma Physics (Springer New York, 2008).

[66] J. Čapek and S. Kadlec, J. Appl. Phys. **121**, 171911 (2017).

[67] S. Inoue, H. Uchida, A. Hioki, K. Koterazawa, and R. P. Howson, Thin Solid Films **271**, 15 (1995).

[68] K. Sarakinos, J. Alami, and S. Konstantinidis, Surf. Coatings Technol. **204**, 1661 (2010).

[69] D. Lundin, J. T. Gudmundsson, and T. Minea, *High Power Impulse Magnetron Sputtering* (Elsevier, 2020) pp. 1–384.

[70] A. P. Ehiasarian, Pure Appl. Chem. **82**, 1247 (2010).

[71] J. Bohlmark, J. Alami, C. Christou, A. P. Ehiasarian, and U. Helmersson, J. Vac. Sci. Technol. A Vacuum, Surfaces, Film. **23**, 18 (2005).

[72] A. Anders, J. Čapek, M. Hála, and L. Martinu, J. Phys. D. Appl. Phys. **45**, 012003 (2012).

[73] G. Greczynski and L. Hultman, Vacuum **124**, 1 (2016).

[74] G. Greczynski, I. Zhirkov, I. Petrov, J. E. Greene, and J. Rosen, J. Vac. Sci. Technol. A Vacuum, Surfaces, Film. **35**, 060601 (2017).

[75] A. Anders, Surf. Coatings Technol. **205**, S1 (2011).

[76] H. Fager, O. Tengstrand, J. Lu, S. Bolz, B. Mesic, W. Kölker, C. Schiffers, O. Lemmer, J. E. Greene, L. Hultman, I. Petrov, and G. Greczynski, J. Appl. Phys. **121**, 171101 (2017).

[77] X. Li, B. Bakhit, M. P. Johansson Jõesaar, I. Petrov, L. Hultman, and G. Greczynski, Sci. Rep. **12**, 2166 (2022).

[78] T. Shimizu, H. Komiya, Y. Teranishi, K. Morikawa, H. Nagasaka, and M. Yang, Thin Solid Films **624**, 189 (2017).

[79] G. Greczynski, J. Lu, M. Johansson, J. Jensen, I. Petrov, J. Greene, and L. Hultman, Surf. Coatings Technol. **206**, 4202 (2012).

[80] G. Greczynski, S. Mráz, L. Hultman, and J. M. Schneider, Sci. Rep. **7**, 17544 (2017).

Die approbierte gedruckte Originalversion dieser Dissertation ist an der TU Wien Bibliothek verfügbar.
The approved original version of this doctoral thesis is available in print at TU Wien Bibliothek.
TU Bibliothek Your knowledge hub WIEN

[81] G. Greczynski, J. Lu, M. Johansson, J. Jensen, I. Petrov, J. E. Greene, and L. Hultman, Vacuum **86**, 1036 (2012).

[82] C. Fuger, R. Hahn, A. Hirle, P. Kutrowatz, M. Weiss, A. Limbeck, O. Hunold, P. Polcik, and H. Riedl, Surf. Coatings Technol. **446**, 128806 (2022).

[83] B. A. Movchanm and A. Demchishin, Fiz Met Met. **28**, 83 (1969).

[84] J. A. Thornton, J. Vac. Sci. Technol. **11**, 666 (1974).

[85] R. Messier, A. P. Giri, and R. A. Roy, J. Vac. Sci. Technol. A Vacuum, Surfaces, Film. **2**, 500 (1984).

[86] A. Anders, Thin Solid Films **518**, 4087 (2010).

[87] P. B. Barna and M. Adamik, Thin Solid Films **317**, 27 (1998).

[88] D. Gross and T. Seelig, *Bruchmechanik*, 5th ed. (Springer, Berlin, Heidelberg, 2011).

[89] M. Janssen, J. Zuidema, and R. Wanhill, *Fracture Mechanics* (CRC Press, 2004).

[90] D. Broek, *Elementary engineering fracture mechanics* (Springer Netherlands, Dordrecht, 1986).

[91] T. Anderson, *Fracture Mechanics*, 4th ed. (CRC Press, 2017).

[92] O. Kolednik, Wiley Encycl. Compos. **38**, 1271 (2012).

[93] M. Alfreider, *Locally resolved deformation and fracture processes near interfaces*, Doctoral thesis, Montanuniversität Leoben (2021).

[94] A. A. Griffith, Philos. Trans. R. Soc. London. Ser. A, Contain. Pap. a Math. or Phys. Character **221**, 163 (1921).

[95] C. E. Inglis, Spring Meet. Fifty-fourth Sess. Inst. Nav. Archit. **55**, 219 (1913).

[96] G. R. Irwin, Am. Soc. Met. Cleveland, Ohio **147**, 296 (1948).

[97] E. Orowan, Reports Prog. Phys. **12**, 309 (1949).

[98] G. Irwin, *Elasticity and Plasticity / Elastizität und Plastizität* (Springer, Berlin, Heidelberg, 1958).

[99] G. R. Irwin, J. Appl. Mech. **24**, 361 (1957).

[100] G. C. Janssen, Thin Solid Films **515**, 6654 (2007).

[101] J. R. Rice, J. Appl. Mech. Trans. ASME **35**, 379 (1964).

Die approbierte gedruckte Originalversion dieser Dissertation ist an der TU Wien Bibliothek verfügbar.
The approved original version of this doctoral thesis is available in print at TU Wien Bibliothek.
TU Bibliothek Your knowledge hub WIEN

[102] J. D. Eshelby, Philos. Trans. R. Soc. London. Ser. A, Math. Phys. Sci. **244**, 87 (1951).

[103] B. Karihaloo and Q. Xiao, in *Compr. Struct. Integr.*, Vol. 2 (Elsevier, 2003) pp. 81–212.

[104] ASTM International, "ASTM E1820 - Standard Test Method for Measurement of Fracture Toughness," (2021).

[105] ISO, "ISO 12135:2021 Metallic materials — Unified method of test for the determination of quasistatic fracture toughness," (2021).

[106] J. Hutchinson, J. Mech. Phys. Solids **16**, 337 (1968).

[107] J. Hutchinson, J. Mech. Phys. Solids **16**, 13 (1968).

[108] J. R. Rice and G. F. Rosengren, J. Mech. Phys. Solids **16**, 1 (1968).

[109] W. Ramberg and W. R. Osgood, Natl. Advis. Comm. Aeronaut. **902** (1943).

[110] O. Kolednik, J. Predan, F. D. Fischer, and P. Fratzl, Adv. Funct. Mater. **21**, 3634 (2011).

[111] J. Ast, M. Ghidelli, K. Durst, M. Göken, M. Sebastiani, and A. M. Korsunsky, Mater. Des. **173**, 107762 (2019).

[112] B. Lawn and R. Wilshaw, J. Mater. Sci. **10**, 1049 (1975).

[113] A. G. EVANS and E. A. CHARLES, J. Am. Ceram. Soc. **59**, 371 (1976).

[114] D. B. Marshall, B. R. Lawn, and P. Chantikul, J. Mater. Sci. 1979 149 **14**, 2225 (1979).

[115] B. R. LAWN, A. G. EVANS, and D. B. MARSHALL, J. Am. Ceram. Soc. **63**, 574 (1980).

[116] S. Zhang and X. Zhang, Thin Solid Films **520**, 2375 (2012).

[117] N. Cuadrado, J. Seuba, D. Casellas, M. Anglada, and E. Jiménez-Piqué, J. Eur. Ceram. Soc. **35**, 2949 (2015).

[118] M. T. Laugier, J. Mater. Sci. Lett. **6**, 355 (1987).

[119] J. H. Lee, Y. F. Gao, K. E. Johanns, and G. M. Pharr, Acta Mater. **60**, 5448 (2012).

[120] M. Sebastiani, K. Johanns, E. Herbert, and G. Pharr, Curr. Opin. Solid State Mater. Sci. **19**, 324 (2015).

[121] J. P. Best, J. Zechner, J. M. Wheeler, R. Schoeppner, M. Morstein, and J. Michler, Philos. Mag. **96**, 3552 (2016).

Die approbierte gedruckte Originalversion dieser Dissertation ist an der TU Wien Bibliothek verfügbar.
The approved original version of this doctoral thesis is available in print at TU Wien Bibliothek.
TU Bibliothek Your knowledge hub WIEN

[122] C. M. Lauener, L. Petho, M. Chen, Y. Xiao, J. Michler, and J. M. Wheeler, Mater. Des. **142**, 340 (2018).

[123] J. P. Best, J. Wehrs, M. Polyakov, M. Morstein, and J. Michler, Scr. Mater. **162**, 190 (2019).

[124] M. Ghidelli, M. Sebastiani, K. E. Johanns, and G. M. Pharr, J. Am. Ceram. Soc. **100**, 5731 (2017).

[125] S. Bruns, L. Petho, C. Minnert, J. Michler, and K. Durst, Mater. Des. **186**, 108311 (2020).

[126] M. J. Pfeifenberger, M. Mangang, S. Wurster, J. Reiser, A. Hohenwarter, W. Pfleging, D. Kiener, and R. Pippan, Mater. Des. **121**, 109 (2017).

[127] G. Žagar, V. Pejchal, M. G. Mueller, L. Michelet, and A. Mortensen, Scr. Mater. **112**, 132 (2016).

[128] B. N. Jaya, C. Kirchlechner, and G. Dehm, J. Mater. Res. **30**, 686 (2015).

[129] I. Issa, C. Gammer, S. Kolitsch, A. Hohenwarter, P. J. Imrich, R. Pippan, and D. Kiener, Mater. Today **48**, 29 (2021).

[130] M. G. Mueller, G. Žagar, and A. Mortensen, J. Mater. Res. **32**, 3617 (2017).

[131] S. Brinckmann, K. Matoy, C. Kirchlechner, and G. Dehm, Acta Mater. **136**, 281 (2017).

[132] S. Brinckmann, C. Kirchlechner, and G. Dehm, Scr. Mater. **127**, 76 (2017).

[133] F. Iqbal, J. Ast, M. Göken, and K. Durst, Acta Mater. **60**, 1193 (2012).

[134] H. Tada, P. C. Paris, and G. R. Irwin, *Stress Anal. Cracks Handbook, Third Ed.* (ASME Press, 2010).

[135] A. Riedl, R. Daniel, M. Stefenelli, T. Schöberl, O. Kolednik, C. Mitterer, and J. Keckes, Scr. Mater. **67**, 708 (2012).

[136] K. Matoy, T. Detzel, M. Müller, C. Motz, and G. Dehm, Surf. Coatings Technol. **204**, 878 (2009).

[137] J. Schaufler, C. Schmid, K. Durst, and M. Göken, Thin Solid Films **522**, 480 (2012).

[138] J. P. Best, J. Zechner, I. Shorubalko, J. V. Oboňa, J. Wehrs, M. Morstein, and J. Michler, Scr. Mater. **112**, 71 (2016).

[139] S. Wurster, C. Motz, and R. Pippan, Philos. Mag. **92**, 1803 (2012).

Die approbierte gedruckte Originalversion dieser Dissertation ist an der TU Wien Bibliothek verfügbar.
The approved original version of this doctoral thesis is available in print at TU Wien Bibliothek.
TU Bibliothek Your knowledge hub WIEN

[140] D. Kupka and E. T. Lilleodden, Exp. Mech. **52**, 649 (2012).

[141] J. Ast, B. Merle, K. Durst, and M. Göken, J. Mater. Res. **31**, 3786 (2016).

[142] M. Alfreider, D. Kozic, O. Kolednik, and D. Kiener, Mater. Des. **148**, 177 (2018).

[143] M. Alfreider, J. Zechner, and D. Kiener, JOM **72**, 4551 (2020).

[144] M. Alfreider, S. Kolitsch, S. Wurster, and D. Kiener, Mater. Des. **194**, 108914 (2020).

[145] M. Burtscher, M. Alfreider, K. Schmuck, H. Clemens, S. Mayer, and D. Kiener, J. Mater. Res. **36**, 2465 (2021).

[146] J. R. Rice, P. C. Paris, and J. G. Merkle, Prog. Flaw Growth Fract. Toughness Testing, ASTM STP 536 , 231 (1973).

[147] X. K. Zhu and J. A. Joyce, Eng. Fract. Mech. **85**, 1 (2012).

[148] N. Schwarzer, Q. H. Duong, N. Bierwisch, G. Favaro, M. Fuchs, P. Kempe, B. Widrig, and J. Ramm, Surf. Coatings Technol. **206**, 1327 (2011).

[149] Austrian Standards Institute, "ÖNORM EN ISO 20502 Hochleistungskeramik — Bestimmung der Haftung von keramischen Schichten mit dem Ritztest," (2016).

[150] Austrian Standards Institute, "ÖNORM EN ISO 26443 Hochleistungskeramik — Rockwell-Eindringprüfung zur Bewertung der Haftung von keramischen Schichten," (2016).

[151] Y. X. Wang and S. Zhang, Surf. Coatings Technol. **258**, 1 (2014).

[152] S. Zhang, D. Sun, Y. Fu, and H. Du, Surf. Coatings Technol. **198**, 2 (2005).

[153] D. G. Sangiovanni, L. Hultman, and V. Chirita, Acta Mater. **59**, 2121 (2011).

[154] D. G. Sangiovanni, L. Hultman, V. Chirita, I. Petrov, and J. E. Greene, Acta Mater. **103**, 823 (2016).

[155] H. Kindlund, D. G. Sangiovanni, L. Martínez-De-Olcoz, J. Lu, J. Jensen, J. Birch, I. Petrov, J. E. Greene, V. Chirita, and L. Hultman, APL Mater. **1**, 042104 (2013).

[156] D. G. Sangiovanni, V. Chirita, and L. Hultman, Phys. Rev. B - Condens. Matter Mater. Phys. **81**, 104107 (2010).

[157] T. Glechner, P. H. Mayrhofer, D. Holec, S. Fritze, E. Lewin, V. Paneta, D. Primetzhofer, S. Kolozsvári, and H. Riedl, Sci. Rep. **8** (2018).

[158] N. Koutná, A. Brenner, D. Holec, and P. H. Mayrhofer, Acta Mater. **206** (2021).

Die approbierte gedruckte Originalversion dieser Dissertation ist an der TU Wien Bibliothek verfügbar.
The approved original version of this doctoral thesis is available in print at TU Wien Bibliothek.
TU Bibliothek Your knowledge hub WIEN

[159] M. E. Launey and R. O. Ritchie, Adv. Mater. **21**, 2103 (2009).

[160] E. Munch, M. E. Launey, D. H. Alsem, E. Saiz, A. P. Tomsia, and R. O. Ritchie, Science (80-.). **322**, 1516 (2008).

[161] R. Daniel, M. Meindlhumer, J. Zalesak, B. Sartory, A. Zeilinger, C. Mitterer, and J. Keckes, Mater. Des. **104**, 227 (2016).

[162] A. K. Mishra, H. Gopalan, M. Hans, C. Kirchlechner, J. M. Schneider, G. Dehm, and B. N. Jaya, Acta Mater. **228** (2022).

[163] U. Helmersson, S. Todorova, S. A. Barnett, J. E. Sundgren, L. C. Markert, and J. E. Greene, J. Appl. Phys. **62**, 481 (1987).

[164] X. Chu and S. A. Barnett, J. Appl. Phys. **77**, 4403 (1995).

[165] A. Wagner, D. Holec, P. H. Mayrhofer, and M. Bartosik, Mater. Des. **202**, 109517 (2021).

[166] N. Koutná, L. Löfler, D. Holec, Z. Chen, Z. Zhang, L. Hultman, P. H. Mayrhofer, and D. G. Sangiovanni, Acta Mater. **229** (2022).

[167] M. Schlögl, C. Kirchlechner, J. Paulitsch, J. Keckes, and P. H. Mayrhofer, Scr. Mater. **68**, 917 (2013).

[168] R. Daniel, M. Meindlhumer, W. Baumegger, J. Todt, J. Zalesak, T. Ziegelwanger, C. Mitterer, and J. Keckes, Mater. Des. **161**, 80 (2019).

[169] M. Sperr, Z. L. Zhang, Y. P. Ivanov, P. H. Mayrhofer, and M. Bartosik, Scr. Mater. **170**, 20 (2019).

[170] S. Suresh, *Fatigue of Materials* (Cambridge University Press, 1998).

[171] C. Bathias and A. Pineau, *Fatigue of Materials and Structures* (Wiley, 2013).

[172] P. J. Forsyth, Nature **171**, 172 (1953).

[173] E. Schmid and W. Boas, *Kristallplastizität* (Springer, Berlin, Heidelberg, 1935).

[174] P. C. Paris, M. P. Gomez, and W. E. P. Anderson, Trend Eng. **13**, 9 (1961).

[175] P. Paris and F. Erdogan, J. Fluids Eng. Trans. ASME **85**, 528 (1963).

[176] R. O. Ritchie, Int. J. Fract. **100**, 55 (1999).

[177] L. J. Coffin, Appl. Mat. Res **1**, 129 (1962).

Die approbierte gedruckte Originalversion dieser Dissertation ist an der TU Wien Bibliothek verfügbar.
The approved original version of this doctoral thesis is available in print at TU Wien Bibliothek.

[178] S. S. Manson and M. H. Hirschberg, in *10th Sagamore Army Mater. Res. Conf.* (Scientific Research Publishing, 1963) pp. 13–16.

[179] R. O. Ritchie, C. J. Gilbert, and J. M. McNaney, Int. J. Solids Struct. **37**, 311 (2000).

[180] A. G. Evans, J. Am. Ceram. Soc. **73**, 187 (1990).

[181] R. O. Ritchie, Mater. Sci. Eng. **103**, 15 (1988).

[182] B. Lawn, *Fracture of Brittle Solids* (Cambridge University Press, 1993).

[183] A. G. Evans and E. R. Fuller, Metall. Trans. **5**, 27 (1974).

[184] A. G. Evans, Int. J. Fract. **16**, 485 (1980).

[185] C. J. Gilbert and R. O. Ritchie, Fatigue Fract. Eng. Mater. Struct. **20**, 1453 (1997).

[186] R. O. RITCHIE and R. H. DAUSKARDT, J. Ceram. Soc. Japan **99**, 1047 (1991).

[187] T. Guo, L. Qiao, X. Pang, and A. A. Volinsky, Acta Mater. **99**, 273 (2015).

[188] S. BARAGETTI, G. LAVECCHIA, and A. TERRANOVA, Int. J. Fatigue **27**, 1541 (2005).

[189] E. S. Puchi-Cabrera, F. Matínez, I. Herrera, J. A. Berríos, S. Dixit, and D. Bhat, Surf. Coatings Technol. **182**, 276 (2004).

[190] A. P. Gopkalo and A. V. Rutkovskyy, Fatigue Fract. Eng. Mater. Struct. **34**, 1012 (2011).

[191] S. Glodež, M. Podgrajšek, B. Podgornik, and Z. Ren, Surf. Coatings Technol. **321**, 358 (2017).

[192] S. Baragetti and F. Tordini, SID Struct. Integr. Durab. **3**, 165 (2007).

[193] L. Zauner, R. Hahn, E. Aschauer, T. Wojcik, A. Davydok, O. Hunold, P. Polcik, and H. Riedl, Acta Mater. **239**, 118260 (2022).

[194] P. Willmott, *An Introduction to Synchrotron Radiation* (Wiley, 2011).

[195] F. Hinterberger, *Physik der Teilchenbeschleuniger und Ionenoptik* (Springer, Berlin, Heidelberg, 2008).

[196] A. Bharti and N. Goyal, *Synchrotron Radiation - Useful and Interesting Applications* (IntechOpen, 2019).

[197] J. Keckes, M. Bartosik, R. Daniel, C. Mitterer, G. Maier, W. Ecker, J. Vila-Comamala, C. David, S. Schoeder, and M. Burghammer, Scr. Mater. **67**, 748 (2012).

Die approbierte gedruckte Originalversion dieser Dissertation ist an der TU Wien Bibliothek verfügbar.
The approved original version of this doctoral thesis is available in print at TU Wien Bibliothek.
TU Bibliothek Your knowledge hub WIEN

[198] M. Birkholz, *Thin Film Analysis by X-Ray Scattering* (Wiley, 2005) pp. 1–356.

[199] L. Spieß, G. Teichert, R. Schwarzer, H. Behnken, and C. Genzel, *Moderne Röntgenbeugung* (Vieweg+Teubner, Wiesbaden, 2009).

[200] V. Hauk and H. Behnken, *Structural and Residual Stress Analysis by Nondestructive Methods* (Elsevier, 1997).

[201] H. Stanjek and W. Häusler, Hyperfine Interact. **154**, 107 (2004).

[202] W. H. Bragg and W. L. Bragg, Proc. R. Soc. A Math. Phys. Eng. Sci. **88**, 428 (1913).

[203] J. Keckes, R. Daniel, J. Todt, J. Zalesak, B. Sartory, S. Braun, J. Gluch, M. Rosenthal, M. Burghammer, C. Mitterer, S. Niese, and A. Kubec, Acta Mater. **144**, 862 (2018).

[204] G. Benecke, W. Wagermaier, C. Li, M. Schwartzkopf, G. Flucke, R. Hoerth, I. Zizak, M. Burghammer, E. Metwalli, P. Müller-Buschbaum, M. Trebbin, S. Förster, O. Paris, S. V. Roth, and P. Fratzl, J. Appl. Crystallogr. **47**, 1797 (2014).

[205] J. Kieffer and D. Karkoulis, J. Phys. Conf. Ser. **425**, 202012 (2013).

[206] A. P. Hammersley, "FIT2D: An Introduction and Overview," Tech. Rep. (ESRF, Grenoble. France, 1997).

[207] D. P. Gruber, J. Todt, N. Wöhrl, J. Zalesak, M. Tkadletz, A. Kubec, S. Niese, M. Burghammer, M. Rosenthal, H. Sternschulte, M. J. Pfeifenberger, B. Sartory, and J. Keckes, Carbon N. Y. **144**, 666 (2019).

[208] M. Stefenelli, R. Daniel, W. Ecker, D. Kiener, J. Todt, A. Zeilinger, C. Mitterer, M. Burghammer, and J. Keckes, Acta Mater. **85**, 24 (2015).

[209] N. Jäger, M. Meindlhumer, S. Spor, H. Hruby, J. Julin, A. Stark, F. Nahif, J. Keckes, C. Mitterer, and R. Daniel, Acta Mater. **186**, 545 (2020).

[210] M. Meindlhumer, S. Klima, N. Jäger, A. Stark, H. Hruby, C. Mitterer, J. Keckes, and R. Daniel, Sci. Rep. **9**, 18027 (2019).

[211] E. Aschauer, M. Bartosik, H. Bolvardi, M. Arndt, P. Polcik, A. Davydok, C. Krywka, H. Riedl, and P. H. Mayrhofer, Surf. Coatings Technol. **361**, 364 (2019).

[212] D. P. Gruber, J. Zalesak, J. Todt, M. Tkadletz, B. Sartory, J. P. Suuronen, T. Ziegelwanger, C. Czettl, C. Mitterer, and J. Keckes, Surf. Coatings Technol. **399** (2020).

[213] G. Abadias, E. Chason, J. Keckes, M. Sebastiani, G. B. Thompson, E. Barthel, G. L. Doll, C. E. Murray, C. H. Stoessel, and L. Martinu, J. Vac. Sci. Technol. A Vacuum, Surfaces, Film. **36**, 020801 (2018).

Die approbierte gedruckte Originalversion dieser Dissertation ist an der TU Wien Bibliothek verfügbar.
The approved original version of this doctoral thesis is available in print at TU Wien Bibliothek.
TU Bibliothek Your knowledge hub WIEN

[214] W. Voigt, *Lehrbuch der Kristallphysik* (Teubner Verlag, Leipzig, 1928).

[215] A. Reuss, ZAMM - Zeitschrift für Angew. Math. und Mech. **9**, 49 (1929).

[216] R. Hill, Proc. Phys. Soc. Sect. A **65**, 349 (1952).

[217] H. Behnken and V. Hauk, Zeitschrift fuer Met. Res. Adv. Tech. **77**, 620 (1986).

[218] P. D. Evenschor and V. Hauk, Int. J. Mater. Res. **66**, 210 (1975).

[219] The Materials Project, "Materials Data on Cr2O3 by Materials Project," (2020).

[220] M. Bartosik, R. Daniel, C. Mitterer, I. Matko, M. Burghammer, P. Mayrhofer, and J. Keckes, Thin Solid Films **542**, 1 (2013).

[221] N. Jäger, M. Meindlhumer, M. Zitek, S. Spor, H. Hruby, F. Nahif, J. Julin, M. Rosenthal, J. Keckes, C. Mitterer, and R. Daniel, J. Mater. Sci. Technol. **100**, 91 (2022).

[222] M. Meindlhumer, J. Zalesak, W. Ecker, M. Rosenthal, S. Niese, P. Gawlitza, H. Hruby, C. Mitterer, R. Daniel, J. Keckes, and J. Todt, Mater. Des. **195** (2020).

[223] W. Ecker, J. Keckes, M. Krobath, J. Zalesak, R. Daniel, M. Rosenthal, and J. Todt, Mater. Des. **188**, 108478 (2020).

[224] M. Meindlhumer, L. R. Brandt, J. Zalesak, M. Rosenthal, H. Hruby, J. Kopecek, E. Salvati, C. Mitterer, R. Daniel, J. Todt, J. Keckes, and A. M. Korsunsky, Mater. Des. **198** (2021).

[225] M. Meindlhumer, N. Jäger, S. Spor, M. Rosenthal, J. Keckes, H. Hruby, C. Mitterer, R. Daniel, J. Keckes, and J. Todt, Scr. Mater. **182**, 11 (2020).

[226] A. Drnovšek, H. T. Vo, M. R. de Figueiredo, S. Kolozsvári, P. Hosemann, and R. Franz, Surf. Coatings Technol. **409**, 126909 (2021).

[227] G. Greczynski, J. Lu, J. Jensen, S. Bolz, W. Kölker, C. Schiffers, O. Lemmer, J. E. Greene, and L. Hultman, Surf. Coatings Technol. **257**, 15 (2014).

Die approbierte gedruckte Originalversion dieser Dissertation ist an der TU Wien Bibliothek verfügbar.
The approved original version of this doctoral thesis is available in print at TU Wien Bibliothek.
TU Bibliothek Your knowledge hub WIEN

Chapter 6

Scientific Contributions

The following presents an overview of all publications that originated in the framework of this thesis, with the contributions summarized into two different fields. *Publications I* to *III* contribute towards an improved understanding of the damage tolerance and thermal stability of ceramic thin film materials under static, cyclic, and thermal loads. *Publications IV* and *V* deal with the complexity of ion-assisted film growth of a metastable nitride thin film when using a HiPIMS discharge and multi-element target materials. The publications are organized to outline the train of thought, starting with the initial question for each topic and following the insights gained in every work. The section concludes with a list of further peer-reviewed publications that have been co-authored as part of this thesis, a list of supervised undergraduate students, and an overview of the contributions to national/international conferences.

6.1 Damage tolerance & thermo-physical properties of ceramic coatings

Publication I

Assessing the fracture and fatigue resistance of nanostructured thin films

L. Zauner, R. Hahn, E. Aschauer, T. Wojcik, A. Davydok, O. Hunold, P. Polcik, H. Riedl, *Acta Materialia*, 239 (2022): 118260.

Extensive research efforts are focused towards unravelling the intrinsic damage tolerance of ceramic thin film materials under quasi-static loads, with activities ranging from electronic structure calculations, to the experimental synthesis of complex architectural designs. In comparison, research of thin film materials exposed to cyclic mechanical loads remains a

Die approbierte gedruckte Originalversion dieser Dissertation ist an der TU Wien Bibliothek verfügbar.
The approved original version of this doctoral thesis is available in print at TU Wien Bibliothek.
TU Bibliothek Your knowledge hub WIEN

vastly uncharted territory, wherein the limited number of studies followed a macro-scale approach of testing the combined substrate-coating behavior. However, this leaves important questions, including whether thin film materials experience fatigue degradation in the sense of bulk metals or ceramics, open.

Therefore, this publication presents a novel perspective on the intrinsic fracture and fatigue properties of thin film materials based on a combinatorial approach of micromechanics and *in-situ* synchrotron nanodiffraction. The systematic analysis focusses on a model material system composed of metallic *bcc*-Cr and Cr-based compounds (*fcc*-CrN, *hcp*-CrB_2, and *rh*-Cr_2O_3) to cover a range of different bonding characters and crystal structures. Quasi-static bending experiments on free-standing microcantilever specimen reveal a large variation in fracture toughness between the materials, ranging from 1.6±0.2 MPa$\sqrt{m}$ for $Cr_{1.79}O_3$, to as high as 4.3±0.3 MPa$\sqrt{m}$ for $Cr_{1.03}B_2$. This difference is discussed in the framework of linear elastic fracture theory – from the viewpoint of Griffith's surface energy in relation to the bond characteristics – but also with respect to the elastic-plastic material response recorded from micropillar compression tests. In particular, $Cr_{1.03}B_2$ showed extensive plastic deformation, which may contribute to the exceptional fracture resistance recorded for the material. The results of cyclic bending experiments indicated, that instead of material damage induced from dislocation motion or microstructural irreversibilities, fatigue strengths of nanostructured thin films are limited by the intrinsic fracture toughness. Consequently, each material sustained up to 10^7 load cycles at stress amplitudes closely matching the respective critical stress intensity, without suffering noticeable fatigue damage or stress-state changes. In conclusion, the work demonstrates that increasing the fracture resistance of thin film materials provides a principal avenue to obtain fatigue resistant coatings.

Publication II

Role of Si segregation in the structural, mechanical, and compositional evolution of high-temperature oxidation resistant Cr-Si-$B_{2\pm z}$ thin films

L. Zauner, A. Steiner, T. Glechner, A. Bahr, B. Ott, R. Hahn, T. Wojcik, O. Hunold, J. Ramm, S. Kolozsvári, P. Polcik, P. Felfer, and H. Riedl, under review at *Acta Materialia* since 30.09.2022.

The key message of *Publication I*, to explore thin film materials with exceptional fracture toughness for simultaneously increased fatigue strength, paired with the intrinsically high fracture resistance of $Cr_{1.03}B_2$, provided the impetus for *Publications II* and *III*.

In this work, a Si alloying route is followed for the Cr-B_2 system which was previously

Die approbierte gedruckte Originalversion dieser Dissertation ist an der TU Wien Bibliothek verfügbar.
The approved original version of this doctoral thesis is available in print at TU Wien Bibliothek.
TU Bibliothek Your knowledge hub WIEN

demonstrated to yield a drastically improved oxidation resistance beyond temperatures of 1000 °C [52]. Moreover, in view of the enhanced fracture properties of Si alloyed nitride thin films [33, 226], a general screening of the structural, mechanical, and compositional properties of the Cr-Si-B_2 material was conducted. Therefore, AlB_2-structured Cr-Si-B_2 thin films with Si-content up to 17 at.% were synthesized by magnetron sputtering. Initial density-functional theory calculations of prototypical compositions indicated a Si solubility limit in the CrB_2 structure, which was experimentally specified between 3 to 4 at.% using detailed atom probe tomography. Complementary microstructural analysis revealed that the excess Si promotes refinement of the growth morphology related to the formation of mechanically weak Si segregates on grain boundary sites. The inherently two-phased architecture results in a continuous degradation of the mechanical properties with increasing Si content, reflected in a decrease in film hardness and Young's modulus from $H \sim 24$ to 17 GPa and $E \sim 300$ to 240 GPa, respectively. The outstanding oxidation resistance of the material above an alloying content of 8 at.% was correlated with the thermally activated volume- and surface-precipitation of Si from the Cr-Si-B_2 solid solution at 600 °C, which enables the growth of a stable SiO_2-based scale. High resolution chemical analysis highlighted the complete separation of Si from the CrB_2 structure at 1400 °C as well as a distinct oxide scale architecture – consisting of a few nanometers thick amorphous SiO_2, underneath ∼200 nm of nanocrystalline Cr_2O_3.

Publication III

Influence of Si segregates on the structural evolution, mechanical properties, and high-temperature fracture toughness of Cr-Si-$B_{2\pm z}$ coatings

L. Zauner, R. Hahn, O. Hunold, J. Ramm, S. Kolozsvári, P. Polcik, and H. Riedl, under review at *Materials & Design* since 30.10.2022.

Publication II presented an initial perspective on the capabilities of the Cr-Si-B_2 system. While the material exhibits excellent high-temperature oxidation resistance, the microstructural separation between the binary diboride and Si remains detrimental for the room-temperature mechanical properties. Based on the known anisotropy for transition metal diborides [44], *Publication III* is aimed at improving the film hardness by tuning the deposition conditions as well as to analyze the temperature-dependence of the structural and mechanical properties.

Indeed, utilizing an increased bias potential of -120 V for the deposition of AlB_2-type Cr-Si-B_2 thin films results in the growth of boron-rich, (001)-oriented, and mechanically superior coatings up to a Si content of 3 at.%. In contrast, higher Si-alloyed compositions show a significant reduction in film hardness and fracture toughness, related to an unchanged solubility limit in the binary diboride and the resulting growth of brittle Si grain-boundary

Die approbierte gedruckte Originalversion dieser Dissertation ist an der TU Wien Bibliothek verfügbar.
The approved original version of this doctoral thesis is available in print at TU Wien Bibliothek.
TU Bibliothek Your knowledge hub WIEN

segregates. In particular, Si alloying of 10 at.% reduces the room-temperature hardness from $H \sim 30$ to 20 GPa, whereas the fracture resistance decreases from $K_{Ic} \sim 2.9$ to as low as 1.7 MPa$\sqrt{m}$. Revisiting the oxidation resistance of the material up to 1400 °C highlighted a B/Cr-ratio independent behavior, while confirming the growth of a protective oxide scale for Si alloying above 8 at.%. Starting at 600 °C, separate vacuum annealing treatments indicate material recovery and pronounced Si precipitation within all compositions. While the film hardness remains unaffected from the thermal treatment, *in-situ* fracture toughness measurements up to 800 °C expose a distinct temperature-dependence of the fracture resistance. The binary CrB_2 initially shows a linear decrease in fracture toughness up to 600 °C, while a brittle-to-ductile-like transition at 800 °C enables an overall increased value of ∼3.3 MPa$\sqrt{m}$. Si-alloyed thin films show comparable behavior up to 400 °C, whereas at higher temperatures Si-precipitates introduce extensive plastic deformation and a damage tolerance that exceeds the experimental boundaries.

6.2 Ion-assisted deposition of Ti-Al-N thin films

Publication IV

Reactive HiPIMS deposition of Ti-Al-N: Influence of the deposition parameters on the cubic to hexagonal phase transition

L. Zauner, Ph. Ertelthaler, T. Wojcik, H. Bolvardi, S. Kolozsvári, P.H. Mayrhofer, H. Riedl, *Surface & Coatings Technology*, 382 (2020): 125007.

High-power impulse magnetron sputtering has evolved to an industrial scale technology, capable of merging the advantages of macro-particle free sputtering, with the high flux of ionized target material from cathodic arc evaporation. While the technology offers greater flexibility in tuning the deposition process, in particular through altered adatom mobility, a fundamental knowledge on the role of ion-irradiation during film growth is required. The HiPIMS technology was rapidly applied onto the well-established Ti-Al-N system, only to realize that the presence of doubly charged titanium ions causes the premature precipitation of stable wurtzite AlN within the metastable, cubic Ti-Al-N matrix [79, 227]. These results are of particular relevance for industrial $Ti_{1-x}Al_x$ composite targets, where the contribution of Ti-ions cannot be avoided. Therefore, *Publications IV* and *V* were devoted to an in-depth analysis of the reactive HiPIMS deposition of Ti-Al-N thin films from various $Ti_{1-x}Al_x$ targets. Moreover, the regions of cubic phase stability in dependence of the deposition parameters and ion-flux composition were unveiled.

Publication IV studies the effect of synthesis parameters such as the HiPIMS pulse frequency

Die approbierte gedruckte Originalversion dieser Dissertation ist an der TU Wien Bibliothek verfügbar.
The approved original version of this doctoral thesis is available in print at TU Wien Bibliothek.
TU Bibliothek Your knowledge hub WIEN

and duration, the peak power density, the nitrogen-to-argon flow-ratio, and the substrate bias potential on the reactive HiPIMS deposition of Ti-Al-N. The systematic variation performed on powder-metallurgical $Ti_{1-x}Al_x$ targets with increasing Al content ($x = 0.4$ to 0.6) yields a set of optimized deposition parameters for single-phase, cubic $Ti_{1-x}Al_xN$ coatings with a maximum Al solubility of $x_{max} \sim 55\%$. The thin films exhibit high hardness of up to 33 GPa, while maintaining a moderate compressive stress state at -2 GPa. While the results confirm the detrimental impact of Ti-ions on the cubic phase stability, reasonably high Al solubility was observed in cubic structured Ti-Al-N compared to similar plasma-based deposition techniques. However, slight deviations in the synthesis conditions resulted in the promoted wurtzite Al-Ti-N phase growth for similar Al concentrations. Particular sensitivity is revealed to the bias potential, being strongly related to surface diffusion and sufficient intermixing of the film species during the deposition of high Al-containing coatings. Despite minor contributions of the wurtzite phase on grain boundaries in $Ti_{0.40}Al_{0.60}N$, excellent film hardness of ∼36 GPa – which increased to ∼40 GPa upon annealing at 700 °C – was observed when using the increased ion-assistance during film growth. In addition, the impact of HiPIMS pulse-synchronized bias potentials was studied. Varying the time delay of the bias pulse suggests that avoiding the attraction of primary ions arriving on the growing film surface contributes to stabilizing the cubic structure. Hence, the results underline that the fraction and energy of Ti^{n+}- and Al^{n+}-ions contributing to film growth is decisive for the phase stability of cubic Ti-Al-N.

Publication V

Time-averaged and time-resolved ion fluxes related to reactive HiPIMS deposition of Ti-Al-N films

L. Zauner, A. Bahr, T. Kozák, J. Čapek, T. Wojcik, O. Hunold, S. Kolozsvári, P. Zeman, P.H. Mayrhofer, H. Riedl, *Surface & Coatings Technology*, 424 (2021): 127638.

An aspect that remained unanswered in *Publication IV* is the actual impact of varying deposition parameters on the ion distribution arriving at the substrate surface.

With reference to the deposition parameters specified in *Publication IV*, this study provides an in-depth characterization of the time-averaged and time-resolved ion flux generated during the reactive HiPIMS deposition of Ti-Al-N thin films. Ion mass spectroscopy unravels the ionized species emitted from a HiPIMS discharge on $Ti_{1-x}Al_x$ ($x = 0.4$ and 0.6) composite targets, particularly highlighting the influence of different nitrogen-to-argon flow ratios on the population of metal and process gas ions. The systematic study emphasizes that the flux of Al^+-ions is significantly enhanced for higher Al containing targets or reduced nitrogen flow-rates, while the fraction of Ti^{n+}-ions ($n = 1, 2$) remains unaffected and low. Moreover, it

Die approbierte gedruckte Originalversion dieser Dissertation ist an der TU Wien Bibliothek verfügbar.
The approved original version of this doctoral thesis is available in print at TU Wien Bibliothek.
TU Bibliothek Your knowledge hub WIEN

is observed that Ti^{2+} ions account for the smallest fraction in the total ion flux, irrespective of the discharge conditions. These results are of particular interest considering the comparable primary ionization energies for Al and Ti, as well as the adverse effect of Ti^{2+} ions on the cubic phase stability. Additional time-resolved plasma analysis reveals no separation in the arrival of metal- and process-gas-ions during the entire HiPIMS pulse cycle. Overall, the investigated deposition conditions enabled the low-temperature synthesis of cubic structured $Ti_{0.37}Al_{0.63}N$ thin films with exceptional hardness of ∼36 GPa, while maintaining a low compressive stress state at σ = -1.3 GPa. The high Al solubility of 63% – being close to the theoretically proposed limit of $x_{lim} \sim 0.67$ – is attributed to the prevalent ion bombardment conditions, which were dominated by process gas ions with a significant contribution of the Al^+-species (up to 20%).

Die approbierte gedruckte Originalversion dieser Dissertation ist an der TU Wien Bibliothek verfügbar.
The approved original version of this doctoral thesis is available in print at TU Wien Bibliothek.

6.3 Further peer-reviewed publications

Thermally stable superhard diborides: An ab initio guided case study for VW-diboride thin films, V. Moraes, **L. Zauner**, T. Wojcik, M. Arndt, P. Polcik, H. Riedl, P.H. Mayrhofer, *Acta Materialia*, 186 (2020): 487-493.

Reactive HiPIMS deposition of Al-oxide thin films using W-alloyed Al targets, S. Kagerer, **L. Zauner**, T. Wojcik, S. Kolozsvári, T. Kozák, J. Čapek, P.Zeman, H. Riedl, P.H. Mayrhofer, *Surface & Coatings Technology*, 422 (2021): 1247467.

Structure and mechanical properties of reactive and non-reactive sputter deposited WC based coatings, T. Glechner, R. Hahn, **L. Zauner**, S. Rißlegger, A. Kirnbauer, P. Polcik, H. Riedl, *Journal of Alloys and Compounds*, 885 (2021): 161129.

Anisotropic super-hardness of hexagonal $WB_{2\pm z}$ thin films, C. Fuger, R. Hahn, **L. Zauner**, T. Wojcik, M. Weiss, A. Limbeck, O. Hunold, P. Polcik, H. Riedl, *Materials Research Letters*, 10.2 (2022): 70-77.

Die approbierte gedruckte Originalversion dieser Dissertation ist an der TU Wien Bibliothek verfügbar.
The approved original version of this doctoral thesis is available in print at TU Wien Bibliothek.

6.4 Supervised students

Lorenz Lobmaier
Intermetallic target materials in PVD based deposition techniques: A case study for Ti-Al-N coatings
Master thesis
Finished 03/2020

Sophie Richter
Einfluss von hochschmelzenden Verbindungen auf das Sputterverhalten von Cr basierten Targets
Bachelor thesis
Finished 09/2020

Andreas Steiner
Influence of refractory elements on the properties of Cr-based thin films
Bachelor thesis
Finished 11/2020

Tobias Reining
Fatigue testing of PVD thin films using DMA based testing methods
Bachelor thesis
Finished 11/2021

Arno Gitschthaler
Influence of arc evaporated TiAlN-based coatings on the fatigue life of Ti-6Al-4V
Master thesis
Ongoing 10/2022

Die approbierte gedruckte Originalversion dieser Dissertation ist an der TU Wien Bibliothek verfügbar.
The approved original version of this doctoral thesis is available in print at TU Wien Bibliothek.

6.5 Participation at international conferences

Plathinium 2019
Antibes, France, 23.-27.09.2017
Reactive HiPIMS deposition of Ti-Al-N: Influencing the Cubic to Wurtzite phase transition
L. Zauner, T. Wojcik, T. Kozák, J. Čapek, H. Bolvardi, S. Kolozsvári, P. H. Mayrhofer, and H. Riedl

Special PSE 2020
Erfurt, Germany, 07.-10.09.2020
Reactive HiPIMS deposition of Ti-Al-N: Influence of the deposition parameters on the cubic to hexagonal phase transition
L. Zauner, T. Wojcik, T. Kozák, J. Čapek, H. Bolvardi, S. Kolozsvári, P. H. Mayrhofer, and H. Riedl

ICMCTF 2021 Virtual Conference
Online, 26.-30.04.2021
Influence of the bonding nature on the fatigue resistance of Cr-based thin films
L. Zauner, R. Hahn, M. Alfreider, O. Hunold, P. Polcik, D. Kiener, H. Riedl

ÖGV Seminar 2021
Wien, Austria, 24.09.2021
Time-averaged and time-resolved ion fluxes related to reactive HiPIMS deposition of Ti-Al-N films
L. Zauner, A. Bahr, T. Kozák, J. Čapek, T. Wojcik, O. Hunold, S. Kolozsvári, P. Zeman, P.H. Mayrhofer, and H. Riedl

HiPIMS Today 2022
Online, 25.-27.01.2022
Invited talk: *Time-averaged and time-resolved ion fluxes related to reactive HiPIMS deposition of Ti-Al-N films*
L. Zauner, A. Bahr, T. Kozák, J. Čapek, T. Wojcik, O. Hunold, S. Kolozsvári, P. Zeman, P.H. Mayrhofer, and H. Riedl

Die approbierte gedruckte Originalversion dieser Dissertation ist an der TU Wien Bibliothek verfügbar.
The approved original version of this doctoral thesis is available in print at TU Wien Bibliothek.

ICMCTF 2022

San Diego, 22.-27.05.2022

Influence of Si alloying on the high-temperature mechanical properties of CrB2 based thin films

L. Zauner, T. Glechner, R. Hahn, O. Hunold, J. Ramm, P. Polcik, and H. Riedl

Insights on fracture and fatigue mechanisms of hard protective coatings

L. Zauner, R. Hahn, O. Hunold, P. Polcik, and H. Riedl

Plansee Seminar 2022

Reutte, Austria, 30.05.-03.06.2022

Durability of hard protective coatings: Insights on fracture and fatigue mechanisms

L. Zauner, R. Hahn, O. Hunold, P. Polcik, and H. Riedl

Die approbierte gedruckte Originalversion dieser Dissertation ist an der TU Wien Bibliothek verfügbar.
The approved original version of this doctoral thesis is available in print at TU Wien Bibliothek.

Chapter 7

Concluding Remarks & Outlook

This thesis focused on establishing a framework to investigate essential aspects at both ends of the life cycle for PVD-deposited thin films – from the synthesis, to the application-oriented analysis of thermo-physical properties. Special focus was placed on unravelling the complex structure-property relationship for metastable thin films deposited with a significant metal-ion contribution, as well as on the mechanical and high-temperature stability of ceramic coating materials exposed to static and cyclic loads.

In *Publication I*, a novel investigation technique was developed based on the quasi-static and dynamic loading of microcantilever bending specimens combined with *in-situ* synchrotron nanodiffraction. The experimental setup allowed for the first time a detailed stiffness-based monitoring of fatigue damage in thin film materials exposed to oscillating unidirectional loads, while simultaneously providing information on nanoscale stress-gradients and structural changes within the film cross-section. The results uncovered an extreme crack growth resistance of nanostructured thin film materials, irrespective of the bonding character and crystal structure. In fact, a family of Cr-based thin films was essentially found immune to the established concepts of fatigue damage – through cyclic dislocation motion or microstructural irreversibilities – up to the high cycle fatigue regime ($N = 10^7$). Instead, experiments pointed out that the individual limitations in fatigue strength lie in the material-specific, intrinsic fracture toughness. These results will help to facilitate future research on fatigue resistant PVD thin films, with the task of extending the service lives for coated components essentially condensed to maximizing the fracture toughness of coating materials. While this endeavor is certainly among the great challenges of PVD research in itself, it minimizes the necessity for the laborious process of fatigue testing. The results confirmed that the presented setup is capable of resolving nanoscale changes in thin film materials as a result of external mechanical loads, although the absence of fatigue damage certainly leaves a desire for additional investigations. In terms of scientific directions, the employed methodology opens the door for further projects related to the damage tolerance of PVD thin films. For one, it

Die approbierte gedruckte Originalversion dieser Dissertation ist an der TU Wien Bibliothek verfügbar.
The approved original version of this doctoral thesis is available in print at TU Wien Bibliothek.
TU Bibliothek Your knowledge hub WIEN

would be interesting to monitor the long-term response of heterogenous cantilever specimen (*i.e.*, containing coating and substrate material) under cyclic loads, to better evaluate the transition towards the bulk-scale behavior. Furthermore, *in-situ* tracing the stress-dependent structural change of metastable phases within a thin film material and capturing the direct impact on the fracture resistance, would be well worth a try. With the proposed capabilities of next-generation synchrotron facilities to routinely supply X-ray beam diameters in the low nanometer regime, the methodology surely holds further interesting results in the near future.

Publications II and *III* investigated the temperature-dependent role of Si alloying in the structural, mechanical, and compositional evolution of Cr-Si-B_2 thin films. A distinct Si solubility limit was determined for the AlB_2-structured material, promoting the formation of mechanically dominating grain boundary segregates during film growth and upon thermal annealing. The microstructural separation was found decisive for the exceptional high-temperature oxidation resistance up to 1400 °C, thus exceeding the protective capabilities of state-of-the-art coating materials. However, the stability in high-temperature environments comes at the expense of degrading mechanical properties, revealing a pronounced Si-dependent decrease of the room-temperature hardness and fracture resistance. Although altered synthesis conditions partially compensated for this reduction at lower Si concentrations – taking advantage of the anisotropy of the diboride material – the simultaneous achievement of enhanced oxidation protection and mechanical properties remained mutually exclusive. Still, high-temperature fracture toughness experiments resulted in interesting and unexpected material behavior. While temperatures up to 600 °C led to a decreasing fracture toughness of the unalloyed CrB_2, a brittle-to-ductile-like transition at 800 °C increased the fracture tolerance above the room temperature value. In addition, the plastic deformability of Si precipitates enables severe high-temperature deformation and a fracture resistance beyond the boundaries of LEFM. Hence, the detailed analysis in both works did not conclude in a complete description of the Cr-Si-B_2 material, but rather led to new questions about Si alloyed transition metal diborides. In particular, preventing the segregation of Si from the solid solution is a central aspect for future research, to possibly combine excellent mechanical properties with the outstanding oxidation resistance. Given the overall limited number of publications reporting on high-temperature fracture toughness experiments, the work in *Publication III* also serves a broader mechanics and materials science community.

Finally, *Publications IV* and *V* investigate the complex film growth and plasma conditions during the reactive HiPIMS deposition of metastable Ti-Al-N thin films from $Ti_{1-x}Al_x$ composite targets. A systematic variation of the deposition and discharge parameters exposed the conditions for cubic phase stability, which were discussed in relation to the ion-flux composition arriving at the substrate surface. Moreover, the results concluded in optimized deposition parameters which allowed for the low-temperature growth of cubic structured $Ti_{0.37}Al_{0.63}N$, with an Al solubility close the theoretical threshold. The thin films

Die approbierte gedruckte Originalversion dieser Dissertation ist an der TU Wien Bibliothek verfügbar.
The approved original version of this doctoral thesis is available in print at TU Wien Bibliothek.
TU Bibliothek Your knowledge hub WIEN

showed the benefits of metal-ion assisted film growth, obtaining a densified microstructure with exceptional hardness of 36 GPa and a simultaneously low residual stress state. As demonstrated by time-averaged and time-dependent plasma analysis, the growth of these thin films is particularly related to a high influx of Al^{+}-ions on the substrate surface when using a $Ti_{1-x}Al_x$ target, whereas the ion contribution of Ti^{n+}-species ($n = 1, 2$) remained sufficiently low. However, the results also highlight the stringent necessity for precise tuning of the deposition process, with slightest deviations in the synthesis environment significantly contributing to the wurtzite AlN phase growth. Compared to previous works, the conducted research showed significant improvement in the mechanical properties and Al solubility limit for reactive HiPIMS deposited Ti-Al-N thin films. Moreover, both studies confirmed that the use of industrial $Ti_{1-x}Al_x$ targets in a reactive HiPIMS process can yield cubic structured Ti-Al-N thin films with superb properties, thus particularly contributing to the industrialization of the HiPIMS technology.

In summary, this thesis provides new insights in the micro-scale behavior of thin film materials exposed to cyclic loads, which results in the design and characterization of a promising TM-Si-B_2-based coating material for high-temperature environments. Moreover, the applicability of the HiPIMS technology for the deposition of metastable nitride thin films with high Al contents is summarized in optimum deposition conditions and thin films with excellent mechanical properties.

Die approbierte gedruckte Originalversion dieser Dissertation ist an der TU Wien Bibliothek verfügbar.
The approved original version of this doctoral thesis is available in print at TU Wien Bibliothek.
TU Bibliothek Your knowledge hub WIEN

Publication I

Die approbierte gedruckte Originalversion dieser Dissertation ist an der TU Wien Bibliothek verfügbar.
The approved original version of this doctoral thesis is available in print at TU Wien Bibliothek.

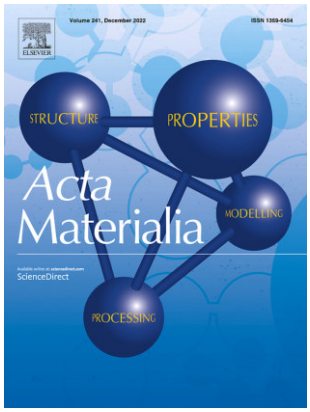

Assessing the fracture and fatigue resistance of nanostructured thin films

L. Zauner, R. Hahn, E. Aschauer, T. Wojcik, A. Davydok, O. Hunold, P. Polcik, H. Riedl

Acta Materialia, 239 (2022): 118260.
DOI: 10.1016/j.actamat.2022.118260

Acta Materialia 239 (2022) 118260

Contents lists available at ScienceDirect

Acta Materialia

journal homepage: www.elsevier.com/locate/actamat

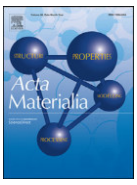

Full length article

Assessing the fracture and fatigue resistance of nanostructured thin films

L. Zauner[a,*], R. Hahn[a], E. Aschauer[a], T. Wojcik[a,b], A. Davydok[c], O. Hunold[d], P. Polcik[e], H. Riedl[a,b]

[a] Christian Doppler Laboratory for Surface Engineering of high-performance Components, TU Wien, Austria
[b] Institute of Materials Science and Technology, TU Wien, Austria
[c] Helmholtz-Zentrum Hereon, Institut für Werkstoffphysik, Germany
[d] Oerlikon Balzers, Oerlikon Surface Solutions AG, Liechtenstein
[e] Plansee Composite Materials GmbH, Germany

ARTICLE INFO

Article history:
Received 11 April 2022
Revised 6 August 2022
Accepted 8 August 2022
Available online 10 August 2022

Keywords:
Fatigue
Thin films
Synchrotron diffraction
Physical vapor deposition
Micromechanics
Ductility
Ceramics

ABSTRACT

Fatigue failure through sustained loading of ductile materials manifests in irreversible motion of dislocations, followed by crack initiation and growth. This contrasts with the mechanisms associated with brittle ceramics, such as nanostructured physical vapor deposited thin films, where inhibited dislocation mobility typically leads to interface-controlled damage. Hence, understanding the fatigue response of thin films from a fundamental viewpoint – including altered atomic bonds, crystal structures, and deformation mechanisms – holds the key to improved durability of coated engineering components. Here, a novel method utilizing quasi-static and cyclic-bending of pre-notched, unstrained microcantilever beams coupled with *in situ* synchrotron X-ray diffraction is presented to study the fracture toughness and fatigue properties of thin films under various loading conditions. Investigating a model system of sputter-deposited Cr and Cr-based ceramic compounds (CrN, CrB_2, and Cr_2O_3) demonstrates that the fatigue resistance of such thin films is limited by the inherent fracture toughness. In fact, cantilever cycling close to the critical stress intensity is sustained up to 10^7 load cycles on all materials, without inducing noticeable material damage, structural or stress-state changes. The observed variation in fracture toughness is put into context with linear-elastic fracture theory and complementary micro-pillar compression, thereby elucidating the wide range of values from as low as 1.6±0.2 MPa$\sqrt{m}$ for $Cr_{1.79}O_3$ up to 4.3±0.3 MPa$\sqrt{m}$ for $Cr_{1.03}B_2$, respectively. Moreover, possible mechanisms governing the elastic-plastic deformation response of all coatings, both in quasi-static and cyclic-loading conditions, are discussed. Our findings contribute key-insights into the underlying mechanisms dictating the damage tolerance of PVD coated components by relating fatigue strength limits to fundamental material properties.

© 2022 The Authors. Published by Elsevier Ltd on behalf of Acta Materialia Inc.
This is an open access article under the CC BY license (http://creativecommons.org/licenses/by/4.0/)

1. Introduction

Creating a fundamental understanding of the fracture and fatigue resistance of state-of-the-art materials is invariably associated with predicting the accessible lifespan for engineering components in aerospace, electronics, or energy applications [1]. The term “fatigue” comprises the cumulative material damage induced by cyclic loading, frequently leading to fracture and failure of structural components. In metals, where plasticity takes the dominating role in controlling cyclic deformation, fatigue damage accumulates upon irreversible plastic flow, initiated by irreversible dislocation motion. The latter mechanism cumulates in the formation of cracks at preferential sites such as persistent slip bands and related surface irregularities (*i.e.*, intrusions or extrusions), high-angle grain boundaries, or twin-boundaries [2–5]. Conversely, on the opposite end of the ductility spectrum, highly brittle ceramic materials are characterized by strong ionic and/or covalent bonds with limited dislocation mobility. In turn, the resistance to fracture and fatigue failure in these brittle solids is inherently determined by the atomic bond strength and activation of pre-existing flaws (*i.e.*, grain boundaries, voids, inclusions, etc.) under loading [2,6,7]. Yet, regardless of the apparent bonding character, the material response under repeating loads is closely linked to the microstructure at hand.

* Corresponding author at: Christian Doppler Laboratory for Surface Engineering of high-performance Components, TU Wien, Getreidemarkt 9, 1060 Wien, Austria.
E-mail address: lukas.zauner@tuwien.ac.at (L. Zauner).

https://doi.org/10.1016/j.actamat.2022.118260
1359-6454/© 2022 The Authors. Published by Elsevier Ltd on behalf of Acta Materialia Inc. This is an open access article under the CC BY license (http://creativecommons.org/licenses/by/4.0/)

Die approbierte gedruckte Originalversion dieser Dissertation ist an der TU Wien Bibliothek verfügbar.
The approved original version of this doctoral thesis is available in print at TU Wien Bibliothek.
TU Bibliothek Your knowledge hub WIEN

By decreasing the overall microstructural domain size, as is the case for physical vapor deposited micro- or nanostructured thin films, it is obvious that the governing deformation mechanisms are affected by the increased fraction of interfaces, grain boundaries, and free surfaces. These features introduce additional constraints on the availability of dislocation sources, their activity, and mutual interaction so that macroscopic dislocation features are reduced and interface-mediated damage, similar to brittle materials, becomes prevalent [3,8-11].

While general, bulk-scale fracture toughness and fatigue experiments provide means of identifying the crack resistance and lifespan of a material, assessing the failure-responsible atomistic or structural origin is difficult to accomplish. Thus, shrinking the examined material volume to characteristic thin film dimensions allows to fundamentally probe the influence of such features and unravel the origins of material failure [12–15].

Using micro sized cantilever beams and pillars, the intrinsic fracture toughness and failure strength of thin films – especially that of hard protective coatings – has been investigated extensively [16–23]. In contrast, reports on fatigue testing of coating materials are disproportionally less, with a strong focus towards metallic materials (*e.g.*, copper, nickel-base alloys, etc.) [24–28] or macroscale testing of the entire coating-substrate arrangement [29–35].

Employing TiN coated Ti-6Al-4V tension-tension fatigue specimen, Bai et al. [36] recently identified a stress-sensitive crack initiation mechanism. While below a critical stress amplitude dislocation pile-up and slip-steps in the substrate induced crack formation close to the coating interface, increasing the applied stress resulted in accelerated, coating-fracture-induced cleavage cracking of the substrate (see also Ref. [37]). Based on these mechanisms, enhancing the coating toughness or introducing a ductile interlayer is suggested to alleviate the adverse effect of the coating on the substrate fatigue properties. In addition, Sivagnanam Chandra et al. [38,39] discussed the influence of varying both the thickness and compressive stress state of Ti-Al-N coated Ti-alloys by correlating the observed fatigue failure with the imposed stress profile. There, critical aspects of the residual stress state across the coating and interface region were highlighted with respect to preferred crack nucleation sites.

Shifting the viewpoint to microscale fatigue testing, Kiener et al. [40] first performed fully-reversed *in situ* bending experiments on free standing single-crystalline copper micro cantilevers, thereby excluding any interference of substrates or microstructures with the resulting material behavior. The combined theoretical and experimental approach provided insights into the deformation mechanisms during fatigue loading at the micro-scale, up to a total number of $n = 100$ load cycles. Using an analogous approach for low cycle bending tests, a study by Kirchlechner et al. [3] coupled fatigue experiments of single-crystal copper beams with *in situ* synchrotron micro Laue diffraction to reveal the interplay of dislocation motion and slip planes under reversible load. Moreover, in works by Wimmer et al. [41] and Lavenstein et al. [42], vastly increased numbers of load cycles were accessed for cantilever bending experiments on poly-crystalline copper ($n \sim 1.5 \times 10^5$) and a single-crystalline Ni-base superalloy ($n \sim 10^7$), respectively, providing insights into small-scale fatigue failure within the high cycle fatigue regime. Especially the approach of the latter study is unique in its utilization of a permanent bond between the actuator tip and cantilever free-end, which allows to maintain zero mean stress while avoiding load gaps during strain reversal. In addition, similar to a work by Schwaiger and Kraft [10], a stiffness based technique was employed to probe cyclic damage accumulation and discuss the fatigue crack evolution [43].

Despite the extent of studies carried out, only little is known about the micro-scale material response of cyclically loaded ceramic thin film materials. Especially the aspect of varying material classes, which includes altered interatomic bond characters, crystal structures, and hence available deformation mechanisms, lacks an in-depth understanding. In this study, various free-standing micro-geometries fabricated from Cr-based thin film materials (*i.e.*, body-centered cubic Cr, face-centered cubic CrN, hexagonal CrB_2, and rhombohedral Cr_2O_3) are utilized to unravel the fracture and fatigue properties of nanostructured thin films. Both, micro-cantilever bending and -pillar compression tests are conducted to discuss the apparent fracture resistance and elasto-plastic deformation behavior in relation to the structural properties. An approach based on synchrotron X-ray nanodiffraction coupled fatigue experiments reveals the in-plane stress distribution of statically and dynamically loaded microcantilevers. Moreover, the methodology provides a direct comparison between the observed high cycle fatigue properties and the individual single cycle strength, *i.e.*, the fracture toughness.

2. Experimental

2.1. Coating deposition

Cr-based thin films were deposited onto (100)-oriented silicon substrates by unbalanced DC magnetron sputtering (DCMS) using a modified Leybold Z400 deposition system. The metallic Cr as well as the CrN and Cr_2O_3 compound thin films were deposited from a powder-metallurgically prepared Cr target (99.95 % purity, Plansee Composite Materials GmbH) operated in pure Ar-, mixed Ar/N_2-, or mixed Ar/O_2-atmosphere, respectively. The CrB_2 thin film was synthesized from a powder-metallurgically prepared CrB_2 target (99.3 % purity) in pure Ar-atmosphere. For all thin films, a constant target-to-substrate distance of 40 mm was maintained. Prior to each deposition, all substrates were ultrasonically pre-cleaned using acetone and ethanol consecutively. After reaching a base pressure of $p \leq 0.2$ mPa, the substrate was heated to the desired temperature T_{dep}, followed by an Ar-ion etching step with an applied substrate bias potential of U_S = -150 V (pulsed DC, 150kHz, 2496 ns pulse duration) at a total Ar gas pressure of $p = 1.3$ Pa. The subsequent depositions were carried out using parameter sets (*i.e.*, average cathode power density P_C, total deposition pressure p_{dep}, process gas composition, substrate bias potential U_S, etc.) determined during preliminary studies. Moreover, the deposition temperature (T_{dep}) was adjusted to maintain a uniform value of ~0.35 for the homologous temperature (T_H) of all Cr-based compounds, while that for metallic Cr was reduced to T_H ~0.22 to prevent extensive grain coarsening observed for higher T_H values. The deposition time was individually adjusted to yield a uniform thickness of $h = 3$ µm for all coatings. A summary of all deposition parameters and the resulting chemical composition including the content of undesired residuals *Res* (*i.e.*, argon and oxygen) are included in Table 1.

2.2. Coating characterization

Investigations on the coating structure were conducted using X-ray diffraction (XRD) on a PANalytical XPert Pro MPD system equipped with a Cu-Kα radiation source ($\lambda = 1.5418$ Å) and operated in θ-θ geometry. The X-ray probe size obtained a constant width of 14 mm and a decreasing length from 15 to 5 mm with increasing diffraction angle (the coated sample area measured 18 × 7 mm^2). The chemical composition of all Cr-based thin films was determined in top-view configuration by energy dispersive X-ray spectroscopy (EDS) utilizing an FEI Philips XL30 SEM equipped with an EDAX EDS detector (15 kV acceleration voltage). Furthermore, scanning electron microscopy (SEM) in an FEI Quanta 200 FEGSEM system (operated at 10 kV) was used to characterize the

Die approbierte gedruckte Originalversion dieser Dissertation ist an der TU Wien Bibliothek verfügbar.
The approved original version of this doctoral thesis is available in print at TU Wien Bibliothek.
TU Bibliothek Your knowledge hub WIEN

Table 1
Detailed overview of the deposition conditions and chemical composition of the synthesized coatings.

Coating	3"-target (purity, %)	P_C (Wcm^{-2})	T_{dep} (°C)	T_H (-)	p_{dep} (Pa)	Ar (sccm)	N_2 (sccm)	O_2 (sccm)	U_S (V)	Res (at.%)
Cr	Cr (99.95)	4.0	200	0.22 [44]	0.37	30	-	-	-75	≤ 0.8
$Cr_{0.94}N$	Cr (99.95)	4.6	400	0.34 [45]	0.37	16	16	-	-60	≤ 0.4
$Cr_{1.03}B_2$	CrB_2 (99.3)	5.5	600	0.35 [46]	0.37	30	-	-	-50	≤ 0.4
$Cr_{1.79}O_3$	Cr (99.95)	4.9	600	0.34 [47]	0.37	26	-	6.5	-50	≤ 0.6

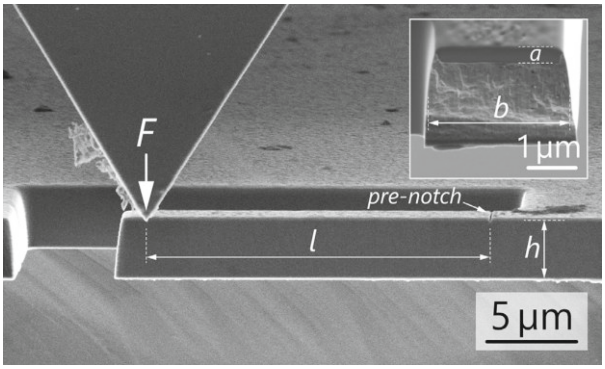

Fig. 1. SEM micrograph of a FIB prepared, pre-notched micro-cantilever as used for fracture toughness and fatigue testing experiments. The insert shows a post-mortem SEM micrograph of the fractured cantilever cross-section with the pre-notch depth *a*.

film growth morphology based on fracture cross-sections of single-side coated silicon substrates. Complementary information on the growth characteristics and grain size distribution was obtained via transmission electron microscopy (TEM) on an FEI TECNAI F20 system (200 kV acceleration voltage) utilizing samples prepared in top-view orientation. Both, the hardness (H) and Young's modulus (E) were determined by an ultra-micro indentation system (UMIS) equipped with a Berkovich diamond tip. For each thin film, at least 30 load-displacement curves were analyzed according to Oliver and Pharr [48] in the load ranges of 5 to 22 mN (steps of 0.5 mN), with additional measurements up 45 mN to probe for any substrate influence. Moreover, the recorded E values were fitted using a power law as function of the penetration depth and subsequently extrapolated to zero indentation depth to extract the film-only modulus [49].

Following the methodology introduced by Di Maio and Roberts [50], micromechanical bending experiments were performed on cantilever geometries to characterize the critical fracture force (F_C) and fracture toughness (K_{IC}) of all thin films investigated (see Fig. 1). Therefore, the silicon substrate of a mirror polished fracture cross-section was initially dissolved in aqueous KOH (40 wt.% concentration at a temperature of 70°C) to yield a section of free-standing thin film material. Focused ion beam milling (FIB) using Ga^+-ions on an FEI Quanta 200 3D DBFIB system was subsequently employed to produce microcantilever geometries in accordance with the guidelines given in Ref. [51]. A beam current of 1 nA was used for initial milling sequences, subsequently reduced to 0.5 nA to minimize ion induced material damage. The cantilevers were produced to a final geometry of length (l) × width (b) × height (h) = 22 × 3 × 3 μm^3, respectively (see Fig. 1). An initial notch was fabricated at a beam current of 50 pA, resulting in final depths of 300 - 400 nm for all thin films (depth fluctuations between cantilevers of the same material were below 50 nm). The notch did not extend over the entire cantilever width, instead small material bridges (50 - 100 nm wide) were left to initiate a very sharp crack at the notch base upon fracture (see Fig. 1 - insert).

During testing, the cantilevers were loaded with an *in situ* FemtoTools FT-NMT04 nanoindentation system equipped with a diamond wedge tip (contact length of 10 µm) in an FEI Quanta 200 FEGSEM. The experiments were performed in displacement-controlled mode with a deflection rate of 5 nms^{-1}, so that the maximum force at failure (*i.e.*, F_C) could be determined. All load-displacement curves were further analyzed to assure pure linear-elastic material behavior. The fracture toughness was then evaluated according to Matoy *et al.* [16]:

$$K_{IC} = \frac{F_C l}{b h^{\frac{3}{2}}} \times f\left(\frac{a}{h}\right) \tag{1}$$

with

$$f\left(\frac{a}{h}\right) = 1.46 + 24.36\left(\frac{a}{h}\right) - 47.21\left(\frac{a}{h}\right)^2 + 75.18\left(\frac{a}{h}\right)^3 \tag{2}$$

where a is the depth of the initial notch. A total of five bending experiments were performed for each material system.

Furthermore, using a micropillar geometry, all coating materials were investigated in their plastic deformation response under uniaxial compression. The micropillars were analogously prepared by FIB milling of the as-deposited coatings at a height to diameter aspect ratio of $h{:}d \sim 3{:}2$ (h equals the coating thickness) and a taper angle below 2°. Stepwise decreased ion-currents from 15 nA to 50 pA were employed for coarse and fine milling, respectively. The pillars were compressed in displacement-controlled mode at 5 nms^{-1} using a diamond flat punch tip (contact diameter of 5 µm) mounted to the above mentioned *in situ* nanoindentation system. The recorded load - displacement curves were used to calculate the engineering stress following an approach by Wheeler and Michler [52], where the top diameter of the pillar is taken as the reference contact area. The engineering strain was obtained from the displacement data using the coating thickness as the initial pillar height reference. Moreover, the displacement data was corrected by accounting for the base compliance following Sneddon's correction [53] given by

$$\Delta L_{Sneddon} = \frac{1 - \nu_{Sub}^2}{E_{Sub}} \frac{F}{d} \tag{3}$$

where ν_{Sub} and E_{Sub} are the Poisson's ratio and Young's modulus of the substrate, respectively, and F is the applied force.

Additional investigations on the fatigue resistance of all Cr-based coatings under oscillating, unidirectional load were performed through cyclic cantilever bending experiments (*i.e.*, fatigue tests), employing the same cantilever specimen and nanoindentation system (see Fig. 1). The test setup was targeted towards cyclically loading the cantilever close to the instantaneous fracture threshold – within the boundaries given by geometrical deviations between the samples and thus differences in the actual fracture limit – to promote the accumulation of fatigue damage in the material and eventually cause failure of the micro specimen. Therefore, the oscillating force $F(t)$ was based on the previously recorded, material specific critical stress intensity, consisting of a mean force $F_M = 0.75 \times F_C$ overlaid with a sinusoidal amplitude force $F_A = 0.15 \times F_C$. This resulted in the applied stress

Publication I
Die approbierte gedruckte Originalversion dieser Dissertation ist an der TU Wien Bibliothek verfügbar.
The approved original version of this doctoral thesis is available in print at TU Wien Bibliothek.
TU Bibliothek Your knowledge hub WIEN

intensity oscillating between 60 and 90% of K_{IC}, where a margin of 10% was maintained to accommodate for any geometrical inconsistencies between the cantilevers. The fatigue tests were conducted in force-controlled mode, meaning that F_M and F_A are maintained throughout the test duration, irrespective of any cantilever deterioration (*i.e.*, crack growth). Furthermore, all experiments were performed at a loading frequency of $f = 500$ Hz for a duration of $t = 334$ min, which equates to a total number of $n = 10^7$ load cycles. In addition to the load - displacement data, also the dynamic cantilever stiffness S was recorded, which is defined as the real part of the ratio between the applied force- and displacement-amplitude (w_A) and takes the form:

$$S = \frac{F_A(t)}{w_A(t)}\cos(\varphi) \tag{4}$$

where φ denotes the phase angle between the load and displacement response. Within the framework of this work, changes to the parameter "stiffness" are used as the main indicator for cyclic degradation of the cantilever specimen.

2.3. Coupled synchrotron X-ray nanodiffraction and fatigue experiments

Initially, a double-side polished, cross-sectional substrate-coating lamella with a thickness of ~35 µm in beam direction was prepared by mechanical polishing of a $Cr_{0.94}N$ coated Si substrate. The lamella was subsequently secured to a sample holder, which allows for a precise horizontal alignment, guaranteeing a 90° contact angle of the coating surface to the nanoindenter tip, while avoiding any interference with diffracted beam paths during *in situ* cross-sectional X-ray nanodiffraction experiments (see Fig. 2a). Using the above-mentioned FIB workstation, larger microcantilever specimens with a dimension of $l \times b \times h = 25 \times 25 \times 3$ µm^3 were ion-milled into the sample lamella. Therefore, a gradually reduced Ga^+-ion current of 20, 5, and 1 nA was employed to remove the silicon substrate material underneath the coating on a length of 30 µm, producing a clamped cantilever of the coating material. The final geometry of the cantilever (*i.e.*, releasing one of the clamped ends, milling the contour to final shape) was fabricated at an ion-current of 1 nA. Analogous to the smaller cantilever specimens, an initial pre-crack was introduced in the form of a through-thickness notch at a beam current of 0.1 nA. Prior to the fatigue experiments, conventional bending tests were performed on three of these cantilevers to determine a new reference value for F_C and K_{IC}*. Here it is important to mention that the fracture toughness evaluation for K_{IC}* is conducted outside the geometrical boundaries given in Ref. [16], with the sole purpose of obtaining the apparent fracture limit of the material in the given geometry.

The coupled synchrotron X-ray nanodiffraction and fatigue experiments were performed at the nanofocus endstation of beamline P03 at PETRA III located within the synchrotron facility "Deutsches Elektronen-Synchrotron" DESY (Hamburg, GERMANY). The monochromatic X-ray source was operated at a wavelength of $\lambda = 0.82656$ Å (beam energy of ~15 keV) and focused to a probe cross-section of ~250 nm. The above mentioned nanoindentation system was fixtured inside the measurement endstation such that the cantilever samples were placed in transmission geometry with the X-ray beam in line to the pre-notch [54]. Furthermore, the X-ray beam was centered at the pre-notch position, while the diamond wedge tip of the indenter system was located ~23 µm from this position at the opposite end and centered along the cantilever width (see Figs. 2a and b). Positioning of the entire nanoindenter-sample arrangement was conducted using a hexapod (tilt alignment) and linear nanopositioning stages (x-y- as well as z-alignment). The 2D diffraction signals were recorded on an Eiger X M9 photon-counting detector, with an acquisition time of 10 s per frame. The exact detector arrangement with respect to the sample position was calibrated using a standardized LaB_6 reference powder, resulting in a fixed sample-detector distance of 319.2 mm. This allowed for the recording of diffraction patterns with Bragg angles of up to ~27°.

Area scans covering a 20 × 20 mesh-grid in steps of 300 nm along the y- and z-axis were performed prior to the fatigue experiments to characterize the cross-sectional area of the cantilever around the pre-notch position (see Fig. 2c). Thereby, three different static loading scenarios were investigated, with the cantilever incrementally loaded from (*i*) no force applied, to (*ii*) ~35 % of K_{IC}* (not shown here), and to (*iii*) ~70 % of K_{IC}*. Subsequently, fatigue tests were conducted in alignment with the above-mentioned procedure and parameters, with the applied forces adjusted to $F_M = 0.65 \times F_C$ and $F_A = 0.15 \times F_C$, respectively, resulting in the overall stress intensity oscillating between 50 and 80 % of K_{IC}*. During these experiments, three distinct positions along the cantilever height, spaced 1 µm apart (top, middle, bottom; see Fig. 2d), were repeatedly scanned for the duration of the loading procedure. This allowed for a detailed analysis of the phase and stress evolution within the cantilever material up to a total number of $n = 5 \times 10^6$ load cycles.

2.4. Synchrotron X-ray nanodiffraction data analysis

The recorded 2D diffraction patterns were analyzed with respect to the phase evolution and the in-plane stress state $\sigma_{\parallel}$, both for static as well as dynamic loading conditions. To evaluate the stress state of the cantilever cross-section $\sigma_{\parallel}(y,z)$ an integration of the recorded patterns was performed in direction of the azimuthal angle ψ in segments of 10° from $\psi = 0$ to 90° (see Fig. 2e). Within the so obtained radial intensity distributions $I(\theta,\psi)$ the positions of distinct diffraction peaks $2\theta(\psi)_{hkl}$ (*e.g.*, (200)-peak for CrN), and thus also the orientation-dependent lattice spacing $d(\psi)_{hkl}$, were determined by fitting a Pseudo-Voigt function to the spectrum (see Figs. 2f and g). Subsequently, the orientation-dependent lattice strain $\varepsilon(\psi)_{hkl}$ was calculated following

$$\varepsilon_{hkl}(\psi) = \frac{d(\psi)_{hkl} - d_0(\psi^*)_{hkl}}{d_0(\psi^*)_{hkl}} \tag{5}$$

where $d_0(\psi^*)_{hkl}$ is the lattice spacing in the stress-free direction ψ^*_{hkl}, which itself is expressed by a set of X-ray diffraction elastic constants (XEC) $s_{1,hkl}$ and $\frac{1}{2}s_{2,hkl}$ in the form of

$$\sin\left(\psi^*_{hkl}\right) = \sqrt{\frac{-2s_{1,hkl}}{\frac{1}{2}s_{2,hkl}}} \tag{6}$$

Both the XEC were adopted from literature, *e.g.*, as $s_{1,hkl}^{CrN,(200)} = -0.3013 \times 10^{-3}$ GPa^{-1} and $\frac{1}{2}s_{2,hkl}^{CrN,(200)} = 2.584 \times 10^{-3}$ GPa^{-1} for CrN [55,56]. Following the $sin^2(\psi)$-method and the assumption of an elastically isotropic material under a biaxial stress state the fundamental equation for the in-plane stress state follows

$$\varepsilon_{hkl}(\psi) = \frac{1}{2}s_{2,hkl}\sigma_{\parallel}(y,z) \times \sin^2(\psi) + 2s_{1,hkl}\sigma_{\parallel}(y,z) \tag{7}$$

The described 2D pattern and data processing was conducted using the open-source software package DPDAK [57] as well as a self-written MATLAB script [58] (The MathWorks Inc., version R2019b, Natick, Massachusetts).

3. Results & discussion

In the following, the results of the experimental work are presented and discussed thoroughly. Fig. 3 shows a schematic overview of the entire coating synthesis and characterization

Die approbierte gedruckte Originalversion dieser Dissertation ist an der TU Wien Bibliothek verfügbar.
The approved original version of this doctoral thesis is available in print at TU Wien Bibliothek.
TU Bibliothek Your knowledge hub WIEN

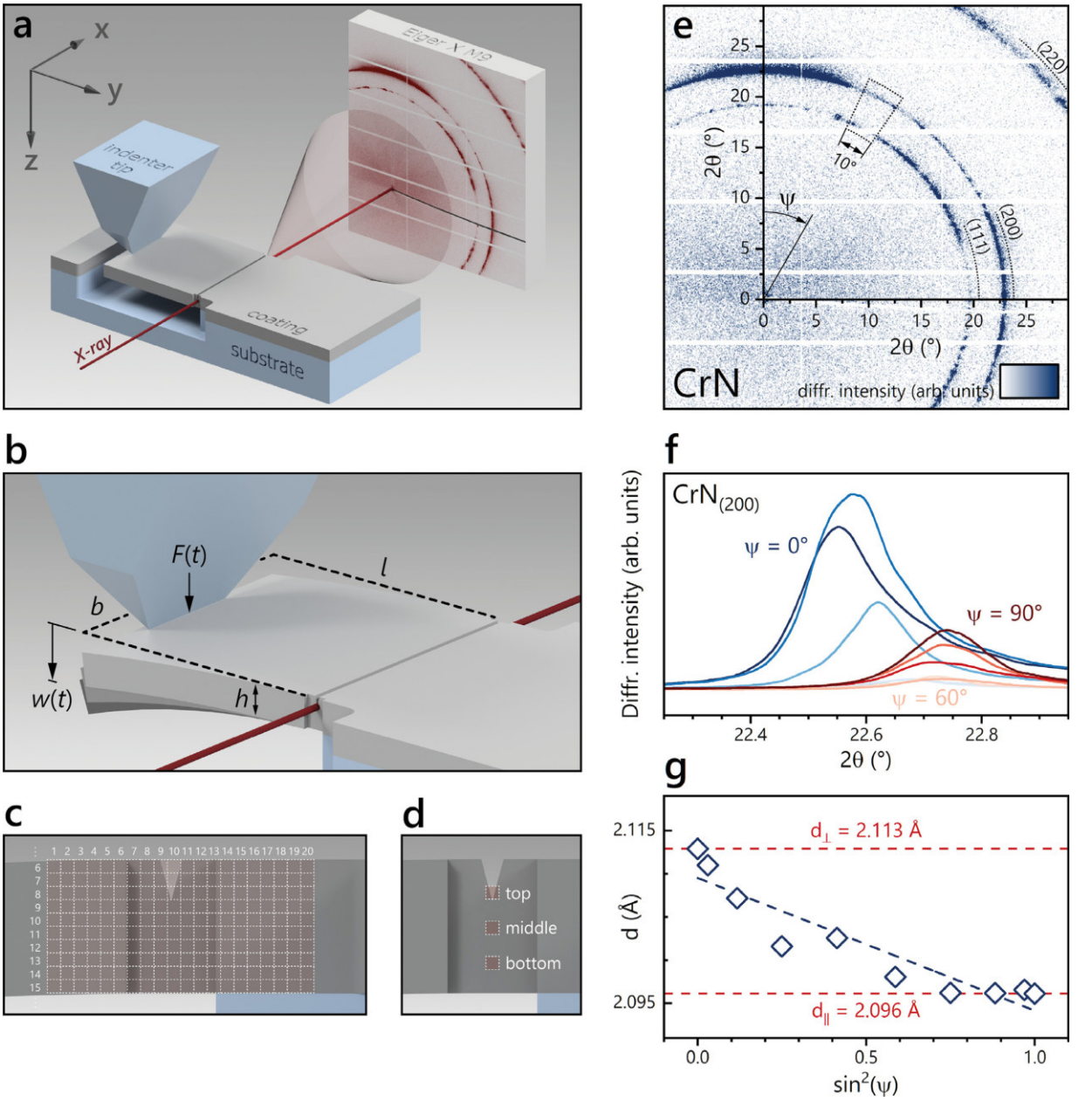

Fig. 2. (a) Schematic view of the *in situ* cross-sectional X-ray nanodiffraction setup. A $Cr_{0.94}N$ microcantilever sample with dimensions 25 × 25 × 3 µm³ (length × width × height), cut from a substrate-coating lamella, was scanned with an X-ray beam obtaining a cross-section of ~250 nm. The microcantilever was loaded using a diamond wedge tip with a contact length of 10 µm, positioned at a distance of 23 µm from the pre-notch, and centered along the cantilever width. The 2D Debye-Scherrer diffraction patterns were recorded using an Eiger X M9 photon-counting detector. (b) Detail showing the geometry and deflection $w(t)$ of the microcantilever under a static and/or cyclic load $F(t)$, applied using the nanoindenter tip. (c) During static loading, the X-ray beam was scanned along the *y*- and *z*-axis in steps of 300 nm creating a 20 × 20 grid centered around the pre-notch position, whereas during (d) cyclic loading, three positions along the cantilever height ("top", "middle", "bottom"; located at the pre-notch position in *y*-direction) were repeatedly scanned for the duration of the loading experiment. (e) Representative intensity plot of the recorded Debye-Scherrer patterns. The intensities of the (200)-peak were integrated in direction of the azimuthal angle ψ within 10° segments (dot-marked area) for ψ = 0 to 90° and (f) plotted as function of the diffraction angle. (g) Lattice parameters derived from the peaks plotted in (f) as function of $sin^2(\psi)$ including a corresponding linear fit for stress analysis.

workflow (Figs. 3a-e), as well as exemplarily the material response during fracture and fatigue experiments (Figs. 3f-j). In Section 3.1, the general framework of this study is established, outlining the materials selection and thin film properties with respect to phase formation, crystal structure, chemical composition, and apparent growth morphology (Figs. 3a-b, and f). This framework subsequently allows for closer insights into the fracture resistance (Fig. 3c-left) and elasto-plastic deformation behavior (Fig. 3d) of thin film materials under quasi-static loads, as discussed in Section 3.2. Therein, focused ion beam machining is used to produce free-standing microcantilever and micropillar specimen to determine the material specific fracture toughness (Fig. 3g)

Die approbierte gedruckte Originalversion dieser Dissertation ist an der TU Wien Bibliothek verfügbar.
The approved original version of this doctoral thesis is available in print at TU Wien Bibliothek.
TU Bibliothek Your knowledge hub WIEN

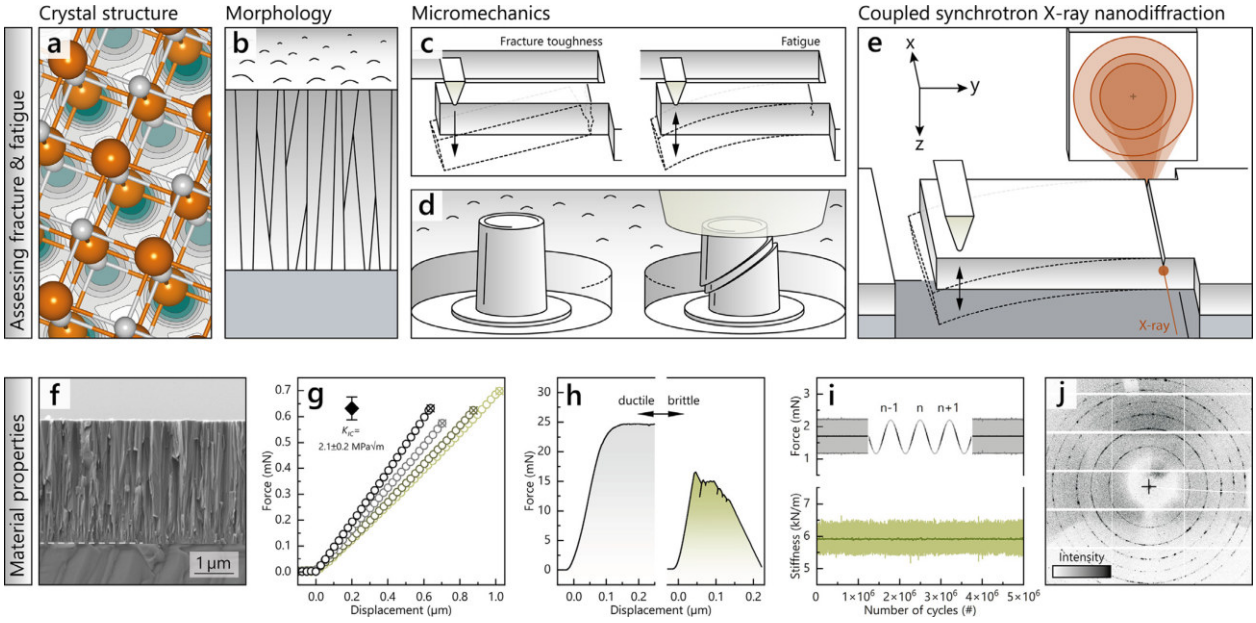

Fig. 3. Illustration showing the methodical approach to assess the fracture and fatigue resistance of thin films. (a-b) depict the fundamental thin film constitution in the form of the apparent crystal structure and growth morphology, respectively. (c) comprises microcantilever bending experiments to determine the coating fracture toughness (left) or the material response under prolonged cyclic loading (right). (e) shows the configuration for coupling *in situ* synchrotron X-ray nanodiffraction with cyclic bending experiments. Exemplary data obtained following the approach in (a-e) is further presented: (f) thin film fracture cross-section revealing the growth morphology of a Cr thin film; (g) force - displacement data obtained from fracture toughness experiments; (h) force - displacement data obtained from micropillar compression experiments indicating a ductile and brittle material response; (i) microcantilever stiffness and loading force data obtained from cyclic cantilever bending experiments; (j) diffraction pattern obtained from *in situ* synchrotron X-ray nanodiffraction.

and amenability to plastic deformation (Fig. 3h), respectively. Taking the observed deformation mechanisms into account, the established knowledge is further developed towards dynamic loading conditions in Section 3.3. Performing cyclic cantilever bending experiments up to the high cycle fatigue regime (Fig. 3c-right) provides details on the fatigue resistance of each coating material (Fig. 3i), and highlights the correlation between the fatigue strength and fundamental material properties. In Section 3.4., the micromechanical fatigue experiment is coupled with a novel *in situ* synchrotron X-ray nanodiffraction setup (Figs. 3e and j). Through this approach, the direct effect of imposing cyclic loads on larger cantilever structures is reviewed, revealing the cross-sectional stress distribution, phase evolution, and fatigue resistance of selected thin films.

3.1. Phase formation and growth morphology

The structural analysis of all Cr-based thin films obtained by X-ray diffraction is summarized in Fig. 4. The diffractograms are arranged from bottom to top as metallic Cr (*bcc*, squares), $Cr_{0.94}N$ (*fcc*, circles), $Cr_{1.03}B_2$ (*hcp*, triangles, space group 191), and $Cr_{1.79}O_3$ (*rh*, diamonds), respectively, and further complemented by the standardized 2θ reference peak positions [59–62]. The data clearly shows the phase-pure crystal structure of all coatings, alongside an almost perfect stoichiometry for all Cr-based compounds with respect to their nominal composition. Moreover, all diffractograms indicate a polycrystalline, randomly oriented crystal growth except for $Cr_{1.03}B_2$, which obtains a clearly preferred orientation in the (001)-direction.

All coatings were additionally investigated in more detail regarding their growth morphology and grain boundary constitution using cross-sectional SEM and top-view TEM, respectively. Figs. 5a,c,e, and g depict the fracture cross-sections of single side coated silicon substrates, whereas Figs. 5b,d,f, and h include the

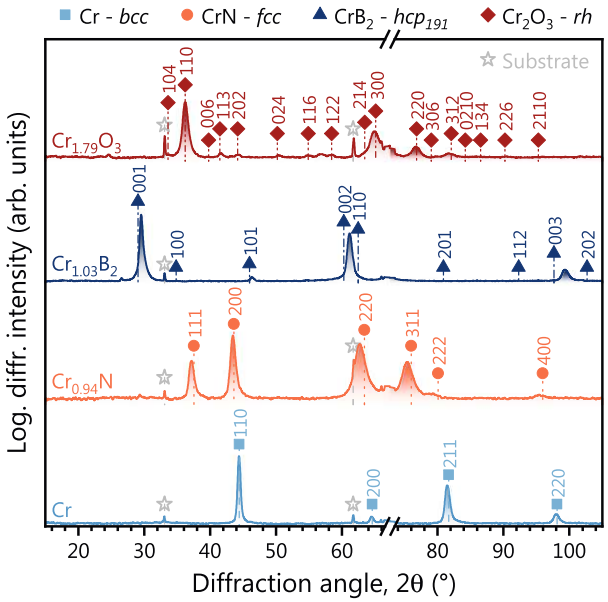

Fig. 4. XRD diffractograms of all Cr-based thin films measured on (100)-oriented silicon substrates (cubic, open star, [63]) including the corresponding 2θ peak positions of standardized reference patterns [59–62]. The diffractograms are arranged with metallic Cr (*bcc*, squares), $Cr_{0.94}N$ (*fcc*, circles), $Cr_{1.03}B_2$ (*hcp*, triangles, space group 191), and $Cr_{1.79}O_3$ (*rh*, diamonds) from bottom to top, respectively.

corresponding top-view TEM micrographs prepared from the identical specimen. All thin film materials obtain a dense, homogenous growth morphology over the entire coating thickness, which eventually concludes in a smooth top surface. Here, especially the thin

Die approbierte gedruckte Originalversion dieser Dissertation ist an der TU Wien Bibliothek verfügbar.
The approved original version of this doctoral thesis is available in print at TU Wien Bibliothek.
TU Bibliothek Your knowledge hub WIEN

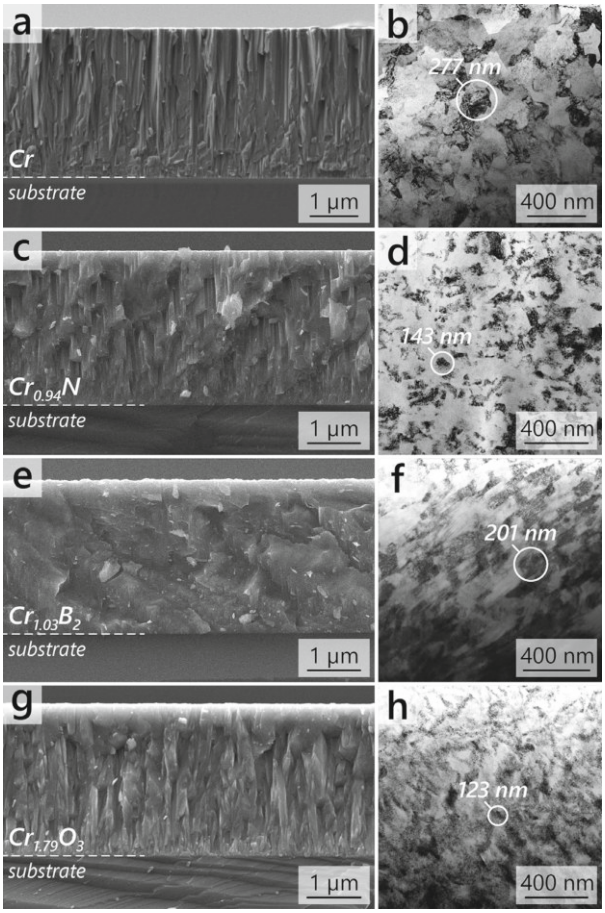

Fig. 5. (a), (c), (e), and (g) show SEM fracture cross-sections of all Cr-based thin films deposited on (100)-oriented silicon substrates. (b), (d), (f), and (h) present corresponding top-view bright-field TEM micrographs including the average crystallite grain size of the film cross-sections depicted in (a), (c), (e), and (g).

films synthesized from metallic Cr, $Cr_{0.94}N$ as well as $Cr_{1.79}O_3$ exhibit a pronounced formation of crystal columns, growing perpendicular to the coating-substrate interface. Typical for DCMS sputtered thin films, the columns appear to be interrupted and regularly forced to re-nucleate due to competitive crystal growth [64]. Contrary, $Cr_{1.03}B_2$ presents a rather featureless cross-section, lacking in clearly separated morphological features. These findings are largely supported by the corresponding bright-field TEM micrographs, presenting a dense and void-free growth structure for all coatings. Furthermore, the micrographs of metallic Cr and $Cr_{0.94}N$ especially highlight the individual crystal columns by a distinct orientation dependent contrast, whereas those for $Cr_{1.03}B_2$ and $Cr_{1.79}O_3$ obtain a slightly less pronounced visual separation. Using a line intercept method, the average crystal size was determined for all thin film materials. Within the analyzed volumes, the pure Cr thin film was evaluated with the largest crystal size of ~277 nm, followed by $Cr_{1.03}B_2$ with ~201 nm, and then $Cr_{0.94}N$ as well as $Cr_{1.79}O_3$ with ~143 and ~123 nm, respectively. These results suggest that the coatings synthesized in pure Argon atmosphere tend to form larger crystals, whereas both coatings sputtered in reactive environment are subject to enhanced re-nucleation and thus obtain slightly smaller grains. The TEM micrographs allowed for further microstructural analysis of the grain-boundary constitution. Here, the absence of distinct grain-boundary phases was confirmed, which is in line with the exact stoichiometry obtained for all Cr-based coatings and the results received during XRD analysis.

These results outline the framework for all subsequent fracture and cyclic loading experiments. Considering that the ensemble of synthesized coatings shows a vastly comparable thin film structure, the observed material properties will be particularly connected to the apparent bonding nature of the individual thin film [65]. This is considered as an essential aspect for elucidating possible origins for varying fracture and fatigue characteristics.

3.2. Fracture characteristics

A comprehensive overview of the thin film properties recorded and discussed within this Section is given in Table 2. In addition, literature references to corresponding bulk and thin film materials, as well as results from density-functional-theory (DFT) calculations are included to reveal possible scaling effects caused by the PVD synthesis route.

Micromechanical bending experiments on all four coating materials reveal a pronounced variation in the fracture resistance as depicted by the raw indenter force-displacement curves shown in Fig. 6a. In addition, Fig. 6b presents the data normalized in terms of stress intensity and bending strain. Upon examining the fracture cross-section of the cantilevers, all materials are found to fracture preferably along the grain boundaries. The results show that $Cr_{1.03}B_2$ obtains the highest critical fracture force during micro cantilever bending tests at $F_C \sim 810\pm65$ µN. Consequently, this also translates into the highest calculated fracture toughness with $K_{IC} \sim 4.3\pm0.3$ MPa$\sqrt{m}$. Compared to previous studies reporting on the fracture toughness of protective thin films, this material system appears to outperform many industrially relevant coatings such as Ti-Si-N (~3 MPa$\sqrt{m}$) or α-Al_2O_3 (~4 MPa$\sqrt{m}$) [66,67]. Moreover, the fracture toughness is increased over monolithic bulk CrB_2 (~3 MPa$\sqrt{m}$, [68]), likely due to the differences in microstructure and the intrinsic stresses caused by the high number of point-defects within the PVD thin film. In contrast, the data recorded for $Cr_{0.94}N$ and $Cr_{1.79}O_3$ indicates drastically lower critical fracture loads of $F_C \sim 332\pm14$ and 232 ± 22 µN, thus resulting in fracture toughness values of $K_{IC} \sim 2.1\pm0.1$ and 1.6 ± 0.2 MPa$\sqrt{m}$, respectively. The values obtained for the metallic Cr coating are located in between these boundaries, obtaining a critical fracture force of $F_C \sim 462\pm31$ µN and a corresponding fracture toughness of $K_{IC} \sim 3.6\pm0.3$ MPa$\sqrt{m}$. Here, it is essential to note that the metallic material is particularly prone to dislocation motion and hence plastic deformation, which manifests in a slight curvature of the load - displacement curve prior to the ultimate fracture- or yield-point (see Fig. 6a). This, however, stands in partial violation of the testing conditions outlined within the frameworks of linear elastic fracture mechanics (LEFM). Consequently, the fracture toughness values for the Cr thin film should be treated carefully, especially when compared to results deduced from different procedures. Overall, the results for the Cr thin film are considerably lower in contrast to the bulk material fracture toughness [69] – a known effect for sputter deposited metallic thin films [70] (see Table 2).

Upon specifically regarding the elastic deformability of the thin films, all Cr-based compounds show a comparable maximum bending strain in the range of ε = 1-1.2 %, whereas the metallic coating exhibits an extended displacement up to $w > 1.5$ µm and $\varepsilon > 1.5$ % prior to failure. Apart from varying maximum fracture strengths, this is especially interesting when considering the absence of elastic differences as obtained from instrumented nanoindentation experiments, where an almost identical Young's modulus of $E \sim 310$ GPa was determined for all investigated coatings (see Table 2). These observations eventually raise several intriguing questions: What are possible origins for the marked difference in fracture toughness of the coating materials? Is there a particu-

Die approbierte gedruckte Originalversion dieser Dissertation ist an der TU Wien Bibliothek verfügbar.
The approved original version of this doctoral thesis is available in print at TU Wien Bibliothek.
TU Bibliothek Your knowledge hub WIEN

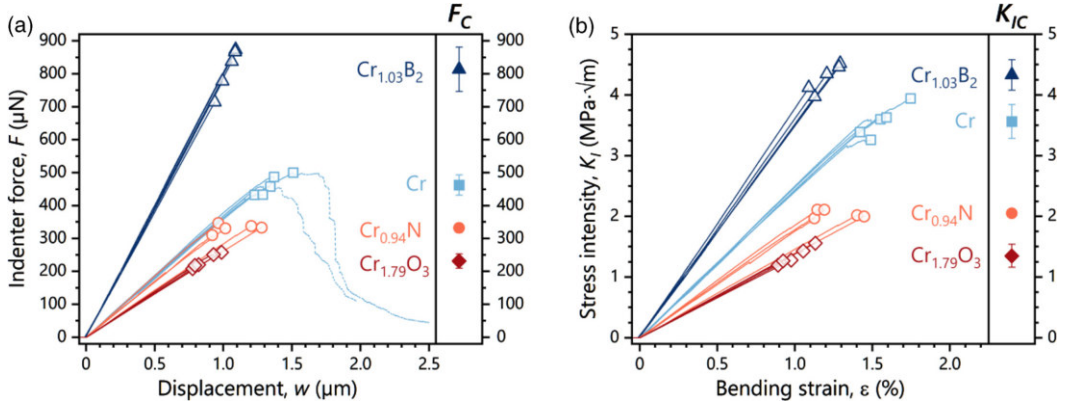

Fig. 6. (a) Indenter force - displacement curves of all Cr-based thin films recorded during *in situ* bending experiments on free-standing microcantilever geometries. Critical fracture loads and deflections are indicated using the material corresponding symbols introduced in Fig. 4. The mean value and standard deviation of the critical fracture load is included for each thin film on the right axis. (b) Normalized stress intensity - bending strain curves calculated from the data in (a) and post-mortem analysis of the individual geometry of each fractured cantilever cross-section. Critical stress intensities and bending strains, as well as mean values for the apparent fracture toughness of all thin films, are again included analogous to (a).

lar connection to intrinsic (toughening) mechanism that counteract crack propagation?

Assuming morphological consistency between the thin films, a primary connection can be drawn to the apparent bonding structure and strength of each material (*i.e.*, metallic, covalent, ionic, or a combination thereof). In principle, any fracture process ultimately involves the rupture of interatomic bonds – occurring on intra-crystalline lattice planes or generic grain boundary sites. Thus, the stronger the bonds, the higher the resistance against fracture. This holds particularly true for brittle fracture processes, which are entirely determined by atomistic events at the crack tip location [85]. This becomes particularly evident, when put into context with an expression for the fracture toughness of thin films in the form [86]:

$$K_{IC} = \sqrt{4\gamma E} \tag{8}$$

where γ denotes the surface energy – so that a principal origin for the measured variation may be attributed to the altered surface energies between the coating materials (given the minute variance in elastic moduli). Note, γ can also be interpreted as/exchanged by the ideal debonding energy along an interface E_{hkl}^{sep} [87,88]. Apparently, this explanation can only capture the studied thin films and their prevailing bonding character, thus may not be generalized to the corresponding material families (*i.e.*, not all nitride and oxide thin films show inferior fracture toughness compared to borides). In consequence, using Equation 8 assumes that any contribution from dissipative mechanisms (*e.g.*, crack tip plasticity, morphology induced micro-cracking or crack-branching) to counteract crack growth is negligible, especially within mode I based cantilever bending experiments.

However, calculating a theoretical estimate for the fracture toughness of CrN based on surface energies derived from DFT calculations [89], only a maximum value of $K_{IC} \sim 1.2$ MPa$\sqrt{}$m is obtained (see Equation 8, Young's modulus taken from Table 2). Hence, regardless of the variation in γ, this result proposes that intrinsic mechanisms may still contribute to the apparent fracture toughness. In fact, recent studies proposed that plasticity related effects at the crack-tip location [90] or morphological features [91] play a role in such brittle materials. Moreover, also increasing the ductile character in generally brittle ceramic thin films by tailoring the fraction of metallic bonds is suggested to enhance the fracture toughness in mode I testing [92,93].

Quantitatively grasping these bonding character related differences is, however, extremely difficult. Though at this point, the authors would like to add that DFT-based techniques do provide a general classification of bonding models – *i.e.*, by calculating the density of states (DOS) or the crystal orbital Hamilton population (COHP) [94]. In this work, a descriptive approach using micropillar compression experiments is selected to further elucidate the bond structure variation and to obtain a qualitative insight, especially on the elastic-plastic deformation response of all Cr-based materials. Specifically, within the Cr-based compounds, the atoms are bound by a mixture of strong covalent, ionic, and metallic bonds, as such they are less ductile compared to pure Cr, which is predominantly characterized by the latter type. Nevertheless, especially CrB_2 may possess a significant ductile character – in combination with a strong, covalently bound 2D boron network [95] – thus supporting the high fracture toughness value.

Engineering stress (σ_{eng}) vs. compressive strain (ε_{comp}) curves from uniaxial compression tests of micropillars prepared from all Cr-based thin films are summarized in Fig. 7. In addition, Fig. 8 contains exemplary SEM micrographs of compressed micropillars to further elucidate the observed deformation behavior. Regarding the calculated yield strengths (see Fig. 7, left column), strong similarities were found with the fracture limits depicted in Figs. 6. Although the materials were stressed in the opposite regime, the material response showed that $Cr_{1.03}B_2$ again obtains the highest yield strength at $\sigma_y \sim 8.9\pm0.5$ GPa, followed by $Cr_{0.94}N$ and $Cr_{1.79}O_3$ with values of $\sigma_y \sim 6.0\pm0.4$ and 4.0 ± 0.1 GPa, respectively. Related to the pure metallic bonding character of the Cr thin film, the lowest yield strength with $\sigma_y \sim 2.4\pm0.1$ GPa was observed, which is in excellent agreement with previous values obtained for nanocrystalline bulk Cr [72]. Moreover, the compression tests reveal vastly different stress-strain responses past the yield point, from which varying "levels" of plasticity can be deduced. Most prominent, both Cr and $Cr_{1.03}B_2$ show very similar behavior, with extensive plastic flow upon reaching σ_y (see Fig. 7 center column as well as Fig. 8a-b and 8e-f). Instead of forming distinct slip planes, the Cr pillars show uniform compression and bulging, next to crack initiation along column boundaries. The homogeneous plastic deformation can be attributed to the polycrystallinity of the material, preventing deformation in a preferred orientation. Moreover, Cr even shows a tendency towards steady rate work hardening [14]. The $Cr_{1.03}B_2$ pillars on the other hand reveal slip on a single or few adjacent glide planes. Given the preferred (001)-orientation for this

Die approbierte gedruckte Originalversion dieser Dissertation ist an der TU Wien Bibliothek verfügbar.
The approved original version of this doctoral thesis is available in print at TU Wien Bibliothek.
TU Bibliothek Your knowledge hub WIEN

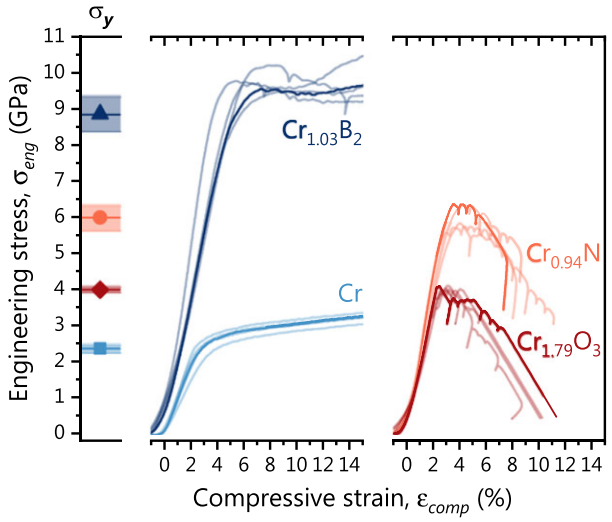

Fig. 7. Engineering stress - compressive strain curves of all Cr-based thin films recorded during *in situ* micropillar compression experiments. The data is arranged according to the predominant material response, hence results for Cr and $Cr_{1.03}B_2$ are merged in the center section, whereas the results for $Cr_{0.94}N$ and $Cr_{1.79}O_3$ are included in the right-hand section. Note the extended plastic deformation of Cr and $Cr_{1.03}B_2$ after reaching the yield point, contrary $Cr_{0.94}N$ and $Cr_{1.79}O_3$ are characterized by consecutive strain burst events and a lack of deformation stability. The mean value and standard deviation of the yield stress are included for each thin film in the left-hand section.

material (see Fig. 4), the observed deformation could be attributed to shearing along the $\{10\bar{1}1\}\langle 11\bar{2}0\rangle$ slip plane (yet, detailed TEM analysis would be needed for clarification). Contrary, $Cr_{0.94}N$ and $Cr_{1.79}O_3$ pillars exhibit a strongly brittle behavior, being characterized by discrete strain burst events and a lack of deformation stability (see Fig. 7 right column as well as Fig. 8c-d and 8g-h). Especially for CrN, previous studies have also reported on significant material densification and plastic flow during nanoindentation experiments [75], clearly contrasting to the observed material response. A possible explanation could lie in the varying deposition conditions or that indentation experiments force the activation of plastic flow even more than pillar compression tests. Both materials again obtain a polycrystalline structure, with a strong tendency towards shear fracture along a ~45° plane, followed by grain boundary slip of adjacent crystal columns. Apart from the randomly oriented crystals, this behavior is seen in the absence of active deformation mechanisms due to the high energy barrier preventing dislocation motion (Peierl's stress), consequently impeding continuous plastic deformation [96]. In this sense, the calculated yield strength can also be referred to as the compressive strength of both materials. In general, the recorded results not only confirm the suggested accessibility of plastic flow within nanostructured Cr and $Cr_{1.03}B_2$ thin films but also support the correlation between the intrinsic ductile character and the apparent fracture resistance observed in the cantilever bending tests.

3.3. Fatigue characteristics

To further develop the established picture for the mechanical response of all Cr-based thin films towards dynamic loading conditions, *in situ* cyclic cantilever bending tests were performed. Here, an identical setup as used during the fracture toughness experiments was employed, except the applied force being oscillated at a frequency of $f = 500$ Hz between 60 and 90 % of the material specific critical fracture limit (see Figs. 1 and 6). A representative evolution of the indenter force is depicted as a function of the number of load cycles for the $Cr_{0.94}N$ specimen in Fig. 9a. The recorded data gives the continuous force application onto the micro cantilever, comprised of a mean force (dark blue line) overlaid with a sinusoidal amplitude force (light blue area around the mean force) up to $n = 10^7$ cycles (see Figs. 9a and b). Examining the cantilever stiffness evolution showed a very alike behavior for all Cr-based materials, given that the initial stiffness values were preserved throughout the entire loading duration (see Fig. 9c). Con-

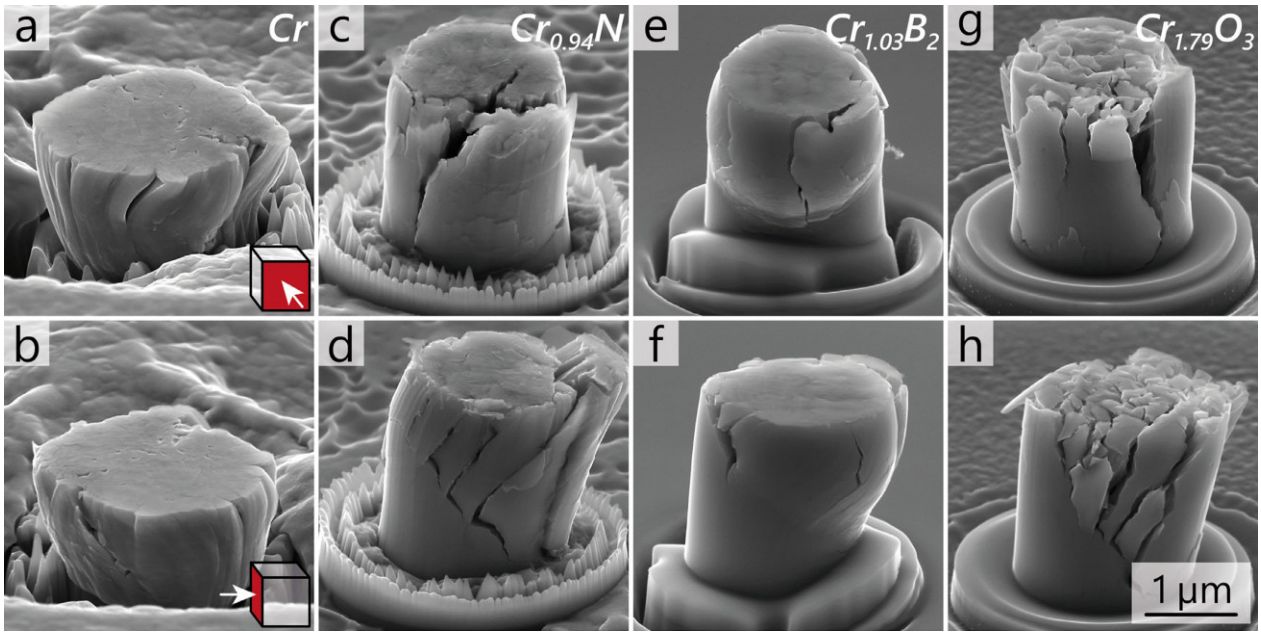

Fig. 8. Exemplary SEM micrographs of compressed micro-pillar specimen for (a-b) Cr, (c-d) $Cr_{0.94}N$, (e-f) $Cr_{1.03}B_2$, and (g-h) $Cr_{1.79}O_3$. The upper image row depicts the micro-pillars in frontal view, whereas the lower image row contains the 90° side view.

Die approbierte gedruckte Originalversion dieser Dissertation ist an der TU Wien Bibliothek verfügbar.
The approved original version of this doctoral thesis is available in print at TU Wien Bibliothek.
TU Bibliothek Your knowledge hub WIEN

TU Bibliothek Your knowledge hub
Die approbierte gedruckte Originalversion dieser Dissertation ist an der TU Wien Bibliothek verfügbar.
The approved original version of this doctoral thesis is available in print at TU Wien Bibliothek.

Table 2
Detailed overview of the mechanical properties for all thin film materials as well as the corresponding data derived from literature on bulk materials and DFT calculations.

Material	Length-scale	Grain size (nm)	H (GPa)	E (GPa)	υ (-)	F_C (μN)	K_{IC} (MPa$\sqrt{}$m)	σ_y (GPa)	Reference & related works
Cr	thin film, this work	~277	9.4±0.3	308±7	-	462±31	3.6±0.3	2.4±0.1	[71]
	bulk	-	1.2-4.3	245-294	0.2-0.22	-	5-10.5	~0.6	[69,72,73]
	DFT	-	-	332.8	0.29	-	-	-	[74]
CrN	thin film, this work	~143	26.6±1.3	311±17	-	332±14	2.1±0.1	6.0±0.4	[75]
	bulk	-	-	285-305*	0.27-0.34*	-	2-3.5*	-	[76]*
	DFT	-	-	224.5	0.29	-			[77]
CrB_2	thin film, this work	~201	24.4±1.6	312±8	-	810±65	4.3±0.3	8.9±0.5	[78]
	bulk	-	11-20	443-481, $E_{(100)}$=531.4, $E_{(001)}$=302.4	0.21	-	3.1-3.7	-	[68,79,80]
	DFT	-	-	442.9	0.21	-		-	[81]
Cr_2O_3	thin film, this work	~123	31.8±1.8	306±8	-	232±22	1.6±0.2	4.0±0.1	[82]
	Bulk	-	9-29.5	-	-	-	-	-	[83]
	DFT	-	-	287	0.27	-	-	-	[84]

* Spark-plasma sintered CrN/Cr_2N material.

Fig. 9. (a) Representative indenter force (left axis) vs. load cycle evolution recorded during cyclic loading of a free-standing microcantilever prepared from a Cr-based thin film (here $Cr_{0.94}N$). The applied stress intensity, including the reference fracture toughness determined in Fig. 6b, is included on the right axis. (b) Schematic detail of the load evolution showing the continuous force application on the microcantilever as well as individual data points recorded every 50th load cycles. (c) Corresponding cantilever stiffness - load cycle evolution for all Cr-based thin films (material corresponding symbols apply according to Fig. 4).

trary, any crack propagation would result in a drastic reduction of the cross-sectional area, in turn showing in a decrease of the recorded stiffness. Since no material damage was induced through the cyclic loading, all fatigue tested micro-cantilevers returned to their initial position upon unloading with an identical appearance as in their as-prepared state.

Considering that the applied loads approached the instantaneous fracture threshold, the displayed mechanical response closely resembles that observed for highly brittle materials. In monolithic bulk ceramics, active and stable crack growth under cyclic loading conditions is typically confined to a narrow range in terms of the stress intensity, below which pre-existing cracks are considered dormant, while above rapid failure occurs. Moreover, crack formation is invariably associated with activating these pre-existing flaws rather than a natural initiation related to dislocation glide [6,7,97]. The actual fatigue induced crack advance is typically comparable to the crack growth mechanism under quasi-static load and shows a strong dependence on the fracture toughness, with only limited capabilities for intrinsic or extrinsic toughening. Hence, possible cyclic degradation mechanisms include microcracking and crack coalescence in front of the crack tip (grain boundary located microcracks), or degradation of the grain bridging capacity in the crack wake [6,98,99]. These mechanisms, however, seem to be inoperable within the studied thin films, yet the exact cause – *e.g.*, growth morphology related, constraints induced by the microstructural domain size, or others – remains elusive.

Nevertheless, the non-existent crack extension and preserved endurance strength of as high as 90 % of the respective single cy-

cle strength (*i.e.*, the fracture toughness) – maintained well within the high cycle fatigue (HCF) regime – are distinct from typical bulk material behavior. This becomes especially striking when considering the pre-notch at the fixed end of the cantilever, serving as stress concentration and possible crack nucleation site. Here it should be added that ceramic materials show a similar sensitivity towards the prevailing crack length as metals, so that crack growth rates for microstructurally small cracks are far in excess of large cracks, resulting from a diminishing effect of shielding mechanisms by virtue of the limited wake (no pre-notch depth variation was conducted in this work to study the influence on the fatigue response) [7,98].

Within the tested material spectrum, interestingly, also the metallic Cr coating follows the ceramic material behavior, despite the metallic bond structure and previously observed plasticity under quasi-static loading conditions (see Figs. 6-8). However, as mentioned in the opening section of this work, recent studies on the fatigue behavior of metallic thin films such as copper showed a length-scale dependent transition of the active fatigue mechanisms. In fact, decreasing the characteristic microstructural dimensions to the nanometer regime (*i.e.*, a similar grain size of ~200 nm) imposes growing constraints on dislocation activities – necessary to form extrusions or intrusions – resulting in the observed crack dominated fatigue failure [8,11,28]. Contrary, as shown by Ritchie and Gilbert et al. [6,100,101], monolithic bulk ceramics such as alumina show a significant microstructural size-dependence towards accelerated fatigue crack growth rates with decreasing grain size and concomitant decrease in fracture toughness, yet the actual failure mechanism remains unchanged. Since the here tested ceramic materials did not reveal any cyclic damage, this effect could not be verified on the nanometer scale.

The general picture that emerges from the fatigue tests on all Cr-based thin films suggests that the applied loads and cycle numbers exclusively trigger an elastic material response without causing any noticeable material damage. In turn, this means that the actual fatigue resistance or endurance strength of such nanostructured coating materials is primarily defined and limited by the intrinsic fracture toughness – a material property closely related to the prevalent bonding character. Hence, upon eliminating the influence of a substrate-coating interface (*i.e.,* especially any contribution from residual stresses), the fatigue strength is given when the following condition holds true:

$$K_I \leq K_{IC} \tag{9}$$

In summary, we could not determine any variation in the fatigue resistance with respect to the prevailing crystal structure or bonding character of the thin films, except for the implication on the fracture toughness and its restriction on the fatigue resistance in turn.

3.4. Coupled synchrotron X-ray nanodiffraction and fatigue experiments

A more elaborate, detailed understanding of this observed material response from the aspect of intrinsic stress distributions and local phase formation was obtained by coupling the fatigue experiments with synchrotron X-ray nanodiffraction. Using this *in situ* synchrotron X-ray nanodiffraction setup, the phase evolution and stress state of larger micro-cantilever specimen was studied around the notch area in both the as-fabricated as well as under static (see Fig. 2c) and dynamic loading conditions (see Fig. 2d). These experiments aimed to correlate the observed fracture behavior and absence of fatigue induced damage with the intrinsic properties of the tested thin film materials.

A representative stress distribution around the pre-notch position, calculated according to the procedure described in Figs. 2e-g,

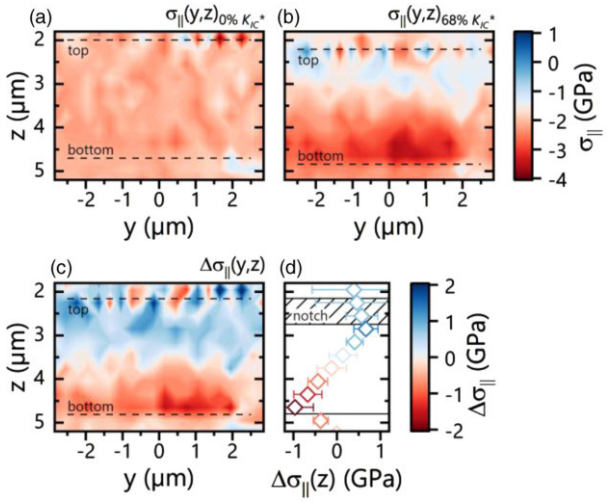

Fig. 10. In-plane stress map of a $Cr_{0.94}N$ cantilever around the pre-notch position (y = 0) in the (a) unloaded and (b) loaded state (stress intensity equals 68 % of the reference fracture toughness K_{IC}^*). Note the uniform compressive stress state in (a) violates the equilibrium condition and is attributed to a consistent measurement artifact throughout all diffraction experiments. (c) Corresponding delta map showing the difference between the stress states depicted in (a) and (b), including the (d) cross-sectional row-average of the data in (c). The top and bottom surface of the cantilever as well as the notch depth are indicated as guidance in all Figs.

is shown in Fig. 10 for a cantilever produced from the $Cr_{0.94}N$ coating. Fig. 10a presents the in-plane stress distribution in the as-fabricated state (K_I = 0 % of K_{IC}^*), exhibiting a uniform compressive stress distribution of $\sigma_{\parallel}(y,z) \sim$ -2.1 GPa. K_{IC}^* equals the reference fracture toughness of the cantilever specimen – for further details see the Experimental Section. At first glance, these data suggest that the residual stress is closely associated with the apparent film growth kinetics during PVD synthesis, leading to the visualized compressive stress state. However, considering the free-standing end of the micro-cantilever and the removal of substrate material constraints, this calculated in-plane stress map is in violation of the force and momentum equilibrium for the coating cross-section. In fact, given by the uniform appearance of the stress distribution, the area surrounding the pre-notch position should be rather interpreted as stress free, with the data corrected by shifting the mean value of $\sigma_{\parallel}(y,z)$ to 0 GPa. This offset is understood as an artifact of the experimental setup and prevailing X-ray beam conditions. Moreover, these results also imply homogeneous growth conditions since the deduced data presents no stress gradients across the entire coating thickness.

Upon loading the cantilever to K_I = 68 % of K_{IC}^* (see Fig. 10b), which closely resembles the mean stress intensity applied during subsequent fatigue experiments, the upper segment depicts an expected reduction in the compressive stress state, while the bottom segment shows a proportional increase. The applied stress intensity is referenced to the actual K_{IC}^* value of the examined cantilever sample, determined after recording the static stress map. In order to compensate for the stress data offset identified in Fig. 10a, both stress distributions are subtracted to yield the relative change in the in-plane stress state $\Delta\sigma_{\parallel}(y,z)$ (*i.e.*, the apparent stress during bending), which is presented in Fig. 10c as well as in Fig. 10d in the form of a cross-sectional average. Applying load onto the cantilever is shown to cause a perfectly linear change of the in-plane stress over the cantilever cross-section, with the neutral axis centered along the height. The maximum stress change occurs on the upper and lower segments, with $\Delta\sigma_{\parallel}(z)_{max} \sim \pm 1$ GPa for the given load. However, the stresses in the upper-most part of the cantilever

Die approbierte gedruckte Originalversion dieser Dissertation ist an der TU Wien Bibliothek verfügbar.
The approved original version of this doctoral thesis is available in print at TU Wien Bibliothek.
TU Bibliothek Your knowledge hub WIEN

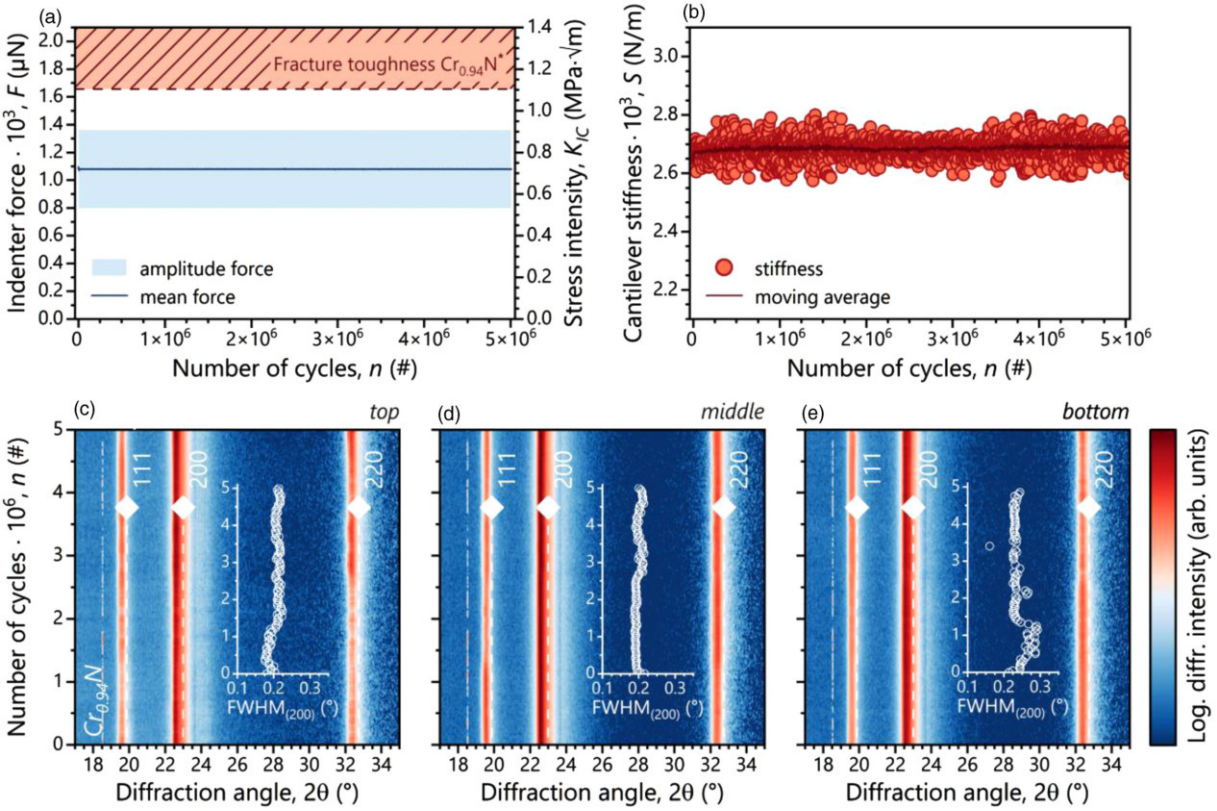

Fig. 11. (a) Representative indenter force (left axis) vs. load cycle evolution recorded during cyclic loading of a microcantilever prepared from a Cr-based thin film (here $Cr_{0.94}N$). The applied stress intensity, including the fracture toughness threshold $K_{IC}{}^*$ determined during pre-testing on identical cantilever samples, are included on the right axis. (b) Corresponding cantilever stiffness - load cycle evolution, including a moving average fit. (c - e) Intensity plots from *in situ* X-ray nanodiffraction experiments depicting the phase evolution of a $Cr_{0.94}N$ microcantilever over 5×10^6 load cycles for the measurement positions defined in Fig. 2d, respectively. The individual diffractographs are derived from azimuthal integration of the recorded Debye-Scherrer ring patterns. All intensity plots contain insets depicting the evolution of the FWHM of the (200)-peak as a function of the number of cycles.

– approximately to a depth of the pre-notch – deviate from this linear behavior, instead an almost constant tensile stress of $\Delta\sigma_{\parallel}(z) \sim$ 0.5-0.6 GPa is observed. In accordance with Ref. [51], this could be explained by the strain relief on the cantilever surface introduced by the pre-notch (note the through-thickness type notch), which locally reduces the tensile stress component imposed by the bending moment. Consequently, this shifts the maximum tensile stress to the tip of the pre-notch. Yet, despite the small X-ray probe diameter of ~250 nm, the local stress concentration occurring close to the pre-notch tip could not be resolved within the accuracy of this method. Nevertheless, the bottom surface of the loaded cantilever obtains a distinct compressive stress region with $\Delta\sigma_{\parallel}(y, 4.75)$ values exceeding -4 GPa (≙ -1.9 GPa after correction) within y = 0 - 1 µm (see Fig. 10b), confirming the stress concentration introduced by the pre-notch.

Knowing the actual stress distribution during the bending experiments, additional fatigue tests were conducted on these large cantilever specimens. Coupled with the cyclic loading, three distinct positions across the cantilever height were probed (see Fig. 2d) using the *in situ* X-ray nanodiffraction setup to resolve the structural and stress state evolution. Fig. 11a exemplarily depicts the results obtained for the $Cr_{0.94}N$ coating, showing the applied indenter force (left axis) as a function of the number of load cycles and an additional reference in terms of the critical stress intensity (right axis). The cantilever was stressed in a range of K_I = 48 - 83 % of $K_{IC}{}^*$ for a total duration of $n = 5 \times 10^6$ cycles. The recorded response of the cantilever stiffness (see Fig. 11b) was, analogous to the previous observations in Fig. 9c, maintained throughout the experiment at $S \sim$ 2680 N/m. This value is linearly proportional to the stiffness recorded for the smaller cantilever and scales with the sample width. Hence, despite the larger specimen size and consequently an increased probability for pre-existing critical flaws – apart from the pre-notch – no fatigue induced damage was observed. This was additionally confirmed by measuring the apparent fracture toughness of the examined cantilever, where a value of $K_{IC}{}^* = 1.1\ \mathrm{MPa}\sqrt{\mathrm{m}}$ was calculated, matching the previously established reference (see Fig. 11a; note, $K_{IC}{}^*$ serves as a reference within this work, the actual value is however calculated outside the geometrical boundaries given in Ref. [16]).

The associated X-ray intensity plots are summarized in Figs. 11c-e, showing the azimuthally integrated Debye-Scherrer patterns as function of the diffraction angle and number of load cycles. Not surprisingly, correlating the structural evolution with a standardized reference pattern of face-centered cubic CrN [60] illustrates that no change in the apparent crystal structure occurs as consequence of the applied mechanical stress. Although the Cr-N system includes a nitrogen depleted hexagonal Cr_2N phase, fatigue or crack growth induced phase transformation – *i.e.,* transformation toughening – is generally associated with metastable phases stabilized by a stress field, rather than the transformation of a monolithic material entirely (*e.g.,* as extensively studied for zirconia based ceramics [102,103]). In addition, the observed diffraction maxima are consistently shifted towards lower 2θ angles on all cross-sectional positions, which is associated with the minute

Die approbierte gedruckte Originalversion dieser Dissertation ist an der TU Wien Bibliothek verfügbar.
The approved original version of this doctoral thesis is available in print at TU Wien Bibliothek.
TU Bibliothek Your knowledge hub WIEN

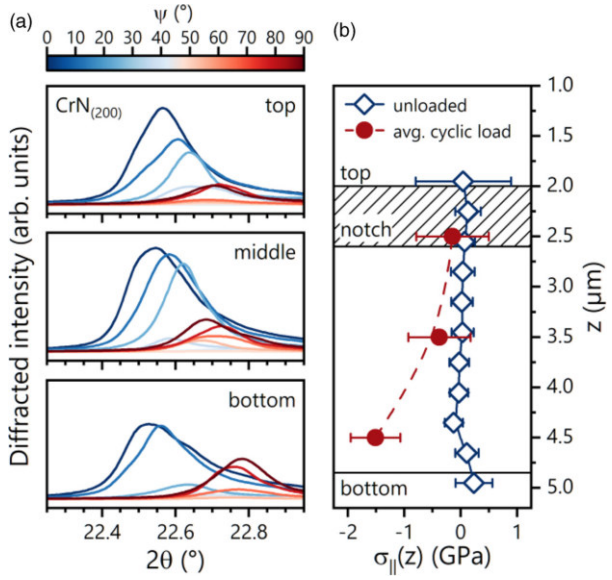

Fig. 12. (a) Diffraction intensities of $Cr_{0.94}N$ for all measurement positions defined in Fig. 2d, acquired during *in situ* nanodiffraction experiments. The data was calculated from the (200)-peak of the Debye-Scherrer ring patterns recorded at $n = 3 \times 10^6$ load cycles as described in Figs. 2e-f. (b) Comparison of the stress distribution over the cantilever cross-section at the pre-notch position (y = 0) between the unloaded (blue diamonds; corrected row-average of the data included in Fig. 10a) and the average loaded state (red circles) during cyclic bending of the microcantilever geometry. Each Debye-Scherrer ring pattern was acquired with an exposure time of 10 s; hence the latter stress state is averaged over 5000 load cycles. All stress data is corrected to meet the equilibrium condition according to Fig. 10a.

chemical differences between the reference structure and the sample in question.

Looking more closely at the shape and intensity of the recorded diffractographs, the full width at half maximum (FWHM) was quantified for the (200)-peak as function of the load cycles (see inserts in Figs. 11c-e). The results display a slightly increasing average value for the FWHM from positions "top" (∼0.20°) to "bottom" (∼0.23°), which is due to incorporating the primary nucleation front at the former substrate-coating interface into the X-ray gauge volume. Additionally, upon assuming stability of the coherently diffracting domains – in contrast to the mechanically induced grain growth observed for *fcc*-structured metallic thin films [104] – the FWHM suggests that the initial stress state is preserved in all measurement positions. Altering the stress distribution, both towards tensile or compressive, would result in a distortion of the Debye-Scherrer ring pattern and a changed peak shape when fully integrating the diffracted intensity in azimuthal direction. Specifically verifying the stress distribution at $n = 3 \times 10^6$ load cycles (see Fig. 12a and b, red circles) assumes similar values as observed for static loading conditions in $\Delta\sigma_{\parallel}(0, z)$ of Figs. 10c and d. An increased compressive stress of ∼ -1.5 GPa is calculated on the cantilever bottom, while the neutral axis and top surface roughly remain in their initial stress-free condition (blue diamonds, determined as cross-sectional average of Fig. 10a). Again, the absence of an increasing tensile stress in the "top" position is associated with the strain relieve introduced by the pre-notch. Furthermore, it is important to mention that the calculated stress values correspond to an averaged load state, since the associated Debye-Scherrer diffraction patterns were recorded over ∼5000 load cycles each.

Finally, during the first 10^6 load cycles, both the FWHM on the cantilever top and bottom show an opposite behavior by noticeably increasing or decreasing from their initial values, respectively, while the center position remains unchanged. Here, one may speculate a running-in phase where microplasticity at local stress concentrations (*i.e.*, defect sites, column boundaries, etc.) allows for a change in the coherently diffracting domains. Nevertheless, the definite origin of this behavior remains questionable, especially considering that no such change can be observed in the cantilever stiffness during the timeframe.

In summary, the coupled *in situ* synchrotron X-ray nanodiffraction and fatigue experiments confirm the limiting aspect of the fracture toughness on the fatigue strength of our nanostructure thin film materials (see Equation 9). Moreover, the recorded in-plane stress state and phase evolution for $Cr_{0.94}N$ underline the purely elastic material response during the cyclic bending experiments despite the load amplitudes closely approaching the critical stress intensity threshold.

4. Conclusion

This work presents a systematic approach towards unraveling the fracture and fatigue properties of PVD deposited thin films through identifying the key aspects dictating their durability under cyclic unidirectional load. A novel *in situ* synchrotron nanodiffraction setup was developed in combination with micro-cantilever bending tests to determine the fracture toughness and fatigue resistance of a model material system comprised of sputter deposited Cr and Cr-based compounds (*i.e.*, CrN, CrB_2, and Cr_2O_3). This material selection revealed valuable insights into the deformation mechanisms available with respect to the prevalent bonding nature and crystal structure. Given the morphological consistency of the examined materials – as confirmed by SEM and TEM investigations – a large divergence in the fracture toughness was observed, with values ranging from as low as 1.6±0.2 up to 4.3±0.3 $MPa\sqrt{m}$ for $Cr_{1.79}O_3$ and $Cr_{1.03}B_2$, respectively. The apparent difference in the fracture resistance is elucidated in the context of linear-elastic fracture theory and additional micro-pillar compression tests, thereby spanning a clear connection between the intrinsic bonding character, prevalent crystal structure, and the accessible elastic-plastic deformation behavior of each material. In fact, room-temperature plastic deformation is found within both Cr and $Cr_{1.03}B_2$, while $Cr_{0.94}N$ and $Cr_{1.79}O_3$ showed brittle fracture along grain boundaries under compressive loading. Discussed from this bonding nature inspired viewpoint, it could further be demonstrated that the apparent fatigue strength of such nanostructured coatings is solely limited by the fracture toughness. Provided the condition $K_I \leq K_{IC}$ holds true during fatigue testing, all materials showed a purely elastic material response, so that cyclic bending tests up to $n = 10^7$ cycles were realized without any noticeable material damage, structural change, or shift in the cross-sectional stress distribution. In addition, these findings are correlated with a detailed stress map of the cantilever pre-crack region under quasi-static loads close to the critical stress intensity. In general, we conclude that improving the intrinsic fracture toughness of nanostructured thin film materials is a pathway to facilitate enhanced fatigue strengths.

Data availability statement

The data that support the findings of this study are available from the corresponding author upon reasonable request.

Declaration of Competing Interest

The authors declare that they have no known competing financial interests or personal relationships that could have appeared to influence the work reported in this paper.

Die approbierte gedruckte Originalversion dieser Dissertation ist an der TU Wien Bibliothek verfügbar.
The approved original version of this doctoral thesis is available in print at TU Wien Bibliothek.
TU Bibliothek Your knowledge hub WIEN

Acknowledgments

The financial support by the Austrian Federal Ministry for Digital and Economic Affairs, the National Foundation for Research, Technology and Development and the Christian Doppler Research Association is gratefully acknowledged (Christian Doppler Laboratory "Surface Engineering of high-performance Components"). We also thank for the financial support of Plansee SE, Plansee Composite Materials GmbH, and Oerlikon Balzers, Oerlikon Surface Solutions AG. The authors highly appreciate the insightful discussions and technical assistance by Prof. D. Kiener and Dr. M. Alfreider at Erich Schmid Institute of Materials Science of the Austrian Academy of Sciences, Leoben, Austria. In addition, we want to thank the X-ray center (XRC) of TU Wien for beam time as well as the electron microscopy center - USTEM TU Wien - for providing the SEM and TEM facilities. The authors acknowledge TU Wien Bibliothek for financial support through its Open Access Funding Programme.

References

[1] P. Cavaliere, Fatigue and Fracture of Nanostructured Materials, Springer International Publishing, Cham, 2021, doi:10.1007/978-3-030-58088-9.
[2] S. Suresh, Fatigue of Materials, Cambridge University Press, 1998, doi:10.1017/CBO9780511806575.
[3] C. Kirchlechner, P.J. Imrich, W. Liegl, J. Pörnbacher, J.-S. Micha, O. Ulrich, C. Motz, On the reversibility of dislocation slip during small scale low cycle fatigue, Acta Mater. 94 (2015) 69–77, doi:10.1016/j.actamat.2015.04.029.
[4] H. Mughrabi, Cyclic slip irreversibilities and the evolution of fatigue damage, Metall. Mater. Trans. B Process Metall. Mater. Process. Sci. 40 (2009) 431–453, doi:10.1007/s11663-009-9240-4.
[5] S. Lavenstein, Y. Gu, D. Madisetti, J.A. El-Awady, The heterogeneity of persistent slip band nucleation and evolution in metals at the micrometer scale, Science (80) (2020) 370, doi:10.1126/science.abb2690.
[6] R.O. Ritchie, Mechanisms of fatigue-crack propagation in ductile and brittle solids, 1999. doi:10.1023/A:1018655917051.
[7] R.O. Ritchie, R.H. Dauskardt, Cyclic fatigue of ceramics. A fracture mechanics approach to subcritical crack growth and life prediction, Nippon Seramikkusu Kyokai Gakujutsu Ronbunshi/Journal Ceram. Soc. Japan 99 (1991) 1047–1062, doi:10.2109/jcersj.99.1047.
[8] G.P. Zhang, C.A. Volkert, R. Schwaiger, P. Wellner, E. Arzt, O. Kraft, Length-scale-controlled fatigue mechanisms in thin copper films, Acta Mater. 54 (2006) 3127–3139, doi:10.1016/j.actamat.2006.03.013.
[9] O. Kraft, P.A. Gruber, R. Mönig, D. Weygand, Plasticity in confined dimensions, Annu. Rev. Mater. Res. 40 (2010) 293–317, doi:10.1146/annurev-matsci-082908-145409.
[10] R. Schwaiger, O. Kraft, Size effects in the fatigue behavior of thin Ag films, Acta Mater. 51 (2003) 195–206, doi:10.1016/S1359-6454(02)00391-9.
[11] X.J. Sun, C.C. Wang, J. Zhang, G. Liu, G.J. Zhang, X.D. Ding, G.P. Zhang, J. Sun, Thickness dependent fatigue life at microcrack nucleation for metal thin films on flexible substrates, J. Phys. D. Appl. Phys. 41 (2008) 195404, doi:10.1088/0022-3727/41/19/195404.
[12] R. Pippan, S. Wurster, D. Kiener, Fracture mechanics of micro samples: fundamental considerations, Mater. Des. 159 (2018) 252–267, doi:10.1016/j.matdes.2018.09.004.
[13] G. Dehm, C. Motz, C. Scheu, H. Clemens, P.H. Mayrhofer, C. Mitterer, Mechanical size-effects in miniaturized and bulk materials, Adv. Eng. Mater. 8 (2006) 1033–1045, doi:10.1002/adem.200600153.
[14] M.D. Uchic, D.M. Dimiduk, J.N. Florando, W.D. Nix, Sample dimensions influence strength and crystal plasticity, Science 305 (80) (2004) 986–989, doi:10.1126/science.1098993.
[15] C.J. Szczepanski, S.K. Jha, P.A. Shade, R. Wheeler, J.M. Larsen, Demonstration of an in situ microscale fatigue testing technique on a titanium alloy, Int. J. Fatigue. 57 (2013) 131–139, doi:10.1016/j.ijfatigue.2012.08.008.
[16] K. Matoy, H. Schönherr, T. Detzel, T. Schöberl, R. Pippan, C. Motz, G. Dehm, A comparative micro-cantilever study of the mechanical behavior of silicon based passivation films, Thin Solid Films 518 (2009) 247–256, doi:10.1016/j.tsf.2009.07.143.
[17] J.P. Best, J. Zechner, J.M. Wheeler, R. Schoeppner, M. Morstein, J. Michler, Small-scale fracture toughness of ceramic thin films: the effects of specimen geometry, ion beam notching and high temperature on chromium nitride toughness evaluation, Philos. Mag. 96 (2016) 3552–3569, doi:10.1080/14786435.2016.1223891.
[18] C. Kainz, M. Pohler, G.C. Gruber, M. Tkadletz, A.S. Ebner, C. Czettl, N. Schalk, Influence of bias voltage on microstructure, mechanical properties and thermal stability of arc evaporated Cr0.74Ta0.26N coatings, Surf. Coatings Technol. 417 (2021) 127212, doi:10.1016/j.surfcoat.2021.127212.
[19] R. Soler, S. Gleich, C. Kirchlechner, C. Scheu, J.M. Schneider, G. Dehm, Fracture toughness of Mo2BC thin films: intrinsic toughness versus system toughening, Mater. Des. 154 (2018) 20–27, doi:10.1016/J.MATDES.2018.05.015.
[20] R. Hahn, N. Koutná, T. Wójcik, A. Davydok, S. Kolozsvári, C. Krywka, D. Holec, M. Bartosik, P.H. Mayrhofer, Mechanistic study of superlattice-enabled high toughness and hardness in MoN/TaN coatings, Commun. Mater. 1 (2020) 62, doi:10.1038/s43246-020-00064-4.
[21] I. El Azhari, J. Garcia, M. Zamanzade, F. Soldera, C. Pauly, L. Llanes, F. Mücklich, Investigations on micro-mechanical properties of polycrystalline Ti(C,N) and Zr(C,N) coatings, Acta Mater 149 (2018) 364–376, doi:10.1016/j.actamat.2018.02.053.
[22] T. Csanádi, J. Wehrs, S. Grasso, M. Reece, J. Michler, J. Dusza, Anomalous slip of ZrB 2 ceramic grains during in-situ micropillar compression up to 500 °C, Int. J. Refract. Met. Hard Mater. 80 (2019) 270–276, doi:10.1016/j.ijrmhm.2019.01.021.
[23] T. Glechner, R. Hahn, T. Wojcik, D. Holec, S. Kolozsvári, H. Zaid, S. Kodambaka, P.H. Mayrhofer, H. Riedl, Assessment of ductile character in superhard Ta-C-N thin films, Acta Mater 179 (2019) 17–25, doi:10.1016/j.actamat.2019.08.015.
[24] X.-M. Luo, B. Zhang, G.-P. Zhang, Fatigue of metals at nanoscale: Metal thin films and conductive interconnects for flexible device application, Nano Mater. Sci. 1 (2019) 198–207, doi:10.1016/j.nanoms.2019.02.003.
[25] S. Wurster, S. Bigl, M.J. Cordill, D. Kiener, Accelerated thermo-mechanical fatigue of copper metallizations studied by pulsed laser heating, Microelectron. Eng. 167 (2017) 110–118, doi:10.1016/j.mee.2016.08.004.
[26] W. Heinz, W. Robl, G. Dehm, Influence of initial microstructure on thermomechanical fatigue behavior of Cu films on substrates, Microelectron. Eng. 137 (2015) 5–10, doi:10.1016/j.mee.2014.10.024.
[27] T. Walter, G. Khatibi, M. Nelhiebel, W. Heinz, W. Robl, High cycle fatigue properties of Cu films, Microelectron. Eng. 137 (2015) 64–69, doi:10.1016/j.mee.2014.12.003.
[28] J.Y. Zhang, X. Zhang, G. Liu, R.H. Wang, G.J. Zhang, J. Sun, Length scale dependent yield strength and fatigue behavior of nanocrystalline Cu thin films, Mater. Sci. Eng. A. 528 (2011) 7774–7780, doi:10.1016/j.msea.2011.06.083.
[29] A.G. Evans, J.W. Hutchinson, The thermomechanical integrity of thin films and multilayers, Acta Metall. Mater. 43 (1995) 2507–2530, doi:10.1016/0956-7151(94)00444-M.
[30] O. Kraft, R. Schwaiger, P. Wellner, Fatigue in thin films: lifetime and damage formation, Mater. Sci. Eng. A. 319–321 (2001) 919–923, doi:10.1016/S0921-5093(01)00990-X.
[31] C.M. Lee, J.P. Chu, W.Z. Chang, J.W. Lee, J.S.C. Jang, P.K. Liaw, Fatigue property improvements of Ti–6Al–4V by thin film coatings of metallic glass and TiN: a comparison study, Thin Solid Films 561 (2014) 33–37, doi:10.1016/j.tsf.2013.08.027.
[32] G. Cassar, J.C. Avelar-Batista Wilson, S. Banfield, J. Housden, M. Fenech, A. Matthews, A. Leyland, Evaluating the effects of plasma diffusion processing and duplex diffusion/PVD-coating on the fatigue performance of Ti-6Al-4V alloy, Int. J. Fatigue. 33 (2011) 1313–1323, doi:10.1016/j.ijfatigue.2011.04.004.
[33] M.Y.P. Costa, M.L.R. Venditti, M.O.H. Cioffi, H.J.C. Voorwald, V.A. Guimarães, R. Ruas, Fatigue behavior of PVD coated Ti-6Al-4V alloy, Int. J. Fatigue. 33 (2011) 759–765, doi:10.1016/j.ijfatigue.2010.11.007.
[34] C. Kirchlechner, K.J. Martinschitz, R. Daniel, M. Klaus, C. Genzel, C. Mitterer, J. Keckes, Residual stresses and thermal fatigue in CrN hard coatings characterized by high-temperature synchrotron X-ray diffraction, Thin Solid Films 518 (2010) 2090–2096, doi:10.1016/j.tsf.2009.08.011.
[35] Y. Bai, Y. Xi, K. Gao, H. Yang, X. Pang, X. Yang, A.A. Volinsky, Brittle coating effects on fatigue cracks behavior in Ti alloys, Int. J. Fatigue. 125 (2019) 432–439, doi:10.1016/j.ijfatigue.2019.04.017.
[36] Y. Bai, T. Guo, J. Wang, J. Gao, K. Gao, X. Pang, Stress-sensitive fatigue crack initiation mechanisms of coated titanium alloy, Acta Mater 217 (2021) 117179, doi:10.1016/j.actamat.2021.117179.
[37] T. Guo, Y. Chen, R. Cao, X. Pang, J. He, L. Qiao, Cleavage cracking of ductile-metal substrates induced by brittle coating fracture, Acta Mater. 152 (2018) 77–85, doi:10.1016/j.actamat.2018.04.017.
[38] N.P. Sivagnanam Chandra, Y. Otsuka, Y. Mutoh, K. Yamamoto, Effect of coating thickness on fatigue behavior of TiAlN coated Ti-alloys, Int. J. Fatigue. 140 (2020) 105767, doi:10.1016/j.ijfatigue.2020.105767.
[39] N.G.P. Sivagnanam Chandra, Y. Otsuka, Y. Mutoh, K. Yamamoto, Fatigue strength and mechanism of Ti6242S titanium alloy with TiAlN coating deposited under various bias voltages, Int. J. Fatigue. 131 (2020) 105338, doi:10.1016/j.ijfatigue.2019.105338.
[40] D. Kiener, C. Motz, W. Grosinger, D. Weygand, R. Pippan, Cyclic response of copper single crystal micro-beams, Scr. Mater. 63 (2010) 500–503, doi:10.1016/j.scriptamat.2010.05.014.
[41] A. Wimmer, W. Heinz, T. Detzel, W. Robl, M. Nellessen, C. Kirchlechner, G. Dehm, Cyclic bending experiments on free-standing Cu micron lines observed by electron backscatter diffraction, Acta Mater. 83 (2015) 460–469, doi:10.1016/j.actamat.2014.10.012.
[42] S. Lavenstein, B. Crawford, G.-D. Sim, P.A. Shade, C. Woodward, J.A. El-Awady, High frequency in situ fatigue response of Ni-base superalloy René-N5 microcrystals, Acta Mater. 144 (2018) 154–163, doi:10.1016/j.actamat.2017.10.049.
[43] M. Alfreider, D. Kozic, O. Kolednik, D. Kiener, In-situ elastic-plastic fracture mechanics on the microscale by means of continuous dynamical testing, Mater. Des. 148 (2018) 177–187, doi:10.1016/j.matdes.2018.03.051.
[44] D.R. Lide, CRC Handbook of Chemistry and Physics, 84th Ed., CRC Press, 2003.
[45] K. Frisk, A thermodynamic evaluation of the Cr-N, Fe-N, Mo-N and Cr-Mo-N systems, Calphad 15 (1991) 79–106, doi:10.1016/0364-5916(91)90028-I.
[46] P.K. Liao, K.E. Spear, The B-Cr (boron-chromium) system, Bull. Alloy Phase Diagrams 7 (1986) 232–237, doi:10.1007/BF02868996.
[47] L. Kaufman, H. Nesor, Calculation of quasibinary and quasiternary oxide systems - I, Calphad 2 (1978) 35–53, doi:10.1016/0364-5916(78)90004-4.

Die approbierte gedruckte Originalversion dieser Dissertation ist an der TU Wien Bibliothek verfügbar.
The approved original version of this doctoral thesis is available in print at TU Wien Bibliothek.
TU Bibliothek Your knowledge hub WIEN

[48] G.M. Pharr, An improved technique for determining hardness and elastic modulus using load and displacement sensing indentation experiments, J. Mater. Res. 7 (1992) 1564–1583, doi:10.1557/JMR.1992.1564.
[49] A.C. Fischer-Cripps, Critical review of analysis and interpretation of nanoindentation test data, Surf. Coatings Technol. 200 (2006) 4153–4165, doi:10.1016/j.surfcoat.2005.03.018.
[50] D. Di Maio, S.G. Roberts, Measuring fracture toughness of coatings using focused-ion-beam-machined microbeams, J. Mater. Res. 20 (2005) 299–302, doi:10.1557/JMR.2005.0048.
[51] S. Brinckmann, K. Matoy, C. Kirchlechner, G. Dehm, On the influence of microcantilever pre-crack geometries on the apparent fracture toughness of brittle materials, Acta Mater 136 (2017) 281–287, doi:10.1016/j.actamat.2017.07.014.
[52] J.M. Wheeler, J. Michler, Elevated temperature, nano-mechanical testing in situ in the scanning electron microscope, Rev. Sci. Instrum. 84 (2013) 045103, doi:10.1063/1.4795829.
[53] I.N. Sneddon, The relation between load and penetration in the axisymmetric boussinesq problem for a punch of arbitrary profile, Int. J. Eng. Sci. 3 (1965) 47–57, doi:10.1016/0020-7225(65)90019-4.
[54] J. Keckes, M. Bartosik, R. Daniel, C. Mitterer, G. Maier, W. Ecker, J. Vila-Comamala, C. David, S. Schoeder, M Burghammer, X-ray nanodiffraction reveals strain and microstructure evolution in nanocrystalline thin films, Scr. Mater. 67 (2012) 748–751, doi:10.1016/j.scriptamat.2012.07.034.
[55] M. Birkholz, Thin Film Analysis by X-Ray Scattering, Wiley, 2006, doi:10.1002/3527607595.
[56] J. Almer, U. Lienert, R.L. Peng, C. Schlauer, M. Odén, Strain and texture analysis of coatings using high-energy x-rays, J. Appl. Phys. 94 (2003) 697–702, doi:10.1063/1.1582351.
[57] G. Benecke, W. Wagermaier, C. Li, M. Schwartzkopf, G. Flucke, R. Hoerth, I. Zizak, M. Burghammer, E. Metwalli, P. Müller-Buschbaum, M. Trebbin, S. Förster, O. Paris, S.V. Roth, P. Fratzl, A customizable software for fast reduction and analysis of large X-ray scattering data sets: applications of the new DPDAK package to small-angle X-ray scattering and grazing-incidence small-angle X-ray scattering, J. Appl. Crystallogr. 47 (2014) 1797–1803, doi:10.1107/S1600576714019773.
[58] L. Zauner, A Matlab Toolbox for Synchrotron Stress Analysis, 2022, doi:10.5281/ZENODO.6248169.
[59] ICDD, Powder Diffraction File - cubic Cr - 00-006-0694, Powder Diffr. File - Cubic Cr - 00-006-0694. (1970).
[60] ICDD, Powder Diffraction File - cubic CrN - 01-077-0047, Powder Diffr. (2015) File - Cubic CrN - 01-077-0047.
[61] ICDD, Powder Diffraction File - hexagonal CrB2 - 04-004-1734, Powder Diffr. (2011) File - HexagCrB2 - 04-004-1734.
[62] ICDD, Powder Diffraction File - rhombohedral Cr2O3 - 00-006-0504, Powder Diffr. (1970) File - Rhombohedral Cr2O3 - 00-006-0504.
[63] ICDD, Powder Diffraction File - cubic Si - 00-027-1402, Powder Diffr. (2017) File - Cubic Si - 00-027-1402.
[64] A. Anders, A structure zone diagram including plasma-based deposition and ion etching, Thin Solid Films 518 (2010) 4087–4090, doi:10.1016/j.tsf.2009.10.145.
[65] S. Zare Chavoshi, P.S. Branicio, Q. An, Transition between Hall-Petch and inverse Hall-Petch behavior in nanocrystalline silicon carbide, Phys. Rev. Mater. 5 (2021) 073606, doi:10.1103/PhysRevMaterials.5.073606.
[66] M. Bartosik, R. Hahn, Z.L. Zhang, I. Ivanov, M. Arndt, P. Polcik, P.H. Mayrhofer, Fracture toughness of Ti-Si-N thin films, Int. J. Refract. Met. Hard Mater. 72 (2018) 78–82, doi:10.1016/j.ijrmhm.2017.12.015.
[67] F. Konstantiniuk, M. Tkadletz, C. Kainz, C. Czettl, N. Schalk, Mechanical properties of single and polycrystalline α-Al2O3 coatings grown by chemical vapor deposition, Surf. Coatings Technol. 410 (2021) 126959, doi:10.1016/j.surfcoat.2021.126959.
[68] R.D. Bedse, J.K. Sonber, K. Sairam, T.S.R.C. Murthy, R.C. Hubli, Processing and characterization of CrB2-based novel composites, High Temp. Mater. Process. 34 (2015) 683–687, doi:10.1515/HTMP-2014-0084/MACHINEREADABLECITATION/RIS.
[69] R. Wadsack, R. Pippan, B. Schedler, Chromium - a material for fusion technology, Fusion Eng. Des. 58–59 (2001) 743–748, doi:10.1016/S0920-3796(01)00554-3.
[70] A.K. Mishra, H. Gopalan, M. Hans, C. Kirchlechner, J.M. Schneider, G. Dehm, B.N. Jaya, Strategies for damage tolerance enhancement in metal/ceramic thin films: lessons learned from Ti/TiN, Acta Mater 228 (2022), doi:10.1016/j.actamat.2022.117777.
[71] G. Greczynski, J. Lu, O. Tengstrand, I. Petrov, J.E. Greene, L. Hultman, Nitrogen-doped bcc-Cr films: combining ceramic hardness with metallic toughness and conductivity, Scr. Mater. 122 (2016) 40–44, doi:10.1016/j.scriptamat.2016.05.011.
[72] R. Fritz, V. Maier-Kiener, D. Lutz, D. Kiener, Interplay between sample size and grain size: single crystalline vs. ultrafine-grained chromium micropillars, Mater. Sci. Eng. A. 674 (2016) 626–633, doi:10.1016/j.msea.2016.08.015.
[73] ANSYS Inc, Ansys GRANTA Edupack, (2021) Cambridge, UK. www.ansys.com/materials.
[74] K. Persson, Materials Data on Cr (SG: 229) by Materials Project, (2022). https://materialsproject.org/materials/mp-90/(accessed June 29, 2022).
[75] K. Rzepiejewska-Malyska, M. Parlinska-Wojtan, K. Wasmer, K. Hejduk, J. Michler, In-situ SEM indentation studies of the deformation mechanisms in TiN, CrN and TiN/CrN, Micron 40 (2009) 22–27, doi:10.1016/j.micron.2008.02.013.
[76] T. Aizawa, H. Kuwahara, M. Tamura, Fabrication of CrN/Cr2N bulk composites and their mechanical properties, J. Am. Ceram. Soc. 85 (2004) 81–85, doi:10.1111/j.1151-2916.2002.tb00043.x.
[77] K. Persson, Materials Data on CrN (SG:225) by Materials Project, (2014). https://materialsproject.org/materials/mp-2132/(accessed June 29, 2022).
[78] M. Audronis, A. Leyland, P.J. Kelly, A. Matthews, The effect of pulsed magnetron sputtering on the structure and mechanical properties of CrB2 coatings, Surf. Coatings Technol. 201 (2006) 3970–3976, doi:10.1016/j.surfcoat.2006.08.006.
[79] V. Reddy, J.K Sonber, K. Sairam, T.S.R.C Murthy, S. Kumar, G.V.S Nageswara Rao, T Srinivasa Rao, J.K. Chakravartty, Densification and mechanical properties of CrB2+MoSi2 based novel composites, Ceram. Int. 41 (2015) 7611–7617, doi:10.1016/j.ceramint.2015.02.086.
[80] N.L. Okamoto, M. Kusakari, K. Tanaka, H. Inui, S. Otani, Anisotropic elastic constants and thermal expansivities in monocrystal CrB2, TiB2, and ZrB2, Acta Mater. 58 (2010) 76–84, doi:10.1016/j.actamat.2009.08.058.
[81] K. Persson, Materials Data on CrB2 (SG:191) by Materials Project, (2016). https://materialsproject.org/materials/mp-374/(accessed June 29, 2022).
[82] B. Bhushan, G.S.A.M. Theunissen, X. Li, Tribological studies of chromium oxide films for magnetic recording applications, Thin Solid Films 311 (1997) 67–80, doi:10.1016/S0040-6090(97)00453-7.
[83] X. Pang, K. Gao, H. Yang, L. Qiao, Y. Wang, A.A. Volinsky, Interfacial microstructure of chromium oxide coatings, Adv. Eng. Mater. 9 (2007) 594–599, doi:10.1002/adem.200700057.
[84] K. Persson, Materials Data on Cr2O3 (SG:167) by Materials Project, (2014). https://materialsproject.org/materials/mp-19399/(accessed June 29, 2022).
[85] E. Bitzek, J.R. Kermode, P. Gumbsch, Atomistic aspects of fracture, Int. J. Fract. 191 (2015) 13–30, doi:10.1007/s10704-015-9988-2.
[86] Milton Ohring, Materials Science of Thin Films, Elsevier, 2002, doi:10.1016/B978-0-12-524975-1.X5000-9.
[87] M. Bielawski, K. Chen, Computational evaluation of adhesion and mechanical properties of nanolayered erosion-resistant coatings for gas turbines, J. Eng. Gas Turbines Power. 133 (2011), doi:10.1115/1.4002158/439378.
[88] N. Koutná, A. Brenner, D. Holec, P.H. Mayrhofer, High-throughput first-principles search for ceramic superlattices with improved ductility and fracture resistance, Acta Mater 206 (2021), doi:10.1016/j.actamat.2020.116615.
[89] Q. Kang, G. Wang, Q. Liu, X. Sui, Y. Liu, Y. Chen, S. Luo, Z. Li, Investigation for oxidation mechanism of CrN: a combination of DFT and ab initio molecular dynamics study, J. Alloys Compd. 885 (2021), doi:10.1016/j.jallcom.2021.160940.
[90] D.G. Sangiovanni, Descriptors for mechanical strength and slip-induced crack-blunting in refractory ceramics, Arxiv 61 (2019) 1926, doi:10.48550/arxiv.2203.00622.
[91] R. Daniel, M. Meindlhumer, W. Baumegger, J. Zalesak, B. Sartory, M. Burghammer, C. Mitterer, J. Keckes, Grain boundary design of thin films: using tilted brittle interfaces for multiple crack deflection toughening, Acta Mater. 122 (2017) 130–137, doi:10.1016/j.actamat.2016.09.027.
[92] H. Kindlund, D.G. Sangiovanni, I. Petrov, J.E. Greene, L. Hultman, A review of the intrinsic ductility and toughness of hard transition-metal nitride alloy thin films, Thin Solid Films 688 (2019) 137479, doi:10.1016/j.tsf.2019.137479.
[93] K. Balasubramanian, S.V. Khare, D. Gall, Valence electron concentration as an indicator for mechanical properties in rocksalt structure nitrides, carbides and carbonitrides, Acta Mater 152 (2018) 175–185, doi:10.1016/j.actamat.2018.04.033.
[94] V.L. Deringer, A.L. Tchougréeff, R. Dronskowski, Crystal orbital Hamilton population (COHP) analysis as projected from plane-wave basis sets, J. Phys. Chem. A. 115 (2011) 5461–5466, doi:10.1021/jp202489s.
[95] C. Fuger, R. Hahn, L. Zauner, T. Wojcik, M. Weiss, A. Limbeck, O. Hunold, P. Polcik, H. Riedl, Anisotropic super-hardness of hexagonal WB2±z thin films, Mater. Res. Lett. 10 (2022) 70–77, doi:10.1080/21663831.2021.2021308.
[96] F.F. Csikor, C. Motz, D. Weygand, M. Zaiser, S. Zapperi, Dislocation avalanches, strain bursts, and the problem of plastic forming at the micrometer scale, Science 318 (80) (2007) 251–254, doi:10.1126/science.1143719.
[97] S.-Y. Liu, I.-W. Chen, Fatigue of Yttria-Stabilized Zirconia: II, crack propagation, fatigue striations, and short-crack behavior, J. Am. Ceram. Soc. 74 (1991) 1206–1216, doi:10.1111/j.1151-2916.1991.tb04089.x.
[98] R.O. Ritchie, J.O. Peters, Small Fatigue Cracks: Mechanics, Mechanisms and Engineering Applications, Mater. Trans. 42 (2001) 58–67, doi:10.2320/matertrans.42.58.
[99] A.G. Evans, Fatigue in ceramics, Int. J. Fract. 16 (1980) 485–498, doi:10.1007/BF02265214.
[100] C.J. Gilbert, R.O. Ritchie, Mechanisms of cyclic fatigue-crack propagation in a fine-grained alumina ceramic: The role of crack closure, Fatigue Fract. Eng. Mater. Struct. 20 (1997) 1453–1466, doi:10.1111/j.1460-2695.1997.tb01502.x.
[101] C.J. Gilbert, R.H. Dauskardt, R.O. Ritchie, Microstructural mechanisms of cyclic fatigue-crack propagation in grain-bridging ceramics, Ceram. Int. 23 (1997) 413–418, doi:10.1016/S0272-8842(96)00048-X.
[102] A.G. Evans, Perspective on the development of high-toughness ceramics, J. Am. Ceram. Soc. 73 (1990) 187–206, doi:10.1111/j.1151-2916.1990.tb06493.x.
[103] R.H. Dauskardt, W. Yu, R.O. Ritchie, Fatigue crack propagation in transformation-toughened zirconia ceramic, J. Am. Ceram. Soc. 70 (1987) C-248-C-252, doi:10.1111/J.1151-2916.1987.TB04889.X.
[104] X.M. Luo, X.F. Zhu, G.P. Zhang, Nanotwin-assisted grain growth in nanocrystalline gold films under cyclic loading, Nat. Commun. 5 (2014) 1–8, doi:10.1038/ncomms4021.

TU Bibliothek Your knowledge hub WIEN
Die approbierte gedruckte Originalversion dieser Dissertation ist an der TU Wien Bibliothek verfügbar.
The approved original version of this doctoral thesis is available in print at TU Wien Bibliothek.

Publication II

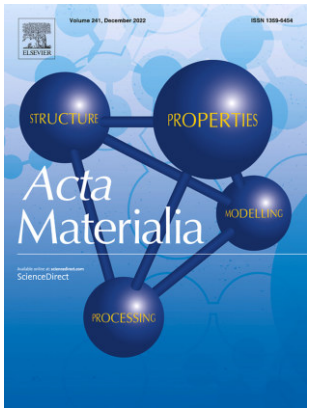

Role of Si segregation in the structural, mechanical, and compositional evolution of high-temperature oxidation resistant Cr-Si-$B_{2\pm z}$ thin films

L. Zauner, A. Steiner, T. Glechner, A. Bahr, B. Ott, R. Hahn, T. Wojcik, O. Hunold, J. Ramm, S. Kolozsvári, P. Polcik, P. Felfer, and H. Riedl

under review at *Acta Materialia* since 30.09.2022.

Die approbierte gedruckte Originalversion dieser Dissertation ist an der TU Wien Bibliothek verfügbar.
The approved original version of this doctoral thesis is available in print at TU Wien Bibliothek.

Role of Si segregation in the structural, mechanical, and compositional evolution of high-temperature oxidation resistant Cr-Si-$B_{2\pm z}$ thin films

L. Zauner,[1,*] A. Steiner,[1] T. Glechner,[1] A. Bahr,[1] B. Ott,[2] R. Hahn,[1] T. Wojcik,[1,3] O. Hunold,[4] J. Ramm,[4] S. Kolozsvári,[5] P. Polcik,[5] P. Felfer,[2] and H. Riedl[1,3]

[1] *Christian Doppler Laboratory for Surface Engineering of high-performance Components, Austria*
[2] *Department of Materials Science, Friedrich-Alexander-Universität Erlangen-Nürnberg, Germany*
[3] *Institute of Materials Science and Technology, Austria*
[4] *Oerlikon Balzers, Oerlikon Surface Solutions AG, Liechtenstein*
[5] *Plansee Composite Materials GmbH, Germany*

(Dated: November 3, 2022)

Alloying concepts targeting improved high-temperature oxidation resistance in protective coatings are valued in their simultaneous influence on phase stability and mechanical properties. Within this study, we investigate the influence of Si-alloying up to 17 at.% on the structural, mechanical, and oxidation properties of magnetron sputtered $CrB_{2\pm z}$-based thin films. Density-functional theory calculations combined with atom probe tomography reveal the preferred Si occupation of Cr-lattice sites and an effective solubility limit between 3 to 4 at.% in AlB_2-structured solid solutions. The addition of Si results in refinement of the columnar morphology, accompanied by enhanced segregation of excess Si along grain boundaries. The microstructural separation leads to a decrease in both film hardness and Young's modulus from H ∼24 to 17 GPa and E ∼300 to 240 GPa, respectively, dominated by the inferior mechanical properties of the intergranular Si-rich regions. Dynamic thermogravimetry up to 1400 °C proves a significant increase in oxidation onset temperature from 600 to 1100 °C above a specific Si content of 8 at.%. *In-situ* X-ray diffraction correlates the protective mechanism with thermally activated precipitation of Si from the Cr-Si-$B_{2\pm z}$ solid solution at 600 °C, enabling the formation of a stable, nanometer-sized SiO_2-based scale. Moreover, high-resolution TEM analysis reveals the scale architecture after oxidation at 1400 °C – consisting only of ∼20 nm amorphous SiO_2 beneath ∼200 nm of nanocrystalline Cr_2O_3. In summary, the study underpins the promising capabilities of Cr-Si-$B_{2\pm z}$ coatings applied in high-temperature oxidative environments and provides detailed guidelines connecting the chemical composition to the resulting thin film properties.

Keywords: Chromium; Borides; PVD; Thin films; Si alloying; Oxidation resistance; DFT; APT;

I. INTRODUCTION

Transition metal diboride (TMB_2) thin films are promising candidates to replace state-of-the-art functional and protective coating materials in a wide range of applications [1–8]. TMB_2s typically feature a high melting temperature, excellent thermal stability, as well as high hardness and strength, thus providing a strong incentive for ultra-high temperature applications [9–13]. However, this outstanding property spectrum is usually confined to inert atmospheres due to the consecutive/competitive formation of both, TM- and B-based oxide scales, both usually incapable of forming a fully protective layer at temperatures beyond 600-700 °C [14–18]. More drastically, above ∼1100 °C linear mass gain kinetics are regularly observed, which coincides with the evaporation of the glassy-like boria (B_2O_3) embedded within the non-protective, porous metal oxide [18, 19].

Different alloying concepts have been studied and implemented successfully to address the poor oxidation resistance of TMB_2 bulk and thin film materials. Adding Si-containing compounds such as SiC, $MoSi_2$, Si_3N_4, or Ta_5Si_3 is the most commonly used method for bulk diboride materials and improves the oxidation resistance by forming a stable, amorphous (boro-)silicate surface layer [19–21]. For instance, Fahrenholtz *et al.* demonstrated that adding SiC to ZrB_2 and HfB_2 permits drastically decreased oxidation rates up to 1600 °C [19].

Regarding TMB_2-based thin film materials, several ternary alloying routes, *e.g.*, the addition of Al(B_2), TaB_2, or CrB_2, have been explored to improve the oxidation resistance [14–16, 22, 23]. Bakhit *et al.* [15] demonstrated that Al alloying into TiB_2-based thin films significantly retards the oxide scale growth at temperatures up to 800 °C based on the formation of a dense Al-oxide surface layer. Moreover, Kashani *et al.* [17] showed that the Ti-Al-$B_{2\pm z}$ system even outperforms the corresponding nitride system at 700 °C, especially for stoichiometric compositions close to B/TM ratios of 2. Indeed, this necessity for tailoring the B/TM-ratio within $TiB_{2\pm z}$ thin films to optimize oxidation properties is highlighted in several works and rationalized by the fast-track oxidation pathway created through excess B-rich phases preferentially located at column and grain boundaries [24–26]. However, this effect appears specific to the material system and/or annealing treatment conditions, since a stable, protective boria surface layer was observed for $HfB_{2.3}$ thin films up to 900 °C [27].

* lukas.zauner@tuwien.ac.at

Die approbierte gedruckte Originalversion dieser Dissertation ist an der TU Wien Bibliothek verfügbar.
The approved original version of this doctoral thesis is available in print at TU Wien Bibliothek.

Publication II

A seemingly universal alloying route for improved oxidation resistance was recently published by Glechner *et al.* [28, 29], showing that co-sputtering of pure Si to various TMB_2 (TM = Ti, Cr, Hf, Ta, W) drastically improves the oxidation resistance in all materials, with the onset of oxidation elevated to 1200 °C specifically for Cr-Si-B_2 and Hf-Si-B_2. Thereby, the protective mechanism relies on the formation of a stable Si-rich oxide scale above the formed TM-Si-B_2 solid solution.

Inevitably, the ensemble of available tools to improve the oxidation resistance within TMB_2 thin films influences the property spectrum of the initial binary alloy. While strategies involving ternary TM_1-TM_2-$B_{2\pm z}$ thin films proved successful only below 800 °C, their mechanical properties, including hardness and fracture toughness, can often be preserved or even improved over the corresponding binary constituents [13–15]. Contrary, Si-based protective mechanisms can result in superior high-temperature performance of TM-Si-B_2 thin films, however, typically at the expense of reduced mechanical properties at higher Si contents [28, 30]. Consequently, finding the optimum alloying content to achieve the desired oxidation resistance while maintaining good mechanical properties is a vital prerequisite for an industrial application of the entire TM-Si-B_2 material family.

Therefore, within this work we systematically study the influence of Si-alloying on the structural evolution, phase stability, as well as the mechanical and oxidation properties of magnetron sputtered Cr-Si-$B_{2\pm z}$ thin films. This novel high-temperature ceramic is modelled by density functional theory calculations to reveal the energetically preferred lattice occupation of the alloying atom within various AlB_2-structured compositions. Furthermore, limitations in the accessible alloying range to yield solid solutions are discussed in conjunction with detailed atom probe tomography, thereby spanning a clear connection to the observed thin film growth and mechanical properties. The mechanism leading to the drastically increased oxidation resistance is revisited through dynamic oxidation, *in-situ* X-ray diffraction, and transmission electron microscopy, thus providing an in-depth correlation to the thin film properties towards finding an optimum Si alloying composition.

II. EXPERIMENTAL

Cr-Si-$B_{2\pm z}$ thin films were synthesized from a 3-inch CrB_2 target (Plansee Composite Materials GmbH, 99.3% purity) in a pure Ar atmosphere (99.999% purity) using direct current magnetron sputtering in an in-house developed deposition system (base pressure below 1.0×10^{-6} mbar). The Si content was adjusted by placing 0, 2, 4, 6, 8, 12, or 16 Si platelets ($3.5\times3.5\times0.38$ mm^3) on the target racetrack. The rotating substrate holder (0.25 Hz) was positioned at a target-to-substrate distance of 90 mm. All thin films were grown on Si ((100)-oriented, $20\times7\times0.38$ mm^3), single crystalline Al_2O_3 ($(1\bar{1}02)$-oriented, $10\times10\times0.53$ mm^3), and poly-crystalline Al_2O_3 ($20\times7\times0.38$ mm^3) substrates, which were ultrasonically pre-cleaned in acetone and isopropanol, respectively. Following a heating sequence to a substrate temperature of 550 °C, an Ar-ion etching step was performed at a total pressure of 50 μbar and an applied substrate bias potential of -800 V for 10 min. The target and Si alloying platelets were sputter-cleaned for 3 min prior to all depositions to reduce oxygen contamination. The thin films were then grown at a total Ar pressure of 0.7 Pa, a target current of 0.4 A (corresponds to a power density of ~5 W/cm^2), and a bias potential of -40 V. The deposition time was adjusted to yield a constant coating thickness of ~3 μm.

The overall chemistry of the Cr-Si-$B_{2\pm z}$ coatings was obtained using liquid inductively coupled plasma-optical emission spectroscopy (ICP-OES). A detailed explanation of this methodology is given in Ref. [28]. Structural analysis was performed by X-ray diffraction on a PANalytical XPert Pro MPD equipped with a Cu-Kα radiation source (wave-length λ=1.54 Å, operated at 45 kV and 40 mA) in Bragg-Brentano geometry. The cross-sectional growth morphology was further investigated by scanning-electron microscopy (ZEISS Sigma 500VP, operated at 5 kV) on coated Si substrates.

The hardness and elastic modulus of all coatings was studied using instrumented nanoindentation (ultra-micro indentation system, UMIS) with a minimum of 30 load-displacement curves evaluated according to Ref. [31] for each coating. Increasing indentation loads ranging from 5 to 22 mN (steps of 0.5 mN), with additional measurements up to 45 mN to probe for any substrate influence, were applied. Moreover, the obtained E values were fitted over the indentation depth using a power law function and extrapolated to the sample surface to receive the film-only modulus [32]. Macro-stresses in the coatings were additionally analyzed through curvature measurements using optical profilometry (PS50, Nanovea) and the modified Stoney equation [33, 34]. All mechanical properties were determined on coated sapphire substrates.

The oxidation behavior of the Cr-Si-$B_{2\pm z}$ thin films was determined from thermogravimetric analysis (TGA, Netzsch STA 449 F1, equipped with a Rhodium furnace) performed on coated poly-crystalline Al_2O_3 substrates. The substrates were weighed before and after deposition to determine the coating-only mass. This value serves as a reference during dynamic oxidation experiments up to 1400 °C (heating rate of 10 °C/min) in a synthetic air environment (50 ml/min flow rate). Any oxidation-related mass change was recorded at a resolution of 0.1 μg. Pretests on uncoated Al_2O_3 substrates additionally proved their inertness during the oxidation treatment [28].

Additional oxidation experiments combined with *in-situ* X-ray diffraction analysis were carried out on a PANalytical XPert Pro MPD (Cu-Kα radiation source, wave-length λ=1.54 Å, operated at 45 kV and 40 mA) in Bragg-Brentano geometry using an Anton Paar high-temperature furnace chamber (HTK 1200N). Measure-

Die approbierte gedruckte Originalversion dieser Dissertation ist an der TU Wien Bibliothek verfügbar.
The approved original version of this doctoral thesis is available in print at TU Wien Bibliothek.
TU Bibliothek Your knowledge hub WIEN

ments were taken in a lab-air environment (0.3 l/min flow rate) at room-temperature and from 400 to 1200 °C in 50 °C steps. The sample was heated at a rate of 50 °C/min between the individual temperature steps, with each diffraction measurement taking ∼21 min.

Furthermore, detailed microstructural and chemical analysis on selected oxidized samples was performed using transmission electron microscopy (TEM, FEI TECNAI F20, operated at 200 kV). Bright-field (BF) and high-angle annular dark field (HAADF) imaging are utilized to gain information on the microstructure and oxide scale growth. In addition, energy dispersive X-ray spectroscopy (EDX) performed in scanning TEM (STEM) revealed the chemical composition of the entire coating cross-section as well as the oxide layer.

Density functional theory (DFT) coded VASP [35, 36] calculations (projector augmented waves method within the generalized gradient approximation [37]) were performed to study the preferred atomic configuration for silicon alloying atoms within various AlB_2-structured Cr-Si-B_2 compositions. Moreover, the influence of increasing Si content as well as the impact of various vacancy configurations on the phase stability were investigated. The influence of vacancies was studied up to a content of 2 Si atoms within the supercell (corresponds to ∼4 at.%), with 2 vacancies introduced either on the Cr-sublattice, the B-sublattice, or as a Schottky defect. All 2×2×4 supercell structures (16 metal and 32 boron atoms) were generated using the special quasi-random structure (SQS) approach [38]. Values for the formation energy were only extracted from fully converged supercells. A plane wave cut-off energy of 600 eV and an automated k-point mesh (length = 60) were chosen to provide a total energy accuracy of about 10^{-3} eV/at.

Finally, atom probe tomography (APT) analysis was performed on an exemplary coating in the as-deposited state to reveal the initial elemental distribution. Sample preparation involved milling of an initial coating pillar and sharpening to a tip using a focused ion beam microscope ThermoFisher Scios 2 DualBeam operated at 30 kV and stepwise decreasing milling currents. Final tip sharpening was performed at 50 pA, with a subsequent clean-up step at 5 kV and 28 pA to minimize possible Ga^+ ion-induced damage. Subsequent APT analysis was carried out on a CAMECA LEAP 4000X HR in pulsed laser mode with a set pulse energy of 50 pJ. The system uses a 355 nm UV laser equipped with a reflection lens, resulting in a detection efficiency of ∼37%. The sample was cooled to a constant temperature of 44 K. Experiments were performed with a target evaporation rate of 1% and pulse repetition rate of 200 kHz. Data analysis was conducted using an open-source Matlab Toolbox for APT data evaluation [39].

III. RESULTS & DISCUSSION

A. Computational Phase Formation & Stability Boundaries

A regular requirement for alloying strategies to successfully improve the oxidation resistance of a coating material involves unaltered phase stability for the host structure to maintain a distinct property profile. This necessity is demonstrated by the well-studied $Ti_{1-x}Al_xN$ system, where the oxidation resistance of rock-salt structured TiN scales with the AlN alloying fraction [40]. However, upon exceeding the Al solubility threshold on the metal sublattice ($x \sim 67\%$ for DCMS deposited thin films), precipitation of the thermodynamically favored wurtzite-structured $Al_{1-x}Ti_xN$ phase occurs, thus deteriorating both the thermal stability and mechanical properties. Analogously, to probe the effect of an increasing Si alloying content on the phase stability of prototypical Cr-Si-B_2 thin films from a theoretical point of view, Figure 1a presents ab initio calculated formation energies for various AlB_2 structured compositions. This evaluation allows to assess the influence of the addition of Si on the phase stability but also provides information on the energetically preferred lattice occupation within the unit cell and hence a guideline for the Si solubility limit.

The model assumes that up to 8 Si atoms are either placed interstitially or substitutionally within the AlB_2-structured Cr-Si-B_2. Over the entire compositional range, DFT calculations associate the formation of all possible alloying configurations with an increasing E_f compared to the binary CrB_2 composition. This implies an overall reduced stability of the hexagonal structure with increasing Si content. In more detail, all structures where Si is placed interstitially either within B- or Cr-planes show the most substantial increase in E_f, already leading to positive formation energies upon alloying 2 Si atoms (equals ∼4 at.%). Hence, these structures are energetically unstable, and all substitutional configurations are significantly more favored.

The structures where Si is placed in substitution for B/ Cr/ or equally on both sublattices exhibit very similar formation energies in this low alloying regime and thus can co-exist without any preferred atomic position of Si. However, upon increasing the alloying content beyond 3 atoms (equals values ≥6 at.%), structures with Si substituting solely B atoms and later also upon replacing both B and Cr equally become unstable and undergo a phase transformation (*i.e.*, converge into a different structure type) – see red and grey crosses in Figure 1a. Only calculations where Si replaces Cr exclusively within the supercell yield negative formation energies up to 4 Si atoms (equals ∼8 at.%), while maintaining the hexagonal configuration. In fact, compositions with up to 8 Si alloying atoms on the Cr sublattice relax in the AlB_2-type structure, although thermodynamically unstable due to positive E_f. Consequently, these predictions indicate a theoretical Si solubility limit within AlB_2-structured CrB_2 above 4 Si

Publication II

Die approbierte gedruckte Originalversion dieser Dissertation ist an der TU Wien Bibliothek verfügbar.
The approved original version of this doctoral thesis is available in print at TU Wien Bibliothek.

TU Bibliothek Your knowledge hub WIEN

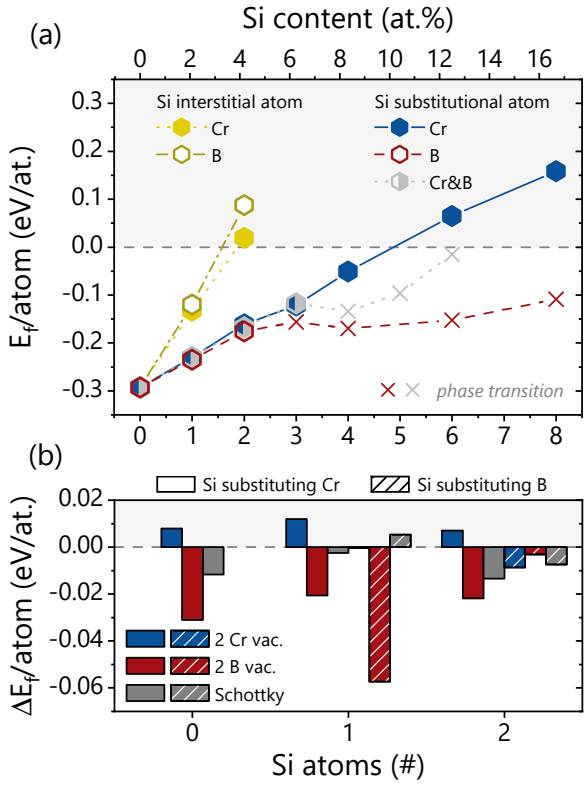

Fig. 1. (a) DFT-calculated E_f per atom for prototypical Cr-Si-B_2 structures (AlB_2-type) with various Si contents. The lower x-axis gives the number of Si atoms within the employed supercell, whereas the upper x-axis gives the corresponding atomic concentration. The Si atoms are either positioned interstitially on Cr- or B-planes, or in substitution for Cr, B, or an equal fraction of both Cr and B atoms. Crossed data points indicate alloying-induced deviations from the prototype structure during supercell relaxation. (b) DFT-evaluated formation energy differences per atom between the prototypical Cr-Si-B_2 structures in (a), with up to two Si atoms replacing either Cr (plane bars) or B (striped bars) atoms in defected structures that hold either two Cr vacancies (blue bars)/ two B vacancies (red bars)/ or one Schottky defect (grey bars), respectively.

atoms, which equals an overall alloying content of about 8 at.%.

Another factor to consider is the presence of point defects, as they are typically related to PVD synthesized films, which can strongly influence the phase stability criteria compared to the thermodynamic equilibrium [41]. Therefore, three different vacancy configurations – either two Cr vacancies, two B vacancies, or one Schottky defect – were analyzed for Cr-Si-B_2 structures with up to 2 alloyed Si atoms. The difference in the energy of formation between the defected and the corresponding prototypical structure ($\Delta E_f = E_f^{def} - E_f^{prot}$) are presented in Figure 1b. In perfect agreement with the findings of Moraes *et al.* [42], the binary CrB_2 compound favors the formation of boron and boron-containing vacancies over Cr point defects. The calculations further confirm this trend for both Si alloyed compositions, again indicating the preferred incorporation of B over Cr vacancies, except for the case of two B atoms exchanging Si. There, both vacancy types contribute to increased stability by slightly lowering E_f. Overall, the DFT calculations suggest the preferred incorporation of synthesis induces point defects on the non-metal sublattice for all compositions, with only minor negative influence from transition-metal vacancies.

B. Structural & Morphological Properties

The chemical composition of all Cr-Si-$B_{2\pm z}$ thin films is presented within a ternary phase diagram in Figure 2. The diagram is extended with guidelines connecting stoichiometric CrB_2 with single-phased Si and $CrSi_2$ (endpoints not visible due to reduced axis ranges), corresponding to narrow two-phase fields according to the equilibrium phase diagram [43]. The chemical analysis revealed an increasing silicon content of 0, 1, 3, 8, 11, and 17 at.% for the alloyed thin films with an increasing number of Si platelets placed on the target racetrack, respectively. The synthesis approach allowed for a predictable and linear adjustment of the Si content within the resulting thin film compositions. The coating prepared with two Si platelets on the target surface obtains an effective Si content below

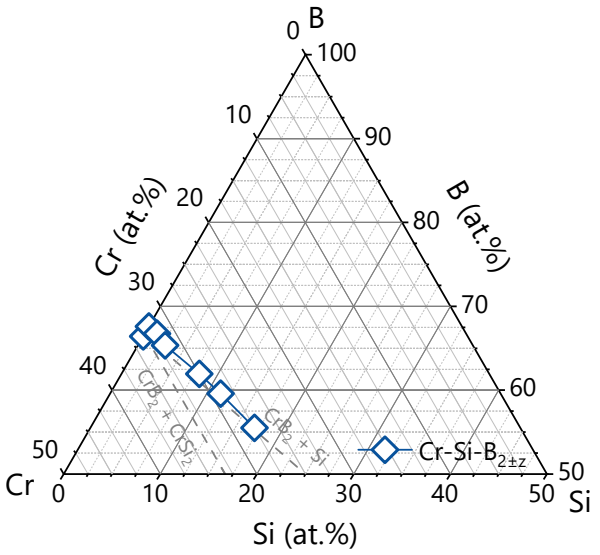

Fig. 2. Ternary phase diagram showing the chemical composition of all synthesized Cr-Si-$B_{2\pm z}$ coatings. The dashed lines connecting CrB_2 with Si and $CrSi_2$ indicate narrow two-phase fields according to the equilibrium phase diagram [43]. The axis ranges are reduced for improved separation of the data points.

Publication II

Die approbierte gedruckte Originalversion dieser Dissertation ist an der TU Wien Bibliothek verfügbar.
The approved original version of this doctoral thesis is available in print at TU Wien Bibliothek.
TU Bibliothek Your knowledge hub WIEN

the detection limit of the employed ICP-OES method, thus the coating is referenced with a content of 0 at.% Si ($Cr_{0.32}Si_{0.00}B_{0.68}$). Nevertheless, compared to the unalloyed coating, a minute fraction of Si is still expected within this thin film.

During the PVD deposition of (ternary) compound materials, coatings usually become enriched or depleted in specific constituents due to their preferred sputtering or scattering behavior within the plasma [26]. Interestingly for the Cr-Si-$B_{2\pm z}$ coatings, increasing the Si content in the thin films leads to a stoichiometric (B:Cr = 2:1) replacement of the CrB_2 mole fraction. This is also indicated by the direct overlap of all data points with the connecting line between stoichiometric CrB_2 and pure Si in Figure 2. Moreover, the Si-free coating $Cr_{0.34}B_{0.66}$ obtains an almost nominal stoichiometry with a B:Cr-ratio close to 2:1, which is consequently preserved for all further Si-containing depositions. Nevertheless, with increasing Si content in the Cr-Si-$B_{2\pm z}$ thin films, the overall B content decreases from 66 at.% down to 55 at.% for the coating with the highest Si-content.

The X-ray diffractograms depicted in Figure 3 demonstrate that all Cr-Si-$B_{2\pm z}$ thin films, regardless of their chemical composition, adopt the hexagonal AlB_2-type structure (space group 191). Moreover, within the accuracy of the employed method, no additional phases could be determined for any coating. All thin films obtain a polycrystalline growth, with slightly preferred orientations

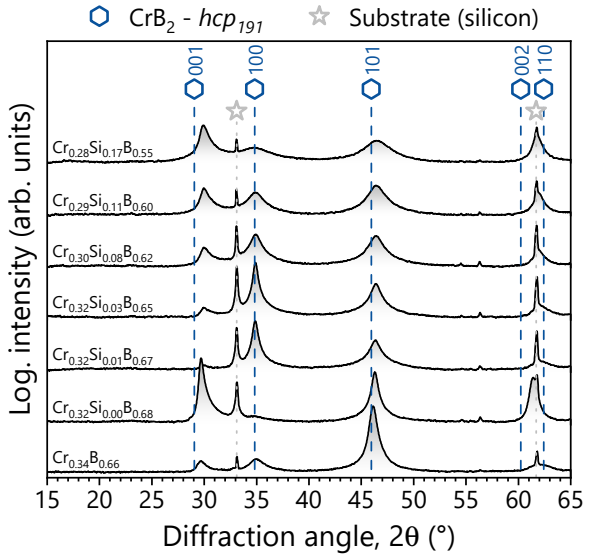

Fig. 3. X-ray diffractograms of all Cr-Si-$B_{2\pm z}$ coatings, arranged with increasing Si content from bottom to top. The diffractographs are correlated with standardized reference patterns for hexagonal CrB_2 (space group 191, AlB_2 prototype, [44]) and cubic silicon (substrate material, [45]). The corresponding coating chemistry for each diffractograph is included on the left side.

noticeable for coatings with a Si content below 8 at.%. Within these samples, the preferred orientation shifts from (101) for the Si-free $Cr_{0.34}B_{0.66}$ coating, towards (001) for $Cr_{0.32}Si_{0.00}B_{0.68}$, to (100)-oriented for both the $Cr_{0.32}Si_{0.01}B_{0.67}$ and $Cr_{0.32}Si_{0.03}B_{0.65}$ thin films, respectively. Further increasing the Si content results in equally oriented grains and causes a reduction of the diffracted intensities, hinting towards a concomitant decrease in the coherently diffracting domains (*i.e.*, a reducing grain size). This structural evolution correlates well with the DFT calculated Si solubility threshold close to 8 at.% (see Figure 1), thus suggesting that the excess alloying fraction preferably occupies grain boundary sites while also rationalizing their suggested increase in volume fraction due to smaller grains. The data further reveals that incorporating Si into the CrB_2 host structure leads to a slight decrease of the lattice parameter c in (001)-direction from 3.00 to 2.97 Å, meaning that the bond distance between adjacent B and Cr lattice planes is reduced. On the other hand, the lattice parameter a remains relatively unchanged at 2.97 Å, hence lateral bond distances between similar atoms are maintained.

Further correlating the phase formation with the chemical composition of all coatings shows that the decrease in the B content with increasing Si fraction takes no influence on the stability of the hexagonal CrB_2 structure in the as deposited state. Considering that only minor quantities of Si are chemically stable when located on the B-sublattice, the missing B-fraction is likely accommodated by introducing vacancies on non-metal sublattice in the deposition process (compare with Cr-rich/B-deficient planar defects previously observed in $CrB_{1.90}$ [46]). This is also in excellent agreement with the above DFT calculations, where enhanced thermodynamic stability is indicated for all structures containing B-vacancies – especially pronounced when Si is introduced on the Cr-sublattice.

The influence of Si on the growth mode of Cr-Si-$B_{2\pm z}$ thin films, specifically the decreasing columnar crystallite

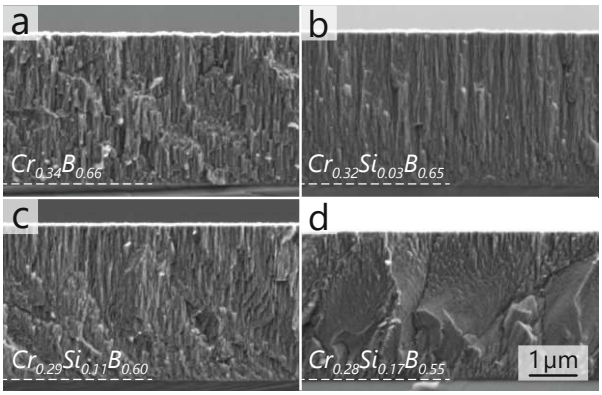

Fig. 4. SEM images depicting the growth morphology of selected Cr-Si-$B_{2\pm z}$ coatings deposited on Si substrate including the corresponding chemical composition.

Die approbierte gedruckte Originalversion dieser Dissertation ist an der TU Wien Bibliothek verfügbar.
The approved original version of this doctoral thesis is available in print at TU Wien Bibliothek.
TU Bibliothek Your knowledge hub WIEN

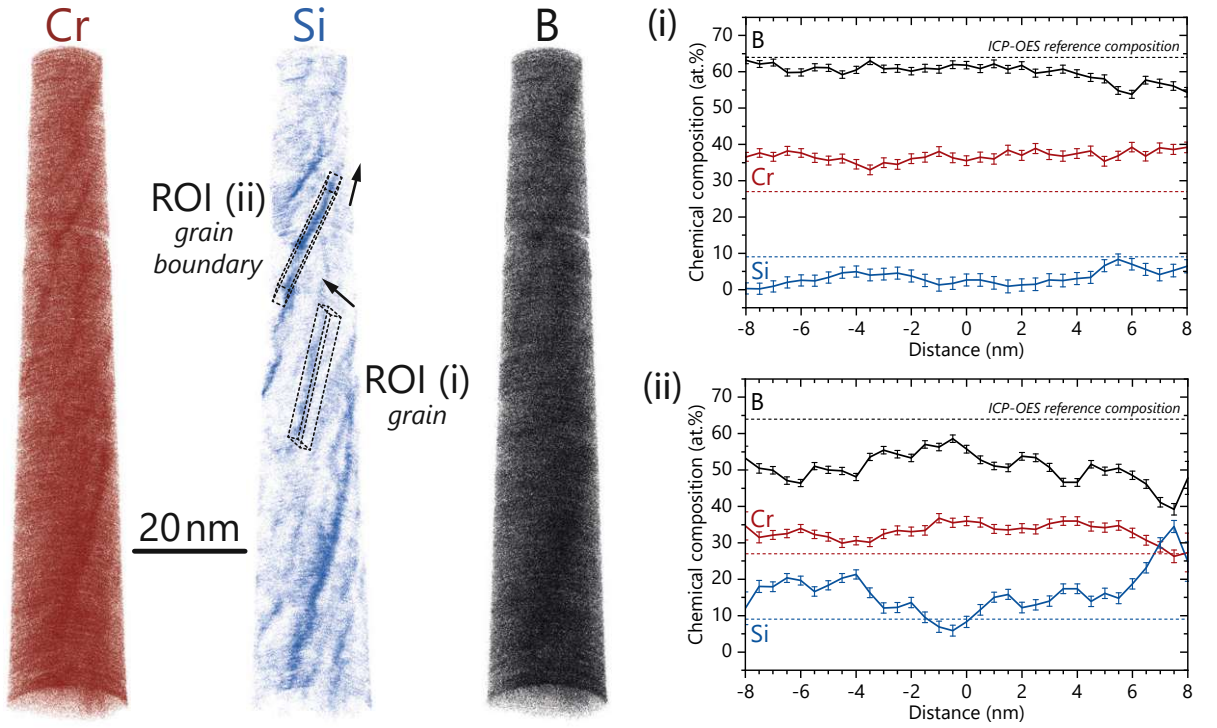

Fig. 5. Atom probe tomography determined chemical composition of a $Cr_{0.27}Si_{0.09}B_{0.64}$ thin film. Reconstructed positions of Cr, Si, and B atoms are presented. Insets (i) and (ii) depict concentration profiles of the grain interior and grain boundary, respectively. Both profiles were collected in the corresponding regions of interest marked in the Si atom distribution. The supplementary material contains animations of the Si distribution to provide an improved view on both regions of interest.

size, is further illustrated in Figure 4 through selected SEM fracture cross-sectional studies. The non and low-alloyed $Cr_{0.34}B_{0.66}$ and $Cr_{0.32}Si_{0.03}B_{0.65}$ coatings show a pronounced columnar structure with grains extending throughout the entire cross-section. The coating with ~11 at.% Si shows denser and increasingly more fibrous crystal columns – see Figure 4c. With the highest alloying content of 17 at.%, the growth morphology appears featureless, with limited indications for individual columnar structures remaining.

C. Atom Probe Tomography

To obtain an improved view of the distribution of Si atoms within the Cr-Si-$B_{2\pm z}$ thin films – especially at concentrations close to the proposed solubility limit – an additional coating with a composition of $Cr_{0.27}Si_{0.09}B_{0.64}$ was analogously prepared and investigated using detailed atom probe tomography. Figure 5 shows reconstructions of the atomic positions for Cr, Si, and B recorded within the tip volume. A random distribution is observed for both Cr and B atoms in the entire volume, although slight clustering of Cr atoms is noticeable in certain regions. In contrast, local chemical analysis of the Si distribution reveals the formation of Si-enriched regions at defect sites, identified as grain boundaries and triple junctions within the as-deposited thin film. A concentration profile in the grain interior (see Figure 5i and Supplementary) shows an entirely homogeneous distribution of the constitutional elements within the undisturbed, crystalline region. The calculated average chemistry reveals a composition close to $Cr_{0.37}Si_{0.04}B_{0.60}$, thus indicating that the actual Si solubility within the CrB_2-structure could be even lower than the DFT calculated limitation. The corresponding concentration profile taken at a grain boundary location (see Figure 5ii and Supplementary) depicts an increased fluctuation of all elements and a drastically increased Si content of up to 30 at.% in specific locations. The latter findings clearly underline the preferred segregation of surplus Si during the deposition process.

Overall, these findings experimentally underpin the DFT calculated solubility threshold above 8 at.% Si for the analyzed sample composition. Evidently, the conducted calculations neglect the possible impact of temperature and can only incorporate the chemical as well as kinetic limitations during PVD synthesis to a limited extent, thus rationalizing the deviation from the experimentally observed solubility threshold at ~4 at.%. Nevertheless, within the accuracy of the conducted analysis, the agree-

Publication II

Die approbierte gedruckte Originalversion dieser Dissertation ist an der TU Wien Bibliothek verfügbar.
The approved original version of this doctoral thesis is available in print at TU Wien Bibliothek.
TU Wien Bibliothek Your knowledge hub

ment between the chemical analysis and DFT calculations is clearly given. Moreover, the proposed influence of Si segregation to promote grain refinement, as evidenced in XRD analysis above an alloying content of 3 at.%, is additionally confirmed.

D. Mechanical Properties

Figure 6 presents the mechanical properties of all Cr-Si-$B_{2\pm z}$ thin films deposited. The residual stress state, film hardness, and Young's modulus are plotted as function of the Si alloying content. The Si-free $Cr_{0.34}B_{0.66}$ coating obtains a compressive residual stress state with $\sigma \sim$ -0.5 GPa and corresponding hardness and Young's modulus values of $H = 23.5\pm2.7$ GPa and $E = 295\pm18$ GPa, respectively. When compared to other TMB_2 materials, such as TiB_2 [47, 48] or WB_2 [49], CrB_2 typically features a reduced hardness and a relatively low elastic modulus [50]. Nevertheless, related works have also reported vastly higher hardness values for this material systems using similar deposition techniques, yet the origin of the observed variation remains unresolved [51–53]. Alloying a minute fraction of Si into CrB_2 shows a reversed residual stress state, with $Cr_{0.32}Si_{0.00}B_{0.68}$ revealing a tensile stress of $\sigma \sim 0.9$ GPa. Interestingly, despite the adverse effect of tensile stresses on the measurable hardness, this coating shows identical nanoindentation results with $H = 23.9\pm1.1$ and $E = 291\pm6$ GPa. The maintained properties are related to the preferred orientation rather than the influence of Si alloying per se. In line with a work by Fuger *et al.* [54], the preserved hardness is explained by the pronounced orientation towards the (001)-direction (see Figure 3), which was demonstrated to yield the highest hardness for TMB_2 thin films in general. Thus, the anisotropy effect balances the negative impact of the tensile stress state. Consequently, even higher hardness values could be expected for this material system by tailoring the residual stress state towards the compressive regime. The actual shift in the residual stress state between the $Cr_{0.34}B_{0.66}$ and $Cr_{0.32}Si_{0.00}B_{0.68}$ coating may also be related to the preferred orientation. CrB_2 obtains a significant anisotropy in the thermal expansion ($\alpha_a^{CrB_2} = 10.8 \times 10^{-6}$ K^{-1}, $\alpha_c^{CrB_2} = 6.3 \times 10^{-6}$ K^{-1}, [55]), therefore higher in-plane tensile stresses are to be expected for (001)-textured thin film (a-direction parallel to coating-substrate interface) when grown on sapphire substrate ($\alpha_a^{Al_2O_3} = 4.5 - 5.3 \times 10^{-6}$K^{-1}, [56]). With a further increase in Si, the residual tensile stress is gradually reduced from $\sigma \sim 0.9$ GPa for $Cr_{0.32}Si_{0.01}B_{0.67}$ down to $\sigma \sim 0.3$ GPa for $Cr_{0.29}Si_{0.11}B_{0.60}$, before again increasing in the compressive regime to $\sigma \sim$ -0.5 for $Cr_{0.28}Si_{0.17}B_{0.55}$. Concomitantly, with the above observed increase in grain boundary volume – *i.e.*, an increase in regions that are less strongly bound than the surrounding crystal – a linear decrease in the elastic modulus down to $E = 238\pm7$ GPa for the highest Si content of 17 at.% was recorded. Interestingly, Si alloying did not result in any solid solution hardening effect during nanoindentation. Upon introducing more than 1 at.% Si into CrB_2, the hardness gradually decreases from $H = 21.6\pm1.1$ GPa for $Cr_{0.32}Si_{0.01}B_{0.67}$, down to a constant value of $H \sim 17$ GPa for all coatings having a Si content $\geq$8 at.%. In relation to the Si segregations observed on grain boundaries for higher alloying contents (see Figure 5), the measured hardness of these thin films is likely dominated by the inferior mechanical properties of the Si-rich regions.

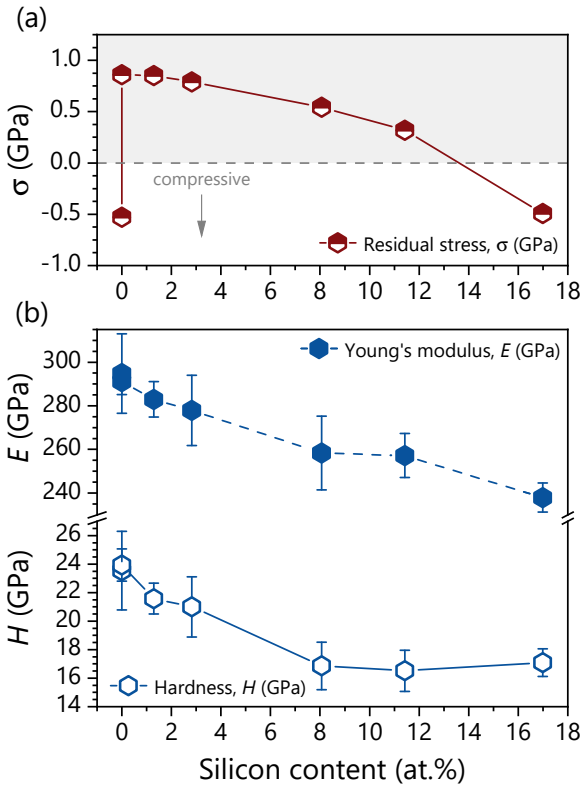

Fig. 6. (a) Residual stress state of all Cr-Si-$B_{2\pm z}$ thin films versus the Si alloying content. (b) Corresponding hardness and Young's modulus data. All mechanical properties were determined on coated sapphire substrates.

E. Dynamic Oxidation

Dynamic oxidation experiments were conducted in a TGA system to revisit [28] the impact of Si alloying on the high-temperature oxidation resistance of CrB_2-based thin films, and to determine the minimum alloying quantity necessary to yield enhanced protective properties. Figure 7 presents the mass change of the coating material, deposited onto pre-weighted polycrystalline Al_2O_3 substrate (inert in the temperature rage up to 1400 °C, [28]), with respect to the annealing temperature T. Up to a range of $T \sim 600$ °C a constant mass signal is recorded

Die approbierte gedruckte Originalversion dieser Dissertation ist an der TU Wien Bibliothek verfügbar.
The approved original version of this doctoral thesis is available in print at TU Wien Bibliothek.
TU Bibliothek Your knowledge hub WIEN

for all Cr-Si-$B_{2\pm z}$ thin films, indicating no progressive oxide scale formation. Only the $Cr_{0.32}Si_{0.01}B_{0.67}$ thin film shows an earlier onset temperature at $T \sim 500$ °C (blue dotted line), visible by the already occurring mass gain due to oxide scale growth. Upon reaching the oxidation onset temperature, all Cr-Si-$B_{2\pm z}$ coatings up to a Si content of 3 at.% show a stepwise increase in the mass signal until reaching a maximum value at $T \sim 1200$ °C, indicating the fully oxidized state. Beyond this temperature, a decreasing sample mass is recorded, which is correlated with the evaporation of B_2O_3-based oxides. The mass signal evolution shows intermitted plateaus for all these coatings between $600 < T < 1200$ °C, hinting towards a competitive formation of B_2O_3- and Cr_2O_3-based scales leading to limited protection against continued oxidation. Moreover, with already small alloying fractions (*e.g.*, $Cr_{0.32}Si_{0.03}B_{0.65}$), both the slope of the increase and the overall mass gain up to $T \sim 1100$ °C are significantly reduced, already pointing towards the effectiveness of the employed alloying routine.

Increasing the Si content within the Cr-Si-$B_{2\pm z}$ thin films beyond 8 at.% leads to a fully preserved coating mass up to $T \sim 1100$ °C due to the formation of a stable, protective oxide scale preventing any oxidative attack of the underlying coating material. Only at $T > 1100$ °C, these higher alloyed thin films show a slight increase in the overall mass signal up to 1400 °C. Unlike the low-alloyed coatings, the protective mechanism relies on the formation of a continuous, dense SiO_2-based scale enabled by a sufficient Si diffusion provided through the Cr-Si-$B_{2\pm z}$ thin film. Moreover, as known for a $Cr_{0.26}Si_{0.16}B_{0.58}$ coating [28], the formed oxide scale after annealing at $T = 1400$ °C should in fact be comprised of a layered amorphous SiO_2-based phase with crystalline Cr_2O_3 scale on top (discussed in more detail in Section III G). Overall,

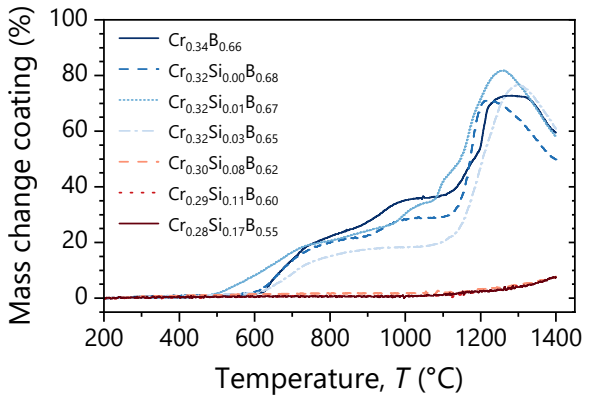

Fig. 7. Mass change of all Cr-Si-$B_{2\pm z}$coatings as function of the annealing temperature, recorded during dynamic oxidation in a TGA system (10 K/min heating rate) in synthetic air environment. The coatings were deposited on pre-weighted Al_2O_3 substrates, which are inert over the entire temperature range.

these results highlight that achieving high-temperature oxidation resistance for Cr-Si-$B_{2\pm z}$ thin films involves a minimum alloying content close to 8 at.% Si to activate the protective mechanism.

F. *In-situ* X-ray diffraction

Comparative *in-situ* X-ray diffraction studies were performed during the oxidation of $Cr_{0.32}Si_{0.03}B_{0.65}$ and $Cr_{0.29}Si_{0.11}B_{0.60}$ in a lab-air environment, to reveal the underlying mechanism causing the drastically improved oxidation resistance above a distinct Si content. Figure 8 depicts the diffractographs taken at room temperature (RT) as well as from 400 to 1200 °C in steps of 50 °C, with the corresponding annealing temperature included on the right axis. In the as-deposited state at RT, the data for $Cr_{0.29}Si_{0.11}B_{0.60}$ shows an analogous diffraction result as depicted in Figure 3, revealing a hexagonal structured CrB_2-based coating with polycrystalline grain distribution (see Figure 8a). Moreover, no additional Cr-Si- or Si-B-based phase is detected, suggesting that Si is dissolved up to the solubility limit of ~3-4 at.% within the CrB_2 structure – note that the excess Si is located at grain boundaries as shown in Figure 5. This structure is fully preserved up to a temperature of $T = 600$ °C. A further increase to $T = 650$ °C leads to first indications for crystalline Si precipitates (*e.g.*, $2\theta \sim 28.7°$, 47.5°, 56.3°). In the temperature regime beyond $T = 750$ - 800 °C, additional recrystallization of the Cr-Si-$B_{2\pm z}$ solid solution is observed, as indicated by the drastically decreasing peak width and increase in diffracted intensities (*e.g.*, $2\theta \sim 29.0°$, 34.7°, 45.8°, etc.). Moreover, in accordance with the three-phase field of CrB_2-$CrSi_2$-Si in Figure 2 (area between the dashed lines), the intermediate formation of a $CrSi_2$ phase is suggested between $T = 750$ and 1050 °C by a set of low intensity reflexes (*e.g.*, $2\theta \sim 26.8°$, 42.3°, 49.6°). However, it should be noted that the deviation from the indexed peak positions is significant, so that additional high-resolution analysis would be required for confirmation. Recrystallization of the Cr-Si-$B_{2\pm z}$ matrix and Si precipitation continue up to $T = 1200$ °C, resulting in sharp peaks for both phases. In addition, several indications for a Cr_2O_3 oxide layer are observed after the annealing experiments above $T \geq 1100$ °C (*e.g.*, $2\theta \sim 33.5°$, 50.0°, 54.5°), yet no diffraction peaks pointing towards a B_2O_3 or the more important SiO_2-based structure occur. Thus, in line with previous findings, especially the latter phase is expected to be in an amorphous state. Overall, pronounced diffraction peaks indicate that the Cr-Si-$B_{2\pm z}$ structure is still intact at $T = 1200$ °C, highlighting the excellent oxidation resistance of this coating and confirming the presence of a stable oxide scale protecting the underlying coating material.

When discussed in relation to the dynamic oxidation experiments (see Figure 7), the precipitation of Si at $T > 600$ °C in this "sufficiently" (Si content $\geq$ ~8 at.%) alloyed coating correlates well with the oxidation onset

Die approbierte gedruckte Originalversion dieser Dissertation ist an der TU Wien Bibliothek verfügbar.
The approved original version of this doctoral thesis is available in print at TU Wien Bibliothek.
TU Bibliothek Your knowledge hub WIEN

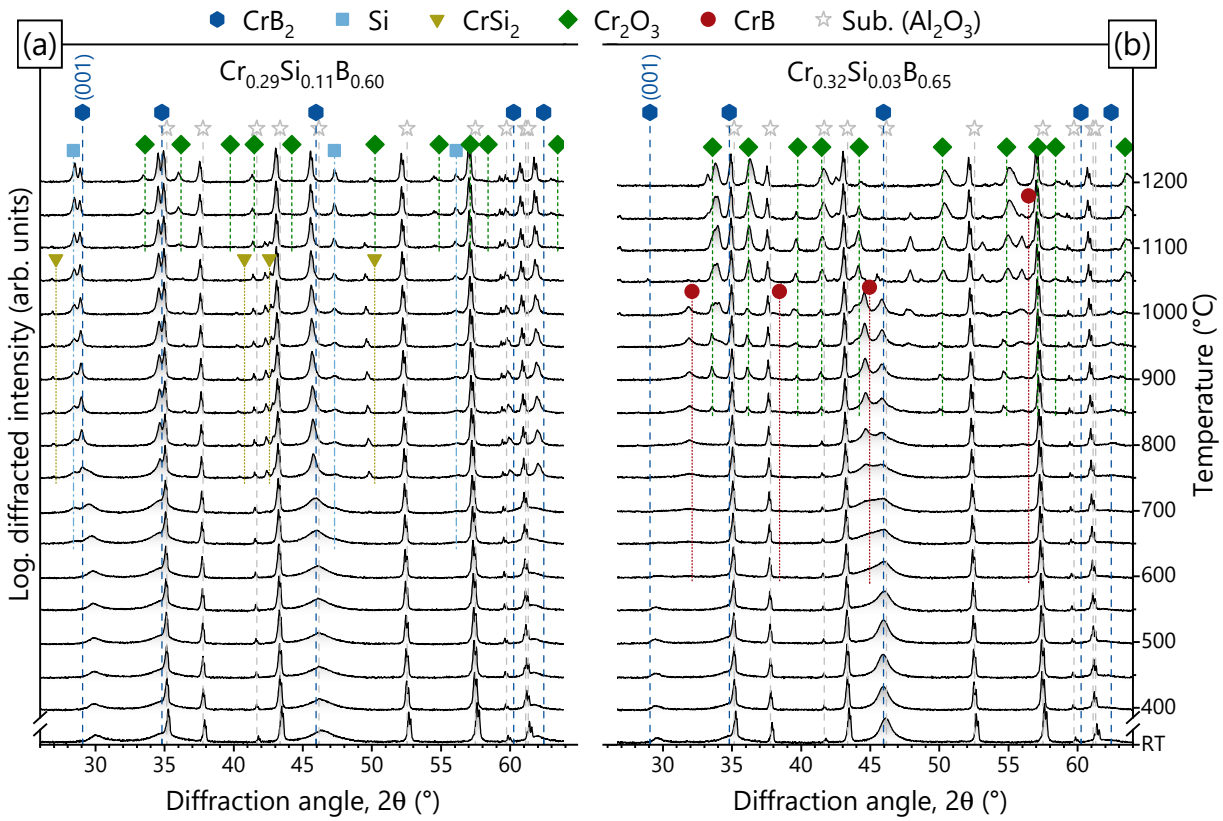

Fig. 8. *In-situ* X-ray diffractographs recorded during subsequent annealing treatments in lab-air environment of (a) $Cr_{0.29}Si_{0.11}B_{0.60}$ and (b) $Cr_{0.32}Si_{0.03}B_{0.65}$ thin films deposited on polycrystalline Al_2O_3. Standardized reference patterns for hexagonal CrB_2 (blue hexagon, [44]), cubic Si (light blue square, [45]), hexagonal $CrSi_2$ (dark yellow triangle, [57]), rhombohedral Cr_2O_3 (green diamond, [58]), orthorhombic CrB (dark red circle, [59]) and rhombohedral Al_2O_3 (grey star, [60]) are included. The sample temperature corresponding to each diffraction experiment is added on the right axis.

temperature of the "insufficiently" alloyed coatings. Consequently, this provides a strong indication that the Si precipitates within the $Cr0_{.29}Si_{0.11}B_{0.60}$ coating – either derived from excess Si on grain boundaries or the surrounding Cr-Si-$B_{2\pm z}$ solid solution (discussed in more detail in Section III G) – are the primary source for the increased oxidation resistance. In addition, the formation of crystalline Cr_2O_3 above $T = 1100$ °C is in excellent agreement with the previous TGA analysis, rationalizing the mass gain for all coatings with Si content above 8 at.% in the same temperature regime.

A direct comparison to results obtained for an "insufficiently" alloyed $Cr_{0.32}Si_{0.03}B_{0.65}$ coating is illustrated in Figure 8b. An unaltered sample structure is recorded up to a temperature of $T = 550$ °C, depicting a preferred (100)-orientation as shown in Figure 3. With the oxidation onset at $T = 600$ °C (see also Figure 7), instead of forming Si precipitates, initial indications towards a boron depleted CrB phase are formed (*e.g.*, $2\theta \sim 32.2°$, 38.5°, 44.9°, etc.), increasing in intensity up to $T = 1100$ °C. This highlights the partial decomposition of the Cr-Si-B_2 structure to form an unprotective B_2O_3 scale, in line with the mass gain towards an initial plateau observed during TGA measurements. This stands in marked contrast to the $Cr_{0.29}Si_{0.11}B_{0.60}$ coating (see Figure 8a), where the precipitation and crystallization of Si in the same temperature regime initiates the high-temperature protective character. Analogously, recrystallization of the CrB_2 structure is again observed before the diffraction signals diminish at $T = 1050$ °C, pointing towards a full decomposition of the diboride phase. Finally, at $T = 900$ °C, an additional Cr_2O_3 scale is formed – compare with the second mass gain plateau observed in Figure 7 – which subsequently consumes the entire coating at $T = 1200$ °C. Over the entire temperature range, no Si-based phase is observed.

Regarding the thermally activated precipitation of Si from the $Cr_{0.29}Si_{0.11}B_{0.60}$ coating, a possible explanation is seen in the continuous increase in the DFT calculated E_f for the AlB_2 structured Cr-Si-B_2 compositions over the binary CrB_2 with increasing Si content. Theoretically comparing the difference in energy of formation

Publication II

Die approbierte gedruckte Originalversion dieser Dissertation ist an der TU Wien Bibliothek verfügbar.
The approved original version of this doctoral thesis is available in print at TU Wien Bibliothek.
TU Bibliothek Your knowledge hub WIEN

between a $Cr_{0.27}Si_{0.06}B_{0.67}$ structure (see Figure 1) with its corresponding decomposition products of CrB_{2+z} and Si according to:

$$\Delta E_f = [(1-x)\cdot E_f^{CrB_2} + x\cdot E_f^{Si} + 2x\cdot E_f^{B}] - E_f^{Cr_{0.27}Si_{0.06}B_{0.67}}, \text{with } x = 0.06 \quad (1)$$

a significant energetic benefit of ΔE_f = -1.34 eV/at. towards the decomposed constituents is attained. The DFT calculated formation energies of elemental Si (cubic, -5.41 eV/atom) and B (rhombohedral, -6.67 eV/atom) correspond to their stable configuration at room-temperature and ambient pressure. Analogous results are obtained for all other theoretically and experimentally studied compositions of Cr-Si-$B_{2\pm z}$, thus underlining that the precipitation follows the thermodynamically prescribed equilibrium condition. Finally, the precipitation is believed to be further supported during recrystallization of the Cr-Si-$B_{2\pm z}$ phase above T = 750 - 800 °C, allowing for even enhanced Si diffusion. Considering a melting temperature of T_M = 2200 °C [61] for pure CrB_2, the recrystallization process occurs at a typical homologous temperature of $T_H \sim 0.4$.

G. Structural & Chemical Analysis Post Annealing

In order to complete the established viewpoint on the morphological evolution and especially the oxide scale growth during high-temperature oxidation of Cr-Si-$B_{2\pm z}$ thin films, complementary detailed TEM analysis (see Figure 9) is performed on the $Cr_{0.29}Si_{0.11}B_{0.60}$ thin film used during the *in-situ* X-ray studies (see Figure 8a). Figures 9a and b depict bright-field and high-angle annular dark field micrographs of the entire sample cross-section, including the interface to the polycrystalline Al_2O_3 substrate and the formed oxide scale, respectively. Both images immediately visualize the pronounced recrystallization of the Cr-Si-$B_{2\pm z}$ thin film, revealing large globular grains throughout the cross-section. Given the atomic number contrast in the HAADF image, regions of different elemental compositions – indicated by lighter and darker grey areas – can be identified next to several black appearing voids. When combined with the elemental mapping in Figure 9c, bright areas can be correlated with a Cr- and B-rich phase (*i.e.*, $CrB_{2\pm z}$), whereas darker regions correspond exclusively to pure Si. Note the superposition of Cr and O signals during EDX analysis, thus creating a slight, artificial O signal (see Figure 9c-iv) overlapping with all $CrB_{2\pm z}$ regions. Furthermore, also Si and W overlap in the EDX spectrum, resulting in a misinterpretation of the W protection layer with an artificial Si region in the top area of Figure 9c-ii. Several conclusions can be drawn from these results: (*i*) Silicon precipitation is not restricted to grain boundary sites already holding excess Si in the as-deposited state. (*ii*) Upon thermal activation, the Cr-Si-$B_{2\pm z}$ solid solution fully decomposes into large globular phase regions containing solely $CrB_{2\pm z}$ or Si. (*iii*) Globular Si precipitates are formed throughout the coating cross-section in addition to a continuous surface layer. As a result, several voids are formed in the thin film volume to compensate for the Si surface diffusion (note, certain voids may also originate from focus-ion beam milling preparation of the TEM lamella, resulting from the weak connection between the individual recrystallized grains). Finally, the elemental distributions of Al and O show that no interaction between the coating and substrate material occurred during the entire oxidation treatment.

Figures 9a and b also clearly show a thin, dense oxide scale formed on the sample surface. Using detailed STEM imaging combined with EDX analysis (see Figure 9d), the oxide reveals a defined, layered architecture composed of a thin amorphous SiO_2 layer on the coating-oxide interface and a nanocrystalline Cr_2O_3 top layer. Similar to the elemental distribution in Figure 9c, no intermixing of Cr- and B-rich sites with Si can be observed in the oxide layer and the unaffected material below. However, it has to be considered that the employed chemical analysis is not suitable for tracing minimum quantities of light elements such as B within, *e.g.*, the SiO_2 layer. Interestingly, despite the extended annealing time at temperatures above $T > 1000$ °C, the SiO_2 layer features a thickness in the range of only 20-40 nm, whereas the Cr_2O_3 top layer extends over 200-250 nm.

Regarding the temporal sequence of forming the highly protective oxide scale, the primary mechanism is seen in the precipitation of Si – especially towards the coating surface – allowing for the initial growth of a stable SiO_2 layer in the temperature range from T = 650 to 1100 °C. Due to the minimal thickness of this layer, even at T = 1200 °C, no mass gain is visible in the TGA signal. Furthermore, in line with the TGA and *in-situ* X-ray diffraction analysis, the additional Cr_2O_3 surface layer is subsequently formed in the temperature regime above T = 1100 °C. Unlike many TM-oxides, Cr-cations primarily diffuse outwards on grain boundaries within the Cr_2O_3 oxide layer, thus allowing for a scale growth on top of the oxide surface rather than the oxide-coating interface [62]. Also, resulting from the vastly increased layer thickness, the formation is clearly relatable to the mass gain signal shown in Figure 7.

IV. CONCLUSIONS

Si alloying is a successful concept to improve the oxidation resistance of transition-metal diboride-based thin films by forming a dense SiO_2-based scale at elevated temperatures. In this work, DC magnetron sputtered, Cr-Si-$B_{2\pm z}$-based coatings with Si contents between 0 and 17 at.% were analyzed to reveal the impact of the alloying element on the structural and mechanical properties of these AlB_2-type thin films. Moreover, the mechanisms involved in the enhanced oxidation resistance were inves-

Publication II

Die approbierte gedruckte Originalversion dieser Dissertation ist an der TU Wien Bibliothek verfügbar.
The approved original version of this doctoral thesis is available in print at TU Wien Bibliothek.

TU Bibliothek Your knowledge hub WIEN

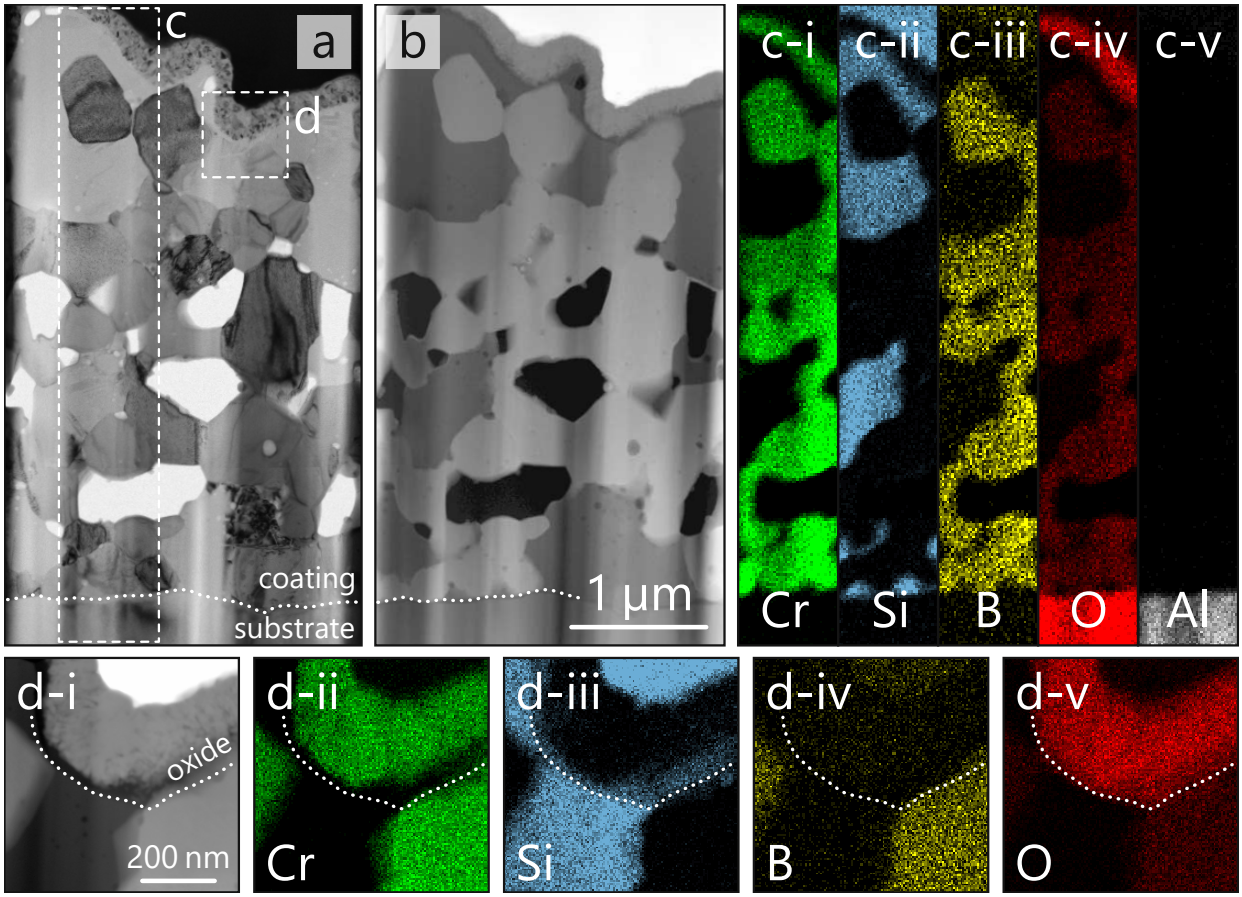

Fig. 9. (a) bright-field and (b) high-angle annular dark field TEM micrographs of a $Cr_{0.29}Si_{0.11}B_{0.60}$ coating on polycrystalline Al_2O_3 substrate, gradually oxidized up to 1200 °C (see Figure 8). (c) elemental EDX mapping of the entire sample cross-section according to the insert in (a). (d) detailed scanning-TEM image of the oxide scale indicated in (a) including the elemental EDX mapping.

tigated to deepen the knowledge of optimized chemical compositions.

DFT calculations performed on various stoichiometric and defected AlB_2-structured Cr-Si-B_2 compositions indicate the energetically preferred incorporation of Si on the Cr-sublattice over a wide alloying range. Contrary, limited occupation of the B-sublattice destabilizes the hexagonal cell before a sufficient alloying fraction for enhanced oxidation resistance is obtained. Furthermore, detailed APT analysis of a $Cr_{0.27}Si_{0.09}B_{0.64}$ thin film revealed Si segregation towards the grain boundaries in the as-deposited state. The corresponding grain interior still holds up to 4 at.% Si, being in line with the DFT-calculated Si solubility limit. Despite a concomitant increase in B understoichiometry with increasing Si content, all synthesized Cr-Si-$B_{2\pm z}$ coatings obtain the hexagonal structure, irrespective of the chemical composition. In fact, the introduction of B vacancies into higher Si alloyed coatings to compensate for the understoichiometry is suggested to increase the chemical stability of the hexagonal CrB_2 structure when correlated with DFT results.

Structural analysis of the Cr-Si-$B_{2\pm z}$ thin films outlines a variation in the preferred growth direction and a gradual reduction of the average columnar grain size with increasing Si content. Complementary nanoindentation measurements showed a direct correlation between these structural features and the mechanical properties. The highest film hardness was revealed for low Si alloyed, (001)-oriented coatings at $H \sim 24$ GPa, whereas increased alloying contents of Si ≥ 8 at.% resulted in $H \sim 17$ GPa due to the promoted grain boundary decoration with excess Si.

Thermogravimetric analysis proofed the excellent oxidation resistance of Cr-Si-$B_{2\pm z}$ coatings with Si fractions ≥ 8 at.% up to $T \sim 1400$ °C, whereas lower alloying contents reveal a stepwise oxidation starting at $T \sim 600$ °C due to a non-protecting Cr- and B-based oxide scale. The mechanism leading to increased oxidation resistance could be linked to the thermally activated precipitation of Si and

Publication II

Die approbierte gedruckte Originalversion dieser Dissertation ist an der TU Wien Bibliothek verfügbar.
The approved original version of this doctoral thesis is available in print at TU Wien Bibliothek.

TU Bibliothek Your knowledge hub WIEN

subsequent recrystallization of the Cr-Si-$B_{2\pm z}$ solid solution, thereby creating a continuous Si-based surface layer as shown by detailed *in-situ* X-ray diffraction and TEM analysis. This layer allows for a dense, amorphous SiO_2-based scale in the temperature range between $T = 650$ to 1100 °C, beyond which an additional nanocrystalline Cr_2O_3 top layer is formed due to increased Cr-outward diffusion.

In summary, this study underpins the promising capabilities of Cr-Si-$B_{2\pm z}$ coatings applied in high-temperature oxidative environments and provides detailed guidelines connecting the chemical composition to the resulting thin film properties.

ACKNOWLEDGMENTS

The financial support by the Austrian Federal Ministry for Digital and Economic Affairs, the National Foundation for Research, Technology and Development and the Christian Doppler Research Association is gratefully acknowledged (Christian Doppler Laboratory "Surface Engineering of high-performance Components"). We also thank for the financial support of Plansee SE, Plansee Composite Materials GmbH, and Oerlikon Balzers, Oerlikon Surface Solutions AG. In addition, we want to thank the X-ray center (XRC) of TU Wien for beam time as well as the electron microscopy center - USTEM TU Wien - for providing the SEM and TEM facilities. We also thank Dr. M. Weiss and Prof. A. Limbeck from the Institute of Chemical Technologies and Analytics, TU Wien, for their support with chemical analysis of our samples. The authors acknowledge TU Wien Bibliothek for financial support through its Open Access Funding Programme.

DATA AVAILABILITY STATEMENT

The data that support the findings of this study are available from the corresponding author upon reasonable request.

DECLARATION OF INTEREST STATEMENT

The authors declare that they have no known competing financial interests or personal relationships that could have appeared to influence the work reported in this paper.

Die approbierte gedruckte Originalversion dieser Dissertation ist an der TU Wien Bibliothek verfügbar.
The approved original version of this doctoral thesis is available in print at TU Wien Bibliothek.

REFERENCES

[1] C.Subramanian, A.K.Suri, and T.S.R.Ch.Murthy, BARC Newsl. , 6 (2010).
[2] D. Sciti, L. Silvestroni, L. Mercatelli, J. L. Sans, and E. Sani, Sol. Energy Mater. Sol. Cells **109**, 8 (2013).
[3] D. C. Larbalestier, L. D. Cooley, M. O. Rikel, A. A. Polyanskii, J. Jiang, S. Patnaik, X. Y. Cai, D. M. Feldmann, A. Gurevich, A. A. Squitieri, M. T. Naus, C. B. Eom, E. E. Hellstrom, R. J. Cava, K. A. Regan, N. Rogado, M. A. Hayward, T. He, J. S. Slusky, P. Khalifah, K. Inumaru, and M. Haas, Nature **410**, 186 (2001).
[4] F. Monteverde and L. Scatteia, J. Am. Ceram. Soc. **90**, 1130 (2007).
[5] M. Magnuson, L. Hultman, and H. Högberg, Vacuum **196**, 110567 (2022).
[6] A. Bellosi and F. Monteverde, in *Eur. Sp. Agency, (Special Publ. ESA SP*, 521 (2003) pp. 65–72.
[7] W. Tan, C. A. Petorak, and R. W. Trice, J. Eur. Ceram. Soc. **34**, 1 (2014).
[8] C. Rhodes, J. Stuart, R. Lopez, X. Li, M. Waje, M. Mullings, J. Lau, and S. Licht, J. Power Sources **239**, 244 (2013).
[9] W. G. Fahrenholtz and G. E. Hilmas, Scr. Mater. **129**, 94 (2017).
[10] C. Mitterer, J. Solid State Chem. **133**, 279 (1997).
[11] J. W. Zimmermann, G. E. Hilmas, W. G. Fahrenholtz, R. B. Dinwiddie, W. D. Porter, and H. Wang, J. Am. Ceram. Soc. **91**, 1405 (2008).
[12] V. Moraes, L. Zauner, T. Wojcik, M. Arndt, P. Polcik, H. Riedl, and P. H. Mayrhofer, Acta Mater. **186**, 487 (2020).
[13] C. Fuger, V. Moraes, R. Hahn, H. Bolvardi, P. Polcik, H. Riedl, and P. H. Mayrhofer, MRS Commun. **9**, 375 (2019).
[14] C. Fuger, B. Schwartz, T. Wojcik, V. Moraes, M. Weiss, A. Limbeck, C. A. Macauley, O. Hunold, P. Polcik, D. Primetzhofer, P. Felfer, P. H. Mayrhofer, and H. Riedl, J. Alloys Compd. **864**, 158121 (2021).
[15] B. Bakhit, J. Palisaitis, J. Thörnberg, J. Rosen, P. O. Persson, L. Hultman, I. Petrov, J. E. Greene, and G. Greczynski, Acta Mater. **196**, 677 (2020).
[16] J. Thörnberg, S. Mráz, J. Palisaitis, F. F. Klimashin, P. Ondracka, B. Bakhit, P. Polcik, S. Kolozsvari, L. Hultman, I. Petrov, P. O. Persson, J. M. Schneider, and J. Rosen, Surf. Coatings Technol. **442**, 128187 (2022).
[17] A. H. Navidi Kashani, S. Mráz, D. M. Holzapfel, M. Hans, L. Löfler, P. Ondračka, D. Primetzhofer, and J. M. Schneider, Surf. Coatings Technol. **442**, 128190 (2022).
[18] T. Parthasarathy, R. Rapp, M. Opeka, and R. Kerans, Acta Mater. **55**, 5999 (2007).
[19] W. G. Fahrenholtz and G. E. Hilmas, Int. Mater. Rev. **57**, 61 (2012).
[20] L. Silvestroni, K. Stricker, D. Sciti, and H. J. Kleebe, Acta Mater. **151**, 216 (2018).
[21] I. G. Talmy, J. A. Zaykoski, and M. M. Opeka, J. Am. Ceram. Soc. **91**, 2250 (2008).
[22] T. S. Murthy, J. K. Sonber, C. Subramanian, R. K. Fotedar, M. R. Gonal, and A. K. Suri, Int. J. Refract. Met. Hard Mater. **27**, 976 (2009).
[23] B. Bakhit, S. Dorri, A. Kooijman, Z. Wu, J. Lu, J. Rosen, J. M. Mol, L. Hultman, I. Petrov, J. E. Greene, and G. Greczynski, Vacuum **185** (2021), 10.1016/j.vacuum.2020.109990.
[24] S. Dorri, J. Palisaitis, G. Greczynski, I. Petrov, J. Birch, L. Hultman, and B. Bakhit, Corros. Sci. **206**, 110493 (2022).
[25] J. Thörnberg, B. Bakhit, J. Palisaitis, N. Hellgren, L. Hultman, G. Greczynski, P. O. Persson, I. Petrov, and J. Rosen, Surf. Coatings Technol. **420**, 127353 (2021).
[26] C. Fuger, R. Hahn, A. Hirle, P. Kutrowatz, M. Weiss, A. Limbeck, O. Hunold, P. Polcik, and H. Riedl, Surf. Coatings Technol. **446**, 128806 (2022).
[27] T. Glechner, O. E. Hudak, T. Wojcik, L. Haager, F. Bohrn, H. Hutter, O. Hunold, J. Ramm, S. Kolozsvári, E. Pitthan, D. Primetzhofer, and H. Riedl, Mater. Des. **211**, 110136 (2021).
[28] T. Glechner, H. G. Oemer, T. Wojcik, M. Weiss, A. Limbeck, J. Ramm, P. Polcik, and H. Riedl, Surf. Coatings Technol. **434**, 128178 (2022).
[29] T. Glechner, A. Bahr, R. Hahn, T. Wojcik, M. Heller, A. Kirnbauer, J. Ramm, S. Kolozsvari, P. Felfer, and H. Riedl, Corros. Sci. **205**, 110413 (2022).
[30] B. Grančič, M. Mikula, T. Roch, P. Zeman, L. Satrapinskyy, M. Gregor, T. Plecenik, E. Dobročka, Z. Hájovská, M. Mičušík, A. Šatka, M. Zahoran, A. Plecenik, and P. Kúš, Surf. Coatings Technol. **240**, 48 (2014).
[31] W. Oliver and G. Pharr, J. Mater. Res. **19**, 3 (2004).
[32] A. C. Fischer-Cripps, Surf. Coatings Technol. **200**, 4153 (2006).
[33] G. Janssen, M. Abdalla, F. van Keulen, B. Pujada, and B. van Venrooy, Thin Solid Films **517**, 1858 (2009).
[34] G. G. Stoney, Proc. R. Soc. A Math. Phys. Eng. Sci. **82**, 172 (1909).
[35] G. Kresse and J. Furthmüller, Phys. Rev. B - Condens. Matter Mater. Phys. **54**, 11169 (1996).
[36] G. Kresse and D. Joubert, Phys. Rev. B **59**, 1758 (1999).
[37] J. P. Perdew, K. Burke, and M. Ernzerhof, Phys. Rev. Lett. **77**, 3865 (1996).
[38] A. Van de Walle, M. Asta, and G. Ceder, Calphad Comput. Coupling Phase Diagrams Thermochem. **26**, 539 (2002), arXiv:0212159 [cond-mat].
[39] P. Felfer, "GitHub - Atom-Probe-Toolbox: Matlab toolbox for APT analysis," (2022).
[40] L. Chen, J. Paulitsch, Y. Du, and P. H. Mayrhofer, Surf. Coatings Technol. **206**, 2954 (2012).
[41] H. Euchner and P. Mayrhofer, Surf. Coatings Technol. **275**, 214 (2015).
[42] V. Moraes, H. Riedl, C. Fuger, P. Polcik, H. Bolvardi, D. Holec, and P. H. Mayrhofer, Sci. Rep. **8**, 9288 (2018).
[43] H. Nowotny, E. Piegger, R. Kieffer, and F. Benesovsky, Monatshefte für Chemie **89**, 611 (1958).
[44] ICDD, Powder Diffr. File - Hexag. CrB2 - 04-004-1734 (2011).
[45] ICDD, Powder Diffr. File - cubic Si - 00-027-1402 (2017).
[46] M. M. Dorri, J. Thörnberg, N. Hellgren, J. Palisaitis, A. Petruhins, F. F. Klimashin, L. Hultman, I. Petrov, P. O. Persson, and J. Rosen, Scr. Mater. **200**, 113915

Publication II

Die approbierte gedruckte Originalversion dieser Dissertation ist an der TU Wien Bibliothek verfügbar.
The approved original version of this doctoral thesis is available in print at TU Wien Bibliothek.

TU Bibliothek Your knowledge hub WIEN

(2021).
[47] M. Stüber, H. Riedl, T. Wojcik, S. Ulrich, H. Leiste, and P. H. Mayrhofer, Thin Solid Films **688**, 137361 (2019).
[48] P. H. Mayrhofer, C. Mitterer, J. G. Wen, J. E. Greene, and I. Petrov, Appl. Phys. Lett. **86**, 1 (2005).
[49] R. Hahn, V. Moraes, A. Limbeck, P. Polcik, P. H. Mayrhofer, and H. Euchner, Acta Mater. **174**, 398 (2019).
[50] L. Zauner, R. Hahn, E. Aschauer, T. Wojcik, A. Davydok, O. Hunold, P. Polcik, and H. Riedl, Acta Mater. **239**, 118260 (2022).
[51] M. Audronis, A. Leyland, P. J. Kelly, and A. Matthews, Surf. Coatings Technol. **201**, 3970 (2006).
[52] K. L. Dahm, L. R. Jordan, J. Haase, and P. A. Dearnley, Surf. Coatings Technol. **108-109**, 413 (1998).
[53] S. Zhang, Z. Wang, P. Guo, P. Ke, M. Odén, and A. Wang, Surf. Coatings Technol. **322**, 134 (2017).
[54] C. Fuger, R. Hahn, L. Zauner, T. Wojcik, M. Weiss, A. Limbeck, O. Hunold, P. Polcik, and H. Riedl, Mater. Res. Lett. **10**, 70 (2022).
[55] C. L. Jiang, Z. L. Pei, Y. M. Liu, H. Lei, J. Gong, and C. Sun, Appl. Surf. Sci. **288**, 324 (2014).
[56] CrysTec GmbH, "Data sheet: Sapphire for Research and Development," (2022).
[57] ICDD, Powder Diffr. File - Hexag. CrSi2 - 04-001-7333 (2011).
[58] ICDD, Powder Diffr. File - rhombohedral Cr2O3 - 00-006-0504 (1970).
[59] ICDD, Powder Diffr. File - orthorhombic CrB - 04-003-6125 (2011).
[60] ICDD, Powder Diffr. File - rhombohedral Al2O3 - 00-046-1212 (1970).
[61] P. K. Liao and K. E. Spear, Bull. Alloy Phase Diagrams **7**, 232 (1986).
[62] N. Birks, G. H. Meier, and F. S. Pettit, *Introd. to High Temp. Oxid. Met. Second Ed.*, 2nd ed. (Cambridge University Press, 2006) pp. 1–338.

Publication II

Die approbierte gedruckte Originalversion dieser Dissertation ist an der TU Wien Bibliothek verfügbar.
The approved original version of this doctoral thesis is available in print at TU Wien Bibliothek.

TU Bibliothek Your knowledge hub WIEN

Publication III

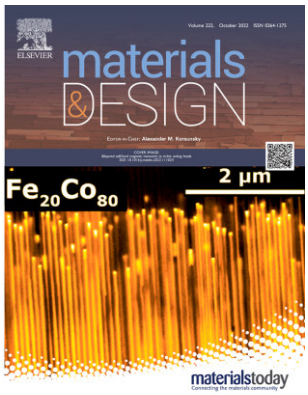

Influence of Si segregates on the structural evolution, mechanical properties, and high-temperature fracture toughness of Cr-Si-$B_{2\pm z}$ coatings

L. Zauner, R. Hahn, O. Hunold, J. Ramm, S. Kolozsvári, P. Polcik, and H. Riedl

under review at *Materials & Design* since 30.10.2022.

Die approbierte gedruckte Originalversion dieser Dissertation ist an der TU Wien Bibliothek verfügbar.
The approved original version of this doctoral thesis is available in print at TU Wien Bibliothek.
TU Bibliothek Your knowledge hub WIEN

Influence of Si segregates on the structural evolution, mechanical properties, and high-temperature fracture toughness of Cr-Si-$B_{2\pm z}$ coatings

L. Zauner,[1,*] R. Hahn,[1] O. Hunold,[2] J. Ramm,[2] S. Kolozsvári,[3] P. Polcik,[3] and H. Riedl[1,4]

[1] *Christian Doppler Laboratory for Surface Engineering of high-performance Components, Austria*
[2] *Oerlikon Balzers, Oerlikon Surface Solutions AG, Liechtenstein*
[3] *Plansee Composite Materials GmbH, Germany*
[4] *Institute of Materials Science and Technology, Austria*

(Dated: November 5, 2022)

The impact of Si-segregates and varying deposition conditions on the structural and mechanical properties of oxidation-resistant Cr-Si-$B_{2\pm z}$ coatings is studied from ambient, to elevated temperatures. Overstoichiometric, AlB_2-structured Cr-Si-$B_{2\pm z}$ thin films with Si-content up to 15 at.% were synthesized on Ti-6Al-4V by magnetron-sputtering using a substrate bias of -120 V. The enhanced surface diffusion promotes mechanically superior, (001)-oriented coatings with hardness of H∼30 GPa up to a Si-content of 3 at.%. Higher Si-concentrations result in significant hardness loss to H∼20 GPa, related to a bias-independent solubility-limit in the CrB_2-structure and the formation of mechanically-weak Si grain-boundary segregates. The as-deposited hardness of all Cr-Si-$B_{2\pm z}$ compositions is maintained after annealing to 800 °C, despite the initiation of material recovery. A B/Cr-ratio-independent oxidation resistance up to 1400 °C is demonstrated, underlining a minimum Si-content of 8 at.% to form a stable SiO_2-based scale. In line with the room-temperature hardness, increasing Si-contents are accompanied by decreasing fracture toughness, reducing from K_{IC}∼2.9 ($Cr_{0.28}B_{0.72}$) to ∼1.7 MPa$\sqrt{m}$ ($Cr_{0.24}Si_{0.10}B_{0.66}$). High-temperature cantilever bending up to 800 °C revealed a brittle-to-ductile-like transition for $Cr_{0.28}B_{0.72}$, resulting in increased fracture toughness of K_{IC}∼3.3 MPa$\sqrt{m}$. Si-alloyed coatings show analogous behavior up to 400 °C, whereas beyond, Si-segregates enable high-temperature plasticity and thus a significantly increased damage tolerance.

Keywords: Borides; PVD; Segregation; Oxidation resistance; High-temperature Micromechanics; Mechanical Properties;

I. INTRODUCTION

The mechanical properties of bulk materials at elevated temperatures cover a well investigated field of materials science [1–4]. This includes the temperature dependent description and analysis of physical properties including the modulus of elasticity, tensile strength, hardness, fatigue limits, and in particular the fracture resistance. Especially the latter property has been thoroughly described for a wide range of metals and alloys [5–10], technical ceramics [3, 11–13], as well as intermetallics [14, 15]. However, the high temperature fracture behavior of thin film materials – particularly ceramic coatings that are regularly applied in harsh environments to compensate for limiting bulk material properties – remain rather unexplored.

An emerging family of ceramic thin film materials that is targeted towards operating in ultra-high temperature applications due to their distinct refractory character, are transition metal diborides (TMB_2). This group of materials offers outstanding melting temperatures in excess of 3000 °C, paired with excellent thermal and chemical stability as well as high hardness and strength [16–20]. However, phase-pure TMB_2 suffer from comparably low oxidation resistance at temperatures beyond 600 °C, related to the formation of volatile B-O-(H)-based compounds when exposed to oxygen and water vapor containing environments [21, 22]. This resulted in various alloying strategies to improve the oxidation behavior by means of solid solutions or multi-phased compounds. For bulk TMB_2, the most promising improvements were achieved via the addition of Si-containing compounds (*e.g.*, SiC or $MoSi_2$), attributed to the formation of a stable, amorphous (boro)-silicate oxide scale [23–25].

Following this alloying strategy, recent studies highlighted the viability of using Si as a similarly potent oxide former in TM-Si-B_2-based coatings, revealing oxidation rates three orders of magnitude lower compared to TMB_2/SiC compounds at 1100 °C [26, 27]. Especially Cr-Si-B_2-based coatings portrayed outstanding oxidation properties, exhibiting minimum mass gain and oxide scale growth rates even up to 1400 °C [28].

Inevitably, the addition of Si and corresponding compounds will alter the mechanical properties of TMB_2 binaries, both in terms of the alloying constituents as well as the temperature regime. Several works that would take advantage of SiC alloying for improved oxidation resistance in bulk ZrB_2, simultaneously reported on enhanced specific strength and fracture resistance over a wide temperature range by tailoring the compositional arrangement [16, 29–31]. In the case of ceramic thin films, a similar effectiveness of Si-alloying was observed for TiN. Despite only achieving limited improvements in oxidation resistance [32], a concomitant increase in hardness and fracture toughness of ∼30 and ∼60% was observed, respectively [33]. Considering the complex bonding nature of AlB_2-structured diborides, the limited research covering compositional and synthesis variations so far suggests a

* lukas.zauner@tuwien.ac.at

Publication III

Die approbierte gedruckte Originalversion dieser Dissertation ist an der TU Wien Bibliothek verfügbar.
The approved original version of this doctoral thesis is available in print at TU Wien Bibliothek.

TU Wien Bibliothek Your knowledge hub

negative impact of Si on the room temperature hardness for several TM-Si-B_2 [27]. Besides the known orientation dependency of the mechanical properties [34], this effect could be linked to Si grain boundary decorations formed during film growth upon exceeding a TMB_2 specific solubility limit [28]. In consequence, it seems imperative to investigate altered synthesis conditions, expanding the current viewpoint of the relationship between deposition parameters and the thermo-physical properties of TM-Si-B_2 thin films. Furthermore, with the improved oxidation behavior, increasing the knowledge on film hardness and fracture resistance at elevated temperatures appears a logical step forward.

While small-scale micromechanical testing at room temperature is crucial for the development of materials operated at ambient conditions, most applications of ceramic coatings necessitate testing at elevated temperatures. However, given the high complexity of low temperature measurements, possible difficulties are certainly amplified when introducing the influence of temperature. Thus, only few examples of high-temperature micromechanical testing on ceramic thin film materials exist to date. In an early work, Wheeler *et al.* [35] studied the temperature dependent compressive strength of CrN-based hard coatings by micro-pillar compression technique. In a series of experiments up to 500 °C, they highlighted that differences in the temperature dependent property evolution can cause a shift between rankings at room temperature and those at elevated temperatures. The results unequivocally demonstrated the necessity for high temperature property analysis. Furthermore, Best *et al.* [36] showed that thermal diffusion of Ga atoms in focused ion beam prepared micro-cantilevers affects the high temperature fracture toughness of CrN through intergranular embrittlement. An analogous micron sized geometry was used by Buchinger *et al.* [37], who studied the high temperature fracture behavior of TiN, both experimentally and theoretically. They revealed the negative impact of point defect annihilation at temperatures exceeding the deposition condition, leading to an irreversible decrease in fracture toughness throughout the entire temperature range. Finally, Drnovšek *et al.* [38] recently investigated the high temperature fracture properties of morphologically varying CrAlN (columnar) and CrAlSiN (nanocrystalline) by microcantilever bending technique. A similar behavior was revealed below the deposition temperature, while above a diverging fracture resistance was observed and attributed to the morphological differences.

In this work, we continue to explore the structural and mechanical properties of Si alloyed $CrB_{2\pm z}$-based thin films through targeted synthesis variations. The resulting compositional and structural ensemble is discussed in the context of room temperature nanoindentation and dynamic thermogravimetry up to 1400 °C. Thereby, novel insights on previously established Si solubility limits and optimum chemical compositions are described. Furthermore, vacuum annealing treatments are performed on coated Ti-6Al-4V, probing the temperature dependent hardness evolution as influenced by thermally activated solid state processes. Finally, the high temperature fracture resistance of selected Cr-Si-$B_{2\pm z}$ compositions is studied by detailed *in-situ* microcantilever bending experiments up to 800 °C.

II. EXPERIMENTAL

Direct current magnetron sputtering was used to grow AlB_2-type Cr-Si-$B_{2\pm z}$ thin films from a 3-inch CrB_2 compound target (Plansee Composite Materials GmbH, 99.3% purity) operated in a lab-scale deposition system (in-house developed, base pressure below 1.0×10^{-6} mbar). Up to 16 Si platelets ($3.5\times3.5\times0.38$ mm^3) were placed on the target racetrack to gradually adjusted the Si content in the synthesized coatings. The thin films were grown on (100)-oriented Si ($20\times7\times0.38$ mm^3), single-crystalline, $(1\bar{1}02)$-oriented Al_2O_3 ($10\times10\times0.53$ mm^3), poly-crystalline Al_2O_3 ($20\times7\times0.38$ mm^3) and mirror-polished Ti-6Al-4V ($10\times10\times1$ mm^3) substrates. Following an ultrasonic pre-cleaning step in acetone and isopropyl, respectively, a heating sequence to a constant substrate temperature of T = 550 °C was performed. Prior to all depositions, Ar-ion etching was used to clean the substrate surface from native oxides and remaining residuals at a total pressure of p = 50 μbar and substrate bias potential of U = -800 V for 10 min. The substrates were fixtured in a rotating sample holder with a constant target-to-substrate distance of 90 mm. To additionally pre-clean the target surface and Si platelets for minimum oxygen contamination within the coatings, they were simultaneously sputter cleaned behind a shutter during the last 3 min of the Ar-ion etching sequence. The coatings were then synthesized at an Ar pressure of p = 7 μbar, a cathode current of I = 0.4 A (≈5 W/cm^2), and a substrate bias potential of U = -120 V. A consistent coating thickness of $t \sim 3$ μm was targeted, therefore the deposition time was adjusted accordingly.

The chemical composition of all Cr-Si-$B_{2\pm z}$ thin films was evaluated using liquid inductively coupled plasma-optical emission spectroscopy (ICP-OES). For more details on the methodical procedure, see Ref. [27]. The crystal structure in the as-deposited as well as several annealed states was analyzed by X-ray diffraction, performed in Bragg-Brentano geometry on a PANalytical XPert Pro MPD equipped with a Cu-Kα radiation source (wave length λ=1.54 Å, operated at 45 kV and 40 mA) and a strip detector (PANalytical X'Celerator). Furthermore, nanoindentation performed with an ultra-micro indentation system (UMIS) was used to determine the hardness and Young's modulus of all Cr-Si-$B_{2\pm z}$ coatings. Stepwise increased indentation loads from 5 up to 22 mN (steps of 0.5 mN) were used to collect a minimum of 30 load-displacement curves for analysis according to the procedure proposed in Ref. [39]. Additional indents at forces up to 45 mN were added to probe for any substrate interference with the calculated results. For hardness

Die approbierte gedruckte Originalversion dieser Dissertation ist an der TU Wien Bibliothek verfügbar.
The approved original version of this doctoral thesis is available in print at TU Wien Bibliothek.
TU Bibliothek Your knowledge hub WIEN

evaluation an indentation depth smaller than 10% of the entire coating thickness was maintained. Furthermore, the recorded Young's modulus data was fitted as function of the indentation depth h_t using a power law relation and subsequently extrapolated to $h_t = 0$ for the coating-only modulus [40]. Finally, optical profilometry performed on a PS50 system (Nanovea) was employed to record the sample curvature of coated Si substrates. Combined with the modified Stoney-equation the residual stress state was determined [41, 42].

The influence of Si alloying on the oxidation resistance of the Cr-Si-$B_{2\pm z}$ coatings was studied by dynamic thermogravimetric analysis (TGA, Netzsch STA 449 F1, conducted in a Rhodium-type furnace). Therefore, polycrystalline Al_2O_3 substrates were weighed prior and after deposition to determine the coating-only mass, which serves as reference during the oxidation treatments performed up to 1400 °C (heating rate of 10 °C/min) in synthetic air (flow of 50 ml/min). The oxidation of the coating material was associated with the recorded mass change (detected at a resolution of 0.1 μg). Reference measurements on uncoated Al_2O_3 substrates showed that the material is inert in the investigated temperature regime, hence a contribution from the substrate to the recorded mass change can be excluded [27].

All Cr-Si-$B_{2\pm z}$ coatings deposited onto Ti-6Al-4V were vacuum annealed in a Centorr LF22-2000 vacuum furnace at temperatures of T = 400, 600, and 800 °C for 30 min (heating rate of 20 K/min, passive cooling at >50 K/min to 200 °C). A base pressure below 1.0×10^{-5} mbar was established before each annealing treatment. Afterwards, all samples were again analyzed by X-ray diffraction and nanoindentation.

Selected Cr-Si-$B_{2\pm z}$ thin films on Ti-6Al-4V were investigated concerning their high-temperature fracture toughness using microcantilever bending experiments [43]. These tests were performed on a FemtoTools FT-NMT04 *in-situ* nanoindentation system equipped with a sample heater stage and a diamond wedge tip (contact length of 10 μm). The experiments were conducted at room temperature (RT) as well as at T = 400, 600, and 800 °C, with additional tests performed in the annealed state after cooling down to room temperature (RT p.a.). Therefore, free standing micro-cantilever specimen were prepared by focused ion beam milling (FIB) using Ga^+-ions in a ThermoFisher Scios 2 DBFIB microscope and in accordance with the guidelines suggested in Ref. [44]. Based on a mirror polished cross-section of a coated Ti-6Al-4V substrate, the micro-cantilevers were prepared by the following milling sequence: (*i*) Rough milling of the cantilever outlines through the coating material and ~10 μm deep into the substrate (ion beam aligned perpendicular to the coated surface, ion beam current of 30 nA). This initial cantilever geometry is aligned parallel to and placed 2 μm from the front edge. (*ii*) Removing of the substrate material beneath the rough-cut cantilever and fine milling to the final thickness, producing a coating-only beam (ion beam aligned perpendicular to cross-section, ion beam current reduced stepwise from 30 to 1 nA). (*iii*) Fine milling of the cantilever contour to the final dimensions and fabrication of a pre-notch (ion beam aligned perpendicular to coated surface, ion beam current reduced stepwise from 5 to 1 nA, pre-notch produced at a milling current of 50 pA). The cantilevers were produced to a final geometry of length (l) × width (b) × height (w) = $t \times t \times 6t$ μm^3, whereby t denotes the coating thickness, with a pre-notch depth of $a_0 \sim$ 400-450 nm. Thin material sections were left intact on both sides of the pre-notch, serving as initiation sites for a sharp crack. Temperature calibration between the tip and sample was conducted using the balancing function provided in the operating software. The procedure performs shallow indentations every few seconds in the bulk coating area close to the cantilever specimen, wherein the force response on the tip upon unloading is recorded. The tip current is adjusted accordingly until a sufficiently low thermal discrepancy (*i.e.*, force response) is achieved. Details on the procedure are listed in Ref. [45]. The bending experiments were performed in displacement-controlled mode at a deflection rate of 10 $nm{\cdot}s^{-1}$.

Based on measurements of the individual fractured cantilever cross-section in combination with the recorded maximum force at failure, a value for the critical stress intensity K_{IC} of each cantilever was calculated utilizing the formalism outlined in [46]:

$$K_{IC} = \frac{F_C l}{b w^{3/2}} \times f(\frac{a_0}{w}) \quad (1)$$

with

$$f(\frac{a_0}{w}) = 1.46 + 24.36(\frac{a_0}{w}) - 47.21(\frac{a_0}{w})^2 + 75.18(\frac{a_0}{w})^3 \quad (2)$$

At least 4 samples were tested and evaluated at every temperature step.

III. RESULTS & DISCUSSION

A. Chemical Composition

Figure 1 presents the chemical compositions of all Cr-Si-$B_{2\pm z}$ thin films in the context of a ternary phase diagram. The depicted compositional range is extended with guidelines (corresponding to narrow two-phase fields) connecting stoichiometric CrB_2 with Si and $CrSi_2$, to indicate possible phase mixtures in the as-deposited state. Chemical analysis using ICP-OES revealed a linear increase in the Si alloying content within the Cr-Si-$B_{2\pm z}$ thin films, showing an almost 1:1 correlation between the number of Si platelets placed on the target racetrack during sputtering and the resulting atomic concentration. Hence, utilizing 2, 4, 6, 8, 12, and 16 Si platelets for the synthesis process resulted in corresponding Si compositions of 2, 3, 4, 6, 10, and 15 at.%, respectively. Furthermore, the data reveals a clear shift of all chemistries towards B-rich compositions – *i.e.*, a deviation from the stoichiometric CrB_2

Publication III

Die approbierte gedruckte Originalversion dieser Dissertation ist an der TU Wien Bibliothek verfügbar.
The approved original version of this doctoral thesis is available in print at TU Wien Bibliothek.

TU Bibliothek Your knowledge hub WIEN

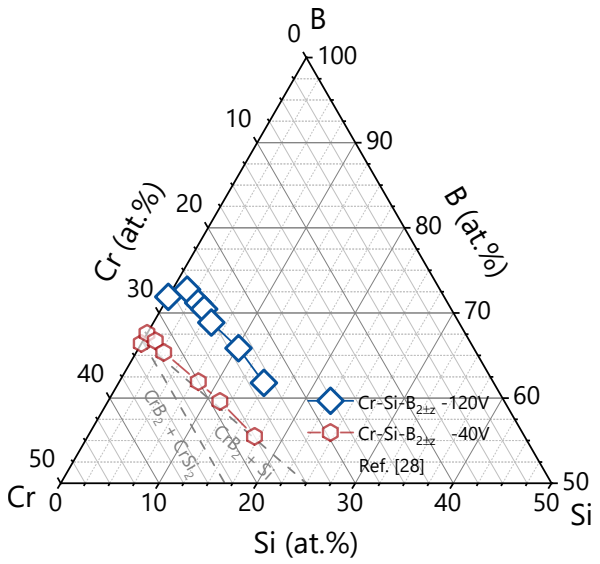

Fig. 1. Ternary phase diagram depicting the chemical composition of all synthesized Cr-Si-$B_{2\pm z}$ coatings (blue diamonds). The chemistry of corresponding thin films deposited at a substrate bias voltage of U = -40 V (red hexagons, Ref. [28]) as well as guidelines for two-phase fields are included. The axis scaling is reduced for improved visibility of the individual data points.

+ Si line – suggesting a B-overstoichiometry especially for lower alloyed thin films. Starting with a B concentration of 72 at.% in the unalloyed coating, an overall decrease is observed from 72 at.% for $Cr_{0.26}Si_{0.02}B_{0.72}$, down to 62 at.% in $Cr_{0.23}Si_{0.15}B_{0.62}$ with increasing Si fraction. Regarding the B:Cr ratios, the impression of excess B content is underlined by values increasing from 2.6 up to 2.8 for the highest Si containing coating. Nevertheless, the chemical compositions reveal an actual replacement of both B and Cr in the stoichiometric 2:1 ratio, respectively.

It is imperative to mention that the overstoichiometry is inherently dependent on the actual lattice occupation of the Si atoms as well as the individual contribution of the constitutional elements to the phase formation. As previously revealed by detailed DFT calculations, the Cr-Si-B_2 system prefers the incorporation of substitutional Si atoms on the Cr- and B-lattice for lower alloying fractions, whereas for higher concentrations only Cr replacement yields chemically stable configurations [28]. Moreover, a theoretically proposed Si solubility limit close to 8 at.% in the AlB_2-structure, which was experimentally determined with a lower value of ∼3-4 at.%, suggests that all coatings with an alloying fraction higher than $Cr_{0.26}Si_{0.03}B_{0.71}$ obtain Si grain boundary segregations in the as-deposited state. Thus, the presence of a B overstoichiometry in all thin films, with possible contributions of B to the Si grain boundary decorations – in agreement with the respective chemical composition within the phase fields in Figure 1 – can be expected.

The observed increase in B over the prototypical $Cr_{0.33}B_{0.67}$ target composition is seen in the prevalent synthesis conditions, especially in the film growth conditions on the substrate surface created by the high bias potential of U = -120 V. When compared to data of previous Cr-Si-$B_{2\pm z}$ thin films deposited at a bias potential of U = -40 V, (see Figure 1, red hexagons, other deposition conditions were analogous), a noticeable impact of the substrate bias to promote higher B contents in the growing thin films is evident. Furthermore, the comparison reveals a very alike behavior in terms of the B- and Cr-replacement with increasing Si alloying fraction, although overall higher Si contents could be reached at a lower substrate bias. Interestingly, the increase in B content with enhanced bias potential appears counterintuitive, since lighter elements typically suffer from increased scattering and resputtering effects during the synthesis process. However, the close matching atomic weight between Ar^+ ions and Cr film atoms yields a more effective energy transfer and lifts the preferred resputtering tendency from the B atoms, which causes the recorded overstoichiometry. A similar effect was previously observed during the sputter deposition of TiB_2 using similar bias voltage variations [47].

B. Phase Formation

Apart from the impact on thin film chemistry, the chosen synthesis conditions will also be reflected in the phase formation of the Cr-Si-$B_{2\pm z}$ coatings. Figure 2 presents the recorded X-ray diffractographs, arranged with increasing Si content from bottom to top. In addition, the right panel includes the (001)-texture coefficient for every diffractograph according to the following equation:

$$TC_{(hkl)} = \frac{I_{(hkl)}/I_{0(hkl)}}{\frac{1}{N}\sum_N I_{(hkl)}/I_{0(hkl)}} \qquad (3)$$

where $I_{(hkl)}$ is the diffracted intensity on the (hkl)-lattice plane, $I_{0(hkl)}$ is the corresponding reference intensity for powdered CrB_2 [48], and N equals 3, representing the (001), (100), and (101) planes. The diffraction studies demonstrate that all Cr-Si-$B_{2\pm z}$ coatings adopt the AlB_2-type hexagonal structure, irrespective of the alloying content and the B overstoichiometry. The distinct impact on phase formation created through the high bias voltage within all depositions is nicely demonstrated when comparing the unalloyed $Cr_{0.28}B_{0.72}$ coating to a $Cr_{0.34}B_{0.66}$ composition, grown at a lower substrate bias of -40 V (see Figure 2, bottom). Apparently, increasing the surface mobility for arriving film constituents through increased Ar^+ bombardment results in a shift from (101)-, towards film growth conditions preferring the (001)-direction. Concomitantly, with a denser microstructure – as evidenced by scanning electron microscopy of Si fracture cross-sections (see Supplementary) – TMB_2 thin films show a desirable optimum in film

Publication III

Die approbierte gedruckte Originalversion dieser Dissertation ist an der TU Wien Bibliothek verfügbar.
The approved original version of this doctoral thesis is available in print at TU Wien Bibliothek.

TU Bibliothek Your knowledge hub WIEN

hardness in the (001)-direction [34] (detailed discussion follows in Section III C). Up to a Si content of 3 at.% in $Cr_{0.26}Si_{0.03}B_{0.71}$, film growth conditions remain unaltered in the preferred (001)-orientation, although an increasing contribution from differently oriented grains is noticeable. Further increasing the alloying content results in a shift towards the (100)-direction for both $Cr_{0.25}Si_{0.04}B_{0.71}$ and $Cr_{0.25}Si_{0.06}B_{0.69}$, before diverting back to (001)-oriented for the $Cr_{0.24}Si_{0.10}B_{0.66}$ composition (see Figure 2, right panel). Finally, the diffractograph for the highest Si containing coating $Cr_{0.23}Si_{0.15}B_{0.62}$ suggests equally oriented grains and a clear reduction of the diffracted intensities, pointing towards a decreasing average grain size. This contrasts with previous findings for Cr-Si-$B_{2\pm z}$ deposited at a bias voltage of -40 V, where a similar grain refinement was already present for lower alloying fractions, starting at Si concentrations of ∼4 at.% [28]. This effect could be correlated with surpassing the Si solubility limit in the hexagonal CrB_2 structure, leading to the energetically favored segregation of the alloying species to grain boundary sites. Although an extension of this solubility limit with increased bias voltage is unlikely, the growth of larger crystalline domains is enabled up to 10 at.%, following the enhanced adatom mobility. Finally, in view of the phase fields included in Figure 1, no additional crystalline structure was detected by X-ray diffraction technique throughout all experimentally studied Cr-Si-$B_{2\pm z}$ compositions.

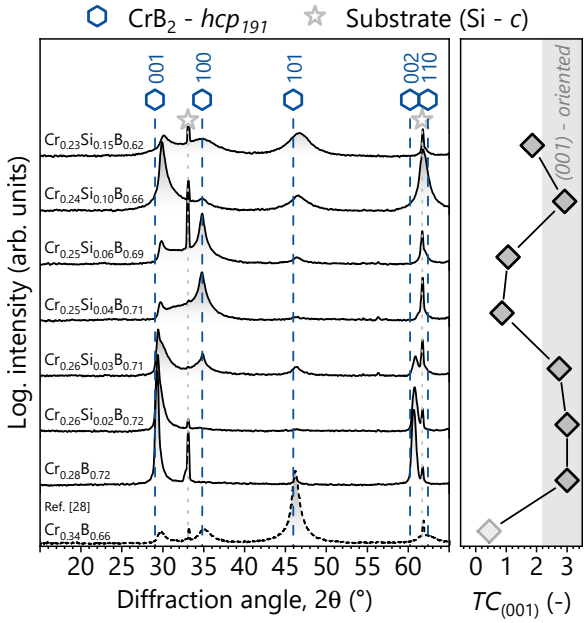

Fig. 2. X-ray diffractographs of Cr-Si-$B_{2\pm z}$ thin films deposited on Si substrate with increasing alloying content from bottom to top. A diffractograph recorded from a $Cr_{0.34}B_{0.66}$ coating deposited with a substrate bias of U = -40 V is included for comparison on the bottom (taken from Ref. [28]). In addition, standardized reference pattern for hexagonal CrB_2 (space group 191, blue hexagons, [48]) and cubic Si (substrate, grey stars, [49]) are added for structural comparison. The intensity ratio of the (001)-peak is further presented in the right panel, with data points matching the diffractographs in y-direction.

C. Mechanical Properties at Room Temperature

The mechanical properties of the Cr-Si-$B_{2\pm z}$ thin films are summarized in Figure 3, presenting the residual biaxial stress state as well as the hardness and Young's modulus versus the Si alloying content. While nanoindentation experiments were obtained from thin films on Ti-6Al-4V, residual stress measurements could solely be obtained from coated Si substrate through curvature measurements. The high degree of (001)-orientation within several Cr-Si-$B_{2\pm z}$ samples prohibits a consistent stress analysis on the Ti-substrate using the $\sin^2(\psi)$-approach. Considering the impact of varying thermal expansion coefficients between the coatings ($\alpha_a^{CrB_2}$ = 10.8 × $10^{-6}K^{-1}$, $\alpha_c^{CrB_2}$ = 6.3 × $10^{-6}K^{-1}$, [50]) and both substrate materials (α^{Si} = 2.5 - 4 × $10^{-6}K^{-1}$ [51], $\alpha^{Ti\text{-}6Al\text{-}4V}$ = 8 - 10 × $10^{-6}K^{-1}$ [52]), a shift towards a more compressed stress state can be assumed for all coatings on the Ti-alloy (note, the absolute value may still be located in the tensile regime). Furthermore, depending on a possible template effect, the different substrate materials may entail altered film growth conditions and thus growth-related stresses. However, comparison of X-ray diffractographs obtained from depositions on both substrates (compare Figures 2 and 6) revealed identical crystallographic distributions as well as diffracted intensities throughout the Cr-Si-$B_{2\pm z}$ compositions. In addition, the influence of altered synthesis conditions is addressed by a complementary data set taken from Ref. [28] for a $Cr_{0.34}B_{0.66}$ coating, deposited with bias voltage of U = -40 V (see also Figure 2, bottom).

Measurements on the unalloyed $Cr_{0.28}B_{0.72}$ coating reveal a slight compressive stress state at $\sigma \sim$ -0.25 GPa combined with an excellent hardness of H = 29.1±1.1 GPa and a Young's modulus of E = 339±7 GPa. When compared to the Si-free reference coating [28], a striking difference of over 5.5 GPa in film hardness is noticed, while the Young's modulus increased by approximately 45 GPa. This improvement is rationalized by the difference in preferred growth orientation and an overall densification of the film microstructure due to the increased bias potential. The results unequivocally highlight the distinct anisotropy of this AlB_2-structured diboride, pointing out highest film hardness in the (001)-orientation [34]. Moreover, the densified film structure is further correlated with the observed increase of the Young's modulus, which is likely the result of enhanced cohesive strength on grain boundary sites.

Introducing Si to the Cr-$B_{2\pm z}$ thin films results in a shift of the residual stress state towards the tensile regime, with the highest value recorded for the $Cr_{0.25}Si_{0.04}B_{0.71}$ composition at $\sigma \sim$ 0.8 GPa. This trend appears to be

Publication III

Die approbierte gedruckte Originalversion dieser Dissertation ist an der TU Wien Bibliothek verfügbar.
The approved original version of this doctoral thesis is available in print at TU Wien Bibliothek.
TU Bibliothek Your knowledge hub WIEN

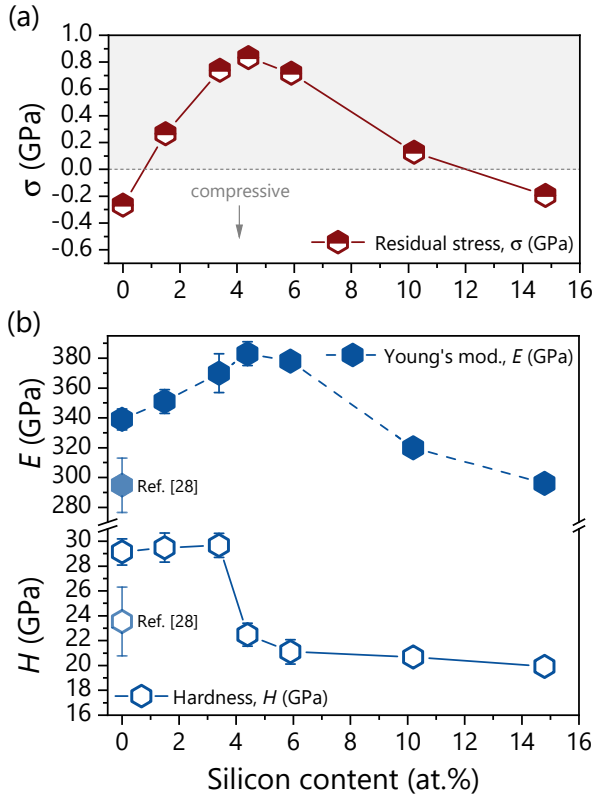

Fig. 3. (a) Residual stress of the synthesized Cr-Si-$B_{2\pm z}$ thin films on Si substrate as function of the Si alloying content. (b) Hardness and Young's modulus data for the corresponding compositions in (a) collected on Ti-6Al-4V substrate. For comparison, (a) and (b) contain data for a $Cr_{0.34}B_{0.66}$ coating deposited with a substrate bias of U = -40 V taken from Ref. [28] (see Figure 2, bottom).

decoupled from the film orientation, since all coatings between 4 and 6 at.% Si maintain a similar stress profile despite exhibiting an increasing (100)-orientation. A possible explanation is seen in reduced compressive growth stresses resulting from the increasing Si alloying content. A comparable evolution is observed for the Young's modulus, revealing a concomitant increase up to E = 383 GPa for $Cr_{0.25}Si_{0.04}B_{0.71}$. In agreement with previous reports on the elastic constants of CrB_2 ($E^{CrB_2}_{(100)}$ = 531 GPa, $E^{CrB_2}_{(001)}$ = 302 GPa), the enhanced contribution of the stiffer (100)-orientation is attributed to cause an increase in the elastic modulus. The hardness data shows a significant decrease for Si concentrations above 4 at.%, with values drastically falling from H = 29.7±1.0 GPa for $Cr_{0.26}Si_{0.03}B_{0.71}$ down to H = 22.5±0.9 GPa for $Cr_{0.25}Si_{0.04}B_{0.71}$. These results reflect the divergence from the (001)-orientation with increasing Si content and the initial segregation of the alloying species towards grain boundary sites during the film growth process. Consequently, this also underpins the previous correlation to a solubility limit located the same alloying regime (see Section III B).

The coatings with the highest Si content, $Cr_{0.24}Si_{0.10}B_{0.66}$ and $Cr_{0.23}Si_{0.15}B_{0.62}$, exhibit rather low residual stress values at $\sigma \sim$ 0.1 and -0.2 GPa, respectively. In addition, the increasing segregation of Si to the grain boundaries (see Section III A and Ref. [28]) leads to a refined microstructure and an overall increase in weaker-connected grain boundary volume, resulting in a decrease of the Young's modulus to E = 296±4 GPa. Moreover, the film hardness assumes rather constant values at $H \sim$ 20 GPa for all Cr-Si-$B_{2\pm z}$ compositions above 6 at.% Si, also reflecting the dominating aspect of the weaker connection on grain boundary sites. Nevertheless, the results highlight that utilizing energetic ion bombardment for the deposition of Cr-Si-$B_{2\pm z}$ thin films lead to an increase in film hardness between 4 and 6 GPa over compositionally similar coatings deposited at U = -40 V.

D. Thermogravimetric Analysis

Previous dynamic oxidation experiments of various Si alloyed TM-$B_{2\pm z}$-based thin films highlighted the capabilities of this alloying route to significantly improve the oxidation resistance over the binary materials [27]. Next to the effective Si alloying content, the ratio between the boron and transition metal was demonstrated to crucially impact the oxidation behavior of these materials. Especially boron deficient TM-B_{2-z} compositions revealed improved oxidation protection related to the absence of B-rich grain boundary decorations, which are usually responsible for providing fast-track oxidation pathways [53, 54]. Therefore, dynamic thermogravimetric experiments were performed on the synthesized Cr-Si-$B_{2\pm z}$ thin films to investigate the oxidation behavior of drastically increased B/TM-ratios and prove the robustness of the Si alloying route (see Figure 4).

In relation to analogous experiments performed on Cr-Si-$B_{2\pm z}$ coatings obtaining a B/TM ratio of ~2.0 [28] and ~2.2 [27], the oxidation tests resulted in an identical protective performance, shifting the onset of oxidative mass gain consistently from T = 600 up to 1100 °C, depending on a "sufficient" Si alloying content. Even for "insufficiently" alloyed compositions, a very similar oxidation response was reported, resulting in a stepwise formation of mixed B_2O_3 and Cr_2O_3 scales. The mass change data during oxidation up to 1400 °C presented in Figure 4 highlights, that even compositions with a B/TM-ratio approaching 2.8 (see also Figure 1) obtain an entirely unchanged, excellent oxidation resistance throughout the corresponding Si compositions. While, the coatings synthesized with a Si content ≤4 at.% undergo progressive oxidation starting at T = 600 °C, both coatings with an alloying content ≥10 at.% depict a fully stable mass signal up to T = 1200 °C. Consequently, the results strongly

Publication III

Die approbierte gedruckte Originalversion dieser Dissertation ist an der TU Wien Bibliothek verfügbar.
The approved original version of this doctoral thesis is available in print at TU Wien Bibliothek.
TU Bibliothek Your knowledge hub WIEN

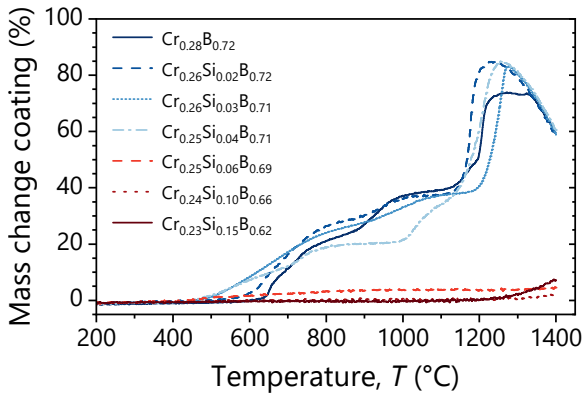

Fig. 4. Thermogravimetric analysis of Cr-Si-$B_{2\pm z}$ thin films on polycrystalline Al_2O_3 substrate up to $T = 1400$ °C (10 K/min heating rate) in synthetic air environment. The mass change of the coating material is presented as function of the annealing temperature and indicates the onset of sample oxidation. Note, pretests confirmed the inert behavior of the substrate material in the analyzed temperature range.

suggest that the mechanism responsible for the oxidation protection – identified as the thermally activated precipitation of Si on the coating surface [28] – is decoupled from the chemical composition of the $CrB_{2\pm z}$ host structure. In other words, the oxidation resistance scales solely with the effective Si concentration. Nevertheless, a possible contribution of excess boron to the high temperature performance is assumed in the shift of the oxidation onset temperature from previous experiments, which is increased by ∼100 °C to $T = 1200$ °C within the highly overstoichiometric Cr-Si-$B_{2\pm z}$ coatings. A possible explanation could be seen in enhanced Si diffusion along the increased grain boundary volume, decorated with both amorphous B- and Si-rich phases.

Regarding the transition from "insufficiently" to "sufficiently" alloyed compositions, the mass signal recorded for the $Cr_{0.25}Si_{0.06}B_{0.69}$ coating points towards a threshold concentration. Despite the premature onset of oxidation close to $T = 600$ °C, the coating is able to form a stable SiO_2-based scale that remains intact up to $T = 1400$ °C. This result is in excellent agreement with a previously determined minimum Si content of 8 at.% to achieve negligible mass gain up to $T = 1100$ °C [28].

E. Hardness & Structural Evolution up to 800 °C

Vacuum annealing treatments were performed on all Cr-Si-$B_{2\pm z}$ thin films for 30 min at temperatures of $T = 400$, 600, and 800 °C. The annealed samples were subsequently investigated by nanoindentation and X-ray diffraction technique to reveal the film hardness in the annealed state as well as the phase stability and diffusion driven interaction with the Ti-6Al-4V substrate. Figure 5 presents the recorded hardness as function of the annealing temperature. Based on the distribution measured in the as-deposited state (see Figure 3), the data reveals an almost unaffected film hardness throughout the temperature range for all compositions with Si content ≤6 at.%. This is especially interesting, considering the Cr-Si-$B_{2\pm z}$ compounds are known to experience thermally induced segregation of the alloying species at $T > 600$ °C, followed by initial recovery/recrystallisation of the remaining solid solution as well as separation into the binary diboride and pure Si [28]. These solid-state reactions are nicely visible in the X-ray diffractographs presented in Figure 6, recorded in the post-annealed state on the binary $Cr_{0.28}B_{0.72}$ (lower section) and $Cr_{0.25}Si_{0.06}B_{0.69}$ coating (middle section). Thermal treatment of the Si-free coating results in minor structural changes throughout all annealing temperatures. Starting at $T = 600$ °C, slight sharpening of the (001)-peak is noticeable, related to initial recovery of point defects (note the deposition temperature of $T = 550$ °C). Moreover, at $T = 800$ °C additional peaks identified as the orthorhombic mono-borides of Cr and Ti, occur. The latter two structures suggest an interdiffusion between (excess) boron from the coating and the Ti-alloy substrate. Given the low intensities recorded for the mono-borides, it is assumed that both structures are confined to the interface near region without affecting the surface hardness of the coating. The higher Si containing $Cr_{0.25}Si_{0.06}B_{0.69}$ sample shows a similar behavior, with a more pronounced recovery/recrystallisation of the CrB_2-structure starting above $T = 600$ °C. Next to the diffraction spots indicating the previously observed mono-borides, the coating also exhibits the precipitation of Si next to the formation of a hexagonal $CrSi_2$ phase at $T = 600$ °C. Comparison to previous oxidation experiments performed on a

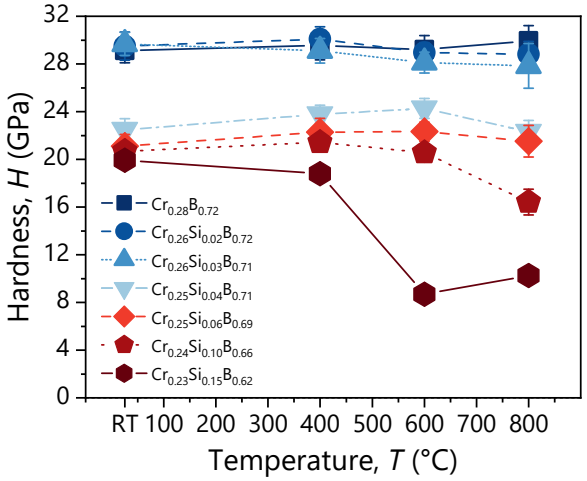

Fig. 5. Hardness values of Cr-Si-$B_{2\pm z}$ thin films on Ti-6Al-4V substrate at room temperature and after vacuum annealing at $T = 400$, 600, and 800 °C (holding duration of 30 min).

Publication III

Die approbierte gedruckte Originalversion dieser Dissertation ist an der TU Wien Bibliothek verfügbar.
The approved original version of this doctoral thesis is available in print at TU Wien Bibliothek.

TU Bibliothek Your knowledge hub WIEN

$Cr_{0.29}Si_{0.11}B_{0.60}$ coated Al_2O_3 substrate [28] reveals that the disilicide formation is independent of the substrate material and annealing environment, hence a distribution around Si precipitates is expected. Still, the structural changes within both coatings appear to be in an initial stage at $T = 800$ °C, where the presence of additional phases is balanced by the unaffected coating material – also in terms of the stress state – resulting in a maintained film hardness.

Increasing the Si content beyond 10 at.% permits a maintained coating hardness up to $T = 600$ °C for the $Cr_{0.24}Si_{0.10}B_{0.66}$, whereas the $Cr_{0.23}Si_{0.15}B_{0.62}$ coating already reveals a decreasing trend. At $T = 800$ °C, both compositions show an effective reduction in hardness from $H = 20.7\pm0.5$ and 19.9 ± 0.4 GPa down to $H = 16.4\pm1.1$ and 10.3 ± 0.5 GPa, respectively. Comparing the structural evolution recorded for the $Cr_{0.23}Si_{0.15}B_{0.62}$ coating in Figure 6 (top section) to lower Si containing compositions (see Figure 6, middle section) reveals a similar trend. However, both the recovery/recrystallisation of the Cr-Si-B_2 solid solution as well as the segregation of Si are more pronounced at $T = 600$ °C, resulting in increased peak intensities for both structures at $T = 800$ °C. This suggests, that the driving force of these solid-state reactions actually scales with the initial Si content in the thin films. An increased diffraction intensity is further observed for the $CrSi_2$ phase, associated with the overall higher Si reservoir available in the coating.

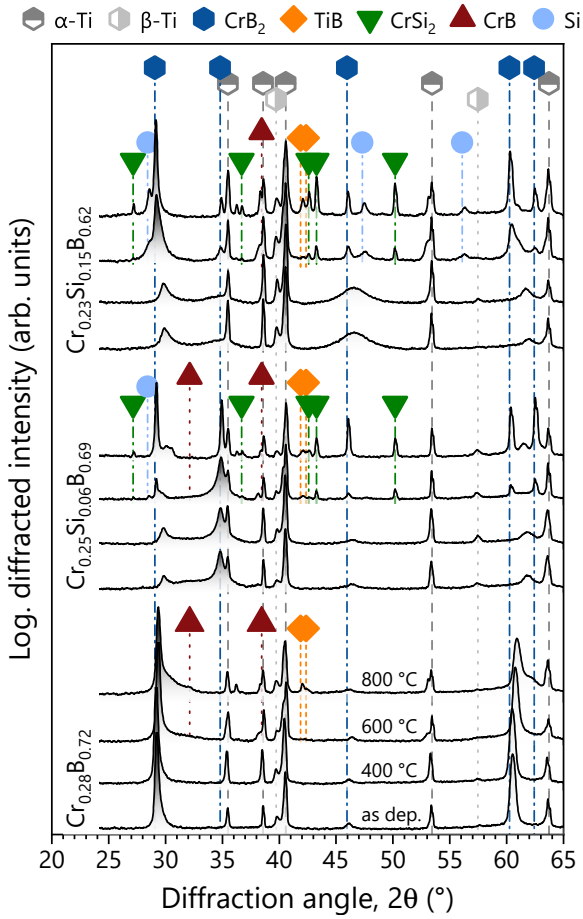

Fig. 6. X-ray diffractographs of three selected Cr-Si-$B_{2\pm z}$ compositions on Ti-6Al-4V are presented in the as-deposited state as well as after vacuum annealing at 400, 600, and 800 °C for 30 min. The diffractographs are arrange in three sections with increasing Si content from bottom to top ($Cr_{0.28}B_{0.72}$, $Cr_{0.25}Si_{0.06}B_{0.69}$, $Cr_{0.23}Si_{0.15}B_{0.62}$). Within each section, the data is sorted with increasing annealing temperature from bottom to top. Standardized reference pattern for hexagonal CrB_2 (space group 191, blue hexagons, [48]), cubic Si (light blue circle, [49]), hexagonal $CrSi_2$ (green triangle, [55]), orthorhombic CrB (red pyramid, [56]) and TiB (orange diamond, [57]), as well as for the dual-phased Ti-6Al-4V substrate material (grey hexagons, α-Ti [58], β-Ti [59]) are included.

Related to the protective mechanism responsible for the increased oxidation resistance, as confirmed by TG analysis in Figure 4, both coatings form a continuous Si surface layer starting at $T = 600$ or 800 °C, depending on the respective Si concentration. Consequently, the recorded loss in hardness for both compositions is attributed to the increasing contribution of this softer surface layer to the nanoindentation experiments. In fact, comparison with literature reports yields a perfect agreement between the hardness of the $Cr_{0.23}Si_{0.15}B_{0.62}$ coating annealed at $T = 600$ and 800 °C with values recorded for pure Si [60].

F. *In-situ* High-Temperature Fracture Toughness

The fracture properties at elevated temperatures were studied for selected Cr-Si-$B_{2\pm z}$ coatings by *in-situ* high-temperature cantilever bending experiments up to $T = 800$ °C. Figure 7 presents the recorded load-displacement data normalized in terms of the stress intensity and bending strain for all compositions within the studied temperature range. In addition, Figure 8 summarizes the calculated critical stress intensity (*i.e.*, the fracture toughness) as function of the annealing temperature.

The bending tests performed on the unalloyed $Cr_{0.28}B_{0.72}$ resulted in a perfectly linear-elastic material response over the entire loading sequence throughout all temperature steps up to $T = 800$ °C (see Figure 7a). The initial fracture toughness in the as-deposited state was calculated with $K_{IC} = 2.87\pm0.05$ MPa$\sqrt{m}$ (see Figure 8). This value is considerably lower when compared to a previous work reporting on a fracture toughness of $K_{IC} = 4.3\pm0.3$ MPa$\sqrt{m}$ for an almost stoichiometric $Cr_{0.35}B_{0.65}$ coating [61]. Apart from the unambiguous influence of varying synthesis conditions, Fuger *et al.* [62] recently highlighted the negative impact of boron enriched grain boundaries – as also assumed within the overstoichiometric $Cr_{0.28}B_{0.72}$ – on the fracture toughness of TiB_{2+z} thin films.

Publication III

Die approbierte gedruckte Originalversion dieser Dissertation ist an der TU Wien Bibliothek verfügbar.
The approved original version of this doctoral thesis is available in print at TU Wien Bibliothek.

TU Bibliothek Your knowledge hub WIEN

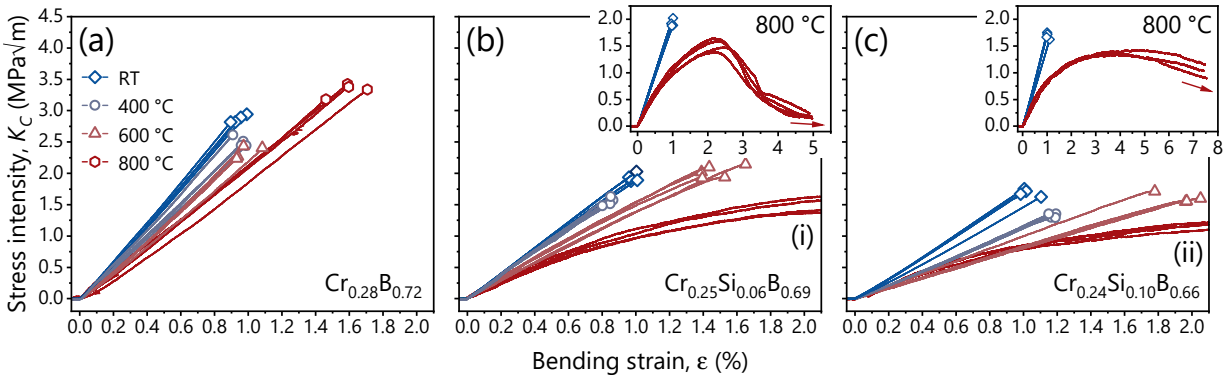

Fig. 7. Normalized stress intensity - bending strain curves recorded during *in-situ* micro-cantilever bending experiments performed at room temperature as well as T = 400, 600, and 800 °C for (a) $Cr_{0.28}B_{0.72}$, (b) $Cr_{0.25}Si_{0.06}B_{0.69}$, and (c) $Cr_{0.24}Si_{0.10}B_{0.66}$. All thin films were deposited on Ti-6Al-4V substrate. The inserts in (b) and (c) depict a comparison of the data recorded at RT and 800 °C over an extended strain range.

Similar to the observations in Ref. [38], increasing the sample temperature from RT to T = 400 and 600 °C is followed by a linear decrease of the fracture toughness to K_{IC} = 2.5±0.07 and 2.34±0.09 MPa$\sqrt{m}$, respectively (see Figure 8). Due to the absence of clear microstructural changes from recovery or recrystallisation in the corresponding temperature regime (compare with Figure 6), a connection is draw to temperature enhanced lattice vibrations and a concomitant decrease of the interatomic bond strength. This explanation is in line with measurements on the thermo-physical properties of several TMB_2, revealing a monotonic decrease of the elastic constants in the temperature range up to T = 1100 °C [63]. Regarding the maximum strain at failure for these samples, all bending experiments up to T = 600 °C resulted in consistent value of $\epsilon \sim 0.9\%$ (see Figure 7a).

Upon increasing the temperature to T = 800 °C during the bending experiments, a significant increase in the fracture resistance to K_{IC} = 3.33±0.09 MPa$\sqrt{m}$ as well as in the strain-to-failure at $\epsilon \sim 1.6\%$ is recorded. Similar trends in the high-temperature fracture toughness can be observed for various fine-grained technical ceramics (*e.g.*, alumina or yttria stabilized zirconia) beyond a brittle-to-ductile transition temperature. Within these materials, thermal activation of grain boundary sliding enables large scale plastic deformation [64, 65]. Although the stress - strain response of the $Cr_{0.28}B_{0.72}$ sample does not reveal any plastic deformation in the sense of a brittle-to-ductile transitions at T = 800 °C (see Figure 7a), an increased contribution from fracture energy dissipating mechanisms is unequivocally demonstrated. To the authors best knowledge, no thermally activated strengthening of atomic bonds on the boron decorated grain boundaries is applicable. Therefore, a temperature dependent mechanism allowing for enhanced movement between adjacent grains through sliding along these amorphous defect sites, is proposed. In line with the structural analysis in Figure 6, this assumes that no significant microstructural change – *i.e.*, a complete recrystallisation or reordering of the original grain boundaries – occurs at T = 800 °C within the material. This is underlined by complementary measurements conducted at room temperature after sample cooling, resulting in a fracture toughness of K_{IC} = 2.91±0.12 MPa$\sqrt{m}$, which is well within the accuracy of the fracture resistance recorded in the as-deposited state (see Figure 8). Furthermore, SEM images taken of the cantilever cross-sections for data analysis show no significant change in the apparent fracture morphology throughout all temperature steps (see Figure 9, upper row $Cr_{0.28}B_{0.72}$). The images consistently

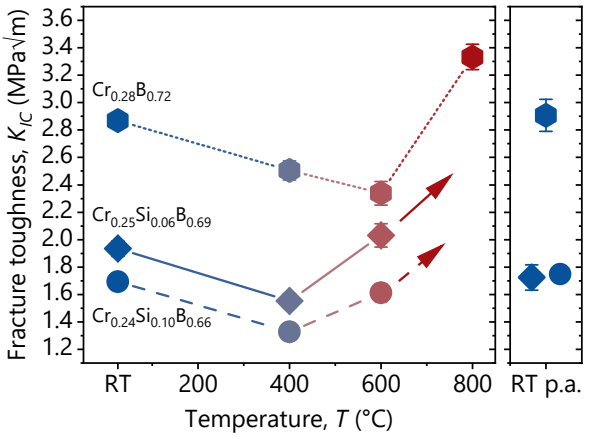

Fig. 8. Calculated fracture toughness at room temperature (RT) as well as T = 400, 600, and 800 °C for $Cr_{0.28}B_{0.72}$ (hexagons), $Cr_{0.25}Si_{0.06}B_{0.69}$ (diamonds), and $Cr_{0.24}Si_{0.10}B_{0.66}$ (circles). The corresponding fracture toughness measured at room temperature after sample cooling (RT p.a.) is included in the right panel (the lower two data points are horizontally offset for better visibility).

Publication III

Die approbierte gedruckte Originalversion dieser Dissertation ist an der TU Wien Bibliothek verfügbar.
The approved original version of this doctoral thesis is available in print at TU Wien Bibliothek.

TU Bibliothek Your knowledge hub WIEN

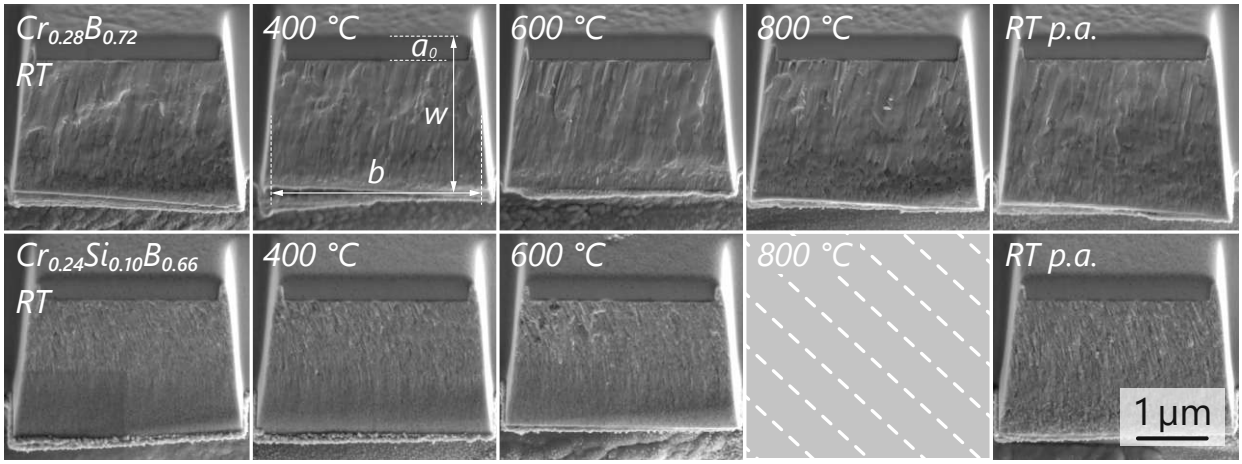

Fig. 9. Representative SEM images of the fractured cantilever cross-sections for all temperature steps on both, $Cr_{0.28}B_{0.72}$ (upper row) and $Cr_{0.24}Si_{0.10}B_{0.66}$ (lower row). The images were recorded after the final experiment at RT, hence all cross-sections exposed during prior tests experienced annealing up to 800 °C. The fracture cross-section for $Cr_{0.24}Si_{0.10}B_{0.66}$ at 800 °C could not be recorded, since the cantilever was still attached to the base after the bending experiment.

suggest a preferred fracture along the column boundaries.

As recently pointed out by Buchinger *et al.* [37], the recovery of the as-deposited fracture toughness strongly depends on the annihilation of point defects at elevated temperatures. However, the study focuses on a highly crystalline TiN coating for their high temperature experiments, which clearly lacks the influence of fracture dominating grain boundary phases when compared to the $Cr_{0.28}B_{0.72}$ coating. This demonstrates, why a fracture toughness matching the as-deposited value could be regained for the diboride thin film, whereas the nitride coating suffered a noticeable decrease in the annealed state. Nevertheless, the proposed high temperature behavior of the binary diborides needs further clarification, thus will be thoroughly reviewed in a follow-up study using a series of over- and understoichiometric TMB_2 thin films.

Room temperature bending experiments on both the $Cr_{0.25}Si_{0.06}B_{0.69}$ and $Cr_{0.24}Si_{0.10}B_{0.66}$ compositions reveal a significantly lower fracture resistance than the unalloyed coating, with values decreasing to $K_{IC} = 1.94\pm0.06$ and 1.69 ± 0.05 MPa$\sqrt{m}$, respectively (see Figure 8). In contrast, the maximum bending strain at failure remained comparable at $\epsilon \sim 1\%$ (see Figures 7b and c). The loss in as-deposited fracture toughness is attributed to the increasing presence of Si precipitates on the grain boundaries beyond an alloying content of 4 at.% – as previously revealed by detailed atom probe tomography [28] and in line with the hardness evolution (see Figure 3). Since these Si-enriched regions are not phase-pure, therefore contain additional contributions from the surrounding Cr-Si-$B_{2\pm z}$ solid solution, good agreement is obtained in the RT fracture toughness located between the unalloyed $Cr_{0.28}B_{0.72}$ and fracture resistance of single crystal Si. Depending on the specimen size, the RT fracture toughness of pure Si is reported at $K_{IC} \sim 0.8$-1.2 MPa$\sqrt{m}$ [66, 67].

Analogous to the $Cr_{0.28}B_{0.72}$ sample, increasing the temperature to $T = 400$ °C causes a decrease in fracture toughness of ∼0.4 MPa$\sqrt{m}$ for both samples, while the maximum bending strain remained almost unaffected. However, continuing to $T = 600$ °C resulted in a significantly changed and highly interesting material response. Both Si containing samples showed drastically increased elastic deformability of the micro-cantilever, with ϵ approaching ∼1.5 and ∼1.9% for $Cr_{0.25}Si_{0.06}B_{0.69}$ and $Cr_{0.24}Si_{0.10}B_{0.66}$, respectively (see Figure 7b and c). Concomitantly, also the fracture resistance reveals an increase to $K_{IC} = 2.03\pm0.09$ and 1.61 ± 0.07 MPa$\sqrt{m}$, thus recovering close to the as-deposited values (see Figure 8). Moreover, the corresponding stress intensity - bending strain data highlights a slight curvature before failure – *i.e.*, deviating from a purely linear-elastic behavior – which suggests a temperature related onset of plastic deformation within the material. Consequently, it is important to note, that the actual fracture toughness may deviate slightly from the reported values, since the calculations were solely based on linear-elastic fracture theory.

At $T = 800$ °C, severe plastic deformation is immediately noticeable in both Si-containing coatings upon cantilever loading (see Figure 7b and c). The actual fracture mode entirely changes from brittle cleavage fracture (see Figure 9, lower row), to a mechanism that results in extensive crack deflection and branching. SEM images of the open crack wake reveal splitting of the microstructure along column boundaries as well as distinct crack bridging ligaments throughout the cantilever cross-section (see Figure 10), pointing out the enhanced resistance to crack growth at elevated temperatures. In fact, the fracture resistance increased to such an extent, that all cantilevers

Publication III

Die approbierte gedruckte Originalversion dieser Dissertation ist an der TU Wien Bibliothek verfügbar.
The approved original version of this doctoral thesis is available in print at TU Wien Bibliothek.
TU Bibliothek Your knowledge hub WIEN

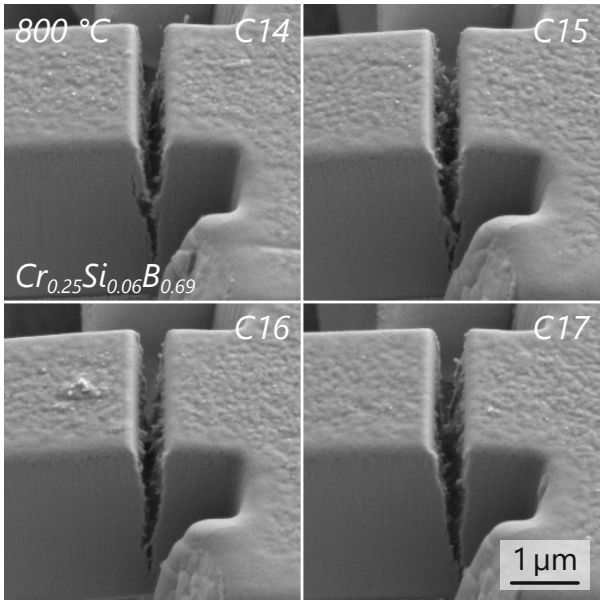

Fig. 10. SEM images of the crack location for all cantilevers (C14-C17) tested at $T = 800$ °C on the $Cr_{0.25}Si_{0.06}B_{0.69}$ coating.

endured an extreme deflection of $\epsilon > 7\%$ (see inserts in Figures 7b and c), at which point the experiments were manually stopped. In this case, the authors refrain from reporting a single value for K_{IC} (see arrows in Figure 8), since the calculated stress intensities are fully outside the boundaries given in Ref. [46]. However, presenting the load-displacement data in this normalized context provides a direct comparison to the curves recorded at lower temperatures. Moreover, since the cantilever cross-sections could not be evaluated – they were still attached to the base after the bending experiment – a mean value calculated from the geometries of samples fractured at lower temperatures was taken for reference.

With respect to temperature dependent structural evolution presented in Figure 6, a sequence of two successive mechanisms at $T = 600$ and 800 °C is considered responsible for the fracture toughness development of the higher Si-containing coatings. Note, the samples were held at each temperature for several hours to reach thermal equilibrium prior to testing, thus all structural changes were able to attain the conditions presented in Figure 6. (*i*) At $T = 600$ °C, both samples undergo enhanced segregation of pure Si from the Cr-Si-$B_{2\pm z}$ solid solution towards the already Si-rich grain boundary sites. This increased occupation of the preferred crack pathways in combination with a brittle-to-ductile transition temperature (BDTT) of Si at $T \sim 600$ °C, leads to the improved fracture toughness over $T = 400$ °C [66, 68–70]. Although the fracture cross-sections appear straight without noticeable crack deflection (see Figure 9, lower row), the incorporation of this increasingly ductile phase between the Cr(-Si-)$B_{2\pm z}$ matrix contributes to enhanced energy dissipation and possible crack arrest (see also the slight curvature of the K_C - ϵ data at 600 °C in Figures 7b and c). (*ii*) At $T = 800$ °C, Si segregation is well-advanced and the BDTT of Si is significantly exceeded. This causes the precipitates to provide the principal deformation regions during cantilever bending by enabling extensive plastic deformation. Furthermore, the weakly bound Si regions allow for crack branching by splitting of the microstructure along crystal columns as well as a crack bridging effect (see Figure 10). The mechanism also enables the vastly extended deformability of both specimen beyond the experimentally accessible range.

The fracture toughness of both samples was additionally evaluated at room temperature after the annealing treatment. A close matching value of $K_{IC} \sim 1.65$ MPa$\sqrt{m}$ was obtained, irrespective of the overall Si composition (see Figure 8). This suggests, that once the thermally grown Si precipitates are embedded in the microstructure, they also dictate the room temperature fracture toughness below the BDTT of Si. In addition, the measured fracture toughness is close to the as-deposited value for the $Cr_{0.24}Si_{0.10}B_{0.66}$ coating. This indicates an already enhanced presence of Si grain boundary decorations in the as-deposited state for the given composition.

IV. CONCLUSIONS

This work investigates the effect of Si segregates and targeted synthesis variations on the structural evolution and mechanical properties of Si alloyed Cr-$B_{2\pm z}$-based thin films at ambient and elevated temperatures. Several AlB_2-structured Cr-Si-$B_{2\pm z}$ thin films with Si concentrations up to 15 at.% were synthesized by DC magnetron sputtering and studied by RT nanoindentation as well as thermogravimetric analysis up to 1400 °C. Vacuum annealing treatments performed on coated Ti-6Al-4V up to 800 °C demonstrated the microstructural changes induced by thermally activated solid-state processes in the thin films as well as on the coatings-substrate interface. Complementary nanoindentation measurements provided details on the post-annealing hardness of these thin films. Moreover, the fracture resistance of selected Cr-Si-$B_{2\pm z}$ compositions was studied by *in-situ* microcantilever bending experiments at temperatures up to 800 °C. The main findings are as follows:

(1) An increased substrate bias of -120 V during film synthesis yields single-phased, B-overstoichiometric Cr-Si-$B_{2\pm z}$ thin films with B/Cr ratios ranging from 2.6 to 2.8, irrespective of the Si concentration. The increased ion bombardment promotes the growth of mechanically superior, (001)-oriented coatings up to a Si concentration of 3 at.%. Enhanced film crystallinity is maintained up to 10 at.%, whereas higher concentrations promote grain refinement.

(2) Highest RT hardness was obtained at $H \sim 30$ GPa

Publication III
Die approbierte gedruckte Originalversion dieser Dissertation ist an der TU Wien Bibliothek verfügbar.
The approved original version of this doctoral thesis is available in print at TU Wien Bibliothek.
TU Bibliothek Your knowledge hub WIEN

for compositions with a Si content ≤3 at.%, beyond which a significant decrease towards $H \sim 20$ GPa is recorded. Concomitant with the change in preferred film orientation, the decrease coincides with a Si solubility limit at ∼4 at.% within the Cr-Si-$B_{2\pm z}$ solid solution, causing the formation of mechanically inferior Si-rich grain boundary precipitates. The corresponding Young's moduli were recorded in a range from $E \sim 340$ ($Cr_{0.28}B_{0.72}$), to 380 ($Cr_{0.25}Si_{0.04}B_{0.71}$), to 300 GPa ($Cr_{0.23}Si_{0.15}B_{0.62}$), respectively.

(3) High temperature oxidation resistance up to 1400 °C was verified for all Cr-Si-$B_{2\pm z}$ thin films with a Si content ≥8 at.%. The protective mechanism relies on the thermally activated precipitation of pure Si beyond 600 °C, coupled with the subsequent formation of a stable SiO_2-based scale. Contrary to the oxidation behavior of related binary TM-B_2s, the oxidation protection was proven independent of the effective B/TM-ratio.

(4) Despite revealing initial stages of recovery/recrystallisation between 600 and 800 °C, an unchanged film hardness was recorded for vacuum annealed Cr-Si-$B_{2\pm z}$ compositions with a Si content below 10 at.%. Related to the oxidation protection mechanism, both $Cr_{0.24}Si_{0.10}B_{0.66}$ and $Cr_{0.23}Si_{0.15}B_{0.62}$ coatings obtain a surface hardness close to pure Si after annealing.

(5) The increased contribution of mechanically weak Si-rich grain boundary regions with higher Si content resulted in decreasing RT fracture toughness, from $K_{IC} \sim 2.9$ MPa$\sqrt{m}$ for $Cr_{0.28}B_{0.72}$, down to $K_{IC} \sim 1.7$ MPa$\sqrt{m}$ for $Cr_{0.24}Si_{0.10}B_{0.66}$. After a slight decrease in fracture resistance between RT and 600 °C, a significantly improved high-temperature fracture toughness of $K_{IC} \sim 3.3$ MPa$\sqrt{m}$ was recorded for the unalloyed Cr-B_{2+z}. Higher alloyed compositions revealed a similar behavior up to 400 °C, whereas at 800 °C Si-precipitation enabled high-temperature plasticity was observed. Surpassing the BDTT of Si introduced toughening mechanisms involving crack branching along column boundaries as well as crack bridging effects, resulting in a significantly improved fracture resistance.

ACKNOWLEDGMENTS

The financial support by the Austrian Federal Ministry for Digital and Economic Affairs, the National Foundation for Research, Technology and Development and the Christian Doppler Research Association is gratefully acknowledged (Christian Doppler Laboratory "Surface Engineering of high-performance Components"). We also thank for the financial support of Plansee SE, Plansee Composite Materials GmbH, and Oerlikon Balzers, Oerlikon Surface Solutions AG. In addition, we want to thank the X-ray center (XRC) of TU Wien for beam time as well as the electron microscopy center - USTEM TU Wien - for providing the SEM and TEM facilities. The authors acknowledge TU Wien Bibliothek for financial support through its Open Access Funding Programme.

DATA AVAILABILITY STATEMENT

The data that support the findings of this study are available from the corresponding author upon reasonable request.

DECLARATION OF INTEREST STATEMENT

The authors declare that they have no known competing financial interests or personal relationships that could have appeared to influence the work reported in this paper.

SUPPLEMENTARY

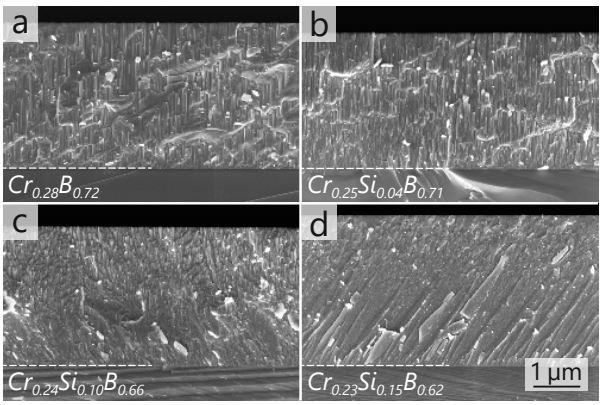

Fig. S1. SEM fracture cross-sections depicting the growth morphology of Cr-Si-$B_{2\pm z}$ thin films deposited on Si substrates. The images are arranged with increasing Si content from (a) to (d).

Publication III

Die approbierte gedruckte Originalversion dieser Dissertation ist an der TU Wien Bibliothek verfügbar.
The approved original version of this doctoral thesis is available in print at TU Wien Bibliothek.

TU Bibliothek Your knowledge hub WIEN

REFERENCES

[1] M. E. Launey and R. O. Ritchie, Adv. Mater. **21**, 2103 (2009).
[2] A. G. Evans, J. Am. Ceram. Soc. **73**, 187 (1990).
[3] R. O. Ritchie, C. J. Gilbert, and J. M. McNaney, Int. J. Solids Struct. **37**, 311 (2000).
[4] R. O. Ritchie, Nat. Mater. **10**, 817 (2011).
[5] B. Gludovatz and R. O. Ritchie, MRS Bull. **47**, 176 (2022).
[6] X. J. Fan, R. T. Qu, and Z. F. Zhang, J. Mater. Sci. Technol. **123**, 70 (2022).
[7] B. Gludovatz, A. Hohenwarter, D. Catoor, E. H. Chang, E. P. George, and R. O. Ritchie, Science (80-.). **345**, 1153 (2014).
[8] Y. Mutoh, K. Ichikawa, K. Nagata, and M. Takeuchi, J. Mater. Sci. **30**, 770 (1995).
[9] J. Xu, U. Ramamurty, and E. Ma, JOM **62**, 10 (2010).
[10] Y. Wang, Y. Zhang, A. Godfrey, J. Kang, Y. Peng, T. Wang, N. Hansen, and X. Huang, Commun. Mater. **2**, 1 (2021).
[11] J. D. French, H. M. Chan, M. P. Harmer, and G. A. Miller, J. Am. Ceram. Soc. **79**, 58 (1996).
[12] Q. Zhu and K. Shobu, J. Mater. Sci. Lett. **19**, 1529 (2000).
[13] J. Shao, W. Li, H. Kou, and Y. Deng, J. Am. Ceram. Soc. **105**, 4348 (2022).
[14] J. A. Lemberg, M. R. Middlemas, T. Weingärtner, B. Gludovatz, J. K. Cochran, and R. O. Ritchie, Intermetallics **20**, 141 (2012).
[15] H. Choe, D. Chen, J. H. Schneibel, and R. O. Ritchie, Intermetallics **9**, 319 (2001).
[16] W. G. Fahrenholtz, G. E. Hilmas, I. G. Talmy, and J. A. Zaykoski, J. Am. Ceram. Soc. **90**, 1347 (2007).
[17] F. Monteverde, A. Bellosi, and L. Scatteia, Mater. Sci. Eng. A **485**, 415 (2008).
[18] H. Deng, E. C. Dickey, Y. Paderno, V. Paderno, V. Filippov, and A. Sayir, J. Mater. Sci. **39**, 5987 (2004).
[19] W. G. Fahrenholtz and G. E. Hilmas, Scr. Mater. **129**, 94 (2017).
[20] C. Fuger, V. Moraes, R. Hahn, H. Bolvardi, P. Polcik, H. Riedl, and P. H. Mayrhofer, MRS Commun. **9**, 375 (2019).
[21] W. G. Fahrenholtz and G. E. Hilmas, Int. Mater. Rev. **57**, 61 (2012).
[22] F. Monteverde and A. Bellosi, J. Electrochem. Soc. **150**, B552 (2003).
[23] F. Monteverde and L. Scatteia, J. Am. Ceram. Soc. **90**, 1130 (2007).
[24] L. Silvestroni, K. Stricker, D. Sciti, and H. J. Kleebe, Acta Mater. **151**, 216 (2018).
[25] I. G. Talmy, J. A. Zaykoski, and M. M. Opeka, J. Am. Ceram. Soc. **91**, 2250 (2008).
[26] T. Glechner, A. Bahr, R. Hahn, T. Wojcik, M. Heller, A. Kirnbauer, J. Ramm, S. Kolozsvari, P. Felfer, and H. Riedl, Corros. Sci. **205**, 110413 (2022).
[27] T. Glechner, H. G. Oemer, T. Wojcik, M. Weiss, A. Limbeck, J. Ramm, P. Polcik, and H. Riedl, Surf. Coatings Technol. **434**, 128178 (2022).
[28] L. Zauner, A. Steiner, T. Glechner, A. Bahr, B. Ott, R. Hahn, T. Wojcik, O. Hunold, J. Ramm, S. Kolozsvári, P. Polcik, P. Felfer, and H. Riedl, SSRN Electron. J. (2022), 10.2139/SSRN.4251252.
[29] A. L. Chamberlain, W. G. Fahrenholtz, G. E. Hilmas, and D. T. Ellerby, J. Am. Ceram. Soc. **87**, 1170 (2004).
[30] F. Monteverde, S. Guicciardi, and A. Bellosi, Mater. Sci. Eng. A **346**, 310 (2003).
[31] F. Monteverde, Appl. Phys. A Mater. Sci. Process. **82**, 329 (2006).
[32] A. Mège-Revil, P. Steyer, S. Cardinal, G. Thollet, C. Esnouf, P. Jacquot, and B. Stauder, Thin Solid Films **518**, 5932 (2010).
[33] M. Bartosik, R. Hahn, Z. L. Zhang, I. Ivanov, M. Arndt, P. Polcik, and P. H. Mayrhofer, Int. J. Refract. Met. Hard Mater. **72**, 78 (2018).
[34] C. Fuger, R. Hahn, L. Zauner, T. Wojcik, M. Weiss, A. Limbeck, O. Hunold, P. Polcik, and H. Riedl, Mater. Res. Lett. **10**, 70 (2022).
[35] J. M. Wheeler, R. Raghavan, V. Chawla, M. Morstein, and J. Michler, Surf. Coatings Technol. **254**, 382 (2014).
[36] J. P. Best, J. Zechner, J. M. Wheeler, R. Schoeppner, M. Morstein, and J. Michler, Philos. Mag. **96**, 3552 (2016).
[37] J. Buchinger, L. Löfler, J. Ast, A. Wagner, Z. Chen, J. Michler, Z. Zhang, P. Mayrhofer, D. Holec, and M. Bartosik, Mater. Des. **194**, 108885 (2020).
[38] A. Drnovšek, H. T. Vo, M. R. de Figueiredo, S. Kolozsvári, P. Hosemann, and R. Franz, Surf. Coatings Technol. **409**, 126909 (2021).
[39] W. Oliver and G. Pharr, J. Mater. Res. **19**, 3 (2004).
[40] A. C. Fischer-Cripps, Surf. Coatings Technol. **200**, 4153 (2006).
[41] G. Janssen, M. Abdalla, F. van Keulen, B. Pujada, and B. van Venrooy, Thin Solid Films **517**, 1858 (2009).
[42] G. G. Stoney, Proc. R. Soc. A Math. Phys. Eng. Sci. **82**, 172 (1909).
[43] D. Di Maio and S. G. Roberts, J. Mater. Res. **20**, 299 (2005).
[44] S. Brinckmann, K. Matoy, C. Kirchlechner, and G. Dehm, Acta Mater. **136**, 281 (2017).
[45] J. Wheeler, P. Brodard, and J. Michler, Philos. Mag. **92**, 3128 (2012).
[46] K. Matoy, H. Schönherr, T. Detzel, T. Schöberl, R. Pippan, C. Motz, and G. Dehm, Thin Solid Films **518**, 247 (2009).
[47] J. Neidhardt, S. Mráz, J. M. Schneider, E. Strub, W. Bohne, B. Liedke, W. Möller, and C. Mitterer, J. Appl. Phys. **104**, 063304 (2008).
[48] ICDD, Powder Diffr. File - Hexag. CrB2 - 04-004-1734 (2011).
[49] ICDD, Powder Diffr. File - cubic Si - 00-027-1402 (2017).
[50] C. L. Jiang, Z. L. Pei, Y. M. Liu, H. Lei, J. Gong, and C. Sun, Appl. Surf. Sci. **288**, 324 (2014).
[51] H. Watanabe, N. Yamada, and M. Okaji, Int. J. Thermophys. **25**, 221 (2004).
[52] Z. Nibennaoune, D. George, S. Ahzi, D. Ruch, Y. Remond, and J. J. Gracio, Thin Solid Films **518**, 3260 (2010).
[53] S. Dorri, J. Palisaitis, G. Greczynski, I. Petrov, J. Birch, L. Hultman, and B. Bakhit, Corros. Sci. **206**, 110493 (2022).

Publication III

Die approbierte gedruckte Originalversion dieser Dissertation ist an der TU Wien Bibliothek verfügbar.
The approved original version of this doctoral thesis is available in print at TU Wien Bibliothek.

TU Bibliothek Your knowledge hub WIEN

[54] J. Thörnberg, B. Bakhit, J. Palisaitis, N. Hellgren, L. Hultman, G. Greczynski, P. O. Persson, I. Petrov, and J. Rosen, Surf. Coatings Technol. **420**, 127353 (2021).
[55] ICDD, Powder Diffr. File - Hexag. CrSi2 - 04-001-7333 (2011).
[56] ICDD, Powder Diffr. File - orthorhombic CrB - 04-003-6125 (2011).
[57] ICDD, Powder Diffr. File - orthorhombic TiB - 04-005-6142 (2005).
[58] ICDD, Powder Diffr. File - alpha Titan. - 04-020-7055 (2016).
[59] ICDD, Powder Diffr. File - beta Titan. - 04-020-5 (2016).
[60] A. C. Fischer-Cripps, *Nanoindentation*, 3rd ed., Mechanical Engineering Series (Springer New York, New York, NY, 2011).
[61] L. Zauner, R. Hahn, E. Aschauer, T. Wojcik, A. Davydok, O. Hunold, P. Polcik, and H. Riedl, Acta Mater. **239**, 118260 (2022).
[62] C. Fuger, R. Hahn, A. Hirle, P. Kutrowatz, M. Weiss, A. Limbeck, O. Hunold, P. Polcik, and H. Riedl, Surf. Coatings Technol. **446**, 128806 (2022).
[63] N. L. Okamoto, M. Kusakari, K. Tanaka, H. Inui, and S. Otani, Acta Mater. **58**, 76 (2010).
[64] J. F. Li and R. Watanabe, Mater. Trans. JIM **40**, 508 (1999).
[65] C. Carry and A. Mocellin, Ceram. Int. **13**, 89 (1987).
[66] B. N. Jaya, J. M. Wheeler, J. Wehrs, J. P. Best, R. Soler, J. Michler, C. Kirchlechner, and G. Dehm, Nano Lett. **16**, 7597 (2016).
[67] I. Issa, C. Gammer, S. Kolitsch, A. Hohenwarter, P. J. Imrich, R. Pippan, and D. Kiener, Mater. Today **48**, 29 (2021).
[68] D. Sen, C. Thaulow, S. V. Schieffer, A. Cohen, and M. J. Buehler, Phys. Rev. Lett. **104**, 235502 (2010).
[69] C. St. John, Philos. Mag. **32**, 1193 (1975).
[70] E. D. Hintsala, S. Bhowmick, X. Yueyue, R. Ballarini, S. A. Asif, and W. W. Gerberich, Scr. Mater. **130**, 78 (2017).

Die approbierte gedruckte Originalversion dieser Dissertation ist an der TU Wien Bibliothek verfügbar.
The approved original version of this doctoral thesis is available in print at TU Wien Bibliothek.
TU Bibliothek Your knowledge hub WIEN

Publication IV

Die approbierte gedruckte Originalversion dieser Dissertation ist an der TU Wien Bibliothek verfügbar.
The approved original version of this doctoral thesis is available in print at TU Wien Bibliothek.

Reactive HiPIMS deposition of Ti–Al–N: Influence of the deposition parameters on the cubic to hexagonal phase transition

L. Zauner, Ph. Ertelthaler, T. Wojcik, H. Bolvardi, S. Kolozsvári, P.H. Mayrhofer, H. Riedl

Surface & Coatings Technology, 382 (2020): 125007.
DOI: 10.1016/j.surfcoat.2019.125007

Surface & Coatings Technology 382 (2020) 125007

Contents lists available at ScienceDirect

Surface & Coatings Technology

journal homepage: www.elsevier.com/locate/surfcoat

Reactive HiPIMS deposition of Ti-Al-N: Influence of the deposition parameters on the cubic to hexagonal phase transition

L. Zauner[a,b,*], Ph. Ertelthaler[a], T. Wojcik[b], H. Bolvardi[c], S. Kolozsvári[d], P.H. Mayrhofer[b], H. Riedl[a,b]

[a] Christian Doppler Laboratory for Surface Engineering of high-performance Components, TU Wien, A-1060 Wien, Austria
[b] Institute of Materials Science and Technology, TU Wien, A-1060 Wien, Austria
[c] Oerlikon Balzers, Oerlikon Surface Solutions AG, FL-9496 Balzers, Liechtenstein
[d] Plansee Composite Materials GmbH, D-86983 Lechbruck am See, Germany

ARTICLE INFO

Keywords:
R-HiPIMS
Ti-Al-N
Phase formation
Deposition parameters
Synchronised bias

ABSTRACT

Reactive high-power impulse magnetron sputtering (R-HiPIMS) is seen as a key-technology for the deposition of future hard and multifunctional coatings. Increased ionisation rates allow for additional possibilities in tuning specific coating characteristics based on growth mechanisms varied by surface-diffusion. Especially within the well-established Ti-Al-N system, the Al solubility limit (x_{max}) of metastable face-centred-cubic (*fcc*) $Ti_{1-x}Al_xN$ is an everlasting scientific topic. Here, we investigate in detail the dependence of x_{max} on various deposition parameters (*i.e.* pulse frequency and duration, N_2-to-Ar flow rate ratio, and substrate bias potential) during R-HiPIMS of Ti-Al-N coatings using $Ti_{0.6}Al_{0.4}$, $Ti_{0.5}Al_{0.5}$ and $Ti_{0.4}Al_{0.6}$ composite targets. The systematic studies showed that the highest solubility limit of x_{max} ~0.55 could be obtained for duty cycles around 3.75 % (peak power densities of ~1.0 kW/cm^2) and a N_2-to-Ar flow rate ratio of 0.3. A further decisive fact for the deposition of high Al containing *fcc*-structured $Ti_{1-x}Al_xN$ coatings is surface diffusion controlled by bias potentials (DC as well as modulated pulses) ensuring sufficient intermixing of the arriving film species. Despite the presence of very small amounts of wurtzite-typed phases, excellent hardness values of ~36 GPa for $Ti_{0.40}Al_{0.60}N$ – which further increased to ~40 GPa upon annealing for 1 h at 700 °C – could be achieved for a DC bias potential of -50 V, irrespective of all variations conducted. Based on our results we can further conclude, that the ratio and energy of Ti^{n+}- and Al^{n+}-ions, simultaneously arriving at the substrate surface, are decisive for stabilising the highly preferred cubic modification. A distinct promotion of specific discharge regimes – selected by synchronised bias pulses – can thus positively influence the cubic phase formation through altered gas-to-metal ion ratios arriving at the film surface.

1. Introduction

Expanding the flexibility in thin film design, while providing enhanced capabilities to tailor coating structures and properties are major incentives for developing novel deposition techniques. Within this context, high-power impulse magnetron sputtering (HiPIMS) has found widespread recognition in recent years as a promising addition to plasma based physical vapour deposition (PVD) techniques [1–5]. In contrast to conventional DC magnetron sputtering (DCMS) – the workhorse of sputter deposition over the past decades – HiPIMS introduces high amplitude pulses at relatively low repetition rates, introducing a drastic increase in ionised species of the film-forming vapour. This highly ionised flux of vaporised target material is known to have a significant influence on the growing film, thus allowing for an enhanced control of the structure-property relationships [6–9]. Moreover, HiPIMS discharges are characterized by ion-driven phenomena near the target surface (*i.e.* process gas recycling, metal self-sputtering or gas rarefaction), leading to novel plasma and process conditions when compared to conventional DCMS [10,11].

Introducing reactive gas mixtures to the process, *e.g.* Ar/N_2 for the deposition of nitride based coatings, adds further complexity to the discharge mechanisms through the well-known "poisoning" phenomenon, thus affecting both the sputter rate as well as the emission of secondary electrons [12]. Furthermore, the formation of these insulating layers on top of the target materials – *e.g.* nitrides or oxides in relation to the used gas mixture – lead to inferior discharge conditions, and hence alters also the film structure and morphology. Nevertheless, various studies could already highlight the beneficial aspects of reactive HiPIMS (R-HiPIMS) on thin film quality, including denser microstructures, higher hardness, lower surface roughness, improved film

* Corresponding author. Christian Doppler Laboratory for Surface Engineering of high-performance Components, TU Wien, A-1060 Wien, Austria.
E-mail address: lukas.zauner@tuwien.ac.at (L. Zauner).

https://doi.org/10.1016/j.surfcoat.2019.125007
Received 30 July 2019; Received in revised form 31 August 2019; Accepted 19 September 2019
Available online 14 October 2019
0257-8972/ © 2019 Elsevier B.V. All rights reserved.

Publication IV

Die approbierte gedruckte Originalversion dieser Dissertation ist an der TU Wien Bibliothek verfügbar.
The approved original version of this doctoral thesis is available in print at TU Wien Bibliothek.
TU Wien Bibliothek Your knowledge hub

adhesion, extended phase stabilities or enhanced surface coverage of complex shaped substrates, just to mention a few examples [13–18]. So far, research efforts put special focus on the complex plasma physics as well as the deposition of single-phased target materials, consequently leaving the application of R-HiPIMS on multi-element materials [19,20] still rather unexplored. Therefore, applying this novel technique on the industrially well-established Ti-Al-N system offers an ideal possibility to establish an in-depth understanding on the effects when using R-HiPIMS on multi-phased target materials [21].

When prepared in the metastable face-centred cubic structure (*c*, B1, NaCl-prototype), Ti-Al-N thin films offer high hardness combined with excellent wear resistance and thermal stability. Furthermore, the well-known age hardening effect through spinodal decomposition leads to additionally improved thermo-mechanical performance at elevated temperatures [22–25]. Owing to these properties, cubic Ti-Al-N thin films evolved as a benchmark for protective coatings utilised in various fields of application, but especially in the tooling industry [26,27]. Since the high temperature oxidation resistance of *c*-$Ti_{1-x}Al_xN$ is in close relationship with the incorporated AlN mole fraction (x), it is of great interest to increase the Al/Ti-ratio on the metal sublattice, while maintaining the cubic phase [28]. In fact, studies employing R-HiPIMS deposition techniques to grow $Ti_{1-x}Al_xN$ thin films [29], report clearly reduced solubility limits (x_{max}) compared to conventional DCMS or arc evaporated coatings; unless a "hybrid" HiPIMS process is utilised, which combines DCMS with HiPIMS. Exceeding the solubility limit results in the formation of dual phased structures, obtaining cubic as well as hexagonal (*w*, B4, ZnS-wurtzite prototype) domains, or even in a fully single-phased wurtzite configuration. While a small fraction of *w*-AlN or *w*-$Al_xTi_{1-x}N$ phases (embedded in an otherwise *c*-$Ti_{1-x}Al_xN$ dominated matrix) still can increase the as-deposited hardness [30], especially the thermomechanical properties and thermal stability is reduced [31–33].

Recently, Greczynski *et al.* employed a hybrid HiPIMS/DCMS approach to characterise the individual influence of Ti^{n+}- and Al^{n+}-ions on the growth of reactively sputtered Ti-Al-N thin films [34,35]. They demonstrated, that defects introduced by intense bombardment of doubly-charged Ti-ions serve as preferred nucleation sites for wurtzite precipitates, resulting in lower x_{max} and hence deteriorated mechanical properties. In contrast, the bombardment of low-energy Al^+-ions, promoting surface near ion mixing during film growth, retards phase decomposition and yields to high hardness and tensile stress states. Furthermore, the beneficial aspects of using a pulse-synchronised bias voltage were pointed out by tuning the average Me^+/Ar^+-ion ratio incident on the substrate surface [36].

Regarding modulations of the discharge signal, Shimizu *et al.* [37] and Severin *et al.* [38] studied the influence of altered pulse durations (t_{on}) and frequencies (f) on the properties of dual phase structured (mixed cubic and wurtzite domains) Ti-Al-N thin films, respectively. Pulse length reductions promote the growth of the wurtzite phase, whereas changes in the pulse frequency are found to have minor effects on the overall phase constitution. Moreover, using the HiPIMS technique to deposit dual phased Ti-Al-N thin films results in improved mechanical properties with high hardness (> 30 GPa), despite the presence of a *w*-AlN phase. Yet, although these studies contributed valuable insights into the correlation of R-HiPIMS deposition of Ti-Al-N coatings, a comprehensive analysis on the coating structure as function of the deposition parameters and the employed target materials is still missing.

In the present work, we discuss the results obtained from detailed studies on the phase formation and resulting impact on the mechanical properties, when utilizing R-HiPIMS on powder-metallurgically prepared Ti-Al targets (multi-phased target materials containing elemental Ti as well as Al grains) for the deposition of Ti-Al-N thin films. Variations of the discharge conditions, such as frequency and pulse duration, are related to structural and compositional changes observed during film growth. Moreover, the influence of altered target compositions, varying nitrogen partial pressures, changed power densities as well as different substrate bias conditions are discussed in detail.

Fig. 1 presents a condensed, yet simplified view of the anticipated effects within a R-HiPIMS discharge, when depositing Ti-Al-N thin films from a composite target. Following a schematic introduced by Anders *et al.* [12,39], the illustration provides the reader with a visual guidance during this work by addressing relevant effects of the plasma-target and plasma-film interaction with respect to the previously cited literature. On the right-hand side, the figure is sectioned into the three main recycling mechanisms that are characteristic for R-HiPIMS conditions: *(i)* working gas recycling, *(ii)* metal self-sputtering, and *(iii)* reactive gas recycling. The ionisation of sputtered target- or gas-atoms within these dense HiPIMS plasmas – ionisation of target-atoms essentially takes place after the sputtering from the target – provides pathways for a reattraction of the species onto the target surface, which contributes to the high current densities and reduced growth rates observed for HiPIMS deposition. Depending on the self-sputter yield of the target material, either gas-recycling or metal self-sputtering dominates the discharge process [12,39]. In addition, the irregular "poisoning" rates of Al- and Ti-grains as well as the influence of individual ions bombarding the film structure are indicated [40], underlining the diverse challenges posed by R-HiPIMS depositions. Moreover, a schematic of the deposition system used during this study is included on the left-hand side of Fig. 1.

2. Experimental

$Ti_{1-x}Al_xN$ thin films were synthesised using an in-house developed HiPIMS system equipped with two industrial sized 6-inch $Ti_{1-x}Al_x$ composite targets (powder-metallurgically prepared, Plansee Composite Materials GmbH), which were powered by Solvix HIP^3 5 kW plasma generators, respectively. Three different target compositions ($Ti_{0.6}Al_{0.4}$, $Ti_{0.5}Al_{0.5}$, $Ti_{0.4}Al_{0.6}$) were utilised in various combinations to alter the chemical composition of the thin films prepared – details can be found in Table 1. The two 6-inch cathodes are arranged in a confocal, bottom-up configuration, resulting in an incident angle between the substrate normal and the targets of about $\alpha = 20°$. For all depositions, the mean-distance from the target to the rotating substrate holder (0.25 Hz) was kept constant at $h = 11$ cm (see Fig. 1). All $Ti_{1-x}Al_xN$ thin films were deposited on Si platelets ((100)-oriented, $20 \times 7 \times 0.38\,mm^3$), monocrystalline Al_2O_3 platelets ((1–102)-oriented, $10 \times 10 \times 0.53\,mm^3$), as well as polished austenite platelets (DIN EN 1.4571, $20 \times 7 \times 0.8\,mm^3$). Prior to the depositions, the substrates were ultrasonically pre-cleaned in acetone and ethanol. Following a 20 min heating step to a constant heater temperature of $T_H = 500\,°C$ (corresponds to a substrate temperature of $T_S = 285 \pm 15\,°C$, measured directly on the substrate), a 10 min Ar-ion etching step was performed at a working gas pressure of $p_{etch} = 5$ Pa using a bias potential of $U_S = -400$ V. The depositions were carried out in mixed Ar/N_2-atmospheres (both gases with 99.999 % purity) utilizing an overall process gas flowrate of 40 sccm, fixed to a total pressure of $p_{dep} = 0.4$ Pa. To ensure proper deposition conditions, a base pressure of at least $3 \cdot 10^{-4}$ Pa was ensured prior to all depositions.

In order to analyse the influence on the process-stability as well as thin film properties, specific HiPIMS deposition parameters were varied. Both, f and t_{on} were gradually modified from 200 to 1000 Hz and 50 to 200 µs, respectively. Combining these pulse modifications with an average target power (P_A) of 1 to 3 kW, resulting peak power

Publication IV

Die approbierte gedruckte Originalversion dieser Dissertation ist an der TU Wien Bibliothek verfügbar.
The approved original version of this doctoral thesis is available in print at TU Wien Bibliothek.

TU Bibliothek Your knowledge hub WIEN

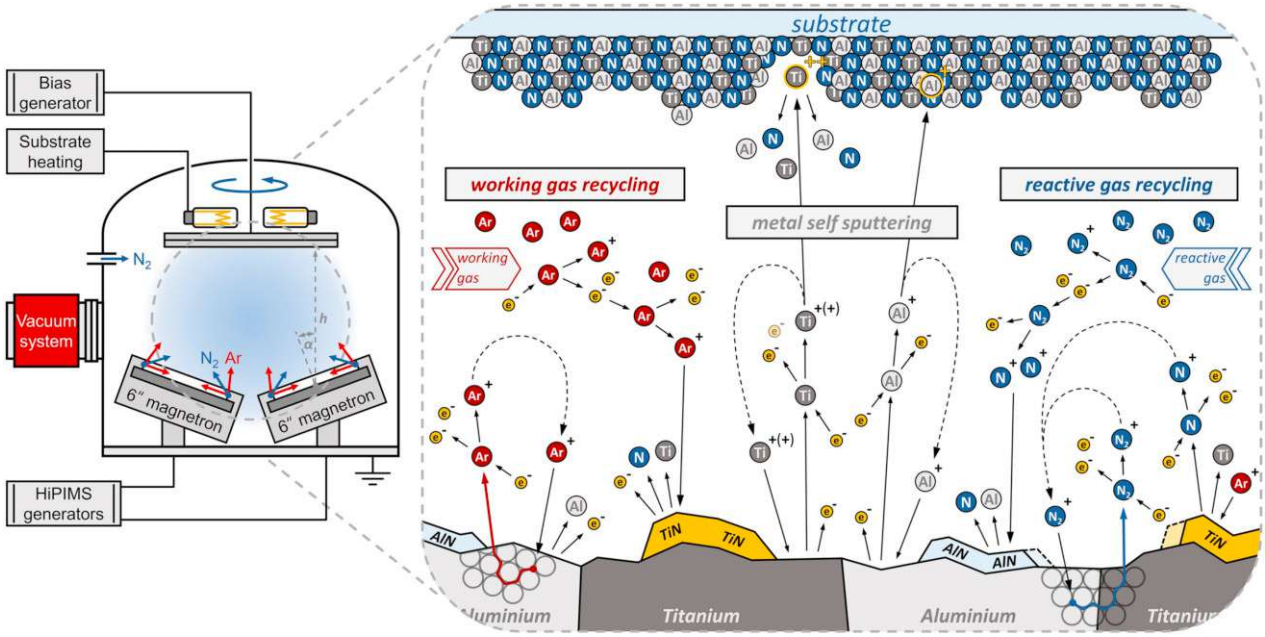

Fig. 1. Simplified schematic of ion-based phenomena (working gas recycling, metal self-sputtering and reactive gas recycling) within a R-HiPIMS discharge, when using a Ti-Al composite target for the reactive deposition of a $Ti_{1-x}Al_xN$ thin film. Furthermore, the interaction of metal ions with the film surface as well as the formation of nitride layers onto the target surface are indicated (adapted from Anders *et al.* [12,39]). A schematic of the deposition system used during this study is included on the left-hand side.

densities (p_{peak}) of 0.04 to 1.3 kW/cm^2 could be achieved at duty cycles between 2 to 20 %. To maintain comparability of these area normalised values throughout this work, peak power densities were calculated using the entire target area ($A_{Target} \sim 182.4$ cm^2). Changes in the reactive gas atmosphere were investigated by altering the nitrogen flow ratio $f_{[N_2]}^{norm} = \frac{f_{[N_2]}}{f_{[N_2]} + f_{[Ar]}}$ from 0.20 to 0.35. Constant (U_S = floating pot., -50 V, -100 V) as well as pulsed bias potentials (U_{synced} = -50 V), synchronised to the HiPIMS discharge with varying pulse durations t_{Bias} and offsets t_{offset}, were applied to the substrate holder. In addition, to analyse also the influence of retarded growth rates, selected coatings were deposited using only one 6-inch cathode. Further details on the deposition parameters and the related coatings can be found in Table 1. Since stoichiometric $(Ti,Al)_{0.50}N_{0.50}$ is considered as the base composition for all experiments, our coatings are referred to in a simplified N-normalised notation as $Ti_{1-x}Al_xN$ for general chemical description – see also Table 1.

Structural investigations were performed using X-ray diffraction (XRD) analysis utilizing a PANalytical XPert Pro MPD equipped with a Cu-K_α radiation source (wave length $\lambda = 1.54$ Å) in Bragg-Brentano geometry. All chemical compositions were characterised by energy dispersive X-ray spectroscopy (EDS, EDAX EDS detector) in top-view configuration (10 kV acceleration voltage). Furthermore, the mechanical properties such as hardness (H) and indentation modulus (E) were analysed using an ultra-micro indentation system (UMIS) equipped with a Berkovich indenter. A minimum of 30 load-displacement curves were recorded at varying indentation loads, ranging from 3 to 45 mN. The evaluation of the gathered data was carried out according to the method established by Oliver and Pharr [41].

The coating morphology as well as specific growth characteristics were investigated using scanning electron microscopy (SEM, FEI Quanta 200, operated at 5 kV) in cross-sectional configuration. For further analysis of the microstructure and localised phase formation, transmission electron microscopy (TEM, FEI TECNAI F20) combined with selected area electron diffraction (SAED) was employed. The evaluation of high-resolution TEM (HR-TEM) images and SAED patterns was conducted using the Digital Micrograph software package (version 3.22) as well as the PASAD add-on module [42]. Residual macro-stresses within the coatings were calculated using the modified Stoney-equation and curvature measurements of single-side coated Si substrates obtained from optical profilometry (Nanovea PS50) [43].

3. Results & discussion

An essential parameter for the discussion of pulsed discharge techniques is the peak power density providing a link to the ionisation degree achieved during film growth. Based on this terminology a differentiation between DCMS, modulated pulsed power (MPP) depositions [44], and HiPIMS can be made by plotting the duty cycle over the peak power density including specific limits for each technique, as suggested by Gudmundsson *et al.* [9]. According to this approach, all process conditions used within this study are compared to these well-known (technique-specific) limits [9] (indicated by dashed lines) – see Fig. 2. In principle, three different sets of R-HiPIMS Ti-Al-N coatings have been synthesised covering a broad set of pulsed discharge conditions and hence ionisation degrees: *(i)* low-energy containing pulses up to p_{peak} around 0.10 kW/cm^2 indicated by open circles (MPP variation), *(ii)* moderate energy containing pulses up to 1.00 kW/cm^2 labelled by diamonds (MPP to HiPIMS), as well as *(iii)* HiPIMS depositions around 1.00 kW/cm^2 and higher, marked by open squares (HiPIMS variation). As one aim of this study was to investigate the influence of highly ionised species on the cubic to wurtzite transition, we left out the low power region for further considerations, as these conditions are highly

Die approbierte gedruckte Originalversion dieser Dissertation ist an der TU Wien Bibliothek verfügbar.
The approved original version of this doctoral thesis is available in print at TU Wien Bibliothek.

Table 1
Detailed overview of the deposition parameters used for the synthesis of the analysed samples.

Nr	Normalised coating composition	Label	Target 6"			p_{dep}	$f_{[N_2]}^{norm}$	f	t_{on}	duty cycle	P_A	p_{peak}	U_S	t_{Bias}	t_{offset}	dep. rate
			$Ti_{0.6}Al_{0.4}$	$Ti_{0.5}Al_{0.5}$	$Ti_{0.4}Al_{0.6}$	[µbar]	[-]	[Hz]	[µs]	[%]	[W]	[kW/cm²]	[V]	[µs]	[µs]	[nm/min]
MPP to HiPIMS																
1	$Ti_{0.50}Al_{0.50}N$	-	1x	-	-	4	0.2	1000	200	20	1000	0.04	-50	DC	-	12.35
2	$Ti_{0.47}Al_{0.53}N$		1x	-	-			500	200	10		0.14				7.65
3	$Ti_{0.48}Al_{0.52}N$		1x	-	-			200	200	4		0.35				5.76
4	$Ti_{0.47}Al_{0.53}N$		1x	-	-			1000	100	10		0.12				7.87
5	$Ti_{0.48}Al_{0.52}N$		1x	-	-			500	100	5		0.29				5.96
6	$Ti_{0.51}Al_{0.49}N^*$		1x	-	-			200	100	2		1.01				3.05
7	$Ti_{0.50}Al_{0.50}N$		1x	-	-			1000	50	5		0.25				5.72
8	$Ti_{0.51}Al_{0.49}N^*$		1x	-	-			500	50	2.5		0.69				3.95
HiPIMS Variation																
9	$Ti_{0.48}Al_{0.52}N$	Target	1x	1x	-	4	0.3	500	75	3.75	3000	1.20/1.23	-50	DC	-	17.60
10	$Ti_{0.45}Al_{0.55}N$	composition	-	2x	-							1.10/1.21				25.63
11	$Ti_{0.40}Al_{0.60}N$		-	1x	1x							1.05/1.02				30.99
12	$Ti_{0.46}Al_{0.54}N$	Nitrogen	-	1x	1x	4	0.25	500	75	3.75	3000	0.92/0.89	-50	DC	-	51.21
13	$Ti_{0.38}Al_{0.62}N$	flow rate	-	1x	1x		0.35					1.20/1.18				24.58
14	$Ti_{0.39}Al_{0.61}N$	Substrate bias	-	1x	1x	4	0.3	500	75	3.75	3000	1.19/1.00	float. pot.	DC	-	27.19
15	$Ti_{0.39}Al_{0.61}N$		-	1x	1x							1.11/0.99	-100			29.91
16	$Ti_{0.55}Al_{0.45}N$	Target	1x	-	-	4	0.3	500	75	3.75	3000	1.30	-50	DC	-	5.27
17	$Ti_{0.41}Al_{0.59}N$	composition	-	1x	-							1.34				9.43
18	$Ti_{0.33}Al_{0.67}N$		-	-	1x							1.21				13.32
19	$Ti_{0.35}Al_{0.65}N$		-	-	1x		0.2					1.00				26.42
20	$Ti_{0.44}Al_{0.56}N$	TEM	-	1x	1x	4	0.25	500	75	3.75	3000	0.90	float. pot.	DC	-	53.12
21	$Ti_{0.41}Al_{0.59}N$	Bias	-	1x	-	4	0.3	500	75	3.75	3000	1.27	-50	75	0	9.76
22	$Ti_{0.41}Al_{0.59}N$	synchronised	-	1x	-							1.28		50	40	9.90
23	$Ti_{0.41}Al_{0.59}N$		-	1x	-							1.30		75		9.73
24	$Ti_{0.42}Al_{0.58}N$		-	1x	-							1.29		100		9.91

* EDS measured nitrogen content > 60 at.%

similar to DCMS. Ion mass spectroscopy measurements (no shown here) confirm these predictions and are the content of a follow-up study. Our data set is in excellent agreement to the commonly accepted power limit (indicated by the hatched area) for typically utilised power supplies, highlighting general restrictions for pulse to power modulations.

Fig. 3 summarises the influence of pulse modifications on the structural and mechanical properties of reactively deposited Ti-Al-N thin films as function of the duty cycle. The corresponding $Ti_{1-x}Al_xN$ coatings (with $0.49 \leq x \leq 0.53$) were grown from a powder-metallurgically prepared $Ti_{0.6}Al_{0.4}$ target, using $P_A = 1.0$ kW, $f_{[N_2]}^{norm} = 0.20$ and a constant substrate bias of $U_S = -50$ V, while both f and t_{on} were decreased from 1000 to 200 Hz and 200 to 50 µs, respectively (for details see Table 1 – MPP to HiPIMS subsection). Maintaining P_A constant for all of these depositions allowed for a comparison of moderate power-density conditions – characterised by a low amount of ionised species – with discharge set-ups for higher ion concentrations within the sputtered flux, situated well within the MPP and HiPIMS regimes. Regarding Fig. 2, the considered samples are indicated by open diamonds (MPP to HiPIMS).

Decreasing f and t_{on}, thus reducing the duty cycle from 20 to 2 %, yields to a drastic increase of the peak target current density (J_T) from 0.1 up to 1.8 A/cm², see blue circles in Fig. 3a. Consequently, this leads to duty cycles of less than 1% (corresponding to $f = 200$ Hz and $t_{on} = 50$ µs) being inaccessible due to limitations in process stability, primarily related to severe arc discharges. On the one hand, the increase in J_T is clearly related to the *U-I*-characteristic and arc handling of the employed power supply, as shorter duty cycles imply a higher amount of energy per pulse in order to maintain constant average power. On the other hand, extended off-times between pulses as well as shortened effective sputtering times, shift the target from a metallic to a more poisoned mode. Since the emission of secondary electrons is known to be significantly higher for AlN, and only slightly lower for TiN, than compared to their pure metallic surfaces, higher peak current densities are observed at lower discharge voltages [45,46]. As the peak current density of the HiPIMS discharge is directly related to the ionisation of the film-forming species, reducing the duty cycle (especially below 10 %) leads to an increased ion-to-neutral ratio as J_T increases significantly. Moreover, the increasing amount of film ions back-attracted onto the target surface upon approaching these highly ionised plasma conditions, also results in a reduction of the deposition rate [8,47]. For the coatings obtained here, reducing the duty cycle from 20 to 2 % yields a decrease of the sputter rate from 12.3 to 3.05 nm/min (see Table 1).

Nevertheless, all $Ti_{1-x}Al_xN$ thin films exhibit a single-phased cubic structure, with a predominant mixed (111) and (200) texture. Fig. 3a further shows the (200) full-width at half maximum ($FWHM_{(200)}$, red squares), indicating the average crystallite size of the coatings (larger $FWHM_{(200)}$ for smaller grains). The $FWHM_{(200)}$ shows a comparable dependence on the duty cycle as J_T, and increases from ~0.5° to ~1.5° when reducing the duty cycle to values below 10 %. Fewer coherently diffracting domain sizes are the result of recurring renucleation events during film growth, triggered by an intense ion bombardment [48]. Except for the half-filled data point marked by an arrow at a duty cycle of 5 % ($FWHM_{(200)} = 1.43°$, corresponding to $f = 1000$ Hz and $t_{on} = 50$ µs), decreased duty cycles emphasise the formation of fine-grained microstructures.

Corresponding to the *FWHM*, also the mechanical properties are nearly independent on the variation of the duty cycle as long as the duty cycle is > 5 %. The hardness slightly decreases from ~33 to ~31 GPa for duty cycles below 3 % (see Fig. 3b, red squares).

Publication IV

Die approbierte gedruckte Originalversion dieser Dissertation ist an der TU Wien Bibliothek verfügbar.
The approved original version of this doctoral thesis is available in print at TU Wien Bibliothek.
TU Bibliothek Your knowledge hub WIEN

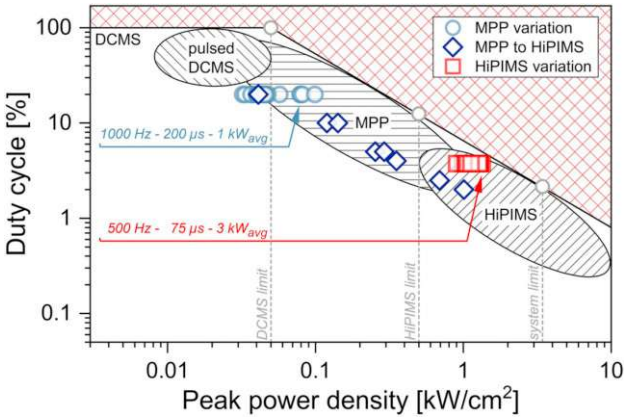

Fig. 2. The deposition sets conducted during this study put into context with an established terminology for pulsed discharge techniques, where the duty cycle is presented with respect to the logarithm of the peak power density, p_{peak}. The regions of pulsed DCMS, MPP and HiPIMS, as well as their peak power limits are indicated based on Ref. [9]. Details about the deposition conditions are given in Table 1.

Decreasing duty cycles lead to an enhanced film bombardment with ionised species and higher nitrogen contents (EDS even suggests for N above 60 at.% if the duty cycle is below 3 %) as well as lower deposition rates. Excess nitrogen can be located at the grain boundaries or trapped as nitrogen-bubbles [49]. Especially at grain boundaries, this would reduce their cohesive strength and deteriorate the mechanical properties of the coatings in general. Another explanation for decreasing hardness with lower duty cycles is the concomitant decreasing film thickness (from 1.20 to 0.50 µm), and thus the increasing substrate interference (which is softer than the coating).

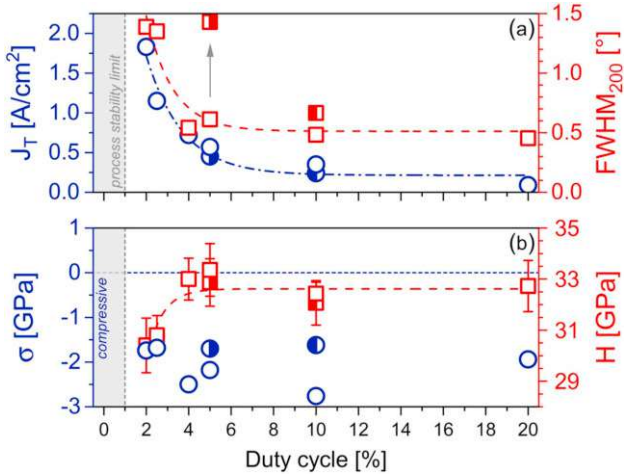

Fig. 3. (a) Current density J_T (blue circles, left axis) and full-width at half maximum of the (200) XRD peak, $FWHM_{(200)}$ (red squares, right axis) and (b) residual biaxial stresses σ (blue circles, left axis) and nanoindentation hardness H (red squares, right axis) of $Ti_{1-x}Al_xN$ thin films prepared with various duty cycles. Half-filled symbols at duty cycles of 5 and 10 % are from coatings prepared with f = 1000 Hz/t_{on} = 100 µs and f = 1000 Hz/t_{on} = 50 µs, respectively. The other duty cycles clearly represent only one deposition condition, which are given in Table 1. (For interpretation of the references to colour in this figure legend, the reader is referred to the Web version of this article.)

Irrespective of the HiPIMS pulse configuration and the chemical composition of the $Ti_{1-x}Al_xN$ coatings, their residual compressive stresses are comparable to conventional DCMS films, ranging from -1.6 to -2.8 GPa (see Fig. 3b, blue circles). These results not only show the distinct influence of the pulse parameters on the discharge conditions, but also their impact on structural and mechanical properties. Moreover, the importance of finding optimised HiPIMS settings and discharge conditions to obtain an appropriate balance between ionised species and film growth rate, is clearly underlined.

In addition to the discharge settings, also the nitrogen partial pressure, bias potential, as well as target chemistry will effectively influence the structure and thus the resulting properties of R-HiPIMS deposited $Ti_{1-x}Al_xN$ thin films. Therefore, we extended our investigations using specified pulse settings, while varying the above-mentioned parameters. Referring to Figs. 2 and 3, duty cycles between 3 and 5 % allow for settings in the or close to the HiPIMS regime, combined with excellent coating properties such as high hardness and medium compressive stresses. Therefore, a duty cycle of 3.75 % (corresponding to f = 500 Hz and t_{on} = 75 µs) was selected. To ensure that the cathodes operate within the HiPIMS regime, an average target power of P_A = 3.0 kW was applied, resulting in peak power densities around 1.0 kW/cm^2 (see the red squares in Fig. 2).

Fig. 4a summarises the structural evolution of $Ti_{1-x}Al_xN$ coatings synthesised from two 6-inch Ti-Al cathodes. The three subgroups (each including three XRD diffractograms) show the impact of the target composition, the N_2-flow-rate-ratio and the substrate bias. The red XRD diffractogram (in the three subgroups) stems from the same coating prepared with the simultaneous sputtering of a $Ti_{0.5}Al_{0.5}$ and $Ti_{0.4}Al_{0.6}$ target, with an N_2-flow-rate-ratio of 0.3 and a constant bias potential of -50 V. Further details on the deposition conditions used for the other coatings (additional to the labelling and figure caption) can be found in Table 1. Furthermore, the chemical composition of the coatings presented in Fig. 4a is given in Fig. 4b with squared data points indicating the Al/(Al + Ti) ratio (bottom axis) and circular data points indicating the N-content (top axis).

Altering the nominal Al content within the targets – here obtained by combining a $Ti_{0.5}Al_{0.5}$ target with either a $Ti_{0.6}Al_{0.4}$, $Ti_{0.5}Al_{0.5}$, or $Ti_{0.4}Al_{0.6}$ target (lower three XRD diffractograms in Fig. 4a), respectively – leads to an increase of the Al/(Al + Ti) ratio within our $Ti_{1-x}Al_xN$ thin films from 0.52 to 0.60 (see Fig. 4b). As thereby also the sputter rate increases (from 17.60 to 30.99 nm/min), the measured N content of the films slightly decreases, from 57 to 55 at.%, respectively (Fig. 4b). When keeping the nominal N_2-flow-rate-ratio constant, an increased sputter rate (the sputter yield of Al is nearly twice that of Ti) causes an increased metal-to-nitrogen arrival rate at the substrate surface. The highest Al-containing coating of this subgroup (presented by the red XRD diffractogram), exhibits already a small XRD peak at $2\Theta \sim 34.4^\circ$, being indicative for the formation of a *w*-AlN based phase. The small offset from the (002)-diffraction peak position of a *w*-AlN reference pattern [50], suggests the formation of a *w*-$Al_xTi_{1-x}N$ solid solution [31,32]. The lower Al-containing coatings do not show such a *w*-$Al_xTi_{1-x}N$ based XRD peak, but also their *c*-$Ti_{1-x}Al_xN$ (111) and (200) peaks are lower in intensity and broader – indicative for decreasing coherently diffracting domain sizes. Based on a work by Greczynski *et al.* [51] (showing that Ti targets generate a high fraction of Ti^{2+}-ions whereas the major fraction of Al-ions remains singly-charged), we suggest that the altered metal-ion distributions (from our powder-metallurgical $Ti_{0.6}Al_{0.4}$, $Ti_{0.5}Al_{0.5}$, $Ti_{0.4}Al_{0.6}$ targets) are responsible for this. Higher Ti-containing targets will thus result in a higher fraction of

Publication IV

Die approbierte gedruckte Originalversion dieser Dissertation ist an der TU Wien Bibliothek verfügbar.
The approved original version of this doctoral thesis is available in print at TU Wien Bibliothek.

TU Bibliothek Your knowledge hub WIEN

doubly-charged Ti^{2+}-ions within the sputter-flux. In combination with a constant bias potential of U_S = -50 V this introduces more lattice distortions and preferred renucleation sites, hence, the decrease in coherently diffracting domain sizes.

Higher Al-containing targets will result in a higher fraction of singly-charged metal-ions, resulting in a milder ion bombardment of the growing film, which essentially promotes surface diffusion, giving rise to larger and less defected crystallites [52]. Moreover, the low initial ionisation energy of Al ($IP_{1,Al}$ = 5.99 eV) contributes to a reduced probability for a twofold ionisation of Ti-atoms ($IP_{2,Ti}$ = 13.58 eV), as the mean energy of colliding electrons is quenched during the metal rich portion of the discharge [51,53]. Based on these results, the $Ti_{0.40}Al_{0.60}N$ coating (prepared by simultaneously sputtering a $Ti_{0.4}Al_{0.6}$ and $Ti_{0.5}Al_{0.5}$ target, with $f_{[N_2]}^{norm}$ = 0.3 and U_S = -50 V) is right at the boarder-line between the single-phased cubic and mixed-phase (cubic and wurtzite) coatings. Therefore, this coating was used as a reference for further studying the impact of varying $f_{[N_2]}^{norm}$ and U_S.

Decreasing $f_{[N_2]}^{norm}$ from 0.3 to 0.25 promotes the formation of a highly 111-oriented, single-phased *c*-$Ti_{0.47}Al_{0.53}N$ coating, whereas an increase to 0.35 results in a nearly X-ray amorphous $Al_{0.62}Ti_{0.38}N$ coating (Fig. 4a, middle subgroup). With increasing $f_{[N_2]}^{norm}$ from 0.25 to 0.3 to 0.35, the Al content increases from x = 0.54 to 0.60 to 0.62, and the N content increases from 52 to 54 to 56 at.%, respectively (Fig. 4b). As suggested by Gall *et al.* [54], the reduction of excess nitrogen (especially dissociated N_2 molecules) leads to a preferred 111 growth, being in good agreement to our observations. Furthermore, a significant impact of the N_2-flow-rate-ratio on the chemical composition of $Ti_{1-x}Al_xN$ coatings is commonly observed when sputtering powder-metallurgically prepared Ti-Al composite targets in mixed Ar/N_2-atmospheres, due to the selective poisoning behaviour of the individual Ti and Al particles [40]. Similar observations have also been reported for segmented Ti-Al targets [55]. As the heat of formation is more negative for TiN than for AlN (-305.6 kJ/mol vs. -241.6 kJ/mol), Ti grains will be poisoned earlier than the Al grains within the Ti-Al composite target [56]. The progressing poisoning state of the Ti-Al targets with increasing $f_{[N_2]}^{norm}$ is also reflected by the drastically decreasing deposition rates from 51 to 25 nm/min. As this simultaneously provides more time for surface-diffusion of the arriving species, the growing phases tend to approach their thermodynamically stable configuration, *i.e.* towards *c*-TiN and *w*-AlN [40]. Their competitive growth then leads to the formation of a nearly X-ray amorphous structure.

Changing the substrate bias from -50 V to floating potential (around -23 V) or to -100 V results in minor changes of the film composition (Al or N content, Fig. 4b). The coating prepared with floating potential still exhibits a small XRD response at the 2Θ position of *w*-$Al_xTi_{1-x}N$ (similar to the coating prepared with U_S = -50 V, used as a reference here). However, this coating also exhibits a pronounced left-hand shoulder of the (111)-diffraction peak, indicating the presence of Al-depleted (*c*-$Ti_{0.4+\Delta x}Al_{0.6-\Delta x}N$) and Al-enriched (*c*-$Ti_{0.4-\Delta x}Al_{0.6+\Delta x}N$) cubic structured regions, respectively [57]. This suggests that the energy input to the growing film from incident ions is low enough to reduce intermixing of the species, yet sufficient to allow approaching a thermodynamically more favourable state than the formation of one supersaturated *c*-$Ti_{1-x}Al_xN$ composition. The formation of Al-depleted (*c*-$Ti_{1-x+\Delta x}Al_{x-\Delta x}N$) and Al-enriched (*c*-$Ti_{1-x-\Delta x}Al_{x+\Delta x}N$) domains, represents such a state [25,31]. Preparing the coating with a higher bias potential of U_S = -100 V promotes the formation of the wurtzite-type phases next to the cubic phase, indicated by the higher intensity of the diffraction peak at 2Θ ~34.4°. The increased lattice damage, due to the high energetic ion bombardment, promotes nucleation of wurtzite-type phases, confirming previous observations for HiPIMS [51] as well as DCMS coatings [40].

When preparing the $Ti_{1-x}Al_xN$ coatings only with one HiPIMS operated $Ti_{0.5}Al_{0.5}$ target (while keeping the other deposition conditions unchanged to the reference coating $Ti_{0.40}Al_{0.60}N$; *i.e.*, with $f_{[N_2]}^{norm}$ = 0.3 and U_S = -50 V), we clearly observe a huge increase of the *w*-$Al_xTi_{1-x}N$ phase fraction despite the coating having a slightly lower Al-content of x = 0.59, Fig. 4c and d, respectively. With respect to the reference coating (prepared with simultaneously operating $Ti_{0.5}Al_{0.5}$ and $Ti_{0.4}Al_{0.6}$ targets), the growth rate decreased by approximately 60 %. Only, if the Al content is significantly lower with x = 0.45 (obtained by using a $Ti_{0.6}Al_{0.4}$ target), a single-phase *c*-$Ti_{1-x}Al_xN$ coating is obtained. In addition, reducing $f_{[N_2]}^{norm}$ from 0.3 to 0.2 while utilizing a $Ti_{0.4}Al_{0.6}$ target, which led to the formation of a nearly single-phase *w*-$Al_{0.65}Ti_{0.35}N$ coating, clearly supports the growth of the cubic phase. This is indicated by the tiny XRD peaks at the position of 111- and 200-oriented cubic-structured crystallites, at 2Θ of 37° and 43°, which were not present for the film prepared with $f_{[N_2]}^{norm}$ = 0.3. Basically, we assign this promotion of the cubic phase to the significantly increased deposition rate (from 13.3 to 26.4 nm/min) when decreasing $f_{[N_2]}^{norm}$ from 0.3 to 0.2 (see Table 1). Hence, in agreement with the results presented above and obtained for DCMS $Ti_{1-x}Al_xN$ [40], especially the deposition rate is a vital parameter when aiming for Al-rich single-phase *c*-$Ti_{1-x}Al_xN$.

The coatings prepared with simultaneously operating $Ti_{0.5}Al_{0.5}$ and $Ti_{0.4}Al_{0.6}$ targets, using floating potential, and with $f_{[N_2]}^{norm}$ = 0.25 and 0.3, are investigated in more detail by cross-sectional and plan-view TEM, respectively. The $Ti_{0.44}Al_{0.56}N$ coating ($f_{[N_2]}^{norm}$ = 0.25) is single-phase cubic structed (with a similar highly (111)-oriented structure as the $Ti_{0.46}Al_{0.54}N$ coating prepared with U_S = -50 V and $f_{[N_2]}^{norm}$ = 0.25, bottom XRD diffractogram of the middle subgroup in Fig. 4a), and the $Ti_{0.39}Al_{0.61}N$ coating ($f_{[N_2]}^{norm}$ = 0.3) exhibits the pronounced left-hand shoulder of the cubic structured (111) reflex (bottom XRD diffractogram of the upper subgroup in Fig. 4a).

The cross-sectional TEM bright field image of $Ti_{0.44}Al_{0.56}N$ (Fig. 5a) shows a dense and highly columnar growth morphology. The corresponding SAED pattern (Fig. 5b, collected close to the substrate) underlines the highly crystalline and single-phase face-centred cubic structure. The relatively long columns (with a high aspect ratio), being proof for a mild ion bombardment, can nicely be identified in the dark-field TEM (Fig. 5c). A pronounced growth in an energetically less favoured direction, *i.e.*, the (111)-orientation for *c*-$Ti_{1-x}Al_xN$, is typically linked to the prevalent growth conditions, being a compromise between surface as well as strain energy minimization [7,58].

Plan-view HRTEM investigations of $Ti_{0.39}Al_{0.61}N$ (floating potential and $f_{[N_2]}^{norm}$ = 0.3), which shows a pronounced left-hand shoulder of the cubic structured (111) reflex (Fig. 4a), confirm the formation of Al-depleted (*c*-$Ti_{0.39+\Delta x}Al_{0.61-\Delta x}N$) and Al-enriched (*c*-$Ti_{0.39-\Delta x}Al_{0.61+\Delta x}N$) domains. The interplanar spacing (d_{hkl}) of the cubic-structured matrix varies between 2.38 Å and 2.43 Å, corresponding to local Al-content fluctuations. The HRTEM micrograph furthermore proofs that at the grain and column boundaries small incoherent wurtzite-type phases are present. This was already indicated by the small reflex at 2Θ ~34° during XRD investigations (Fig. 4a). The Fast Fourier transformations (FFT) of area 1, where both cubic- and wurtzite-type phases are present, confirms their incoherency (insert 1 of Fig. 5d). The diffraction spot positions as well as the lattice plane distances of the wurtzite-type phases suggest a larger cell than stoichiometric *w*-AlN, hence Ti substitutes for Al to form *w*-$Al_xTi_{1-x}N$. The measured lattice plane distances are furthermore in excellent agreement with those obtained from XRD investigations.

The presence of small fractions of *w*-$Al_xTi_{1-x}N$ phases shifts the peak-

Publication IV

Die approbierte gedruckte Originalversion dieser Dissertation ist an der TU Wien Bibliothek verfügbar. The approved original version of this doctoral thesis is available in print at TU Wien Bibliothek.

TU Bibliothek Your knowledge hub WIEN

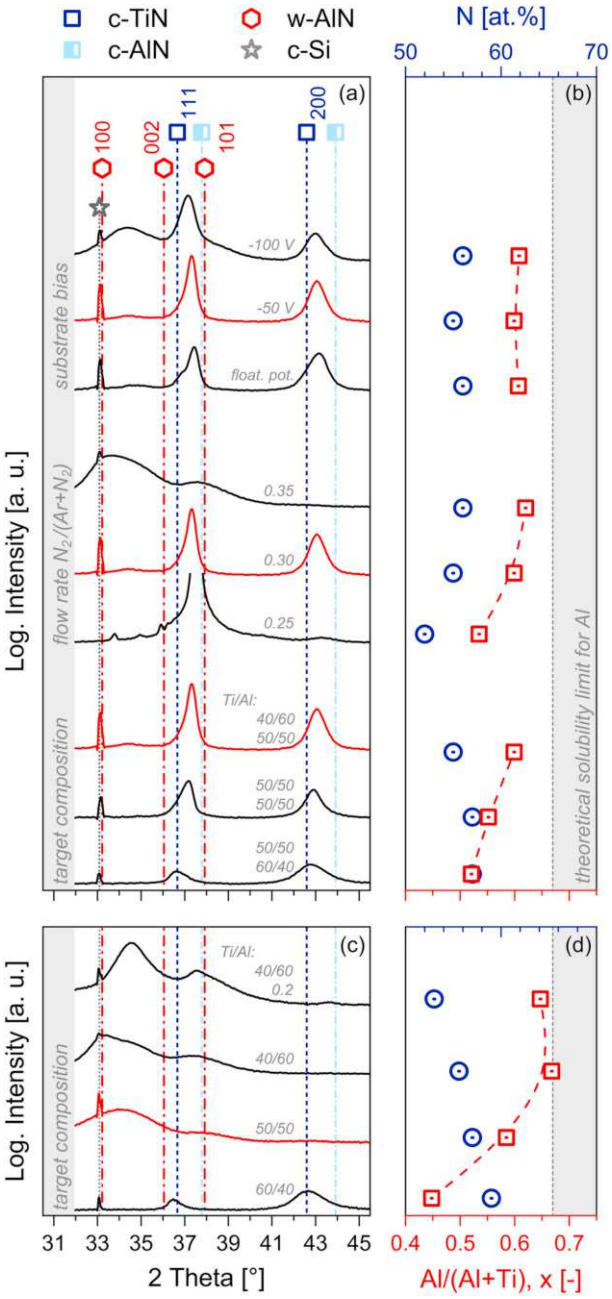

Fig. 4. (a) XRD diffractograms of Ti-Al-N thin films synthesised from two 6-inch Ti-Al cathodes, arranged in subgroups according to the altered deposition parameters: (i) target composition, (ii) nitrogen flow rate, (iii) substrate bias. (b) Chemical composition – bottom axis Al/(Al + Ti) ratio (red squares) and top axis N-content (blue circles) – of these Ti-Al-N thin films. Their data points are aligned in y-position with the corresponding XRD diffractogram presented in (a). (c) XRD diffractograms of Ti-Al-N thin films grown using one 6-inch Ti-Al cathode (except for the diffractogram labelled with 0.2, being from a coating prepared with $f_{[N_2]}^{norm} = 0.2$, $f_{[N_2]}^{norm}$ was 0.3) as well as (d) the respective film chemistries [50,66,67]. The red XRD diffractograms in (a) are from the same coating (prepared by simultaneously using a $Ti_{0.4}Al_{0.6}$ and $Ti_{0.5}Al_{0.5}$ target, U_S = -50 V, and $f_{[N_2]}^{norm} = 0.3$). The red XRD diffractogram in (c) is from a chemically similar coating, which was prepared with only one $Ti_{0.5}Al_{0.5}$ target (U_S = -50 V, $f_{[N_2]}^{norm} = 0.3$). (For interpretation of the references to colour in this figure legend, the reader is referred to the Web version of this article.)

hardness (typically observed for annealing temperatures between 800 °C and 900 °C, depending on the annealing time [24]) to lower temperatures, as highlighted by nanoindentation of annealed $Ti_{0.39}Al_{0.61}N$ and $Ti_{0.40}Al_{0.60}N$ (reference) coatings, see the circular and squared data points in Fig. 6, respectively. The XRD diffractograms of these two coatings in their as-deposited state (Fig. 4a, the diffractograms labelled with float. pot. and -50 V of the upper subgroup) suggest that a similar small fraction of wurtzite-type phases is present prior to

Publication IV

Die approbierte gedruckte Originalversion dieser Dissertation ist an der TU Wien Bibliothek verfügbar.
The approved original version of this doctoral thesis is available in print at TU Wien Bibliothek.
TU Bibliothek Your knowledge hub WIEN

annealing. To ensure for no interdiffusion with the substrate and no oxidation, coatings on single-crystalline Al_2O_3 substrates were used and the annealing (1 h at temperatures up to T_a = 1100 °C) was conducted in a slightly reducing Ar/H_2 atmosphere (98/2 mol.%, both gases with 99.999 % purity).

Based on the well-investigated age-hardening effect [24,25,57], both samples exhibit a pronounce hardness increase of more than 3 GPa compared to the as-deposited state when annealed at T_a = 700 °C. The hardness of $Ti_{0.40}Al_{0.60}N$ climbs from 35.9 ± 1.1 GPa to 39.5 ± 1.3 GPa, whereas that of $Ti_{0.39}Al_{0.61}N$ increases from 32.6 ± 0.8 GPa to 35.8 ± 1.5 GPa. Here, it needs to be mentioned, that the hardness values of the coatings on sapphire substrates are slightly higher as for coatings on Si substrates, due to differences in thermal expansion coefficients and elastic constants as already shown previously [59]. When annealed at higher temperatures, the hardness decreases significantly due to proceeding *w*-AlN phase formation (indicated by XRD investigations, not shown), initiated by the small fraction of wurtzite-type phases present in the as-deposited state. As the *H*-vs.-T_a curves for both coatings are only shifted in the y-axis (absolute hardness values) but not in the x-axis (temperature), the kinetic of the spinodal decomposition and further precipitation of *w*-AlN is similar for both coatings. It is envisioned that the ~3 GPa lower hardness values for $Ti_{0.39}Al_{0.61}N$ are basically due to the different starting point, having a slightly more "relaxed" microstructure as a result of the less-intense ion bombardment during growth (only floating potential was used).

$Ti_{0.40}Al_{0.60}N$, which was prepared with -50 V bias potential, shows an asymmetric (111) XRD peak with a slightly wider tail on its left-hand side. For $Ti_{0.39}Al_{0.61}N$ a clear left-hand shoulder of the (111) XRD peak can be detected. Detailed HRTEM investigations (Fig. 5d) proved that the origin of this shoulder formation is a variation in lattice plane distances based on chemical fluctuations. The less pronounced left-hand shoulder of the (111) XRD peak of $Ti_{0.40}Al_{0.60}N$ suggests that also the chemical fluctuation of its cubic-structured matrix is less pronounced or with a smaller modulation period than within $Ti_{0.39}Al_{0.61}N$. Such chemical fluctuations within cubic-structured supersaturated $Ti_{1-x}Al_xN$ solid solutions are natural [60] due to their chemical instability [61]. The milder ion bombardment during growth of $Ti_{0.39}Al_{0.61}N$ (as here only a floating potential was used instead of -50 V bias for $Ti_{0.40}Al_{0.60}N$) may allow for a larger modulation period between the chemical heterogeneities (both alloys are deep within the chemical spinodal region of $Ti_{1-x}Al_xN$ [61]). Basically, the modulation period caused by spinodal decomposition is material dependent, as it strongly depends on the interfacial energy associated with the formation of coherent domains having different chemistry and lattice constants [62]. However, it is envisioned that a surface-diffusion-initiated spinodal decomposition during film growth (hence, there is a free surface and thus definitely the overall interfacial energies are different) can lead to larger modulation periods than a spinodal decomposition caused within the bulk of the film. Therefore, the two considered films, $Ti_{0.39}Al_{0.61}N$ and $Ti_{0.40}Al_{0.60}N$, are seen as examples for the two processes. The alleged larger modulation period within $Ti_{0.39}Al_{0.61}N$ (as compared to $Ti_{0.40}Al_{0.60}N$) allows for a well-developed left-hand shoulder formation of the (111) XRD peak, and gives rise to the shift of the *H*-vs.-T_a curve to lower values. The evolution of the indentation modulus follows an analogous trend as function of T_a, with peak values of 516 GPa for $Ti_{0.40}Al_{0.60}N$ and 450 GPa for $Ti_{0.39}Al_{0.61}N$.

Now that we have looked on the effect of small changes (floating potential vs. -50 V bias) on the thermomechanical properties of R-HiPIMS deposited $Ti_{1-x}Al_xN$, we will discuss the impact of a wider variation in deposition conditions on their mechanical properties. Fig. 7a and b summarize the indentation hardness and residual film stresses as a function of their Al-concentration. The prevalent phases are indicated by corresponding symbols (squares for the cubic phase, hexagons for the wurtzite-type phase, and half-filled squares for coatings obtaining both phases). Single-phase *c*-$Ti_{1-x}Al_xN$ exhibit increasing hardness with increasing Al-fraction, from 30.3 ± 1.0 GPa (x = 0.45) to 33.2 ± 0.7 GPa (x = 0.55). The highly (111)-oriented *c*-$Ti_{0.46}Al_{0.54}N$ as well as *c*-$Ti_{0.44}Al_{0.56}N$, having a pronounced columnar growth morphology (see also Fig. 5a and c), strongly deviates from this trend by exhibiting a rather low hardness of only ~25 GPa. These are also the only *c*-$Ti_{1-x}Al_xN$ coatings showing essentially zero residual stresses, while the others exhibit compressive stresses between -1.4 and -2.1 GPa. In addition, through the preferred (111) growth, resulting in extremely long columns with a high aspect ratio, a slightly underdense grain boundary interior may lead to the reduced hardness values. Especially, crystallites with (111) faces parallel to the substrate grow faster in height than their (001)-oriented counterparts (which favour lateral expansion) caused through lower adatom potential energy on (111) surface [54]. Such a growth mode is also forced by relatively low deposition temperatures as prevalent for all coatings deposited. Hence, it is envisioned that the specific (111) dominated growth mode causes the increased deposition rates of about 51 nm/min for highly (111) oriented coatings compared to about 25 nm/min for more random oriented ones. Furthermore, reduced nitrogen partial pressures enhance this phenomenon. As long as the fraction of wurtzite-type phases is small, the hardness is at a very high level of ~35 GPa, *e.g.*, 34.6 ± 0.5 GPa for *c*-$Ti_{0.40}Al_{0.60}N$ (on sapphire, its hardness was 35.9 GPa). The predominantly wurtzite structured coatings show hardness values between 20 and 23 GPa as well as relatively low compressive stresses between 0 to -1 GPa.

These findings clearly show that powder-metallurgically prepared Ti-Al targets, when using proper R-HiPIMS settings, are highly beneficial for the synthesis of strong and Al-rich $Ti_{1-x}Al_xN$ thin films. Despite the presence of doubly-charged metal ions (basically due to Ti), thin films of excellent hardness and low compressive stresses are accessible.

One important parameter, especially when having a high fraction of metal-ions, is the bias potential. The impact of a variation in applying various DC bias potentials has been discussed already. A DC bias potential of -50 V is beneficial for our HiPIMS conditions despite also providing a high fraction of doubly-charged Ti-ions from the Ti-Al composite target. A bias potential of -50 V is small enough to avoid extensive lattice distortion and the formation of possible nucleation sites for wurtzite-type phases, but also large enough to guarantee for effective intermixing of the involved metal species. Synchronising the applied bias potential can further help to support the cubic phase formation while still providing sufficient energy for intermixing. To investigate this influence, a sample (and R-HiPIMS conditions) showing a high fraction of wurtzite-type phases and a similar chemical composition as the reference sample $Ti_{0.40}Al_{0.60}N$, which showed only very small indications of wurtzite-type phases in its as-deposited state, were selected. Such a sample is presented in Fig. 4c and was prepared with only one $Ti_{0.5}Al_{0.5}$ target ($f_{[N_2]}^{norm}$ = 0.3 and U_S = -50 V). For the pulsed bias condition (always U_{synced} = -50 V) the following cases have been investigated (as indicated in Fig. 8a): (2) fully synchronised to the cathode pulse (t_{offset} = 0 µs and t_{Bias} = 75 µs) as well as (3–5) with a delay of t_{offset} = 40 µs. For the delayed bias pulse, we furthermore varied the pulse duration itself from t_{Bias} = 50 to 75 to 100 µs. Introducing a delay between the onset of the HiPIMS pulse and the bias pulse will influence the metal-ion and process-gas-ion dominated bombardment situation during film growth. The typical time-evolution of dominating ions during a HiPIMS pulse is headed by energetic process gas-ions to be followed by metal ions (very often the doubly-charged metal ions lead the singly-charged metal ions). Consequently, a

Die approbierte gedruckte Originalversion dieser Dissertation ist an der TU Wien Bibliothek verfügbar.
The approved original version of this doctoral thesis is available in print at TU Wien Bibliothek.
TU Bibliothek Your knowledge hub WIEN

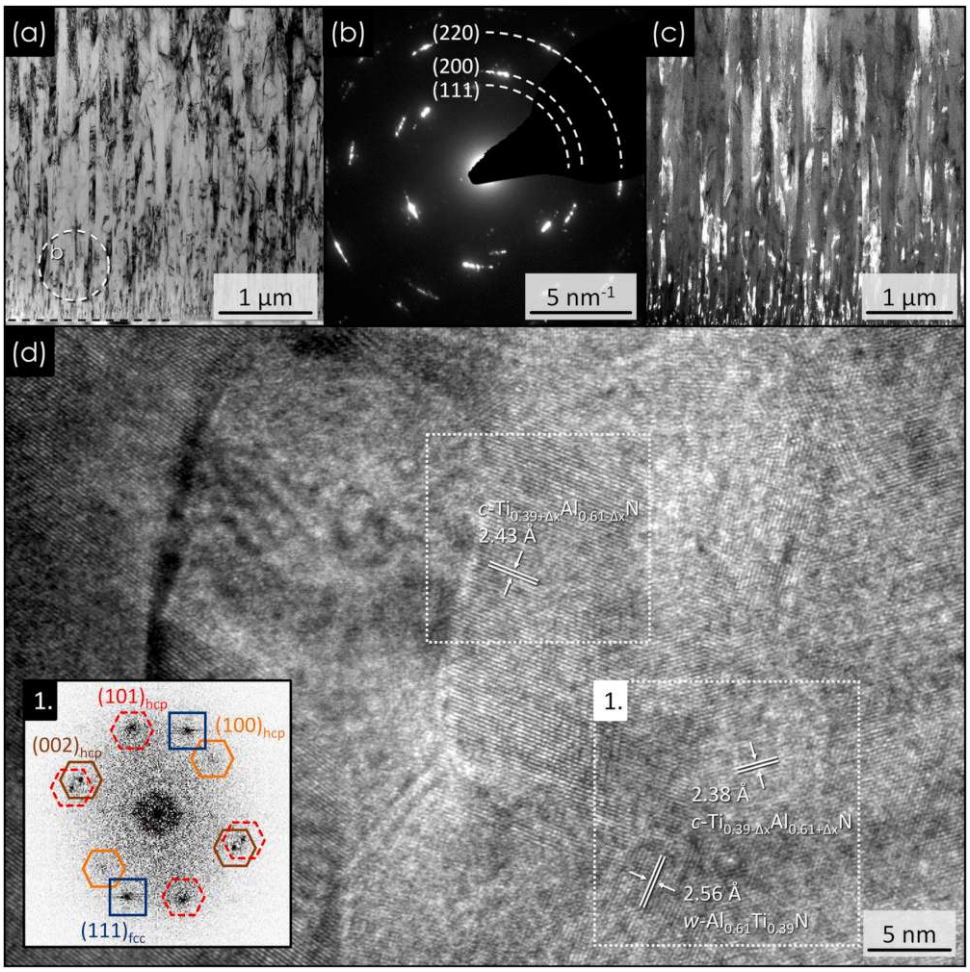

Fig. 5. (a) Cross-sectional bright-field TEM micrograph of a cubic $Ti_{0.46}Al_{0.54}N$ thin film deposited at $f_{[N_2]}^{norm}$ = 0.25 and U_S = floating potential. (b) Corresponding SAED pattern of the interface near region as indicated by a circle in (a). (c) Dark-field acquisition of the same region presented in (a). The XRD diffractogram of this coating is essentially identical to that presented in Fig. 4a (lower diffractogram of the middle subgroup). (d) Plan-view HRTEM image of a $Ti_{0.39}Al_{0.61}N$ thin film grown under $f_{[N_2]}^{norm}$ = 0.3 and U_S = floating potential. Included lattice spacings correspond to *c*-$Ti_{0.39 \mp \Delta x}Al_{0.61 \pm \Delta x}N$ and *w*-$Al_{0.61}Ti_{0.39}N$ structures. The FFT presented in insert 1 was calculated from area 1. The XRD diffractogram of this coating is presented in Fig. 4a (lower diffractogram of the upper subgroup).

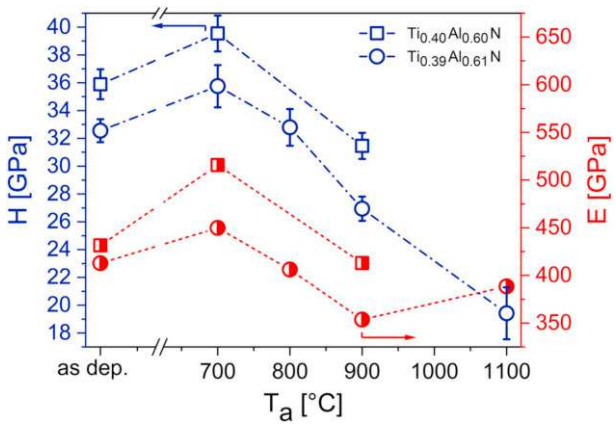

Fig. 6. Thermomechanical properties [*H* vs. T_a (open symbols) and *E* vs. T_a (half-filled symbols)] of coatings prepared with $f_{[N_2]}^{norm}$ = 0.3 and U_S = floating potential ($Ti_{0.39}Al_{0.61}N$, circular symbols) or $f_{[N_2]}^{norm}$ = 0.3 and U_S = -50 V ($Ti_{0.40}Al_{0.60}N$, which is used as a reference here, square symbols). Their XRD diffractograms are given in Fig. 4a (upper subgroup).

Die approbierte gedruckte Originalversion dieser Dissertation ist an der TU Wien Bibliothek verfügbar.
The approved original version of this doctoral thesis is available in print at TU Wien Bibliothek.
TU Bibliothek Your knowledge hub WIEN

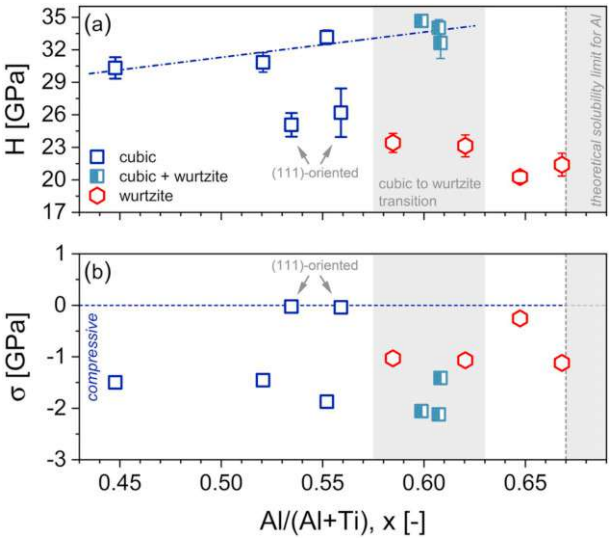

Fig. 7. (a) Nanoindentation hardness (measured on Si substrate) and (b) biaxial residual stress of R-HiPIMS deposited $Ti_{1-x}Al_xN$ thin films as a function of their Al metal-fraction, x. Coatings with a clearly single-phase cubic structure are presented by open squared symbols, those with a predominant cubic phase and a small fraction of wurtzite phase are presented by half-filled squared symbols, and predominant wurtzite-structured coatings are presented with open hexagonal symbols.

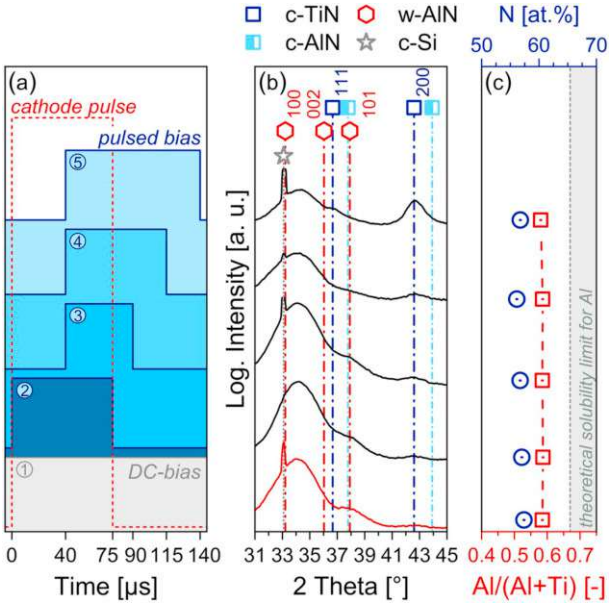

Fig. 8. (a) Schematic of the HiPIMS cathode pulse (red short-dashed line) and the relative position of the -50 V DC bias (1), and the pulsed bias (U_S = -50 V) without delay (2) and with a 40 µs delay (3, 4, 5) to the HiPIMS pulse. The bias pulses (2) and (4) have the same length of 75 µs as the HiPIMS pulse. The bias pulses (3) and (5) are shorter (50 µs) and longer (100 µs), respectively. (b) XRD diffractograms of Ti-Al-N thin films prepared using these bias conditions. Their relative y-position is aligned with the corresponding schematic of the applied bias scenarios (1)-(5) presented in (a). (c) Chemical composition – bottom axis Al/(Al + Ti) ratio (red squares) and top axis N-content (blue circles) – of these 5 coatings, again the relative y-position of the data points is aligned with the corresponding XRD diffractograms presented in (b). (For interpretation of the references to colour in this figure legend, the reader is referred to the Web version of this article.)

delay will avoid the initial influx of high-energy process-gas- as well as metal-ions (singly- and doubly-charged) [36,63–65].

Fig. 8b presents the XRD diffractograms of the $Ti_{1-x}Al_xN$ thin films prepared with the mentioned bias scenarios, schematically depicted in Fig. 8a. The diffractograms are complemented by EDS measurements, indicating similar chemical compositions (Al and N content) for all variations (see Fig. 8c). Fully synchronising the bias pulse to the R-HiPIMS pulse results in no significant change of the film structure (as compared to a DC bias), again revealing a predominantly wurtzite-type coating with a small fraction of cubic phases (see the small XRD response at $2\Theta \sim 43°$, indicating the 200 orientation). Applying a delayed bias pulse promotes the growth of the cubic phase, especially for longer pulse durations. It is therefore suggested, that extending the applied bias past the plasma breakdown shifts the gas-to-metal-ion ratio continuously towards higher values, with an increasing amount of low-energy species attracted from the afterglow regime. This improves near surface diffusion and reduces residual defects introduced by the unavoidable doubly-charged Ti-species, thus contributes to stabilising the metastable cubic phase. Nevertheless, further analysis on the effect of extended bias durations will be necessary, especially regarding time- and energy-resolved ion distributions of the sputtered species. Yet, the presented results hint a further possibility to tune the phase formation of metastable thin films, despite using composite materials in a reactive HiPIMS discharge.

4. Conclusions

In this work, we report on the reactive HiPIMS deposition of Ti-Al-N thin films using $Ti_{1-x}Al_x$ composite targets in mixed Ar/N_2-atmospheres, prepared at a substrate temperature of T_S = 285 ± 15 °C. In particular, the influence of HiPIMS parameters, both pulse frequency and duration, as well as deposition parameters such as the N_2 flow ratio, substrate bias voltage, or target composition are methodically investigated with respect to phase stability, composition, mechanical properties and film morphology.

For Al contents of $x \leq 0.55$, all $Ti_{1-x}Al_xN$ thin films crystallised with a single-phase cubic structure, regardless of the deposition conditions used – involving variations of the nitrogen partial pressure ($f^{norm}_{[N_2]}$ = 0.2 to 0.35), bias voltage (U_S = float. pot. to -100 V), target composition (x = 0.4, 0.5, and 0.6) as well as pulse- (f = 200 to 1000 Hz and t_{on} = 50 to 200 µs) and power-modulations (p_{peak} = 0.04 to 1.34 kW/cm^2). Their hardness generally increases with the Al content and is about 33 GPa (with -2 GPa residual stresses) for c-$Ti_{0.45}Al_{0.55}N$. However, for coatings grown with duty cycles below 3 % a nano-crystalline morphology is obtained and their hardness is only around 31 GPa, although having a cubic structure. Consequently, operating the $Ti_{1-x}Al_x$ composite target with extremely low pulse frequency and duration, negatively affects the coating strength. Based on our results, it can be concluded that operating the $Ti_{1-x}Al_x$ targets with f = 500 Hz and t_{on} = 75 µs (corresponding to a duty cycle of 3.75 %) combined with peak power densities above 1 kW cm^{-2}, leads to films with excellent hardness and only moderate compressive stresses.

With the help of a bias potential not only the surface-diffusion initiated spinodal decomposition during film growth can be influenced (especially due to the metal-ions provided by the HiPIMS discharge), but also the formation of wurtzite-type phases. The bias potential should be moderate but not too low to ensure sufficient intermixing of

Die approbierte gedruckte Originalversion dieser Dissertation ist an der TU Wien Bibliothek verfügbar.
The approved original version of this doctoral thesis is available in print at TU Wien Bibliothek.

TU Bibliothek Your knowledge hub WIEN

the film forming species themselves. For our conditions, the floating potential (around -23 V) was too low, as thereby the chemical fluctuations of the cubic phase formed with larger modulation periods. Applying -50 V bias resulted in a smaller modulation period and consequently $Ti_{0.40}Al_{0.60}N$ films with excellent hardness (~36 GPa on sapphire substrate), which further increased to ~40 GPa upon annealing for 1 h at 700 °C. Contrary, a bias potential of -100 V promoted the wurtzite-type formation already during film growth. When synchronising the bias potential (-50 V) with the HiPIMS signal, the formation of the cubic phase is especially promoted when using a 40 μs offset to the HiPIMS pulse ignition and if the bias pulse is maintained for 100 μs (used HiPIMS setting: $f = 500$ Hz and $t_{on} = 75$ μs with p_{peak} ~1 kW/cm^2). We therefore suggest, that the offset time allows to especially avoid highly-energetic gas- and metal-ions – typically leading the time-evolution of generated ions of the HiPIMS discharge – promoting the attraction of low-energy species from the afterglow regime.

Based on our results, we can conclude that using powder-metallurgically prepared Ti-Al composite targets in a reactive HiPIMS discharge allows for a wide range of possibilities (through deposition parameter adjustments) in influencing the structure and surface-diffusion initiated growth of $Ti_{1-x}Al_xN$ coatings.

Acknowledgements

The financial support by the Austrian Federal Ministry for Digital and Economic Affairs and the National Foundation for Research, Technology and Development is gratefully acknowledged (Christian Doppler Laboratory “Surface Engineering of high-performance Components”). We also thank for the financial support of Plansee SE, Plansee Composite Materials GmbH, and Oerlikon Balzers, Oerlikon Surface Solutions AG. In addition, we want to thank the X-ray center (XRC) of TU Wien for beam time as well as the electron microscopy center - USTEM TU Wien - for using the SEM and TEM facilities.

References

[1] V. Kouznetsov, K. Macák, J.M. Schneider, U. Helmersson, I. Petrov, A novel pulsed magnetron sputter technique utilizing very high target power densities, Surf. Coat. Technol. 122 (1999) 290–293, https://doi.org/10.1016/S0257-8972(99)00292-3.
[2] K. Sarakinos, J. Alami, S. Konstantinidis, High power pulsed magnetron sputtering: a review on scientific and engineering state of the art, Surf. Coat. Technol. 204 (2010) 1661–1684, https://doi.org/10.1016/j.surfcoat.2009.11.013.
[3] A.P. Ehiasarian, High-power impulse magnetron sputtering and its applications, Pure Appl. Chem. 82 (2010) 1247–1258, https://doi.org/10.1351/PAC-CON-09-10-43.
[4] D. Lundin, K. Sarakinos, An introduction to thin film processing using high-power impulse magnetron sputtering, J. Mater. Res. 27 (2012) 780–792, https://doi.org/10.1557/jmr.2012.8.
[5] K. Bobzin, N. Bagcivan, P. Immich, S. Bolz, J. Alami, R. Cremer, Advantages of nanocomposite coatings deposited by high power pulse magnetron sputtering technology, J. Mater. Process. Technol. 209 (2009) 165–170, https://doi.org/10.1016/j.jmatprotec.2008.01.035.
[6] J. Bohlmark, M. Lattemann, J.T. Gudmundsson, A.P. Ehiasarian, Y. Aranda Gonzalvo, N. Brenning, U. Helmersson, The ion energy distributions and ion flux composition from a high power impulse magnetron sputtering discharge, Thin Solid Films 515 (2006) 1522–1526, https://doi.org/10.1016/j.tsf.2006.04.051.
[7] F. Adibi, I. Petrov, J.E. Greene, L. Hultman, J.E. Sundgren, Effects of high-flux low-energy (20-100 eV) ion irradiation during deposition on the microstructure and preferred orientation of Ti0.5Al0.5N alloys grown by ultra-high-vacuum reactive magnetron sputtering, J. Appl. Phys. 73 (1993) 8580–8589, https://doi.org/10.1063/1.353388.
[8] A.P. Ehiasarian, A. Vetushka, Y.A. Gonzalvo, G. Sáfrán, L. Székely, P.B. Barna, Influence of high power impulse magnetron sputtering plasma ionization on the microstructure of TiN thin films, J. Appl. Phys. 109 (2011) 104314, https://doi.org/10.1063/1.3579443.
[9] J.T. Gudmundsson, N. Brenning, D. Lundin, U. Helmersson, High power impulse magnetron sputtering discharge, J. Vac. Sci. Technol. A 30 (2012) 030801, , https://doi.org/10.1116/1.3691832.
[10] C. Huo, D. Lundin, M.A. Raadu, A. Anders, J.T. Gudmundsson, N. Brenning, On the road to self-sputtering in high power impulse magnetron sputtering: particle balance and discharge characteristics, Plasma Sources Sci. Technol. 23 (2014) 025017, , https://doi.org/10.1088/0963-0252/23/2/025017.
[11] J. Čapek, S. Kadlec, Return of target material ions leads to a reduced hysteresis in reactive high power impulse magnetron sputtering: Experiment, J. Appl. Phys. 121 (2017) 171911, https://doi.org/10.1063/1.4977816.
[12] A. Anders, Tutorial: reactive high power impulse magnetron sputtering (R-HiPIMS), J. Appl. Phys. 121 (2017) 171101, https://doi.org/10.1063/1.4978350.
[13] J. Paulitsch, P.H. Mayrhofer, W.D. Münz, M. Schenkel, Structure and mechanical properties of CrN/TiN multilayer coatings prepared by a combined HIPIMS/UBMS deposition technique, Thin Solid Films 517 (2008) 1239–1244, https://doi.org/10.1016/j.tsf.2008.06.080.
[14] M. Lattemann, U. Helmersson, J.E. Greene, Fully dense, non-faceted 111-textured high power impulse magnetron sputtering TiN films grown in the absence of substrate heating and bias, Thin Solid Films 518 (2010) 5978–5980, https://doi.org/10.1016/j.tsf.2010.05.064.
[15] G. Greczynski, S. Mráz, M. Hans, D. Primetzhofer, J. Lu, L. Hultman, J.M. Schneider, Unprecedented Al supersaturation in single-phase rock salt structure VAlN films by Al+subplantation, J. Appl. Phys. 121 (2017) 171907, https://doi.org/10.1063/1.4977813.
[16] M. Samuelsson, D. Lundin, J. Jensen, M.A. Raadu, J.T. Gudmundsson, U. Helmersson, On the film density using high power impulse magnetron sputtering, Surf. Coat. Technol. 205 (2010) 591–596, https://doi.org/10.1016/j.surfcoat.2010.07.041.
[17] T. Shimizu, H. Komiya, Y. Teranishi, K. Morikawa, H. Nagasaka, M. Yang, Pressure dependence of (Ti, Al)N film growth on inner walls of small holes in high-power impulse magnetron sputtering, Thin Solid Films 624 (2017) 189–196, https://doi.org/10.1016/j.tsf.2016.09.041.
[18] M. Lattemann, A.P. Ehiasarian, J. Bohlmark, P.Å.O. Persson, U. Helmersson, Investigation of high power impulse magnetron sputtering pretreated interfaces for adhesion enhancement of hard coatings on steel, Surf. Coat. Technol. 200 (2006) 6495–6499, https://doi.org/10.1016/j.surfcoat.2005.11.082.
[19] C.L. Chang, F.C. Yang, Effect of target composition on the microstructural, mechanical, and corrosion properties of TiAlN thin films deposited by high-power impulse magnetron sputtering, Surf. Coat. Technol. 352 (2018) 330–337, https://doi.org/10.1016/j.surfcoat.2018.08.023.
[20] W.Y. Wu, A. Su, Y. Liu, C.M. Yeh, W.C. Chen, C.L. Chang, Effect of DC input power and nitrogen ratio on the deposition of $Ti_{1-x}Al_xN$ thin films using high power impulse magnetron sputtering technique, Surf. Coat. Technol. 303 (2016) 48–53, https://doi.org/10.1016/j.surfcoat.2016.03.050.
[21] J. Alami, S. Bolz, K. Sarakinos, High power pulsed magnetron sputtering: fundamentals and applications, J. Alloy. Comp. 483 (2009) 530–534, https://doi.org/10.1016/j.jallcom.2008.08.104.
[22] W. Münz, Titanium aluminum nitride films: a new alternative to TiN coatings, J. Vac. Sci. Technol. A 4 (1986) 2717–2725, https://doi.org/10.1116/1.573713.
[23] A. Hörling, L. Hultman, M. Odén, J. Sjölén, L. Karlsson, Mechanical properties and machining performance of Ti1-xAlxN-coated cutting tools, Surf. Coat. Technol. 191 (2005) 384–392, https://doi.org/10.1016/j.surfcoat.2004.04.056.
[24] R. Rachbauer, S. Massl, E. Stergar, D. Holec, D. Kiener, J. Keckes, J. Patscheider, M. Stiefel, H. Leitner, P.H. Mayrhofer, Decomposition pathways in age hardening of Ti-Al-N films, J. Appl. Phys. 110 (2011) 23515, https://doi.org/10.1063/1.3610451.
[25] P.H. Mayrhofer, A. Hörling, L. Karlsson, J. Sjölén, T. Larsson, C. Mitterer, L. Hultman, Self-organized nanostructures in the Ti–Al–N system, Appl. Phys. Lett. 83 (2003) 2049–2051, https://doi.org/10.1063/1.1608464.
[26] D.Y. Wang, C.L. Chang, K.W. Wong, Y.W. Li, W.Y. Ho, Improvement of the interfacial integrity of (Ti,Al)N hard coatings deposited on high speed steel cutting tools, Surf. Coat. Technol. 120–121 (1999) 388–394, https://doi.org/10.1016/S0257-8972(99)00452-1.
[27] L. Chen, Y. Du, P.H. Mayrhofer, S.Q. Wang, J. Li, The influence of age-hardening on turning and milling performance of Ti-Al-N coated inserts, Surf. Coat. Technol. 202 (2008) 5158–5161, https://doi.org/10.1016/j.surfcoat.2008.05.036.
[28] F. Vaz, L. Rebouta, M. Andritschky, M.F. da Silva, J.C. Soares, Thermal oxidation of Ti1 − xAlxN coatings in air, J. Eur. Ceram. Soc. 17 (1997) 1971–1977, https://doi.org/10.1016/S0955-2219(97)00050-2.
[29] G. Greczynski, S. Mráz, M. Hans, J. Lu, L. Hultman, J. Schneider, Control over the Phase Formation in metastable transition metal nitride thin films by tuning the Al+subplantation depth, Coatings 9 (2018) 17, https://doi.org/10.3390/coatings9010017.
[30] D. Rafaja, C. Wüstefeld, C. Baehtz, V. Klemm, M. Dopita, M. Motylenko, C. Michotte, M. Kathrein, Effect of internal interfaces on hardness and thermal stability of nanocrystalline Ti0.5Al0.5N coatings, Metall. Mater. Trans. A Phys. Metall. Mater. Sci. 42 (2011) 559–569, https://doi.org/10.1007/s11661-010-0204-8.
[31] P.H. Mayrhofer, D. Music, J.M. Schneider, Influence of the Al distribution on the structure, elastic properties, and phase stability of supersaturated Ti1 − xAlxN, J. Appl. Phys. 100 (2006) 094906, , https://doi.org/10.1063/1.2360778.
[32] K. Kutschej, P.H. Mayrhofer, M. Kathrein, P. Polcik, R. Tessadri, C. Mitterer, Structure, mechanical and tribological properties of sputtered Ti1-xAlxN coatings with $0.5 \le x \le 0.75$, Surf. Coat. Technol. 200 (2005) 2358–2365, https://doi.org/10.1016/j.surfcoat.2004.12.008.
[33] L. Chen, J. Paulitsch, Y. Du, P.H. Mayrhofer, Thermal stability and oxidation resistance of Ti-Al-N coatings, Surf. Coat. Technol. 206 (2012) 2954–2960, https://doi.org/10.1016/j.surfcoat.2011.12.028.
[34] G. Greczynski, J. Lu, M.P. Johansson, J. Jensen, I. Petrov, J.E. Greene, L. Hultman, Role of Ti n+ and Al n+ ion irradiation (n = 1, 2) during Ti 1-xAl xN alloy film

Publication IV

Die approbierte gedruckte Originalversion dieser Dissertation ist an der TU Wien Bibliothek verfügbar.
The approved original version of this doctoral thesis is available in print at TU Wien Bibliothek.

TU Bibliothek Your knowledge hub WIEN

growth in a hybrid HIPIMS/magnetron mode, Surf. Coat. Technol. 206 (2012) 4202–4211, https://doi.org/10.1016/j.surfcoat.2012.04.024.
[35] G. Greczynski, J. Lu, M. Johansson, J. Jensen, I. Petrov, J.E. Greene, L. Hultman, Selection of metal ion irradiation for controlling Ti1-xAlxN alloy growth via hybrid HIPIMS/magnetron co-sputtering, Vacuum 86 (2012) 1036–1040, https://doi.org/10.1016/j.vacuum.2011.10.027.
[36] G. Greczynski, J. Lu, J. Jensen, I. Petrov, J.E. Greene, S. Bolz, W. Kölker, C. Schiffers, O. Lemmer, L. Hultman, Metal versus rare-gas ion irradiation during Ti1-xAlxN film growth by hybrid high power pulsed magnetron/dc magnetron co-sputtering using synchronized pulsed substrate bias, J. Vac. Sci. Technol. A 30 (2012) 061504, , https://doi.org/10.1116/1.4750485.
[37] T. Shimizu, Y. Teranishi, K. Morikawa, H. Komiya, T. Watanabe, H. Nagasaka, M. Yang, Impact of pulse duration in high power impulse magnetron sputtering on the low-temperature growth of wurtzite phase (Ti,Al)N films with high hardness, Thin Solid Films 581 (2015) 39–47, https://doi.org/10.1016/j.tsf.2014.11.076.
[38] S. Severin, M. Naveed, S. Weiß, Effect of HPPMS pulse-frequency on plasma discharge and deposited AlTiN coating properties, Ann. Mater. Sci. Eng. 2017 (2017) 18, https://doi.org/10.1155/2017/4850908.
[39] A. Anders, J. Čapek, M. Hála, L. Martinu, The 'recycling trap': a generalized explanation of discharge runaway in high-power impulse magnetron sputtering, J. Phys. D Appl. Phys. 45 (2012) 012003, , https://doi.org/10.1088/0022-3727/45/1/012003.
[40] L. Chen, M. Moser, Y. Du, P.H. Mayrhofer, Compositional and structural evolution of sputtered Ti-Al-N, Thin Solid Films 517 (2009) 6635–6641, https://doi.org/10.1016/j.tsf.2009.04.056.
[41] G.M. Pharr, An improved technique for determining hardness and elastic modulus using load and displacement sensing indentation experiments, J. Mater. Res. 7 (1992) 1564–1583, https://doi.org/10.1557/JMR.1992.1564.
[42] C. Gammer, C. Mangler, C. Rentenberger, H.P. Karnthaler, Quantitative local profile analysis of nanomaterials by electron diffraction, Scr. Mater. 63 (2010) 312–315, https://doi.org/10.1016/j.scriptamat.2010.04.019.
[43] G.C.A.M. Janssen, M.M. Abdalla, F. van Keulen, B.R. Pujada, B. van Venrooy, Celebrating the 100th anniversary of the Stoney equation for film stress: developments from polycrystalline steel strips to single crystal silicon wafers, Thin Solid Films 517 (2009) 1858–1867, https://doi.org/10.1016/j.tsf.2008.07.014.
[44] J. Lin, J.J. Moore, W.D. Sproul, B. Mishra, J.A. Rees, Z. Wu, R. Chistyakov, B. Abraham, Ion energy and mass distributions of the plasma during modulated pulse power magnetron sputtering, Surf. Coat. Technol. 203 (2009) 3676–3685, https://doi.org/10.1016/j.surfcoat.2009.05.048.
[45] D. Depla, X.Y. Li, S. Mahieu, R. De Gryse, Determination of the effective electron emission yields of compound materials, J. Phys. D Appl. Phys. 41 (2008), https://doi.org/10.1088/0022-3727/41/20/202003.
[46] R. Ganesan, B. Treverrow, B. Murdoch, D. Xie, A.E. Ross, J.G. Partridge, I.S. Falconer, D.G. McCulloch, D.R. McKenzie, M.M.M. Bilek, Duty cycle control in reactive high-power impulse magnetron sputtering of hafnium and niobium, J. Phys. D Appl. Phys. 49 (2016), http://iopscience.iop.org/article/10.1088/0022-3727/49/24/245201/pdf , Accessed date: 4 January 2019.
[47] G. Greczynski, L. Hultman, Peak amplitude of target current determines deposition rate loss during high power pulsed magnetron sputtering, Vacuum 124 (2016) 1–4, https://doi.org/10.1016/j.vacuum.2015.11.004.
[48] J. Alami, K. Sarakinos, F. Uslu, M. Wuttig, On the relationship between the peak target current and the morphology of chromium nitride thin films deposited by reactive high power pulsed magnetron sputtering, J. Phys. D Appl. Phys. 42 (2009) 015304, , https://doi.org/10.1088/0022-3727/42/1/015304.
[49] L. Hultman, J.E. Sundgren, J.E. Greene, Formation of polyhedral N 2 bubbles during reactive sputter deposition of epitaxial TiN(100) films, J. Appl. Phys. 66 (1989) 536–544, https://doi.org/10.1063/1.343570.
[50] ICDD, Powder Diffraction File - Wurtzite AlN - 04-016-3965, (2013).
[51] G. Greczynski, J. Lu, J. Jensen, S. Bolz, W. Kölker, C. Schiffers, O. Lemmer, J.E. Greene, L. Hultman, A review of metal-ion-flux-controlled growth of metastable TiAlN by HIPIMS/DCMS co-sputtering, Surf. Coat. Technol. 257 (2014) 15–25, https://doi.org/10.1016/j.surfcoat.2014.01.055.
[52] G. Greczynski, J. Lu, J. Jensen, I. Petrov, J.E. Greene, S. Bolz, W. Kölker, C. Schiffers, O. Lemmer, L. Hultman, Strain-free, single-phase metastable Ti0.38Al0.62N alloys with high hardness: metal-ion energy vs. momentum effects during film growth by hybrid high-power pulsed/dc magnetron cosputtering, Thin Solid Films 556 (2014) 87–98, https://doi.org/10.1016/j.tsf.2014.01.017.
[53] D.R. Lide, CRC Handbook of Chemistry and Physics, 84th ed., CRC Press, 2003.
[54] D. Gall, S. Kodambaka, M.A. Wall, I. Petrov, J.E. Greene, Pathways of atomistic processes on TiN(001) and (111) surfaces during film growth: an ab initio study, J. Appl. Phys. 93 (2003) 9086–9094, https://doi.org/10.1063/1.1567797.
[55] S. Inoue, H. Uchida, A. Hioki, K. Koterazawa, R.P. Howson, Structure and composition of (Ti, Al)N films prepared by r.f. planar magnetron sputtering using a composite target, Thin Solid Films 271 (1995) 15–18, https://doi.org/10.1016/0040-6090(95)06817-1.
[56] J.Y. Rauch, C. Rousselot, N. Martin, Structure and composition of TixAll-xN thin films sputter deposited using a composite metallic target, Surf. Coat. Technol. 157 (2002) 138–143, https://doi.org/10.1016/S0257-8972(02)00146-9.
[57] A. Hörling, L. Hultman, M. Odén, J. Sjölén, L. Karlsson, Thermal stability of arc evaporated high aluminum-content Ti1 − xAlxN thin films, J. Vac. Sci. Technol. A 20 (2002) 1815–1823, https://doi.org/10.1116/1.1503784.
[58] H. Riedl, C.M. Koller, F. Munnik, H. Hutter, F. Mendez Martin, R. Rachbauer, S. Kolozsvári, M. Bartosik, P.H. Mayrhofer, Influence of oxygen impurities on growth morphology, structure and mechanical properties of Ti-Al-N thin films, Thin Solid Films 603 (2016) 39–49, https://doi.org/10.1016/j.tsf.2016.01.039.
[59] W.M. Seidl, M. Bartosik, S. Kolozsvári, H. Bolvardi, P.H. Mayrhofer, Influence of coating thickness and substrate on stresses and mechanical properties of (Ti,Al,Ta)N/(Al,Cr)N multilayers, Surf. Coat. Technol. 347 (2018) 92–98, https://doi.org/10.1016/j.surfcoat.2018.04.060.
[60] R. Rachbauer, E. Stergar, S. Massl, M. Moser, P.H. Mayrhofer, Three-dimensional atom probe investigations of Ti-Al-N thin films, Scr. Mater. 61 (2009) 725–728, https://doi.org/10.1016/j.scriptamat.2009.06.015.
[61] P.H. Mayrhofer, D. Music, J.M. Schneider, Ab initio calculated binodal and spinodal of cubic Ti 1-xAl xN, Appl. Phys. Lett. 88 (2006) 071922, , https://doi.org/10.1063/1.2177630.
[62] J.W. Cahn, J.E. Hilliard, Spinodal decomposition: a reprise, Acta Metall. 19 (1971) 151–161, https://doi.org/10.1016/0001-6160(71)90127-1.
[63] G. Greczynski, S. Mráz, L. Hultman, J.M. Schneider, Selectable phase formation in VAlN thin films by controlling Al+ subplantation depth, Sci. Rep. 7 (2017) 17544, https://doi.org/10.1038/s41598-017-17846-5.
[64] G. Greczynski, I. Zhirkov, I. Petrov, J.E. Greene, J. Rosen, Time evolution of ion fluxes incident at the substrate plane during reactive high-power impulse magnetron sputtering of groups IVb and VIb transition metals in Ar/N 2, J. Vac. Sci. Technol. A 36 (2018) 020602, , https://doi.org/10.1116/1.5016241.
[65] G. Greczynski, L. Hultman, Time and energy resolved ion mass spectroscopy studies of the ion flux during high power pulsed magnetron sputtering of Cr in Ar and Ar/N2 atmospheres, Vacuum 84 (2010) 1159–1170, https://doi.org/10.1016/j.vacuum.2010.01.055.
[66] ICDD, Powder Diffraction File - Cubic AlN - 00-025-1495, (1970).
[67] ICDD, Powder Diffraction File - Cubic TiN - 00-038-1420, (1970).

Die approbierte gedruckte Originalversion dieser Dissertation ist an der TU Wien Bibliothek verfügbar.
The approved original version of this doctoral thesis is available in print at TU Wien Bibliothek.
TU Bibliothek Your knowledge hub WIEN

Publication V

Die approbierte gedruckte Originalversion dieser Dissertation ist an der TU Wien Bibliothek verfügbar.
The approved original version of this doctoral thesis is available in print at TU Wien Bibliothek.

Time-averaged and time-resolved ion fluxes related to reactive HiPIMS deposition of Ti-Al-N films

L. Zauner, A. Bahr, T. Kozák, J. Čapek, T. Wojcik, O. Hunold, S. Kolozsvári, P. Zeman, P.H. Mayrhofer, H. Riedl

Surface & Coatings Technology, 424 (2021): 127638.
DOI: 10.1016/j.surfcoat.2021.127638

Surface & Coatings Technology 424 (2021) 127638

Contents lists available at ScienceDirect

Surface & Coatings Technology

journal homepage: www.elsevier.com/locate/surfcoat

Time-averaged and time-resolved ion fluxes related to reactive HiPIMS deposition of Ti-Al-N films

L. Zauner [a,*], A. Bahr [a], T. Kozák [b], J. Čapek [b], T. Wojcik [a,c], O. Hunold [d], S. Kolozsvári [e], P. Zeman [b], P.H. Mayrhofer [c], H. Riedl [a,c]

[a] Christian Doppler Laboratory for Surface Engineering of high-performance Components, TU Wien, Austria
[b] Department of Physics and NTIS – European Center of Excellence, University of West Bohemia, Czech Republic
[c] Institute of Materials Science and Technology, TU Wien, Austria
[d] Oerlikon Balzers, Oerlikon Surface Solutions AG, Liechtenstein
[e] Plansee Composite Materials GmbH, Germany

ARTICLE INFO

Keywords:
Ti-Al-N
HiPIMS
Thin film
Mass spectroscopy
Time-resolved

ABSTRACT

Time-averaged and time-resolved ion fluxes during reactive HiPIMS deposition of $Ti_{1-x}Al_xN$ thin films are thoroughly investigated for the usage of $Ti_{1-x}Al_x$ composite targets – Al/(Ti + Al) ratio $x = 0.4$ and 0.6. Ion mass spectroscopy analysis revealed, that increasing x in the target material or reducing the N_2 flow-rate ratio leads to a proportional increase of the Al^+-ion count fraction, whereas that of Ti^{n+}-ions ($n = 1, 2$) remains unaffected despite of comparable primary ionisation energies between Al and Ti. In fact, energetic Ti^{2+}-ions account for the lowest flux fraction incident on the substrate surface, allowing for a high Al-solubility limit in cubic-structured $Ti_{1-x}Al_xN$ thin films ($x_{max} \sim 0.63$) at low residual stresses. In addition, time-resolved plasma analysis highlights the simultaneous arrival of metal- and process-gas-ions throughout the entire HiPIMS pulse duration. These ion-bombardment conditions, which were dominated by gas-ion irradiation with a significant contribution of Al^+-ions (up to ~20 %) and negligible energetic Ti^{2+}-ions, allowed for the growth of cubic $Ti_{0.37}Al_{0.63}N$ coatings exhibiting high indentation hardness of up to ~36 GPa at a low compressive stress level ($\sigma = -1.3$ GPa).

1. Introduction

The past decades in the development of plasma-based physical vapor deposition (PVD) techniques have meticulously focused on accessing innovative routes of controlled ion-bombardment during thin film growth [1–4]. Within this context, high-power impulse magnetron sputtering (HiPIMS) – a technological advancement to drastically enhance the flux of ionized target species involved in conventional DC magnetron sputtering (DCMS) – is rendered particularly attractive for introducing novel means of influencing working gas- and metal-ions incident on substrate and growing film [5–9]. HiPIMS utilises short (10–500 μs), yet highly energetic plasma discharges (up to several $kW \cdot cm^{-2}$) at relatively low repetition rates (tens of Hertz to kilo-Hertz) to generate significantly increased plasma densities on the target surface, thus leading to an enhanced fraction of ions present in the film-forming vapor [6,7]. The increased contribution of ions to thin film growth allows for an enhanced control over the energy delivered to the growing film, revealing new kinetic pathways of controlling the structure-property relationship [10–14]. Moreover, ion-driven phenomena such as process gas rarefaction, self-sputtering, or working gas recycling are characteristic for HiPIMS discharges, hence creating distinctly different process conditions when compared to DCMS, especially under reactive deposition environments [15–19]. Nevertheless, numerous studies already highlighted the beneficial impact of HiPIMS on thin film quality, producing densified microstructures, improved mechanical properties, reduced surface roughness, or enhanced film uniformity on complex shaped substrates [20–24].

Many of the advantageous aspects of HiPIMS are driven by or related to the dynamics of the ion distribution bombarding the growing film surface. Consequently, complementary detailed plasma analysis in the time- and energy-domain has evolved into a vital extension for such ion-based PVD techniques through unfolding the correlation between deposition parameters and ion distributions (*i.e.*, composition, energy, or temporal sequence) arriving on the substrate surface [11,25–33]. Utilising ion mass spectroscopy allows for methodically altering the incident ion composition – in conjunction with given deposition

* Corresponding author.
E-mail address: lukas.zauner@tuwien.ac.at (L. Zauner).

https://doi.org/10.1016/j.surfcoat.2021.127638
Received 2 August 2021; Received in revised form 17 August 2021; Accepted 18 August 2021
Available online 23 August 2021
0257-8972/© 2021 The Author(s). Published by Elsevier B.V. This is an open access article under the CC BY license (http://creativecommons.org/licenses/by/4.0/).

Publication V

Die approbierte gedruckte Originalversion dieser Dissertation ist an der TU Wien Bibliothek verfügbar.
The approved original version of this doctoral thesis is available in print at TU Wien Bibliothek.
TU Wien Bibliothek Your knowledge hub

parameters – and to identify the distinct influence of individual ionic species on the resulting thin film quality [34]. Moreover, combining a known temporal sequence of process gas- and metal-ions with a specially tailored substrate bias potential synchronised to a precise time-domain within the HiPIMS pulse, provides advanced pathways of controlling coating stoichiometry, film adhesion, and even phase formation during ion-assisted thin film growth [35–38].

Taking up the concept from Ref. [39], Nedfors *et al.* [40] have shown that using time- and energy-resolved ion mass spectroscopy in conjunction with a substrate bias synchronised to different time-frames of the HiPIMS discharge can be utilised to influence the average energy per deposited species $\langle E_D \rangle$ even when using a multi-element target. Moreover, specifically attracting film-forming constituents (there B^+-ions during the deposition of TiB_2) was demonstrated to mitigate Ar^+ incorporation, and thus also residual compressive stresses. A complementary work by Bakhit *et al.* [41] also highlighted an alternative approach of using time-dependent ion mass spectroscopy combined with decreasing HiPIMS pulse lengths to effectively control the B/Ti-ratio in a wide range for this thin films class.

Detailed *in-situ* plasma analysis during HiPIMS deposition of Al alloyed cubic TM-N-based coatings has further contributed to access additional pathways of maintaining, or even exceeding previously established solubility limits for these typically supersaturated cubic structures – *e.g.* the well-studied Ti-Al-N system [42,43]. This benchmark system exemplifies the capabilities of kinetically-limited film growth during PVD, providing excellent high hardness and wear protection when synthesised in the metastable face-centred cubic structure (*c*, B1, NaCl-prototype). Since the high-temperature oxidation resistance of *c*-$Ti_{1-x}Al_xN$ scales with the AlN mole fraction (x), a commonly adopted strategy is to maximise the Al/(Ti + Al)-ratio of the metal sublattice, while aiming to maintain the cubic structure type. Exceeding the solubility limit ($x_{max,} \sim 0.67$ for DCMS or arc evaporation), results in the precipitation of the thermodynamically stable hexagonal (*w*, B4, ZnS-wurtzite prototype) AlN phase, thus deteriorating both the thermal stability and mechanical properties [44–48]. In fact, most studies utilising reactive HiPIMS (R-HiPIMS) for the synthesis of $Ti_{1-x}Al_xN$ thin films reported on drastically reduced solubility limits compared to conventional plasma-based techniques [49–51].

Utilising a "hybrid" Al-DCMS/Ti-HiPIMS (and Al-HiPIMS/Ti-DCMS) approach, Greczynski *et al.* [34] identified the detrimental effect of energetic, doubly-charged Ti-ions on the structure of reactively deposited $Ti_{1-x}Al_xN$ thin films. It was demonstrated that lattice defects induced from intense Ti^{2+}-ion bombardment act as preferred nucleation sites for the wurtzite phase, causing a drastic reduction of x_{max}. Building on this concept, a novel synthesis route was developed where high temporal fluxes of Al^+-ions are specifically employed during a HiPIMS pulse to extend the metastable Al-solubility limit of *c*-TM-Al-N based coatings beyond values observed for conventional PVD techniques. By applying a high substrate bias synchronised to the Al-rich portion of the discharge, energetic Al^+-ions are incorporated into the *c*-TM-N host structure – referred to as "subplantation" – thereby effectively suppressing any diffusion driven precipitation of a second phase. This method was proofed successful especially for the V-Al-N system, where an increase of x_{max} from $x = 0.52$ to 0.75 could be achieved [36,52,53].

The common concept of these advances in the application of (*R*)-HiPIMS technology is built around a precise intersection between a detailed knowledge of the time- and energy-resolved ion distribution originating in the discharge and the structure-property relation of the deposited film. In this work, we present detailed results on the effect of altered deposition parameters on the ion flux distribution arriving at the substrate during R-HiPIMS deposition of $Ti_{1-x}Al_xN$ thin films by means of time- and energy-resolved ion mass spectroscopy. Different discharge conditions involving an increasing Al content in the powder-metallurgically prepared $Ti_{1-x}Al_x$ target ($x = 0.4$ and 0.6) as well as changing nitrogen flow rate ratios are employed. Variations observed in the average ion count fractions as well as the temporal sequence of the arriving ions are related to structural changes observed within the synthesised thin films. Furthermore, the thin films are analysed in more detail with respect to changes in morphology and local phase formation. Finally, the obtained results are discussed in relation to the mechanical properties of all $Ti_{1-x}Al_xN$ thin films investigated.

2. Experimental

Mass spectroscopy measurements were performed to investigate the composition, the energy, as well as the time-resolved sequence of ions incident on the substrate plane during HiPIMS sputtering of $Ti_{1-x}Al_x$ composite targets in various nitrogen containing atmospheres. Two different target compositions ($Ti_{0.6}Al_{0.4}$ and $Ti_{0.4}Al_{0.6}$; powder-metallurgically prepared, Plansee Composite Materials GmbH) were operated in varying N_2/Ar-mixtures, with the nitrogen flow-rate ratio $f^{norm}_{|N2|} = f_{[N2]}/(f_{[N2]} + f_{[Ar]})$ increased from 0, to 0.23, to 0.3, and 1. Prior to all measurements, the cylindrical vacuum system was pumped to a base pressure below $3{\cdot}10^{-4}$ Pa using a diffusion pump, while the total process gas pressure (p) was fixed to $p = 0.4$ Pa during magnetron operation. The system was equipped with a 4-in. cathode (Vtech, Gencoa Ltd), allowing for an *in-situ* control of the magnetic field configuration on the $Ti_{1-x}Al_x$ targets. Since the mass spectroscopy measurements could not be performed in the same chamber used for the subsequent deposition of $Ti_{1-x}Al_xN$ thin films, the magnetic field strength had to be adjusted to reproduce the waveforms of the target voltage $U_T(t)$ and the discharge current $I_D(t)$ observed during the deposition.

The magnetron was powered by a 5 kW plasma generator (ADL GmbH), with the HiPIMS signal modulated using a SIPP2000USB pulse power controller (Melec GmbH). For all measurements, the repetition frequency (f) and pulse duration (t_{on}) were maintained at 500 Hz and 75 μs, respectively, with the corresponding duty cycle $t_{on}/T = 3.75$ %, where the pulse period T equals $1/f$. The waveforms of the magnetron voltage and the discharge current were recorded on a digital oscilloscope (PicoScope 6403C, Pico Technology) utilising a voltage-(Testec TT-HV 150) and current-(Tektronix TCP303) probe. The average target power density in a pulse period was evaluated as

$$\overline{P} = \frac{1}{A_T \cdot T} \int_0^T U_T(t)\, I_D(t) dt$$

where A_T represents the total target area (~ 78.5 cm^2). The discharge peak power density within a period was calculated as

$$P_{pk} = max\left(\frac{U_T(t) \cdot I_D(t)}{A_T}\right)$$

with $U_{T,pk}$ and $I_{D,pk}$ denoting the target peak voltage and discharge peak current, respectively. In the presented experiments, the average power density was maintained constant at $\overline{P} \sim 10.25$ W/cm^2, resulting in peak power densities ranging from $P_{pk} \sim 0.5$ to 1 kW/cm^2, depending on $f_{[N2]}^{flow}$ used. Moreover, both the employed process gas as well as the HiPIMS discharge parameters were based on our recently published work [20].

Time-averaged ion energy distributions of positive ions in the discharge plasma were measured using an energy-resolved mass spectrometer (EQP 300, Hiden Analytical) with the sampling orifice placed parallel to the target surface at a fixed distance of $d = 110$ mm. A shutter construction was further placed in front of the mass spectrometer orifice, to allow for stable discharge conditions prior to all measurements performed. The mass spectrometer was tuned to $^{40}Ar^+$ ions and the obtained setting was kept fixed for all measurements. Standard time-averaged acquisitions of ion spectra were measured for $^{40}Ar^+$, $^{27}Al^+$, $^{27}Al^{2+}$, $^{14}N^+$, $^{28}N_2{}^+$, $^{48}Ti^+$ and $^{48}Ti^{2+}$ ions. The extractor voltage was set

Die approbierte gedruckte Originalversion dieser Dissertation ist an der TU Wien Bibliothek verfügbar.
The approved original version of this doctoral thesis is available in print at TU Wien Bibliothek.
TU Bibliothek Your knowledge hub WIEN

to −10 V with respect to ground potential and the electrode controlling the ion energy was scanned from −5 to 80 V at a step size of 0.1 V ensuring that practically all ions (with different energies) were recorded during the measurement. The dwell time for ion detection at each point was 10 ms. The ion energy distribution for each species was recorded during five consecutive scans to increase the signal-to-noise ratio and to identify any potential long-term changes in the discharge conditions during data acquisition. Assuming consistent sensitivity of the instrument to ions at various energies, the total flux of all species was calculated by integrating the corresponding time-averaged energy distribution over the full energy range. The recorded counts for the $^{48}Ti^{n+}$ species were additionally corrected for natural isotope abundance ($^{48}Ti \sim 73.72$ % of all stable isotopes [54]). Moreover, $^{40}Ar^{+}$ and $^{48}Ti^{n+}$ species were corrected for system transmission using the manufacturers calibration data (transmittance of $^{40}Ar^{+} \sim 86.17$ % and $^{48}Ti^{+} \sim 76.02$ %, respectively [55]). Also, no indications for the molecular species $^{62}TiN^{+}$ and $^{41}AlN^{+}$ were found, hence their fluxes into the mass spectrometer are likely several orders of magnitude lower compared to the fluxes of metal ions. With the assumption of an identical transmission characteristic of the instrument for all species when implementing the corrections, the composition of the total flux of ions onto the substrate surface was calculated on the basis of these integral fluxes determined.

In addition, to obtain the temporal sequence of ions arriving at the substrate, time-resolved ion counts were recorded for specific HiPIMS discharge conditions. In that case, the mass spectrometer was set to continuously scan for one ion species in a narrow energy range (typically 20 eV) corresponding to the signal peak in the ion energy distribution function with a dwell time of 100 ms. The raw pulse-stream output of the ion detector was fed to a multichannel scaler (SR430, Stanford Research Systems). This device registered the incoming pulses and accumulated them successively in evenly spaced time intervals once a trigger signal for the negative voltage pulse of the HiPIMS power supply was registered. Thus, the time of ion arrival onto the detector with respect to the beginning of the negative pulse was discriminated with a time resolution of 1.28 µs (width of the accumulation time interval). A correction for the time-of-flight of ions in the mass spectrometer was applied during post-processing of the data [55,56]. Several tens of thousands of pulse periods were accumulated to increase the signal-to-noise ratio.

To analyse the influence of the recorded ion spectra on the thin film properties, $Ti_{1-x}Al_xN$ coatings were synthesised using a separate, in-house developed magnetron sputtering system holding two 6-in. cathodes equipped with identical $Ti_{1-x}Al_x$ composite targets as were used during the mass spectroscopy studies. The magnetrons (large circular, Gencoa Ltd.) were individually powered by a 5 kW HiPIMS plasma generator (HIP3, Solvix). The system uses a confocal, bottom-up configuration for the two cathodes resulting in an included angle of $\alpha = 20°$ between the target and substrate normal. All depositions were carried out with a fixed distance of $h = 110$ mm between the rotating substrate holder (0.25 Hz) and the target surface in alignment with the mass spectroscopy analysis. Further details on the deposition system can be extracted from [20].

Before each deposition, a base pressure below $3{\cdot}10^{-4}$ Pa was established. The $Ti_{1-x}Al_xN$ thin films were deposited on Si platelets ((100)-oriented, 20 × 7 × 0.38 mm^3), monocrystalline Al_2O_3 platelets ((1−102)-oriented, 10 × 10 × 0.53 mm^3), as well as polished austenite platelets (DIN EN 1.4571, 20 × 7 × 0.8 mm^3). Prior to all depositions, the substrate materials were pre-cleaned in an ultrasonic bath using acetone and isopropyl alcohol, consecutively. A 30 min heating sequence to a substrate temperature of $T_S = 300$ °C (measured directly on the substrate holder, corresponds to a heater temperature of $T_H = 500$ °C) was followed by a 10 min Ar-ion etching step conducted at a process pressure of $p_{etch} = 3$ Pa and a substrate potential of $U_S = -1000$ V. The discharge parameters and overall process conditions (*i.e.*, pulse frequency and duration, average power density, deposition pressure, nitrogen flow-rate ratios) for all $Ti_{1-x}Al_xN$ depositions were selected according to the settings used for the mass spectroscopy measurements. Details of the deposition conditions and coating properties are summarised in Table A1 of Appendix A.

Investigations on the coating structure were performed using X-ray diffraction (XRD) analysis on a PANalytical XPert Pro MPD system equipped with a Cu-Kα radiation source (wave length $\lambda = 1.54$ Å) in Bragg-Brentano geometry. The chemical composition of all $Ti_{1-x}Al_xN$ thin films was characterised utilising energy dispersive X-ray spectroscopy (EDS) in top-view configuration (EDAX EDS detector, 10 kV acceleration voltage). Furthermore, scanning electron microscopy (SEM, FEI Quanta 200, operated at 10 kV) was employed to investigate the coating morphology based on fracture cross-sections of single-side coated Si substrates. Additional analysis on local phase formation as well as growth characteristics of selected $Ti_{1-x}Al_xN$ thin films was obtained by transmission electron microscopy (TEM, FEI TECNAI F20) complemented by selected area electron diffraction (SAED). The evaluation of SAED diffractograms was conducted using the CrysTBox software package [57].

The mechanical properties including both the indentation hardness (H) and modulus (E) were characterised using an ultra-micro indentation system (UMIS) equipped with a Berkovich diamond indenter. For each coating, 30 load-displacement curves were recorded with the indentation load varied between 6 and 45 mN. The evaluation of the collected data was conducted according to the Oliver and Pharr method [58]. Residual macro-stresses within the $Ti_{1-x}Al_xN$ coatings were further calculated from the modified Stoney-equation combined with curvature measurements of single-side coated Si substrates obtained from optical profilometry (PS50, Nanovea) [59].

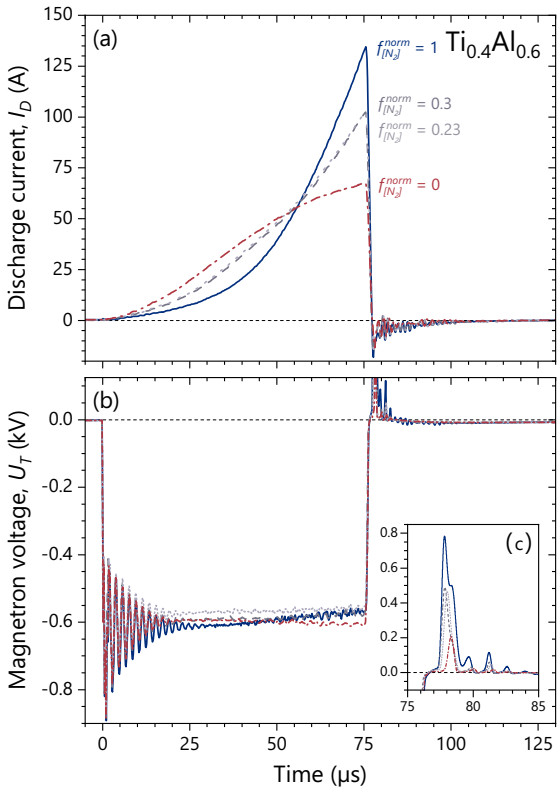

Fig. 1. Time-evolution of (a) the discharge current $I_D(t)$ and (b) the magnetron voltage on a $Ti_{0.4}Al_{0.6}$ target as functions of the applied nitrogen flow rate ratio $f^{norm}_{[N2]}$ for a pre-set pulse duration of 75 µs. Insert (c) shows details of the corresponding positive voltage overshoot recorded at the end of each pulse.

Publication V

Die approbierte gedruckte Originalversion dieser Dissertation ist an der TU Wien Bibliothek verfügbar.
The approved original version of this doctoral thesis is available in print at TU Wien Bibliothek.
TU Bibliothek Your knowledge hub WIEN

3. Results & discussion

3.1. Discharge characteristics

Fig. 1 shows the time-evolution of the discharge current $I_D(t)$ and the magnetron voltage $U_T(t)$ recorded during HiPIMS sputtering of a $Ti_{0.4}Al_{0.6}$ target in mixed N_2/Ar-atmospheres as functions of time. During all measurements, the discharge parameters were kept constant at $f = 500$ Hz, $t_{on} = 75$ µs, and $\overline{P} \sim 10.25$ W/cm^2, respectively, while $f^{norm}_{[N2]}$ was increased from 0 to 1. Irrespective of the nitrogen content in the atmosphere, the discharge current increases over time, reaching a respective maximum at the end of the pulse. When increasing the nitrogen flow-rate ratio from 0 to 0.23, the discharge current shifts from a logistic to an exponential growth until voltage shutdown at $t = 75$ µs, reaching values of $I_{D,pk} = 67$ and 103 A, respectively (see Fig. 1a). Upon further increasing $f^{norm}_{[N2]}$ to 0.3 and 1, the exponential characteristic is even more pronounced, with $I_{D,pk}$ increasing up to 135 A for the highest nitrogen content (corresponds to a peak current density of 1.72 A/cm^2). Concurrently, by increasing the nitrogen flow-rate ratio, the onset of the current rise becomes retarded and the initial slope of the waveforms is observed to be less steep. Moreover, the uniform evolution of the current waveforms suggests that no distinct contribution through working gas recycling and/or self-sputter recycling – indicated by a second maximum in $I_D(t)$ – occurs at higher peak current densities [7]. Since the average energy imparted into each pulse ($E_p = \overline{P}/f$) was constant for all experiments, the increasing peak current densities can be clearly attributed to the altered nitrogen flow-rate ratio, consequently shifting the $Ti_{1-x}Al_x$ composite target from a metallic to a more poisoned sputtering mode. Considering that the emission of secondary electrons is significantly amplified for AlN, and only marginally lowered for TiN, when compared to their pure metallic states, the increasing peak current densities can be explained by the progressive formation of surface nitrides upon increasing $f^{norm}_{[N2]}$ [60]. Moreover, self-sputtering of the nitrided target surface by energetic N^+-ions at high values of $f^{norm}_{[N2]}$ additionally supports the emission of secondary electrons [61].

Following typical oscillations after the discharge ignition, the magnetron voltage is almost constant throughout the pulse for all nitrogen variations conducted, resembling an almost ideal rectangular signal with $U_T \sim -600$ V (see Fig. 1b). The magnetron shutdown at $t = 75$ µs is accompanied by a steep decrease in the applied potential, followed by a 3–5 µs long positive "overshoot" of the magnetron voltage of up to +800 V for $f^{norm}_{[N2]} = 1$ (see insert c). This application of a positive voltage after the HiPIMS pulse derives from the inherent inductance of the power supply used, where the voltage amplitude can be estimated by the following expression:

$$V^+ \propto L \cdot \frac{dI_{D,pk}}{dt}$$

Through this almost instantaneous inversion in magnetron polarity and the resulting difference in plasma and substrate potential, ions located in the vicinity of the target get accelerated towards the substrate plane at energies corresponding to the positive pulse voltage [12].

The measurements were repeated for a $Ti_{0.6}Al_{0.4}$ target (see Fig. A1 in Appendix A) with an identical stepwise increase of the nitrogen flow-rate ratio from 0 to 1, revealing analogous results for both the evolution of the discharge current and magnetron voltage. For a pure Ar-atmosphere, a similar peak current of ~70 A is recorded at the end of the pulse. However, upon increasing $f^{norm}_{[N2]}$ to 0.23 and further, no intermediate target poisoning state can be observed, instead the discharge current immediately saturates at peak values around 135 A. Hence, it can be concluded that upon increasing the Ti/Al-ratio within the target material, less nitrogen will be required to transfer the target to a fully poisoned state under the same HiPIMS conditions, being in perfect agreement with previous observations for DCMS. Moreover, both the magnetron voltage as well as the positive "overshoot" after the pulse were recorded at similar values with $U_T \sim -600$ V and $V^+_{max} \sim 800$ V, when compared to the $Ti_{0.4}Al_{0.6}$ target and the corresponding nitrogen flow-rate ratios.

3.2. Time-averaged composition of the total ion flux

In Fig. 2, the individual fractions of the ionic species as well as the overall composition of the total ion flux measured at a distance of $d = 110$ mm from the magnetron source is presented for all nitrogen flow-rate ratios applied for both $Ti_{1-x}Al_x$ target compositions. The obtained results provide qualitative information on the fractional changes in the total ion flux arriving at the substrate surface with respect to the nitrogen flow-rate variations. Here it should be noted, that the contributions from Al^{2+}- and N^+-ions cannot be separated due to an intensity overlap in the recorded spectra ($m/e = 13.5$ and 14, respectively). However, experiments in pure Ar atmosphere showed that Al^{2+}-signals are insignificant compared to those from Al^+-ions, hence they were not considered in the evaluation even at higher peak current densities with increasing $f^{norm}_{[N2]}$. This is in agreement with previous observations for HiPIMS powered Al targets and mainly related to the considerably

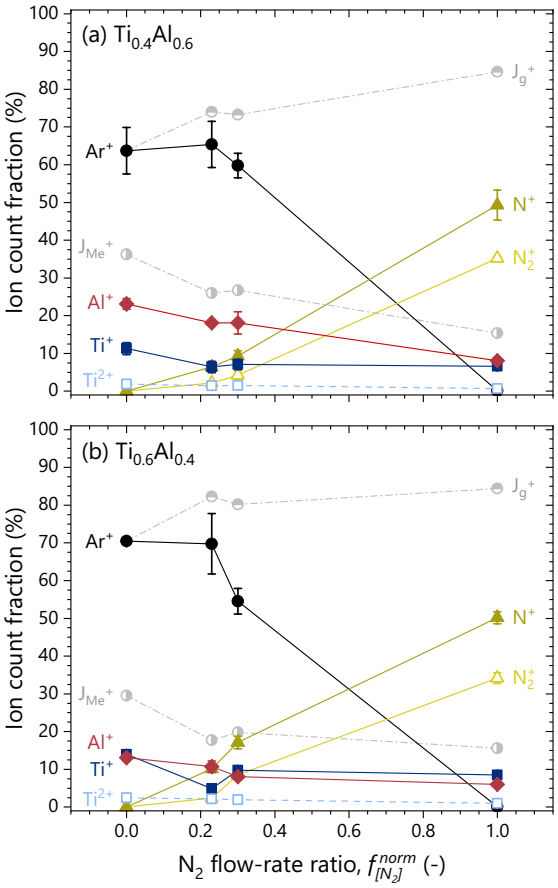

Fig. 2. Integral ion count fractions of the ionic species arriving at the substrate plane as function of the nitrogen flow rate ratio $f^{norm}_{[N2]}$, presented for (a) a $Ti_{0.4}Al_{0.6}$ and (b) a $Ti_{0.6}Al_{0.4}$ target, respectively. The data was acquired at a distance of $d = 110$ mm from the target surface. Singly charged species are presented by filled symbols and solid lines, whereas doubly charged ions are presented by open symbols and dashed lines. In addition, (a) and (b) contain the total flux of process gas ions J_{g^+} and metal ions J_{Me^+}, indicated by half-filled circles and dot dashed lines.

Publication V

Die approbierte gedruckte Originalversion dieser Dissertation ist an der TU Wien Bibliothek verfügbar.
The approved original version of this doctoral thesis is available in print at TU Wien Bibliothek.
TU Bibliothek Your knowledge hub WIEN

higher secondary ionisation energy of aluminium (IP_2^{Al} = 18.83 eV) compared to the primary ionisation energy of argon (IP_1^{Ar} = 15.76 eV) [34,54]. In addition, Fig. 3 presents a direct comparison of the flux compositions recorded at $f_{[N2]}^{norm}$ = 0.3, for both the $Ti_{0.4}Al_{0.6}$ (blue, filled bars) and $Ti_{0.6}Al_{0.4}$ (red, dashed bars) target.

Over the entire range of $f_{[N2]}^{norm}$ considered, the flux of process gas ions J_{g^+} (*i.e.*, the combined flux of Ar^+, N_2^+, and N^+ ions) dominates the composition of the total ion flux emitted from the plasma discharge. In pure argon-atmosphere, the integral flux of metal ions J_{Me^+} (*i.e.*, the combined flux of Al^+, Ti^+, and Ti^{2+} ions) constitutes 36.3 and 29.6 % within the total ionic species ejected from the $Ti_{0.4}Al_{0.6}$ and $Ti_{0.6}Al_{0.4}$ target, respectively. Upon stepwise increase to pure nitrogen-atmosphere at $f_{[N2]}^{norm}$ = 1, the corresponding values for J_{Me^+} decrease almost linearly to 15.4 and 15.6 %, respectively. This reduction in the metal-to-gas ion flux ratio J_{Me^+}/J_{g^+} – from 0.57 to 0.18 for the $Ti_{0.4}Al_{0.6}$ target and from 0.42 to 0.18 for the $Ti_{0.6}Al_{0.4}$ target – with increasing nitrogen flow results from a progressive nitride formation on the target surface, and hence a decreasing sputter yield of the metal constituents. In addition, the higher overall sputter yield of the $Ti_{0.4}Al_{0.6}$ target compared to the $Ti_{0.6}Al_{0.4}$ target – the sputter yield of Al is nearly twice that of Ti [62] – results in higher values of J_{Me^+} throughout all nitrogen flow rates.

The poisoning behaviour of the target material is of course strongly related to the Ti/Al-ratio and driven by the difference in the formation energy of the respective nitrides (−305.6 kJ/mol for TiN *vs.* -241.6 kJ/mol for AlN) [46,63]. This implies that the higher Al-containing $Ti_{0.4}Al_{0.6}$ target can sustain the metallic sputtering behaviour up to higher values of $f_{[N2]}^{norm}$ than the $Ti_{0.6}Al_{0.4}$ target, as seen in the current waveforms presented in Figs. 1 and A1. Accordingly, for $f_{[N2]}^{norm}$ = 0.23 and 0.3 the data also show an increased population of N_2^+ and N^+ ions for the $Ti_{0.6}Al_{0.4}$ target due to less absorption of reactive gas (*i.e.,* a more poisoned target for the same N_2 flow rate), leading to a higher partial pressure and thus ionisation probability for the nitrogen species (see Figs. 2 and 3). In addition, for both target-types a predominance of N^+-ions (dark-yellow, filled triangles) over N_2^+-ions (light-yellow, open triangles) is observed in all flux compositions. This highlights the preferred ionisation of atomic N sputtered from the nitrided target surface as well as the promoted dissociation of N_2-molecules within the dense plasma created for high values of P_{pk} close to 1 kW/cm^2 (see Fig. 2).

Regarding the individual contribution of metal ions generated in the discharge, the data presented in Fig. 2a and b shows that Al^+-ions (red diamonds) account for a major fraction within J_{Me^+}, irrespective of the Al/Ti-ratio in the target material or $f_{[N2]}^{norm}$. Especially for the $Ti_{0.4}Al_{0.6}$ target, high values of J_{Al^+} up to 23 % of the total ion flux are observed in pure Ar-atmosphere (see Fig. 2a). Increasing the nitrogen flow to $f_{[N2]}^{norm}$ = 0.23 and 0.3 – being typical values for the deposition of Ti-Al-N thin films – the fraction of Al^+-ions in the sputtered flux decreases slightly to $J_{Al^+} \sim 18$ %. Following a near linear trend, this value further decreases down to $J_{Al^+} \sim 8.1$ % for $f_{[N2]}^{norm}$ = 1. Contrary, fluxes for singly (dark-blue squares) as well as doubly (light-blue open squares) charged titanium ions remain almost unaffected by the N_2 flow-rate ratio, with J_{Ti^+} and $J_{Ti^{2+}}$ accounting for values below 14 % and 3 % within the total ionic flux from both targets, respectively.

Upon further comparison of J_{Al^+} to the combined flux of process gas ions J_{g^+} for both target chemistries, the increased ionisation of Al-atoms within the $Ti_{0.4}Al_{0.6}$ discharge is predominantly realised at the expense of a less efficient ionisation of the process gas species (see Figs. 2 and 3). This effect could be explained by an enhanced gas rarefaction occurring in front of the higher Al-containing target due to an increased density of metal species entering the plasma – mind the difference in sputter yield Al *vs.* Ti – thus resulting in a higher probability for atomic collisions and gas heating [16]. In addition, the significantly lower ionisation energy of aluminium atoms (IP_1^{Al} = 5.99 eV [54]) over the gaseous species (IP_1^{Ar} = 15.76 eV, IP_1^{N} = 14.53 eV, and IP_1^{N2} = 15.58 eV [54]) results in quenching of the electron energy distribution, thereby further contributing to a less efficient ionisation of process gas atoms [29,35]. This explanation is further underlined when reconsidering the evolution of both J_{Ti^+} and $J_{Ti^{2+}}$ between the two target compositions, revealing negligible differences despite the significant changes in J_{Me^+}/J_{g^+} over the entire N_2 flow range considered.

Consequently, it can be concluded that increasing the Al content in a $Ti_{1-x}Al_x$ composite target can be utilised for amplifying the fraction of Al^+ ions present in the sputtered flux, while reducing the overall fraction of process gas ions. Although a high Al/Ti ratio in a composite target also has to be considered with respect to phase formation and general solubility limits for the deposition of cubic structured $Ti_{1-x}Al_xN$ thin films, this provides a means of tuning J_{Al^+} while maintaining J_{Ti^+}, and especially the detrimental $J_{Ti^{2+}}$, low.

3.3. Time-resolved composition of the total ion flux

In order to study the temporal sequence of ions impinging on the substrate plane – especially from the aspect of time domains with high values of J_{Me^+}/J_{g^+} – time-resolved ion mass spectroscopy was performed

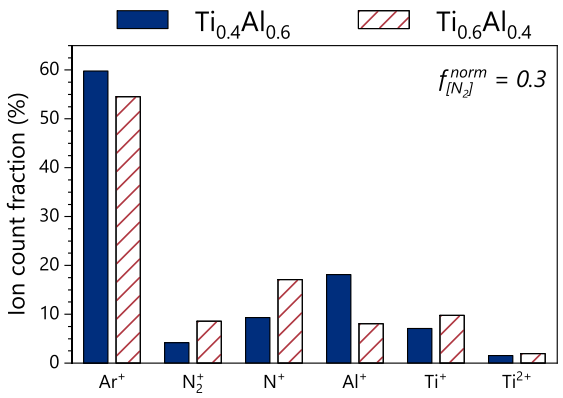

Fig. 3. Integral ion count fractions of the total ionic flux emitted from a HiPIMS discharge for a nitrogen flow rate ratio of $f_{[N2]}^{norm}$ = 0.3, presented for both a $Ti_{0.4}Al_{0.6}$ (blue, filled bars), as well as a $Ti_{0.6}Al_{0.4}$ (red, dashed bars) target.

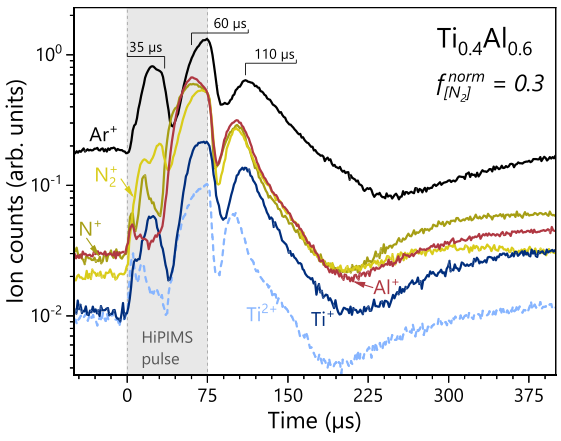

Fig. 4. Normalised time-evolution of the energy-integrated total ionic flux emitted during HiPIMS sputtering of a $Ti_{0.4}Al_{0.6}$ target, measured at $f_{[N2]}^{norm}$ = 0.3 and a distance of d = 110 mm from the target. Singly charged species are presented by solid lines, whereas doubly charged ions are presented by dashed lines.

Publication V

Die approbierte gedruckte Originalversion dieser Dissertation ist an der TU Wien Bibliothek verfügbar.
The approved original version of this doctoral thesis is available in print at TU Wien Bibliothek.
TU Bibliothek Your knowledge hub WIEN

for a specific discharge condition. In Fig. 4, all major ion fluxes (Ar^+, Al^+, N^+, N_2^+, Ti^+ and Ti^{2+}) emitted from the $Ti_{0.4}Al_{0.6}$ target were recorded at the substrate position ($d = 110$ mm) for a nitrogen flow-rate ratio of $f^{norm}_{[N2]} = 0.3$. The total number of ion-counts normalised to the number of recorded pulse cycles is shown as a function of the time delay with respect to the voltage application to the magnetron.

Regarding the flux chemistry prior to the pulse ignition ($t < 0$ μs) – comprised of the residual ionized species from the previous pulse – a predominance of Ar^+ ions over the flux of N_2^+, N^+, Al^+, Ti^+ and Ti^{2+} ions is observed, with the latter two species accounting for the lowest fractions. Upon pulse ignition ($t = 0$ μs), and thus a rapid increase in the electron temperature T_e, all flux signals – especially the process gas ions – immediately gain intensity until reaching a first maximum at $t \sim 25$ μs. Since the ionic species generated in the target vicinity will require at least several tens of μs before arriving at the analyser, this initial influx of ions corresponds to ions created close to the mass spectrometer orifice by the first wave of energetic electrons [64]. In the following time interval until the cathode shutdown at $t = 75$ μs, the ion intensities increase to their respective maximum due to the arrival of ions generated within the main magnetron discharge – to approximately one order of magnitude higher than the corresponding initial values at $t = 0$ μs – coinciding well with $I_{D,pk}$ (see Fig. 1). Interestingly, the fluxes of metal ions J_{Me^+} and N^+-ions show a concomitant increase to their respective maximum at $t \sim 60$ μs, indicating that the latter species originates strongly from sputtering of target surface nitrides. Still, it should be noted that the highly dense plasma additionally contributes to the dissociation of N_2-molecules, thus explaining the extended N^+ peak. Contrary, fluxes for Ar^+- and N_2^+-ions show a slightly delayed arrival with an intensity maximum at $t = 75$ μs, suggesting for the ionisation to occur preferably in the bulk plasma.

After reaching the peak ion flux at the end of the 75 μs pulse, an abrupt decay of all ion signals can be observed, suggesting for a decrease in the number of arriving ions. However, this loss of ion intensity is due to a temporal broadening of the ion energy distribution function (IEDF) due to the positive voltage overshoot occurring on the magnetron at $t \sim 78$ μs (see insert c in Fig. 1, $U_T \sim 500$ V). The application of this positive pulse accelerates ions in the target proximity towards the analyser and the bulk plasma potential increases significantly, as it is always more positively charged than the most positive electrode within the plasma – represented by the magnetron during this time frame. Consequently, all ions obtain kinetic energies beyond the respective scanning range by this instantaneous difference between plasma and mass spectrometer potential, causing the apparent dip in the ion count evolution. This effect of a positive pulse on the IEDF is also described in more detail in recent studies by Kozak *et al.* [11] and Santiago *et al.* [12]. So in fact, the presented ion counts can be rather understood as obtaining a smooth decay between the shown maxima at $t = 75$ and 110 μs for all species. Finally, in the time domain of $t > 80$ μs ($U_T \sim 0$ V), the IEDFs gradually collapse, resulting in the recorded ion counts to slightly regain intensity up to $t \sim 110$ μs, to then decay at an equal rate in the following 150 μs until the initial state between the HiPIMS pulses is attained.

A further interesting observation when considering the collective evolution of all ion signals is that the relative flux composition is preserved throughout the entire pulse duration, with J_{Me^+}/J_{g^+} remaining fairly unchanged except for a slight dip at $t \sim 35$ μs due to the large influx of initial Ar^+ ions. Hence, no time domain obtaining a preferred arrival of either metal or process gas ions can be identified – resulting from well-known effects such as process gas rarefaction or quenching of T_e [16,28,35]. This continuous arrival of J_{Me^+} and J_{g^+} has direct implications on the deposition process, thereby minimising the controllability of film growth kinetics through synchronised metal-ion irradiation when using a $Ti_{1-x}Al_x$ composite target in a reactive HiPIMS process. Moreover, analogous to the results obtained for the integral ion flux (see Figs. 2 and 3), both J_{Ti^+} and $J_{Ti^{2+}}$ constitute the lowest fractions during the entire pulse period with respect to the total ionic flux, and in particular J_{Al^+}. This is especially interesting, when taking the moderate first ionisation energy of titanium ($IP_{Ti} = 6.83$ eV) – which is close to that of Al, yet significantly lower when compared to the present process gas species – as well as the almost equiatomic target composition into account [54]. Nevertheless, the presented results clearly underline our previous observations outlined in Ref. [20], where synchronising the bias potential to the HiPIMS pulse showed only minor effects on the phase formation of cubic structured Ti-Al-N.

3.4. Phase formation and chemical composition

Fig. 5a and b – containing the XRD diffractograms of films deposited from $Ti_{0.6}Al_{0.4}$ or $Ti_{0.4}Al_{0.6}$ targets, respectively – show the influence of different target chemistries and the nitrogen flow-rate ratio $f^{norm}_{[N2]}$ on the cubic phase stability of $Ti_{1-x}Al_xN$. In addition, Fig. 5c and d contain the corresponding chemical composition to the coatings presented in Fig. 5a and b, with square data points indicating the Al/(Ti + Al) ratio on the metal sublattice (lower axis) and circular data points denoting the nitrogen content (upper axis).

For a $Ti_{0.6}Al_{0.4}$ target chemistry (Fig. 5a and c), altering $f^{norm}_{[N2]}$ from 0.23 to 1.0 results in a slight decrease in the Al-content from $x = 0.46$ to 0.42 of the purely *fcc*-structured $Ti_{1-x}Al_xN$ thin films. This decrease can be understood based on the previously discussed difference in the heat of

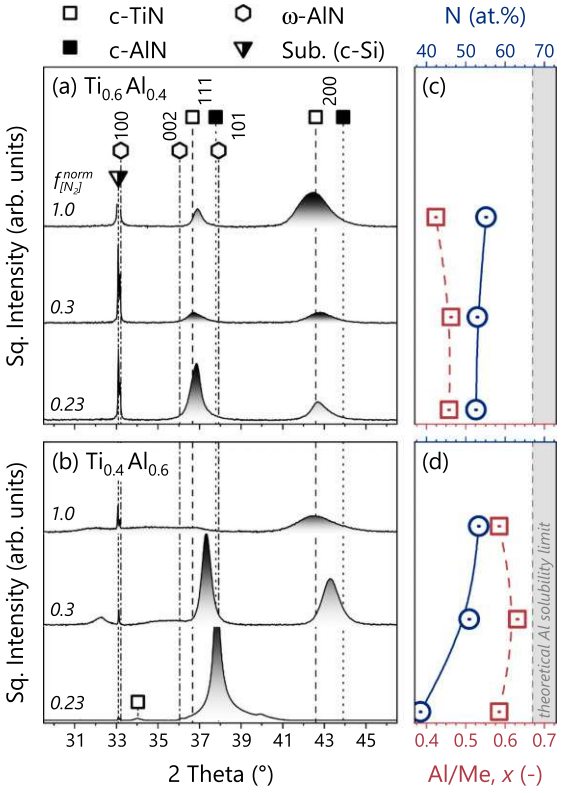

Fig. 5. (a) and (c) show XRD diffractograms of $Ti_{1-x}Al_xN$ thin films deposited from two 6-in. $Ti_{0.6}Al_{0.4}$ and $Ti_{0.4}Al_{0.6}$ cathodes, respectively, arranged with increasing $f^{norm}_{[N2]}$ from bottom (0.23) to top (1.0). The 2θ peak positions for cubic structured TiN (open square, [69]) and AlN (filled square, [70]), wurtzite AlN (open hexagon, [65]) and the substrate material (cubic Si, half-filled triangle, [71]) are indicated in (a) and (c). Furthermore, (b) and (d) show the chemical composition of all $Ti_{1-x}Al_xN$ thin films presented in (a) and (c), respectively – bottom axis Al/Me-ratio (red squares) and top axis N-content (blue circles) – with the data points aligned horizontally with the corresponding XRD diffractogram.

Die approbierte gedruckte Originalversion dieser Dissertation ist an der TU Wien Bibliothek verfügbar.
The approved original version of this doctoral thesis is available in print at TU Wien Bibliothek.
TU Bibliothek Your knowledge hub WIEN

formation for TiN and AlN (see Section 2), the Al target particles commonly show a retarded poisoning state over the Ti particles, thus leading to a preferential Al sputter erosion at lower nitrogen flow rates [46,63]. Also, the N-content on the non-metal sublattice increases accordingly from 52 to 55 at.%, due to the higher availability of N^+- and N_2^+-ions in the plasma (see Fig. 2b) as well as the concomitant decrease in deposition rate at higher values of $f^{norm}_{[N2]}$ – the latter decreasing from 22.1 to 17.4 to 10.8 nm/min. Moreover, with increasing reactive gas flow $f^{norm}_{[N2]}$ from 0.23 to 1, the XRD diffractograms present a transition from a preferred (111)-oriented growth, to a randomly oriented growth with diminishing peak intensities (*i.e.*, smaller coherently diffracting domain sizes), towards a slightly preferred (200)-oriented growth.

In the case of the higher Al containing target $Ti_{0.4}Al_{0.6}$ (see Fig. 5b), the Al metal-fraction of the $Ti_{1-x}Al_xN$ thin films is $x = 0.59$ for a low and high $f^{norm}_{[N2]}$ of 0.23 and 1, while it increases to $x = 0.63$ at $f^{norm}_{[N2]} = 0.3$ (see Fig. 5d). Also, this behaviour is the result of selective poisoning processes of the Ti-Al target. With increasing $f^{norm}_{[N2]}$ from 0.23 to 0.30, the sputter yield of Ti decreases faster than that of Al (as Ti is more affine to N than Al and thus poisons earlier). However, if $f^{norm}_{[N2]}$ is sufficiently high to also poison Al, the reduction in sputter yield is more severe for Al due to the electrically isolating nature of AlN. The XRD diffractogram of the highest Al-containing coating ($x = 0.63$), prepared at $f^{norm}_{[N2]} = 0.3$, depicts a predominantly face-centered cubic structure having a preferred (111)-oriented growth, with slight indications for an additional wurtzite AlN-based phase (see the XRD peaks at $2\theta \sim 32.2°$ and 35°). The offset of these peaks from the ideal *w*-AlN reference pattern [65] hints towards the formation of a *w*-$Al_xTi_{1-x}N$ solid solution [44,47]. Reducing $f^{norm}_{[N2]}$ from 0.3 to 0.23 promotes the growth of a highly (111)-oriented cubic phase (even leading to the formation of the $K_{\beta 1}$ diffraction spot at $2\theta \sim 34°$). This *c*-$Ti_{0.41}Al_{0.59}N$ thin film is understoichiometric with a nitrogen content close to 40 at.%. The diffractogram further shows a clear shift towards the *c*-AlN reference line – despite an actual reduction in the aluminium content – indicative of a reduced compressive stress state and nitrogen deficiency. This drastic transition in film growth characteristics is in excellent agreement with previous studies [20,46] and follows the suggestions by Gall *et al.* [66], that a reduced availability of excess nitrogen (see Fig. 2a) yields a preferred growth in the (111)-direction. An increase of $f^{norm}_{[N2]}$ to 1 results in a multi-phased coating of (200)-oriented *c*-$Ti_{1-x}Al_xN$ and an almost X-ray amorphous *w*-$Al_xTi_{1-x}N$. Analogous to the coatings prepared from the lower Al containing target, increasing $f^{norm}_{[N2]}$ drastically reduces the deposition rate – from 66.2 to 50.6 to 10.9 nm/min. This allows for a less disturbed surface diffusion and provides more time for the growing film to approach the thermodynamically favoured crystal structures (cubic for Ti-rich and wurtzite for Al-rich). Moreover, the increased bombardment with N^+/N_2^+-ions (see Fig. 2a) additionally contributes to the wurtzite phase growth, hence the reduction in cubic phase fraction when increasing $f^{norm}_{[N2]}$ from 0.3 to 1.0 despite the concomitant reduction of the Al/(Ti + Al) ratio [46]. The competitive growth between *c*-TiN and the preferred *w*-AlN phase then results in a nano-composite structure [20]. Overall, the coatings prepared with $f^{norm}_{[N2]} = 0.23$ and 0.3 (Fig. 5b) provide significantly higher diffracted peak intensities when compared with the corresponding films prepared from the Ti-richer $Ti_{0.6}Al_{0.4}$ target (Fig. 5a), indicating altered film growth pathways when increasing the Al content in the target. Taking the ion count fractions presented in Fig. 3 into account, the increased bombardment with medium energetic Al^+-ions in favour of less Ti^{n+}- and N^+/N_2^+- species in the film forming flux contributes to enhanced surface diffusion and thus larger coherently diffracting domain sizes, which is also in good agreement with previous observations [20,49].

3.5. Growth morphology and phase formation

The $Ti_{1-x}Al_xN$ thin films were investigated in more detail with respect to growth morphology and phase formation by means of cross-sectional SEM and TEM, see Fig. 6. The fracture cross-sectional SEM image of $Ti_{0.54}Al_{0.46}N$ (Fig. 6a) shows a dense and highly columnar growth morphology, which is also underlined by the bright- (BF) and dark-field (DF) TEM investigations (Fig. 6b). Furthermore, the corresponding SAED studies taken in the interface near region (Fig. 6c1) as well as close to the film surface (Fig. 6c2) confirm the polycrystalline face-centred cubic crystal structure observed by XRD (Fig. 5a, pattern in the middle) – *i.e.,* with no preferred orientation – by ring-type diffraction patterns throughout the coating thickness. Investigations of the $Ti_{1-x}Al_xN$ coatings synthesised from the Al-richer $Ti_{0.4}Al_{0.6}$ target (Fig. 6d till l) nicely depict the influence of the increasing $f^{norm}_{[N2]}$ on the growth characteristics of these higher Al containing thin films. Both, the SEM fracture cross-sections as well as the corresponding BF- and DF-TEM images indicate the transition from a highly oriented $Ti_{0.41}Al_{0.59}N$ coating (N content of ~40 at.%) with large columnar crystals at $f^{norm}_{[N2]} = 0.23$ (see Fig. 6d, e, and f), to a slightly less preferred-oriented $Ti_{0.37}Al_{0.63}N$ coating at $f^{norm}_{[N2]} = 0.3$ with shorter columnar crystals (see Fig. 6g, h and i). A further increase in $f^{norm}_{[N2]}$ to 1.0 leads to the formation of an even finer microstructure, exhibiting a featureless morphology during SEM (Fig. 6j) with small-sized slightly elongated grains (Fig. 6k). The selected area electron diffraction patterns in Fig. 6f1 and f2 recorded for the $Ti_{0.41}Al_{0.59}N$ coating at $f^{norm}_{[N2]} = 0.23$ confirm the cubic crystal structure suggested by XRD (despite the N sub-stoichiometry) and show the highly crystalline nature of this coating through distinct point type diffractions, especially during later growth stages (see inset f2). Interestingly, the SAED investigations of the $Ti_{0.37}Al_{0.63}N$ coating prepared with $f^{norm}_{[N2]} = 0.3$ show that the wurtzite $Al_xTi_{1-x}N$ phase – as also observed during XRD, Fig. 5c – merely prevails in the interface near region (Fig. 6i1), whereas the main part of the coating is essentially cubic structured (Fig. 6i2). Since the deposition temperature was chosen rather low at $T_S \sim 300$ °C, this effect could be seen in progressive substrate heating due to the interaction with the dense HiPIMS plasma combined with enhanced ion bombardment. Certainly, these results show that the cubic $Ti_{1-x}Al_xN$ structure is accessible from $Ti_{1-x}Al_x$ compound targets even up to $x \sim 0.63$ (*i.e.*, close to the theoretical solubility limit) and despite the presence of doubly charged Ti-ions in the film forming flux. Again, in accordance with the XRD investigations (Fig. 5c), detailed SAED analyses of the coating synthesised with $f^{norm}_{[N2]} = 1.0$ underline the formation of cubic and wurtzite phases (see Fig. 6 l1-l2).

3.6. Mechanical properties

Finally, in addition to the structural and morphological changes discussed from the aspect of changing deposition and HiPIMS discharge conditions, the consequential influence on the mechanical properties of all $Ti_{1-x}Al_xN$ thin films was studied. Fig. 7a-c summarize the biaxial residual stresses, hardness, and indentation modulus for the coatings prepared from the two different targets as function of $f^{norm}_{[N2]}$, respectively. Single-phase cubic $Ti_{1-x}Al_xN$ coatings on Si substrates – sputtered using $Ti_{0.6}Al_{0.4}$ targets (red, filled squares) – exhibit compressive stresses between −1.2 and −2.5 GPa, with the lowest value observed for the fully polycrystalline $Ti_{0.53}Al_{0.46}N$ when using $f^{norm}_{[N2]} = 0.3$ (see Figs. 6a–c and 7a). The corresponding nanoindentation measurements give high hardness values, decreasing from $H = 36.4 \pm 1.5$ to 32.6 ± 2.5 GPa with increasing $f^{norm}_{[N2]}$, whereas the indentation modulus remains at $E \sim 420$ GPa almost unaffected by the nitrogen flow rate ratio variation, Fig. 7b

Die approbierte gedruckte Originalversion dieser Dissertation ist an der TU Wien Bibliothek verfügbar.
The approved original version of this doctoral thesis is available in print at TU Wien Bibliothek.
TU Bibliothek Your knowledge hub WIEN

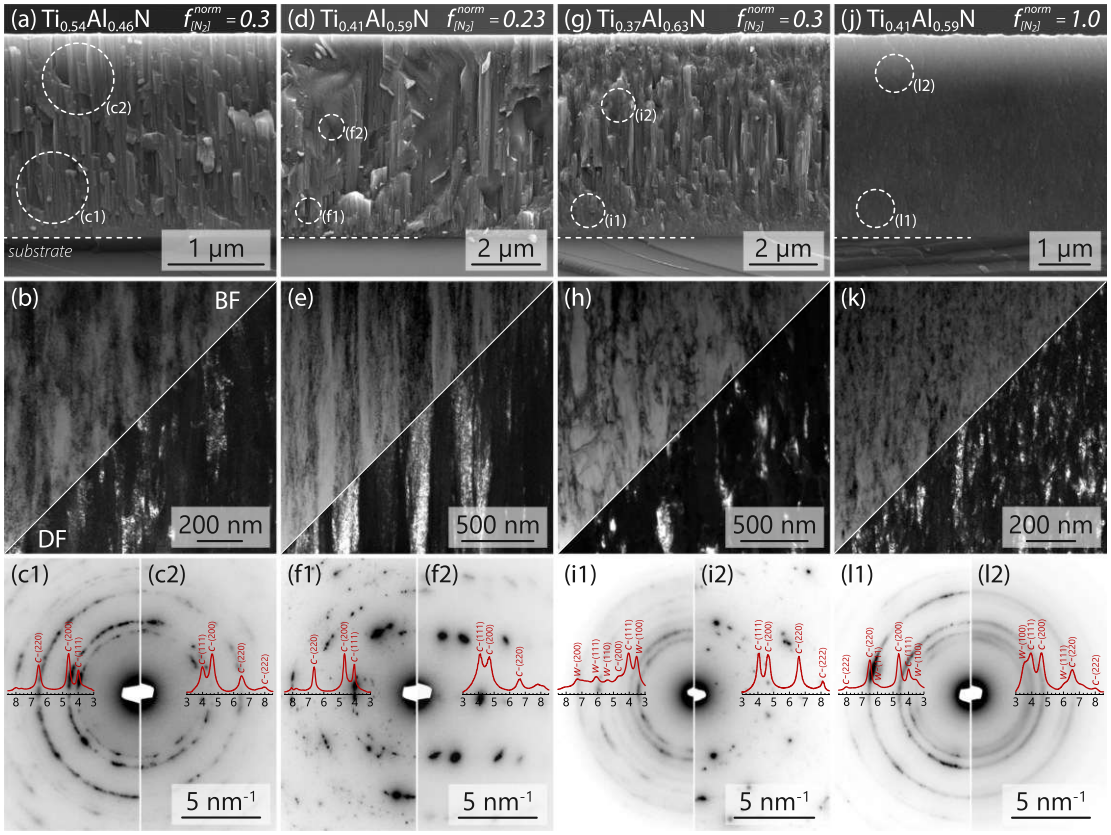

Fig. 6. (a), (d), (g), and (j) show SEM fracture cross-sections including the film chemistry and $f_{[N2]}^{norm}$ of selected $Ti_{1-x}Al_xN$ thin films from Fig. 5. (b), (e), (h), and (k) present bright- and dark-field TEM micrographs of the corresponding film cross-sections depicted in (a), (d), (g), and (j). The respective SAED diffractograms taken in the interface near region are shown in (c1), (f1), (i1), and (l1), whereas (c2), (f2), (i2), and (l2) contain SAED diffractograms recorded closer to the film surface, as indicated by the circles in (a), (d), (g), and (j). In addition, all SAED diffractograms contain an azimuthal integration of the pattern.

and c, respectively. Analogous to the findings in our previous work, the continuous reduction in hardness with increasing $f_{[N2]}^{norm}$ can be attributed to the increased fraction of nitrogen ions bombarding the film surface (see Fig. 2b) – thus leading to a weaker grain boundary structure [20,67]. Upon increasing the Al content in the target material to $Ti_{0.4}Al_{0.6}$ (see Fig. 7, blue, open squares) the obtained coatings exhibit biaxial compressive stresses which increase from −0.4 to −2.5 GPa with increasing $f_{[N2]}^{norm}$ from 0.23 to 1.0, respectively. A maximum hardness of 36.1 ± 3.5 GPa is obtained for the predominantly cubic structured $Ti_{0.37}Al_{0.63}N$ thin film prepared at $f_{[N2]}^{norm} = 0.3$. The minor wurtzite phase content of this coating is essentially present only at the near substrate region (Fig. 7i), thus its contribution to the hardness measurement can be neglected. Whereas preparing the film with $f_{[N2]}^{norm} = 0.23$ results in an understoichiometric phase, too much N_2 ($f_{[N2]}^{norm} = 1.0$) favours the formation of a significant amount of the wurtzite phase. Both scenarios lead to lower hardness (~ 29.5 GPa) and indentation modulus (380 ± 10 and 300 ± 9 GPa), Fig. 7b and c, respectively. Interestingly, when compared with conventional DCMS or cathodic arc evaporation (CAE) techniques, all $Ti_{1-x}Al_xN$ coatings obtained here have relatively low compressive stresses – especially at $f_{[N2]}^{norm} = 0.3$ – which is likely linked to the large fraction of low energetic film forming ions bombarding the growing coating surface, whilst the overall contribution from energetic Ti^{2+}-ions remains low (see Fig. 2). Consequently, this avoids the trapping of excess Ar interstitial atoms and reduces the point defect density [68]. In general, the presented evolution of the mechanical properties follows all previous interpretations on these coatings, yet again highlighting the excellent potential of R-HiPIMS deposited $Ti_{1-x}Al_xN$ thin films synthesised from composite targets.

4. Conclusion

In this work, the correlation between time-averaged and time-resolved ion fluxes to the N_2/Ar-flow-rate ratio utilised during reactive HiPIMS deposition of $Ti_{1-x}Al_xN$ thin films from $Ti_{0.4}Al_{0.6}$ or $Ti_{0.6}Al_{0.4}$ composite targets is studied. Detailed ion mass spectroscopy in the time- and energy-domain shows that for given discharge conditions the fraction of Al^+-ions is significantly affected by the Al/(Ti + Al)-ratio of the target material, whereas the amount of Ti^{n+}-ions ($n = 1, 2$) only shows a minor correlation to the target composition – despite the similar primary ionisation energies for Ti and Al. Moreover, resulting from progressing nitride formation, the data show a concomitant linear decrease for the total metal-to-gas-ion flux ratio J_{Me^+}/J_{g^+} with increasing N_2/Ar-flow-rate ratio, reducing J_{Me^+} from 36.3 and 29.6 % ($f_{[N2]}^{norm} = 0$) down to 15.4 and 15.6 % ($f_{[N2]}^{norm} = 1$) for the $Ti_{0.4}Al_{0.6}$ and $Ti_{0.6}Al_{0.4}$ target, respectively. Interestingly, Ti^{n+}-ion fractions remain almost unaffected by the applied N_2-flow-rate ratio, with the flux fractions of Ti^+- and Ti^{2+}-ions corresponding to less than 14 and 3 % of the total ionic flux from both targets,

Publication V

Die approbierte gedruckte Originalversion dieser Dissertation ist an der TU Wien Bibliothek verfügbar.
The approved original version of this doctoral thesis is available in print at TU Wien Bibliothek.
TU Bibliothek Your knowledge hub WIEN

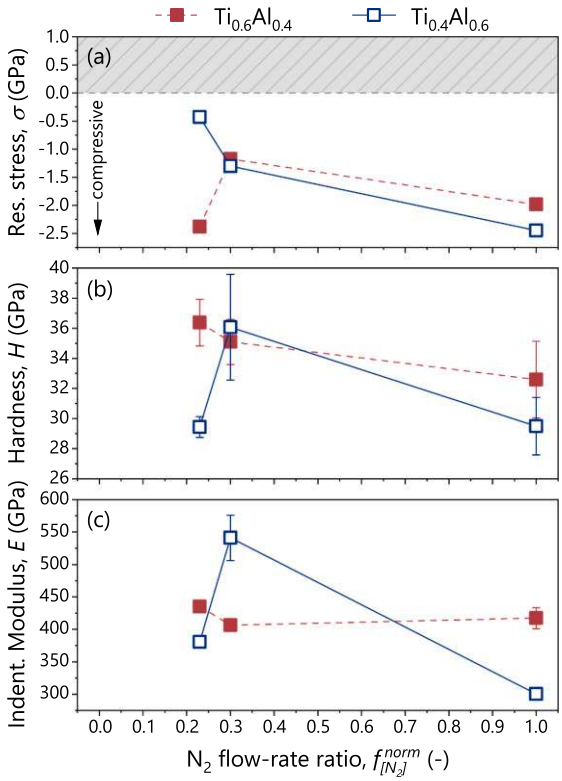

Fig. 7. (a) Biaxial residual stress, (b) nanoindentation hardness, as well as (c) nanoindentation modulus of all $Ti_{1-x}Al_xN$ thin films deposited onto (100)-oriented silicon substrates presented as function of $f^{norm}_{[N2]}$. Coatings deposited from $Ti_{0.6}Al_{0.4}$ cathodes are denoted by red, filled squares, whereas those from $Ti_{0.4}Al_{0.6}$ targets are indicated by blue, open squares.

respectively. Additional time-resolved ion distributions recorded for specific discharge conditions on the $Ti_{0.4}Al_{0.6}$ target confirm the fairly continuous arrival of both metal- and process-gas-ions throughout the entire HiPIMS pulse cycle, thus hinting at the reduced effectiveness of using synchronised bias potentials in tuning the film growth kinetics. Based on the recorded ion fluxes, predominantly cubic-structured $Ti_{1-x}Al_xN$ thin films with x_{max} as high as 0.63 could be synthesised – thoroughly proven by detailed structural analysis using XRD and TEM – exhibiting excellent mechanical properties (H up to ~36 GPa) at moderate stress states. This is realised by an increasing fraction of low-energy film forming ions present in the sputterred flux, while the fraction of energetic Ti^{2+} ions remains low. Thereby, the probability for trapped Ar interstitials and density of structural defects can be kept low.

Overall, the presented results show a clear pathway of controlling the ion flux composition and thin film structure during reactive HiPIMS deposition of $Ti_{1-x}Al_xN$ thin films from composite targets through the use of target-driven ion mass spectrosctopy.

CRediT authorship contribution statement

L. Zauner: Conceptualization, Investigation, Visualization, Writing – original draft. **A. Bahr:** Investigation, Writing – review & editing. **T. Kozák:** Investigation, Writing – review & editing. **J. Čapek:** Investigation, Writing – review & editing. **T. Wojcik:** Investigation, Writing – review & editing. **O. Hunold:** Writing – review & editing. **S. Kolozsvári:** Writing – review & editing. **P. Zeman:** Writing – review & editing. **P.H. Mayrhofer:** Writing – review & editing. **H. Riedl:** Supervision, Conceptualization, Writing – review & editing, Project administration.

Declaration of competing interest

The authors declare that they have no known competing financial interests or personal relationships that could have appeared to influence the work reported in this paper.

Acknowledgements

The financial support by the Austrian Federal Ministry for Digital and Economic Affairs, the National Foundation for Research, Technology and Development and the Christian Doppler Research Association is gratefully acknowledged (Christian Doppler Laboratory “Surface Engineering of high-performance Components”). The ion mass spectroscopy measurements done at University of West Bohemia were supported in part by the project LO 1506 of the Czech Ministry of Education, Youth and Sports under the program NPU I. We also thank for the financial support of Plansee SE, Plansee Composite Materials GmbH, and Oerlikon Balzers, Oerlikon Surface Solutions AG. In addition, we want to thank the X-ray center (XRC) of TU Wien for beam time as well as the electron microscopy center - USTEM TU Wien - for providing the SEM and TEM facilities. The authors acknowledge TU Wien Bibliothek for financial support through its Open Access Funding Programme.

Die approbierte gedruckte Originalversion dieser Dissertation ist an der TU Wien Bibliothek verfügbar.
The approved original version of this doctoral thesis is available in print at TU Wien Bibliothek.
TU Bibliothek Your knowledge hub WIEN

Appendix A

Table A1
Detailed overview of the deposition parameters, chemical composition and mechanical properties of the synthesised coatings.

Coating	Target	$f^{norm}_{[N2]}$	p_{dep}	T_S	f	t_{on}	U_S	Al/Me	N	H	E	σ	dep. Rate
		[−]	[Pa]	[°C]	[Hz]	[μs]	[V]	[−]	[at.%]	[GPa]	[GPa]	[GPa]	[nm/min]
$Ti_{0.54}Al_{0.46}N$	$Ti_{0.6}Al_{0.4}$	0.23	0.4	300	500	75	−50	0.46	52.5	36.4 ± 1.6	435 ± 10	−2.4 ± 0.019	22.1
$Ti_{0.54}Al_{0.46}N$		0.3						0.46	53	35.1 ± 1.5	406 ± 10	−1.2 ± 0.004	17.4
$Ti_{0.58}Al_{0.42}N$		1						0.42	55	32.6 ± 2.6	417 ± 16	−2.0 ± 0.001	10.8
$Ti_{0.41}Al_{0.59}N$	$Ti_{0.4}Al_{0.6}$	0.23						0.59	38.5	29.4 ± 0.7	380 ± 10	−0.4 ± 0.003	66.2
$Ti_{0.37}Al_{0.63}N$		0.3						0.63	51	36.1 ± 3.5	541 ± 35	−1.3 ± 0.011	50.6
$Ti_{0.41}Al_{0.59}N$		1						0.59	53	29.5 ± 1.9	300 ± 9	−2.5 ± 0.012	10.9

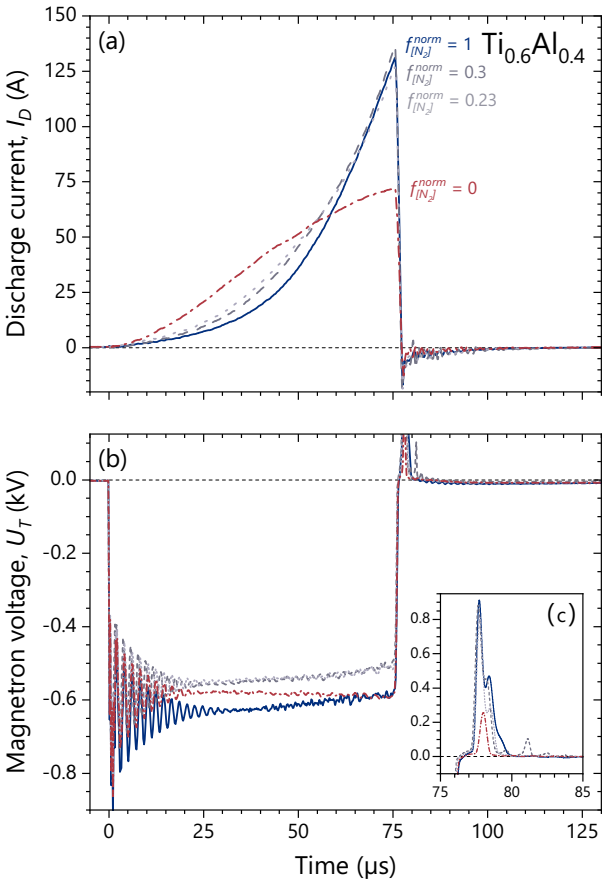

Fig. A1. Time-evolution of (a) the discharge current $I_D(t)$ and (b) the magnetron voltage on a $Ti_{0.6}Al_{0.4}$ target as functions of the applied nitrogen flow rate ratio $f^{norm}_{[N2]}$ for a pre-set pulse duration of 75 μs. Insert (c) shows details of the corresponding positive voltage overshoot recorded at the end of each pulse.

References

[1] D. Gall, C.S. Shin, T. Spila, M. Odén, M.J.H. Senna, J.E. Greene, I. Petrov, Growth of single-crystal CrN on MgO(001): effects of low-energy ion-irradiation on surface morphological evolution and physical properties, J. Appl. Phys. 91 (2002) 3589–3597, https://doi.org/10.1063/1.1446239.

[2] M. Lattemann, U. Helmersson, J.E. Greene, Fully dense, non-faceted 111-textured high power impulse magnetron sputtering TiN films grown in the absence of substrate heating and bias, Thin Solid Films 518 (2010) 5978–5980, https://doi.org/10.1016/j.tsf.2010.05.064.

[3] J.E. Greene, J.-E. Sundgren, L. Hultman, I. Petrov, D.B. Bergstrom, Development of preferred orientation in polycrystalline TiN layers grown by ultrahigh vacuum reactive magnetron sputtering ARTICLES YOU MAY BE INTERESTED IN, Appl. Phys. Lett. 67 (1995) 2928, https://doi.org/10.1063/1.114845.

[4] I. Petrov, P.B. Barna, L. Hultman, J.E. Greene, Microstructural evolution during film growth, J. Vac. Sci. Technol. A Vacuum, Surfaces, Film. 21 (2003) S117–S128, https://doi.org/10.1116/1.1601610.

[5] V. Kouznetsov, K. Macák, J.M. Schneider, U. Helmersson, I. Petrov, A novel pulsed magnetron sputter technique utilizing very high target power densities, Surf. Coat. Technol. 122 (1999) 290–293, https://doi.org/10.1016/S0257-8972(99)00292-3.

[6] J.T. Gudmundsson, N. Brenning, D. Lundin, U. Helmersson, High power impulse magnetron sputtering discharge, J. Vac. Sci. Technol. A 30 (2012), https://doi.org/10.1116/1.3691832, 030801.

[7] D. Lundin, J.T. Gudmundsson, T. Minea, High Power Impulse Magnetron Sputtering, Elsevier, 2020, https://doi.org/10.1016/C2016-0-02463-4.

[8] A.P. Ehiasarian, High-power impulse magnetron sputtering and its applications, Pure Appl. Chem. 82 (2010) 1247–1258, https://doi.org/10.1351/PAC-CON-09-10-43.

[9] K. Sarakinos, J. Alami, S. Konstantinidis, High power pulsed magnetron sputtering: a review on scientific and engineering state of the art, Surf. Coat. Technol. 204 (2010) 1661–1684, https://doi.org/10.1016/j.surfcoat.2009.11.013.

Die approbierte gedruckte Originalversion dieser Dissertation ist an der TU Wien Bibliothek verfügbar.
The approved original version of this doctoral thesis is available in print at TU Wien Bibliothek.
TU Bibliothek Your knowledge hub WIEN

[10] A.P. Ehiasarian, A. Vetushka, Y.A. Gonzalvo, G. Sáfrán, L. Székely, P.B. Barna, Influence of high power impulse magnetron sputtering plasma ionization on the microstructure of TiN thin films, J. Appl. Phys. 109 (2011), 104314, https://doi.org/10.1063/1.3579443.

[11] T. Kozák, A.D. Pajdarová, M. Čada, Z. Hubička, P. Mareš, J. Čapek, Ion energy distributions at substrate in bipolar HiPIMS: effect of positive pulse delay, length and amplitude, Plasma Sources Sci. Technol. 29 (2020), 065003, https://doi.org/10.1088/1361-6595/ab8fbb.

[12] J.A. Santiago, I. Fernández-Martínez, T. Kozák, J. Capek, A. Wennberg, J. M. Molina-Aldareguia, V. Bellido-González, R. González-Arrabal, M.A. Monclús, The influence of positive pulses on HiPIMS deposition of hard DLC coatings, Surf. Coat. Technol. 358 (2019) 43–49, https://doi.org/10.1016/j.surfcoat.2018.11.001.

[13] Batková, J. Čapek, J. Rezek, R. Čerstvý, P. Zeman, Effect of positive pulse voltage in bipolar reactive HiPIMS on crystal structure, microstructure and mechanical properties of CrN films Surf. Coat. Technol. 393 (2020) 125773. doi:https://doi.org/10.1016/j.surfcoat.2020.125773.

[14] G. Greczynski, J. Jensen, J. Böhlmark, L. Hultman, Microstructure control of CrNx films during high power impulse magnetron sputtering, Surf. Coat. Technol. 205 (2010) 118–130, https://doi.org/10.1016/j.surfcoat.2010.06.016.

[15] A. Anders, Tutorial: reactive high power impulse magnetron sputtering (R-HiPIMS), J. Appl. Phys. 121 (2017), 171101, https://doi.org/10.1063/1.4978350.

[16] S.M. Rossnagel, Gas density reduction effects in magnetrons, J. Vac. Sci. Technol. A Vacuum, Surfaces, Film. 6 (1988) 19–24, https://doi.org/10.1116/1.574988.

[17] A. Anders, J. Čapek, M. Hála, L. Martinu, The 'recycling trap': a generalized explanation of discharge runaway in high-power impulse magnetron sputtering, J. Phys. D. Appl. Phys. 45 (2012), 012003, https://doi.org/10.1088/0022-3727/45/1/012003.

[18] J. Čapek, S. Kadlec, Return of target material ions leads to a reduced hysteresis in reactive high power impulse magnetron sputtering: experiment, J. Appl. Phys. 121 (2017), 171911, https://doi.org/10.1063/1.4977816.

[19] A. Anders, Discharge physics of high power impulse magnetron sputtering, Surf. Coat. Technol. 205 (2011) S1–S9, https://doi.org/10.1016/J.SURFCOAT.2011.03.081.

[20] L. Zauner, P. Ertelthaler, T. Wojcik, H. Bolvardi, S. Kolozsvári, P.H. Mayrhofer, H. Riedl, Reactive HiPIMS deposition of Ti-Al-N: influence of the deposition parameters on the cubic to hexagonal phase transition, Surf. Coat. Technol. 382 (2020), 125007, https://doi.org/10.1016/j.surfcoat.2019.125007.

[21] J. Paulitsch, P.H. Mayrhofer, W.D. Münz, M. Schenkel, Structure and mechanical properties of CrN/TiN multilayer coatings prepared by a combined HIPIMS/UBMS deposition technique, Thin Solid Films 517 (2008) 1239–1244, https://doi.org/10.1016/j.tsf.2008.06.080.

[22] M. Samuelsson, D. Lundin, J. Jensen, M.A. Raadu, J.T. Gudmundsson, U. Helmersson, On the film density using high power impulse magnetron sputtering, Surf. Coat. Technol. 205 (2010) 591–596, https://doi.org/10.1016/j.surfcoat.2010.07.041.

[23] T. Shimizu, H. Komiya, Y. Teranishi, K. Morikawa, H. Nagasaka, M. Yang, Pressure dependence of (Ti, Al)N film growth on inner walls of small holes in high-power impulse magnetron sputtering, Thin Solid Films 624 (2017) 189–196, https://doi.org/10.1016/j.tsf.2016.09.041.

[24] M. Balzer, M. Fenker, Three-dimensional thickness and property distribution of TiC films deposited by DC magnetron sputtering and HIPIMS, Surf. Coat. Technol. 250 (2014) 37–43, https://doi.org/10.1016/j.surfcoat.2014.02.011.

[25] G. Greczynski, I. Zhirkov, I. Petrov, J.E. Greene, J. Rosen, Control of the metal/gas ion ratio incident at the substrate plane during high-power impulse magnetron sputtering of transition metals in Ar, Thin Solid Films 642 (2017) 36–40, https://doi.org/10.1016/j.tsf.2017.09.027.

[26] G. Greczynski, I. Petrov, J.E. Greene, L. Hultman, Strategy for tuning the average charge state of metal ions incident at the growing film during HIPIMS deposition, Vacuum. 116 (2015) 36–41, https://doi.org/10.1016/j.vacuum.2015.02.027.

[27] D. Lundin, M. Čada, Z. Hubička, Ionization of sputtered Ti, Al, and C coupled with plasma characterization in HiPIMS, Plasma Sources Sci. Technol. 24 (2015), 035018, https://doi.org/10.1088/0963-0252/24/3/035018.

[28] N. Britun, S. Konstantinidis, R. Snyders, An overview on time-resolved optical analysis of HiPIMS discharge, Plasma Process. Polym. 12 (2015) 1010–1027, https://doi.org/10.1002/ppap.201500051.

[29] G. Greczynski, L. Hultman, Time and energy resolved ion mass spectroscopy studies of the ion flux during high power pulsed magnetron sputtering of Cr in Ar and Ar/N2 atmospheres, Vacuum. 84 (2010) 1159–1170, https://doi.org/10.1016/j.vacuum.2010.01.055.

[30] M. Palmucci, N. Britun, T. Silva, R. Snyders, S. Konstantinidis, Mass spectrometry diagnostics of short-pulsed HiPIMS discharges, J. Phys. D. Appl. Phys. 46 (2013), 215201, https://doi.org/10.1088/0022-3727/46/21/215201.

[31] A. Ferrec, J. Keraudy, S. Jacq, F. Schuster, P.Y. Jouan, M.A. Djouadi, Correlation between mass-spectrometer measurements and thin film characteristics using dcMS and HiPIMS discharges, Surf. Coat. Technol. 250 (2014) 52–56, https://doi.org/10.1016/j.surfcoat.2014.02.030.

[32] J. Bohlmark, M. Lattemann, J.T. Gudmundsson, A.P. Ehiasarian, Y. Aranda Gonzalvo, N. Brenning, U. Helmersson, The ion energy distributions and ion flux composition from a high power impulse magnetron sputtering discharge, Thin Solid Films 515 (2006) 1522–1526, https://doi.org/10.1016/j.tsf.2006.04.051.

[33] G. Greczynski, I. Zhirkov, I. Petrov, J.E. Greene, J. Rosen, Time evolution of ion fluxes incident at the substrate plane during reactive high-power impulse magnetron sputtering of groups IVb and VIb transition metals in Ar/N 2, J. Vac. Sci. Technol. A 36 (2018), 020602, https://doi.org/10.1116/1.5016241.

[34] G. Greczynski, J. Lu, M.P. Johansson, J. Jensen, I. Petrov, J.E. Greene, L. Hultman, Role of tin+ and Aln+ ion irradiation (n=1, 2) during Ti1-xAlxN alloy film growth in a hybrid HIPIMS/magnetron mode, Surf. Coat. Technol. 206 (2012) 4202–4211, https://doi.org/10.1016/j.surfcoat.2012.04.024.

[35] G. Greczynski, I. Petrov, J.E. Greene, L. Hultman, Paradigm shift in thin-film growth by magnetron sputtering: from gas-ion to metal-ion irradiation of the growing film, J. Vac. Sci. Technol. A 37 (2019), 060801, https://doi.org/10.1116/1.5121226.

[36] G. Greczynski, S. Mráz, M. Hans, J. Lu, L. Hultman, J. Schneider, Control over the phase formation in metastable transition metal nitride thin films by tuning the Al+ subplantation depth, Coatings. 9 (2018) 17, https://doi.org/10.3390/coatings9010017.

[37] M. Lattemann, A.P. Ehiasarian, J. Bohlmark, P.Å.O. Persson, U. Helmersson, Investigation of high power impulse magnetron sputtering pretreated interfaces for adhesion enhancement of hard coatings on steel, Surf. Coat. Technol. 200 (2006) 6495–6499, https://doi.org/10.1016/j.surfcoat.2005.11.082.

[38] A.P. Ehiasarian, J.G. Wen, I. Petrov, Interface microstructure engineering by high power impulse magnetron sputtering for the enhancement of adhesion, J. Appl. Phys. 101 (2007), https://doi.org/10.1063/1.2697052.

[39] G. Greczynski, J. Lu, J. Jensen, I. Petrov, J.E. Greene, S. Bolz, W. Kölker, C. Schiffers, O. Lemmer, L. Hultman, Metal versus rare-gas ion irradiation during Ti1-xAlxN film growth by hybrid high power pulsed magnetron/dc magnetron co-sputtering using synchronized pulsed substrate bias, J. Vac. Sci. Technol. A 30 (2012), 061504, https://doi.org/10.1116/1.4750485.

[40] N. Nedfors, O. Vozniy, J. Rosen, Effect of synchronized bias in the deposition of TiB 2 thin films using high power impulse magnetron sputtering, J. Vac. Sci. Technol. A Vacuum, Surfaces, Film. 36 (2018), 031510, https://doi.org/10.1116/1.5003194.

[41] B. Bakhit, I. Petrov, J.E. Greene, L. Hultman, J. Rosén, G. Greczynski, Controlling the B/Ti ratio of TiB x thin films grown by high-power impulse magnetron sputtering, J. Vac. Sci. Technol. A Vacuum, Surfaces, Film. 36 (2018), 030604, https://doi.org/10.1116/1.5026445.

[42] W. Münz, Titanium aluminum nitride films: a new alternative to TiN coatings, J. Vac. Sci. Technol. A 4 (1986) 2717–2725, https://doi.org/10.1116/1.573713.

[43] O. Knotek, T. Leyendecker, On the structure of (Ti, Al)N-PVD coatings, J. Solid State Chem. 70 (1987) 318–322, https://doi.org/10.1016/0022-4596(87)90071-5.

[44] P.H. Mayrhofer, D. Music, J.M. Schneider, Influence of the Al distribution on the structure, elastic properties, and phase stability of supersaturated Ti1−xAlxN, J. Appl. Phys. 100 (2006), 094906, https://doi.org/10.1063/1.2360778.

[45] L. Chen, Y. Du, P.H. Mayrhofer, S.Q. Wang, J. Li, The influence of age-hardening on turning and milling performance of Ti-Al-N coated inserts, Surf. Coat. Technol. 202 (2008) 5158–5161, https://doi.org/10.1016/j.surfcoat.2008.05.036.

[46] L. Chen, M. Moser, Y. Du, P.H. Mayrhofer, Compositional and structural evolution of sputtered Ti-Al-N, Thin Solid Films 517 (2009) 6635–6641, https://doi.org/10.1016/j.tsf.2009.04.056.

[47] K. Kutschej, P.H. Mayrhofer, M. Kathrein, P. Polcik, R. Tessadri, C. Mitterer, Structure, mechanical and tribological properties of sputtered Ti1-xAlxN coatings with $0.5 \leq x \leq 0.75$, Surf. Coat. Technol. 200 (2005) 2358–2365, https://doi.org/10.1016/j.surfcoat.2004.12.008.

[48] L. Chen, J. Paulitsch, Y. Du, P.H. Mayrhofer, Thermal stability and oxidation resistance of Ti–Al–N coatings, Surf. Coat. Technol. 206 (2012) 2954–2960, https://doi.org/10.1016/j.surfcoat.2011.12.028.

[49] G. Greczynski, J. Lu, J. Jensen, S. Bolz, W. Kölker, C. Schiffers, O. Lemmer, J. E. Greene, L. Hultman, A review of metal-ion-flux-controlled growth of metastable TiAlN by HIPIMS/DCMS co-sputtering, Surf. Coat. Technol. 257 (2014) 15–25, https://doi.org/10.1016/j.surfcoat.2014.01.055.

[50] C.L. Chang, F.C. Yang, Effect of target composition on the microstructural, mechanical, and corrosion properties of TiAlN thin films deposited by high-power impulse magnetron sputtering, Surf. Coat. Technol. 352 (2018) 330–337, https://doi.org/10.1016/j.surfcoat.2018.08.023.

[51] S. Severin, M. Naveed, S. Weiß, Effect of HPPMS pulse-frequency on plasma discharge and deposited AlTiN coating properties, Adv. Mater. Sci. Eng. (2017) 18, https://doi.org/10.1155/2017/4850908.

[52] G. Greczynski, S. Mráz, M. Hans, D. Primetzhofer, J. Lu, L. Hultman, J. M. Schneider, Unprecedented Al supersaturation in single-phase rock salt structure VAlN films by Al+subplantation, J. Appl. Phys. 121 (2017), 171907, https://doi.org/10.1063/1.4977813.

[53] G. Greczynski, S. Mráz, L. Hultman, J.M. Schneider, Selectable phase formation in VAlN thin films by controlling Al+ subplantation depth, Sci. Rep. 7 (2017) 17544, https://doi.org/10.1038/s41598-017-17846-5.

[54] D.R. Lide, CRC Handbook of Chemistry and Physics, 84th ed., CRC Press, 2003.

[55] Hiden Analytical Ltd. EQP and EQS Analysers, (n.d.). https://www.hiden.de/wp-content/uploads/pdf/EQP_and_EQS_-_Hiden_Analytical_Techinical_Inofrmation.pdf (accessed November 26, 2020).

[56] Private communications between Hiden Analytical Ltd. and T. Kozák, (2019).

[57] M. Klinger, A. Jäger, Crystallographic tool box (CrysTBox): automated tools for transmission electron microscopists and crystallographers, J. Appl. Crystallogr. 48 (2015) 2012–2018, https://doi.org/10.1107/S1600576715017252.

[58] G.M. Pharr, An improved technique for determining hardness and elastic modulus using load and displacement sensing indentation experiments, J. Mater. Res. 7 (1992) 1564–1583, https://doi.org/10.1557/JMR.1992.1564.

[59] G.C.A.M. Janssen, M.M. Abdalla, F. van Keulen, B.R. Pujada, B. van Venrooy, Celebrating the 100th anniversary of the Stoney equation for film stress: developments from polycrystalline steel strips to single crystal silicon wafers, Thin Solid Films 517 (2009) 1858–1867, https://doi.org/10.1016/j.tsf.2008.07.014.

Die approbierte gedruckte Originalversion dieser Dissertation ist an der TU Wien Bibliothek verfügbar.
The approved original version of this doctoral thesis is available in print at TU Wien Bibliothek.
TU Bibliothek Your knowledge hub WIEN

[60] D. Depla, X.Y. Li, S. Mahieu, R. De Gryse, Determination of the effective electron emission yields of compound materials, J. Phys. D. Appl. Phys. 41 (2008), https://doi.org/10.1088/0022-3727/41/20/202003.
[61] F. Magnus, O.B. Sveinsson, S. Olafsson, J.T. Gudmundsson, Current-voltage-time characteristics of the reactive Ar/N 2 high power impulse magnetron sputtering discharge, J. Appl. Phys. 110 (2011), 083306, https://doi.org/10.1063/1.3653233.
[62] J.Y. Rauch, C. Rousselot, N. Martin, Structure and composition of TixAll-xN thin films sputter deposited using a composite metallic target, Surf. Coat. Technol. 157 (2002) 138–143, https://doi.org/10.1016/S0257-8972(02)00146-9.
[63] S. Inoue, H. Uchida, A. Hioki, K. Koterazawa, R.P. Howson, Structure and composition of (Ti, Al)N films prepared by r.f. planar magnetron sputtering using a composite target, Thin Solid Films 271 (1995) 15–18, https://doi.org/10.1016/0040-6090(95)06817-1.
[64] A.D. Pajdarová, J. Vlček, P. Kudláček, J. Lukáš, Electron energy distributions and plasma parameters in high-power pulsed magnetron sputtering discharges, Plasma Sources Sci. Technol. 18 (2009), https://doi.org/10.1088/0963-0252/18/2/025008, 025008.
[65] ICDD, Powder Diffraction File - wurtzite AlN - 04-016-3965, (2013).
[66] D. Gall, S. Kodambaka, M.A. Wall, I. Petrov, J.E. Greene, Pathways of atomistic processes on TiN(001) and (111) surfaces during film growth: an ab initio study, J. Appl. Phys. 93 (2003) 9086–9094, https://doi.org/10.1063/1.1567797.
[67] L. Hultman, J.E. Sundgren, J.E. Greene, Formation of polyhedral N 2 bubbles during reactive sputter deposition of epitaxial TiN(100) films, J. Appl. Phys. 66 (1989) 536–544, https://doi.org/10.1063/1.343570.
[68] G. Greczynski, J. Lu, J. Jensen, I. Petrov, J.E. Greene, S. Bolz, W. Kölker, C. Schiffers, O. Lemmer, L. Hultman, Strain-free, single-phase metastable Ti0.38Al0.62N alloys with high hardness: metal-ion energy vs. momentum effects during film growth by hybrid high-power pulsed/dc magnetron cosputtering, Thin Solid Films 556 (2014) 87–98, https://doi.org/10.1016/j.tsf.2014.01.017.
[69] ICDD, Powder diffraction file - cubic TiN - 00-038-1420, (1970).
[70] ICDD, Powder diffraction file - cubic AlN - 00-025-1495, (1970).
[71] ICDD, Powder diffraction file - cubic Si - 00-027-1402, (2017) 7–8.

Die approbierte gedruckte Originalversion dieser Dissertation ist an der TU Wien Bibliothek verfügbar.
The approved original version of this doctoral thesis is available in print at TU Wien Bibliothek.